2013

A study of coverage optimized planning incorporating models of geometric uncertainties for prostate cancer

Huijun Xu
Virginia Commonwealth University

A study of coverage optimized planning incorporating models of geometric uncertainties for prostate cancer

A thesis dissertation submitted in partial fulfillment of the requirements for the degree of Doctor of Philosophy at Virginia Commonwealth University.

by

Huijun Xu
Bachelor of Science, Shanghai Jiao Tong University, June 2008

Director: Jeffrey V. Siebers, Ph.D.
Professor and Director, Medical Physics Graduate Program
Department of Radiation Oncology

Virginia Commonwealth University
Richmond, Virginia
May, 2013

Acknowledgements

I would like to thank my advisor, Dr. Jeffrey Siebers, for guiding me through all these years from the very beginning when I was totally new to this research. I am thankful to have leant how to discover, handle and solve problems efficiently from him. I also want to thank my thesis committee members, Drs. John Gordon, Geoffrey Hugo, Jianqiao Luo and Nitai Mukhopadhyay for being supportive and offering helpful insights. Particular thanks to Dr. Gordon who has developed the basic but robust software for me to start with and guided me to finish many interesting projects.

Thanks to NKI for providing patient database for this dissertation. Thanks to Dr. Elisabeth Weiss for contouring all the structures on the images. Thanks to Dr. Gary Christensen for developing the deformable registration algorithm. Also, thanks to NIH and Phillips for providing financial support.

Thanks to my current and previous VCU coworkers, Douglas Vile (especially for his great contribution in PCA code and results), Tyler Watkins, Nahla Sayah, Drs. Manju Sharma, Syed Naeem, Joseph Gardner, Joseph Moore, Mirek Fatyga, Baoshe Zhang and etc. Without your academic, technical or moral support, I may not finish everything on time.

Last but not least, I want to thank my parents and my boyfriend for trusting and caring me with no conditions.

Table of Contents

Acknowledgements ii

Table of Contents iii

List of Tables vii

List of Figures x

List of Abbreviations xxi

Abstract xxiii

1 Introduction 1

1.1 Introduction to GUs in external beam radiation therapy 2

1.1.1 External beam radiation therapy for prostate cancer 2

1.1.2 GUs and their models 5

1.2 Evolution of treatment planning approaches 11

1.2.1 Margin-based planning 11

1.2.2 Probabilistic treatment planning 13

1.2.3 Coverage optimized planning 14

1.2.4 COP in different clinical scenarios 15

1.3 Thesis Objectives and Outlines 16

2 The principle of coverage optimized planning 18

2.1 From IMRT to COP 18

2.2 The starting point — optimization criteria 21
2.3 The central concept — objective functions 23
2.4 Types of objective functions 26
2.4.1 Dose-based objectives 26
2.4.2 Dose-volume based objectives 28
2.4.3 pDVH based objective 29
2.5 Implementation of objective functions in a commercial TPS 33
2.5.1 Reformatted objective functions 33
2.5.2 Beam fluence initialization for COP 34
2.6 Summary 35
3 Metrics for plan evaluation 36
3.1 Dosimetric endpoint: dose-volume metrics 36
3.2 Dosimetric endpoint: coverage probability 39
3.2.1 Coverage probability estimation method: DVCM 40
3.2.2 Coverage probability estimation method: DMD 41
3.3 Biological endpoints: BED, EUD, TCP and NTCP 43
3.3.1 Basic radiobiology: cell survival curves and fractionated dose 44
3.3.2 Equivalent uniform dose 46
3.3.3 Tumor control probability 47
3.3.4 Normal tissue complication probability 48
3.4 Summary 50
4 General materials and methods for COP Study 52
4.1 Patient database and IMRT planning 52

4.2 Software (GUI) for COP study 55
4.3 Planning techniques for comparison 60
4.4 Sensitivity of coverage estimates to treatment courses sampling 62
4.4.1 Accuracy tests 62
4.4.2 Precision tests 64
5 COP to account for interfraction deformable motions 67
5.1 Prostate plans 68
5.2 GU models for deformable organ motions 69
5.2.1 Simple surface variation (SSV) model 70
5.2.2 Principal component analysis (PCA) model 73
5.3 Decision flow to use COP 83
5.4 Results 85
5.4.1 Dosimetric effects on zero-PTV-margin plans 85
5.4.2 COP plans vs. OM plans vs. FM plans 88
5.5 Conclusions 94
6 COP to account for delineation uncertainties 95
6.1 Prostate plans 96
6.1.1 ASSD model 96
6.2 Decision flow to use COP 102
6.3 Results 103
6.3.1 Dosimetric effects on zero-PTV-margin plans 103
6.3.2 COP plans vs. OM plans vs. FM plans 105
6.4 Conclusions 109

7 Discussion, conclusions and future directions 110

7.1 Discussion and Conclusions of COP studies 110

7.1.1 Discussion 110

7.1.2 Conclusions 117

7.2 Future directions of COP studies 118

7.2.1 Realistic clinical implementation issues 118

7.2.2 COP in different IGART strategies 119

7.2.3 Bladder and rectal wall as OAR for prostate cancer 120

7.2.4 Different treatment sites 120

List of References 122

Appendix I. Patient-specific pDVH results of COP studies 131

a. pDVH evaluation with deformable motion model (PCA) incorporated 131

b. Optimized plan comparison with deformable motion model (PCA) incorporated 142

c. pDVH evaluation with delineation uncertainties model (ASSD) incorporated 153

d. Optimized plan comparison with delineation uncertainties model (ASSD) incorporated 164

Appendix II. Related projects 174

a. Plugins developed for IGART plan evaluation 174

b. Coverage estimates vs. dosimetric margin distribution sampling parameters .. 178

c. Interobserver contour variations with respect to margin size 188

d. Bladder wall characteristics 213

Vita 232

List of Tables

Table I. NCCN Risk Groupings on prostate cancer staging (T1-T4) and PSA. (National Comprehensive Cancer Network (NCCN Clinical Practice Guidelines in Oncology v.1.2005).... 2

Table II. Some published models of interfraction, intrafraction variations for prostate, bladder, and rectum. 9

Table III. IMRT optimization criteria of ROIs used for COP and conventional PTV plans. Doses (D) are in the unit gray (Gy). Subscript is percentage volume +/- coverage value. Read $D_{98,95}$ as 98% of volume receiving $\geqslant$ 78 Gy for 95% of simulated treatment courses. Criterion weights are shown in square brackets. PTV1 = $CTV_{prostate}$ + PTV margin and PTV2 = CTV_{SV} + PTV margin. 22

Table IV. Dose-volume metrics that can be obtained from a DVH curve..... 37

Table V. A summary of TCP and NTCP model and parameters for prostate, bladder and rectum used in this dissertation. Note conventionally TCP or NTCP value is calculated for a PTV or PRV volume. Here, TCP or NTCP distribution for a CTV or OAR volume is a novel way to account for GUs 50

Table VI. Summary of metrics for plan evaluation used in this dissertation. All have the con that 3D information is lost..... 51

Table VII. The main functions of the functioning tabs of DVC GUI..... 56

Table VIII. The $|\Delta D_{v,q,precision}|_{max}$ based on repeated estimation of $D_{v,q}$ for 7-10 times for the zero-PTV-margin plan and the COP plan with PCA/ASSD model incorporated for Patient A and S..... 65

Table IX. The mean and the percentage SD relative to mean (%SD) of ROI volumes over all image sets for each patient with ID A-S of the patient database 69

Table X: The mean and SD values of the correlation coefficients between volumes and centroid distances of ROI for 19 NKI patients. Highly correlated variables are highlighted..... 72

Table XI. Patient ID, percentage target dose degradation $\%\Delta D_{98,95}$ for $CTV_{prostate}$ (P) and CTV_{SV} (S), the optimized PTV margins obtained by OM technique, and best planning technique and its gain relative to the other two plans in terms of target dose coverage($D_{98,95}$) , normal tissue coverage ($D_{v,5}$) and probability of complication free control P+. ID with */ † / ‡ denotes COP / OM / FM plan that fails to achieve target $D_{98,95}$ 89

Table XII. Good, moderate and bad changes resulting from COP_{OM} relative to OM 90

Table XIII: SD values in (mm) of in RL (x), PA (y) and SI (z) direction used in ASSD model for ROIs of prostate cancer patients..... 98

Table XIV . Patient ID, percentage target dose degradation $\%\Delta D_{98,95}$ for prostate (P) and seminal vesicles (S), the optimized PTV margins obtained by OM technique, and best planning technique and its gain relative to the other two plans in terms of target dose coverage($D_{98,95}$) and probability of complication free control P+. Patient with */ † / ‡ are those COP / OM / FM plans that fails to achieve target $D_{98,95}$ 106

Table XV. Monitor unit per fraction for COP, OM or FM plan for patients with ID A to S when accommodating deformable motions (modeled by PCA) or delineation uncertainties (modeled by ASSD). 111

Table XVI. Workflow of HXCBCD plugin for copying plan to treatment fractions. 175

List of Figures

Figure 1. EBRT for prostate cancer treatment. (adapted from Patient Health International, © AstraZeneca 2012) 3

Figure 2: A sketch of fluence intensity of 3 beams in an IMRT for prostate cancer treatment. High beam intensity (and therefore high dose) is delivered to the target prostate (red) and low beam intensity (and low dose) is delivered to the surrounding bladder (yellow) and rectum (magenta). 3

Figure 3: Schematic representations of relationship between volumes GTV, CTV, PTV for target structures and OAR, PRV for surrounding normal tissues. 6

Figure 4: Illustration of different types of GUs: (a) setup errors that fail to align patient position to the beam treatment head of LINAC (linear accelerator), (b) inter-observer delineation uncertainties for the same structures, (c) organ motion and deformation that may occur between treatment fractions (interfraction organ variations) or during a single treatment fraction at different treatment fractions (intrafraction organ variations). 7

Figure 5. An illustration of 3-beam 3D-CRT (left) versus IMRT (right). 19

Figure 6. Workflow of how a pDVH of coverage probability q are determined (a–c) and how COP performs optimization (a-d) based on pDVH criteria by simulating n_{tx} virtual treatment courses, each with n_{frac} fractions. (a) For each fraction of a virtual treatment course, find the total offset (black arrow) for all the GUs of each voxel in the ROI (black thick circle) and get the dose

for the displaced voxel, assuming shift-invariance for dose distribution (illustrated as grey thin solid isodose lines). (b) Get n_{tx} accumulative ROI DVHs over all the fractions. (c) The n_{tx} DVH samples are converted into a dose volume coverage map (DVCM), as a 2D grid built with many small grid squares. Each grid square will be assigned a probability value equivalent to the percentile value of DVHs that lie left to this grid squares, according to the distribution of DVH samples. A virtual DVH of a certain percentile value (i.e., coverage) q, namely pDVH of q, can be determined on this map. (d) pDVH criteria (such as $Pr[D_v \geqslant d] \geqslant q$) are used to optimize the dose distribution with the goal of achieving dose-volume metric D_v in the presence of q of GUs. 20

Figure 7. The converged composite objective value (vertical axis) as a function of iterations during the progress of optimization in the case that optimization terminates (a) when constraints and objectives are reasonably met as to the stopping tolerance and (b) when further iteration is determined as helpless. 25

Figure 8. Graphical illustration of variables for (left) a minimum DVH objective (with goal $D_{v_{Rx}} \geq D_{Rx}$) and a maximum DVH objective (with goal $D_{v_{Rx}} \leq D_{Rx}$) The blue curve and the black curve represent desired DVH and current DVH. $D_{v_{Rx}}$ and D_{Rx} are the current and prescription dose to the prescription volume v_{Rx}. The purpose of this DVH objective is to have the DVH $(D_{v_{Rx}}, v_{Rx})$ optimized to the desirable location (D_{Rx}, v_{Rx}). The red shaded region is the penalty region..... 28

Figure 9. Graphical illustration of variables for a minimum pDVH objective (left) and a maximum pDVH objective (right) in the form of $Pr[D_{C_{Rx}} \geq D_{Rx}] \geq q_{Rx}$ and $Pr[D_{C_{Rx}} \leq D_{Rx}] \geq 1 - q_{Rx}$. The blue curve and the black curve represent desired pDVH and current pDVH of coverage

value q_{Rx}. $D_{C_{Rx}}$ and D_{Rx} are the current and prescription dose to the prescription volume v_{Rx}. The purpose of this pDVH objective is to pull the pDVH from ($D_{C_{Rx}}$, v_{Rx}) to the desirable location (D_{Rx}, v_{Rx}) on the pDVH plot. 30

Figure 10. Two examples of (a) a simple (cumulative) DVH comparison and (b) a complex DVH comparison between A and B. Example (b) is complex because two DVHs of same ROI can have same (i.e., min, average and max) dose metrics. 38

Figure 11. Example of how a ROI DVCM is generated for a simple case with only two virtual treatment courses. Get DVH (grey lines) with different GU(s) for each treatment course. For each DVH, increment all grid squares lying below or to the left of the DVH by 1.0. Then normalize the whole grid values. 41

Figure 12. Examples of DMD sampled using fixed angular increment method for (a) CTV $D_{min, 79.2}$(type I), (b) bladder $D_{25, 70}$ (type I) and (d) bladder $D_{25, 70}$ (type II) (Xu *et al.* 2011) 42

Figure 13. Qualitative dependence of coverage probability Q on systematic SD for type I targets and type I/II OAR. (Xu *et al.* 2011) 43

Figure 14. Illustration of (upper) cell survival curve of dose D versus survival fraction S when the α/β ratio = 3 and (lower) example of different cell survival curve of early and late response tissues. 45

Figure 15. A transverse view of IMRT plan settings shared in COP studies: a typical seven-beam arrangement (red lines) with the beam isocenter located at prostate centroid (small red circle in the middle). The dose grid that always covers prostate (red contour), seminal vesicles (green contour), bladder (yellow contour) and rectum (magenta contour) is indicated by the dashed green box. 54

Figure 16. DVC GUI flow for performing COP or margin-based treatment planning (MP) +/- probabilistic plan evaluation by computing and plotting specified pDVHs and/or TCP/NTCP distribution. Colored arrows indicate the flow for the item listed in the same color. The details are described in the text. 57

Figure 17. Interface of DVC GUI tabs: (upper) Tab 1 "Optimization" which is used to set the criteria used for optimization; (middle) Tab 2 " GU Models" used to set the GU models used for COP optimization or plan probabilistic evaluation; (lower) Tab 3 "End Points" used to set the TCP/NTCP model and parameters to calculate TCP/NTCP distribution for probabilistic evaluation and plot it in "Outcomes" tab. The primary GUI design is done by Dr. John James Gordon. (copyright JJ Gordon 2011©, copyright H Xu 2013©)..... 58

Figure 18. Interface of DVC GUI tabs: (upper) Tab 4 "Evaluation" that determines the pDVHs to be plotted in "GU Models" tab; (middle) Tab 5 " GU Models" that plots pDVHs of multiple ROIs on multiple trials (plans) with criteria highlighted as triangles. Here, dose is displayed in the unit cGy while 1 cGy = 0.01 Gy. (lower) Tab 8 "Outcomes" that plots distribution of TCP and NTCP for multiple ROIs on multiple trials (plans). For both Tab 5 and Tab 8, legends are displayed on the left showing pDVH or TCP/NTCP of different ROIs (with different color) on different trials (solid or dashed). (copyright JJ Gordon 2011©, copyright H Xu 2013©) 59

Figure 19. Workflow of COP versus OM and FM planning technique to account for GUs e.g., interfraction organ deformable motions for high-risk prostate cancer patients. Abbreviation: tgt = target, SV = seminal vesicles, PTV1 = $CTV_{prostate}$ + PTV margin of $CTV_{prostate}$ and PTV2 = CTV_{SV} + PTV margin of CTV_{SV}. The PTV margins used in FM for all the patients are

empirically determined based on literature. Here, 5mm for PTV1 and 8mm for PTV2 are an example for the study to accommodate interfraction organ deformable motions. 60

Figure 20. Flow diagram of margin iteration of the OM planning technique used in this dissertation. The PTV margins for $CTV_{prostate}$ and CTV_{SV} are initialized as 0mm and then iteratively adjusted to achieve prescribed $D_{98,95}$ for both $CTV_{prostate}$ and CTV_{SV}. PTV margin is increased by 1mm for the next iteration for any CTV whose $D_{98,95}$ is lower than the prescribed value. If one CTV achieves prescribed $D_{98,95}$ while the other fails, PTV margin for the CTV with desirable $D_{98,95}$ remains the same in the next iteration. 61

Figure 21. $|\Delta D_{98,95\_1000}|$ of $CTV_{prostate}$ (red) and CTV_{SV} (green) as a function of N_{tx} (number of simulated virtual treatment courses) for the zero-PTV margin plan ((a),(c)) and the COP ((b),(d)) plan of patient A (solid lines) and S (dashed lines). The patient-specific PCA model is incorporated to consider deformable motions in (a) and (b) while the patient-specific ASSD model in incorporated to consider delineation uncertainties. 63

Figure 22. $|\Delta D_{v,q\_1000}|$ of OAR of Patient A (left) and S (right) when N_{tx} = 500. $|\Delta D_{v,q\_1000}|$ is obtained for COP plan (blue) and zero-PTV-margin plan (red) with the PCA model incorporated consider deformable motions, and COP plan (green) and zero-PTV-margin plan (purple) with the ASSD model incorporated to consider delineation uncertainties. $|\Delta D_{v,q\_1000}|$ is small in the high dose region and gets larger in the low dose region. 64

Figure 23. The repeated estimated pDVHs 95% (solid lines) and 5% (dashed lines) of $CTV_{prostate}$ (red), CTV_{SV} (green), bladder (yellow) and rectum (magenta) based on the simulations using 1000 virtual treatment courses repeated for 7 times. The differences between the repeated pDVHs are very small. 65

Figure 24. An illustration of how to obtain a new position of surface voxel of a ROI (other than $CTV_{prostate}$) (S_{ROI}') based on a SSV model. As $CTV_{prostate}$-centroid alignment is assumed, the centroid position of $CTV_{prostate}$, old as $C_{CTVprostate}$ and new as $C_{CTVprostate}$', is always known. By sampling a new position of the ROI centroid (C_{ROI}'), the new centroid distance between ROI and $CTV_{prostate}$, ($CD_{ROI-P'}$) and ROI centroid offset (ΔC_{ROI}) can be calculated. Assume that ROI volume change (ΔV_{ROI}) is a function of $CD_{ROI-P'}$, ΔV_{ROI}, and ΔC_{ROI} can be used to estimate the surface point change relative to old position (S_{ROI}) so that S_{ROI}' can be therefore determined. *Abbreviation: P = $CTV_{prostate}$* 70

Figure 25. (a) (Upper panel) The linear, quadratic and cubic fitting of centroid distance between bladder and prostate in z axis $CD_{B-P,z}$ to bladder volume V_B. (Lower panel) The corresponding residual error for the three types of fitting. (b) Histogram of the distribution of residual error over 19 patients and its general Gaussian fit. 73

Figure 26. Illustration of a DVF between reference image set *R* and fractional image set *F* and dose mapping process. Due to the effects of GUs, the shape and position of a ROI change on different image sets (i.e., elliptical on *R* and triangle on *F*). Image *R* and *F* are not necessarily in the same domain. Denote g and h the coordinates in image *R* and *F*, respectively. The geometric transformation between g and h are represented by DVF(g) in the equation g + DVF(g) = h, which relates the intensity R(g) and F(h). For the dose mapping, dose to h is mapped back to g for i.e., dose accumulation of a multi-fractional treatment course. 74

Figure 27. Workflow of construction of a patient-specific PCA model. KDE=kernel density estimator. See the following text for detailed description. 75

Figure 28. An example of coefficient PDF (black thicker line) for l^{th} eigenvector based on KDE using Gaussian kernels of the coefficient data samples (dashed lines). (Modified from Douglas Vile, VCU graduate student) 80

Figure 29. (a) The total fraction of geometric variability $\bar{\lambda}$ as a function of top eigenmode number with 90% threshold line to determine L. (b) Top eigenmode number L used for PCA model for 19 patients. 80

Figure 30. A patient example of pDVH comparisons of zero PTV-margin plans planned (upper) on the $CTV_{prostate}$ centroid aligned anatomy (COM: thick lines) versus on the mean geometry (Mean: thin lines), and (lower) on the $CTV_{prostate}$ centroid aligned anatomy (COM: thick lines) versus bony aligned anatomy (Bony: thin lines). pDVH is obtained from 1000 virtual treatment courses. For target structures $CTV_{prostate}$ (red) and CTV_{SV} (green), pDVH 95% is desired to lie upper or right to the objective values which are denoted by right triangle of corresponding color. For rectum (magenta) and bladder (orange), pDVH 5% is desired to lie lower or left to the objective values which are denoted as the right triangle of corresponding color. pDVH 95% and pDVH 5% are both plotted for each structure to examine the 90% confidence interval of DVH distribution with PCA model incorporated. 82

Figure 31. A patient example of pDVH 95%(solid) and pDVH 5% (dashed) of zero PTV-margin plans obtained from 1000 virtual treatment courses using 1 times (thick) versus (thin) 5 times magnitude of PCA-modeled synthetic DVF for a $CTV_{prostate}$-centroid-aligned anatomy. 83

Figure 32. Decision flow of COP to optimize treatment plans to consider organ deformable motions for prostate cancer patients compared with optimized margin (OM) and fixed margin planning techniques. 84

Figure 33. The average pDVHs 95% (solid) and pDVHs 5% (dashed) evaluated on zero-PTV-margin plans through 19 high-risk prostate cancer patients for anatomies $CTV_{prostate}$ (prostate) (red), CTV_{SV} (green), bladder (orange) and rectum (magenta) with optimization objectives (triangle markers). The PCA model is incorporated to show the dosimetric consequence of organ deformable motions. 86

Figure 34. (a) Percentage degraded dose ($\%\Delta D_{98,95}$) and (b) DVH variability ($\%\Delta DVH_{98,5-95}$) at prescribed dose of $CTV_{prostate}$ (red bins) and CTV_{SV} (green bins) for 19 zero-PTV-margin plans with organ deformable motions considered (using PCA model). 87

Figure 35. Scatter plot of percentage degraded dose ($\%\Delta D_{98,95}$) versus DVH variability ($\%\Delta DVH_{98,5-95}$) for (a) $CTV_{prostate}$ (red dots) and (b) CTV_{SV} (green dots) on 19 zero-PTV-margin plans evaluated with PCA model incorporated for each patient. 88

Figure 36. An example of increasing competition between target and OAR criteria with increasing PTV margins during OM optimization. The target prescribed dose or the OAR tolerance dose is highlighted in the same color as the achieved dose curve for each ROI criterion. 91

Figure 37. For a population-based comparison, the average pDVHs of (upper) COP vs. OM plans and (lower) COP vs. FM plans to account for deformable motions. For target structures $CTV_{prostate}$ and CTV_{SV}, pDVH 95% are the lower bound of target dose-volume metrics. For OAR structures bladder and rectum, pDVH 5% are the upper bound of OAR dose-volume metrics. 93

Figure 38. Flow of ASSD model to get voxel displacement due to delineation uncertainties. See text for details. 98

Figure 39. F_{CT} as a function of CT gradient when different parameter a is used. 100

Figure 40. CT image slice in transverse plane for rectum (magenta contour) and corresponding F_{CT} vectors, using a=50. 101

Figure 41. A patient example of pDVH 95% and 5% using ASSD model using CT-gradient factor: (thick lines) F_{CT} calculated using a = 50 versus (thin lines) F_{CT} = 1 when a is very large. 101

Figure 42. (a) Percentage degraded dose ($\%\Delta D_{98,95}$) and (b) DVH variability ($\%\Delta DVH_{98,5-95}$) at prescribed dose of $CTV_{prostate}$ (red bins) and CTV_{SV} (green bins) for 19 zero-PTV-margin plans with delineation uncertainties considered (using ASSD model). 104

Figure 43. Scatter plot of percentage degraded dose ($\%\Delta D_{98,95}$) versus DVH variability ($\%\Delta DVH_{98,5-95}$) for (a) $CTV_{prostate}$ (red dots) and (b) CTV_{SV} (green dots) on 19 zero-PTV-margin plans evaluated with ASSD model incorporated for each patient. 104

Figure 44. The average pDVHs 95% (solid) and pDVHs 5% (dashed) evaluated on zero-PTV-margin plans for 19 high-risk prostate cancer patients for anatomies $CTV_{prostate}$ (prostate) (red), CTV_{SV} (green), bladder (orange) and rectum (magenta) with optimization objectives (triangle markers). The ASSD model is incorporated to show the dosimetric consequence of delineation uncertainties for prostate cancer patients. 105

Figure 45. For a population-based comparison, the average PDVHs of (upper) COP vs. OM plans and (lower) OM vs. FM plans to account for delineation uncertainties. For target structures $CTV_{prostate}$ and CTV_{SV}, pDVH are of 95% to show the lower bound of target dose-volume metric values of 95% chances. For OAR structures bladder and rectum, pDVH are of 5% to show the upper bound of OAR dose-volume metric values of 95% chances. 108

Figure 46. The dose distribution difference as COP minus FM (left column) and OM minus FM (right column) in SI, RL and PA slice for patient S when deformable motions are

accommodated. ROIs displayed as colorwash are $CTV_{prostate}$ (red), CTV_{SV} (green), bladder (yellow) and rectum (magenta). The dose distribution around $CTV_{prostate}$ in COP plan is quite different from that on OM and FM plans..... 113

Figure 47. Dose distribution of COP versus OM versus FM plans on one slice for patient H when delineation uncertainties are considered. The thick isodose surface are TVs for of 78Gy (seashell) for $CTV_{prostate}$ (red colorwash) and of 66Gy (aquamarine) for CTV_{SV} (green colorwash). The yellow and magenta colorwash are bladder and rectum. The other isodose surfaces are 75 Gy (maroon), 69 Gy (slateblue) and 57 Gy (lightblue). The smaller DMs of COP plan in some directions due to the compromise of OAR are sometimes more likely to fail to achieve the target coverage. 114

Figure 48. An example of the pDVHs of the COP plan that uses inappropriately reduced OAR objective weights (dashed) in the contrast to that uses original OAR objective weights (solid). The pDVHs are of 95% for $CTV_{prostate}$ (red) and CTV_{SV} (green) and 5% for bladder (orange) and rectum (magenta). Inappropriately reduced OAR objective weights may result in high OAR dose beyond the tolerance. 118

Figure 49. The patient-specific pDVHs 95% (solid) and pDVHs 5% (dashed) evaluated on zero-PTV-margin plans for patient with ID A to S(continued below) for anatomies CTVprostate (prostate) (red), CTVSV (green), bladder (orange) and rectum (magenta) with optimization objectives (triangle markers). The PCA model is incorporated to show the dosimetric consequence of organ deformable motions..... 132

Figure 50. The pDVHs 95% of $CTV_{prostate}$ (red) and CTV_{SV} (green) and the pDVHs 5% bladder (orange) and rectum (magenta) for the patient-specific comparison of COP(solid), OM (dashed) and FM (dot) plans for the patient with ID A to S (continued below), with optimization

objectives (triangle markers). The PCA model is incorporated to show the dosimetric consequence of organ deformable motions..... 143

Figure 51. The patient-specific pDVHs 95% (solid) and pDVHs 5% (dashed) evaluated on zero-PTV-margin plans for patient with ID A to S(continued below) for anatomies $CTV_{prostate}$ (red), CTV_{SV} (green), bladder (orange) and rectum (magenta) with optimization objectives (triangle markers). The PCA model is incorporated to show the dosimetric consequence of organ deformable motions. 154

Figure 52. The pDVHs 95% of $CTV_{prostate}$ (red) and CTV_{SV} (green) and the pDVHs 5% bladder (orange) and rectum (magenta) for the patient-specific comparison of COP(solid), OM (dashed) and FM (dot) plans for the patient with ID A to S (continued below), with optimization objectives (triangle markers). The ASSD model is incorporated to show the dosimetric consequence of delineation uncertainties..... 164

Figure 53. Interfraces of the GUI to launch HXVWP and the application to store the information of dose mapping. Note the mapping type for HXVWP is Plugin-based RCF DoseMapping. (Copyright JV Siebers 2011©)..... 177

Figure 54. Workflow of DVH calculation of HXRDP 177

List of Abbreviations

3D-CRT	Three-Dimensional Conformal Radiotherapy
AAPM	American Association of Physicists in Medicine
ASSD	Average-Surface-of-Standard-Deviation
BED	Biological Equivalent Dose
cGy	dose unit, 100 cGy = 1 Gy
CT	Computed Tomography
CTV	Clinical Target Volume
$CTV_{prostate}$	Prostate as CTV
CTV_{SV}	Seminal Vesicles (SV) as CTV
COP	Coverage-Optimized Planning
D_{98}	Dose delivered to 98% volume
$D_{98,95}$	Dose delivered to 98% volume at 95% coverage probability
$D_{98,95,Rx}$	Prescribed dose delivered to 98% volume at 95% coverage probability
D_v	Dose delivered to v% volume
$D_{v,5}$	Dose delivered to v% volume at 5% coverage probability
DVCM	Dose Volume Coverage Map
DVF	Displacement Vector Field
DVH	Dose Volume Histogram
DVPH	Dose–Volume Population Histogram
EBRT	External Beam Radiation Therapy
EUD	Equivalent Uniform Dose
FBCT	Fan-Beam Computed Tomography
FM	Fixed Margin planning
gEUD	generalized Equivalent Uniform Dose

GTV	Gross Target Volume
Gy	dose unit, 1 Gy = 100 cGy
GU(s)	Geometric Uncertainty (Uncertainties)
GUI	Graphical User Interface
ICRU	International Commission on Radiation Units and measurements
IGART	Image Guided Adaptive Radiation Therapy
IGRT	Image Guided Radiation Therapy
IMRT	Intensity Modulated Radiation Therapy
MRI	Magnetic Resonance Imaging
NCCN	National Comprehensive Cancer Network
NKI	Netherlands Cancer Institute
NTCP	Normal Tissue Complication Probability
OAR	Organ At Risk
OM	Optimized Margin planning
P+	probability of complication free control
PDF	Probabilistic Density Function
pDVH	Probabilistic Dose Volume Histogram
PCA	Principal Component Analysis
PRV	Planning organ at Risk Volume
PSA	Prostate-Specific Antigen
PTP	Probabilistic Treatment Planning
PTV	Planning Treated Volume
RT	Radiation Therapy
ROI	Region Of Interest
SD	Standard Deviation
SICLE	Small Deformation Inverse Consistent Linear Elastic
SSV	Simple Surface Variation
TCP	Tumor Control Probability
TPS	Treatment Planning System
VCU	Virginia Commonwealth University
VHFM	van Herk margin formula

Abstract

A STUDY OF COVERAGE OPTIMIZED PLANNING INCORPORATING MODELS OF GEOMETRIC UNCERTAINTIES FOR PROSTATE CANCER
By Huijun Xu, B.S.

A dissertation submitted in partial fulfillment of the requirements for the degree of Doctor of Philosophy at Virginia Commonwealth University.

Virginia Commonwealth University, 2013.

Major Director: Jeffrey V. Siebers, Ph.D.
Professor and Director, Medical Physics Graduate Program
Department of Radiation Oncology

A fundamental challenge in the treatment planning process of multi-fractional external-beam radiation therapy (EBRT) is the tradeoff between tumor control and normal tissue sparing in the presence of geometric uncertainties (GUs). To accommodate GUs, the conventional way is to use an empirical planning treatment volume (PTV) margin on the treatment target. However, it is difficult to determine a near-optimal PTV margin to ensure specified target coverage with as much normal tissue protection as achievable.

Coverage optimized planning (COP) avoids this problem by optimizing dose in possible virtual treatment courses with GU models directly incorporated. A near-optimal dosimetric margin generated by COP was reported to savvily accommodate setup errors of target and normal tissues for prostate cancer treatment.

This work further develops COP to account for (1) deformable organ motion and (2) delineation uncertainties for high-risk prostate cancer patients. The clinical value of COP is investigated by comparing with two margin-based planning techniques: (i) optimized margin (OM) technique that iteratively modifies PTV margins according to the evaluated target coverage probability and (ii) fixed margin (FM) technique that uses empirically selected constant PTV margins.

Without patient-specific coverage probability estimation, FM plans are always less immune to the degraded effect of the modeled GUs than the COP plans or the OM plans. Empirical PTV margins face more risks of undesirable target coverage probability and/or excessive dose to surrounding OAR.

The value of COP relative to OM varies with different GUs. As implemented for deformable organ motions, COP has limited clinical benefit. Due to optimization tradeoffs, COP often results in target coverage probability below the prescribed value while OM achieves better target coverage with comparable normal tissue dose. For delineation uncertainties, the clinical value of COP is potentially significant. Compared to OM, COP successfully maintains acceptable target coverage probability by exploiting the slack of normal tissue dose in low dose regions and maximally limiting high dose to normal tissue within tolerance.

1 Introduction

In external radiation therapy (EBRT), desirable treatment techniques allow tumoricidal dose coverage to malignant tumor cells with dose sparing of normal tissues. Geometric uncertainties (GUs) involved in multi-fractional treatment delivery constrain the available solution space. The conventional way to accommodate GUs, called margin-based planning techniques, uses margins to create expanded volumes as surrogates of regions of interest (ROIs). (ICRU Report 50 1994) This technique inherently assumes that the ROI under the influence of GUs can occupy any location within the expanded volume with equal probability, which may not be true in real cases. Inadequate margin selection may cause poor dose coverage or excessive toxicity to normal tissues. While advanced technologies for target localization and plan adaptation aim to reduce GUs, they are not yet included in the clinical routine. An intermediate solution can be found by using a technique called probabilistic treatment planning (PTP). PTP directly incorporates models of GUs into treatment planning and results in margins customized to the GUs and the orientation of the patient anatomy. As a new frame work of PTP, coverage optimized planning (COP) was tested to give desirable treatment plans for prostate cancer in the presence of setup errors and shows some potential as an alternative to the margin-based planning technique. (Gordon *et al.* 2010) This dissertation further develops COP to explicitly incorporate other GUs using appropriate mathematical models. Virtual clinical trials are performed to assess

the hypothesis that COP produces more desirable plans than those planning techniques that use margin-based surrogate volumes.

Chapter 1 describes some background knowledge of GUs involved in EBRT for prostate cancer (1.1) and evolved treatment planning techniques to consider these GUs (1.1.2). In 1.3, the purposes and the outline for the following chapters (2-0) of this dissertation are given.

1.1 Introduction to GUs in external beam radiation therapy

1.1.1 External beam radiation therapy for prostate cancer

Prostate cancer[1] is the third most common cause of death from cancer in men of all ages. In 2012, there were about 242,000 new cases of prostate cancer in the United States. (National Cancer Institute (NCI) booklet, 2012) With the widespread use of prostate-specific antigen (PSA) screening, radiation therapy (RT) has become a primary treatment for the patients with clinically localized disease. As the National Comprehensive Cancer Network (NCCN) treatment guidelines specified, patients in low, intermediate or high risk groups (Table I) may be treated with RT for therapeutic management.

Table I. NCCN Risk Groupings on prostate cancer staging (T1-T4) and PSA. (National Comprehensive Cancer Network (NCCN Clinical Practice Guidelines in Oncology v.1.2005)

Low risk:	T1-T2a, PSA < 10 ng/mL
Intermediate risk:	T2b-T2c, PSA 10-20 ng/mL
High risk:	T3-T4, PSA > 20 ng/mL

External beam radiation therapy (EBRT) is one of the most common forms of RT for prostate cancer treatment. When a patient lies on a couch, EBRT directs high doses of radiation from a source outside patient body to a particular part of body (Figure 1). With a long history, EBRT has been developed into several advanced delivery modes such as intensity modulated

[1] Note, prostate cancer is studied as a "test bench" in this dissertation. There are no exclusions for the other interesting clinical sites.

radiation therapy (IMRT). IMRT takes the advantage of multi-leaf collimators to produce customized radiation fluence (Figure 2), thereby allowing high-precision radiation doses to be focused to regions to of regular or irregular shaped targets.

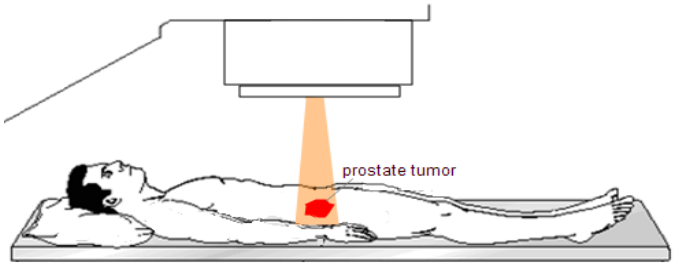

Figure 1. EBRT for prostate cancer treatment. (adapted from Patient Health International, © AstraZeneca 2012)

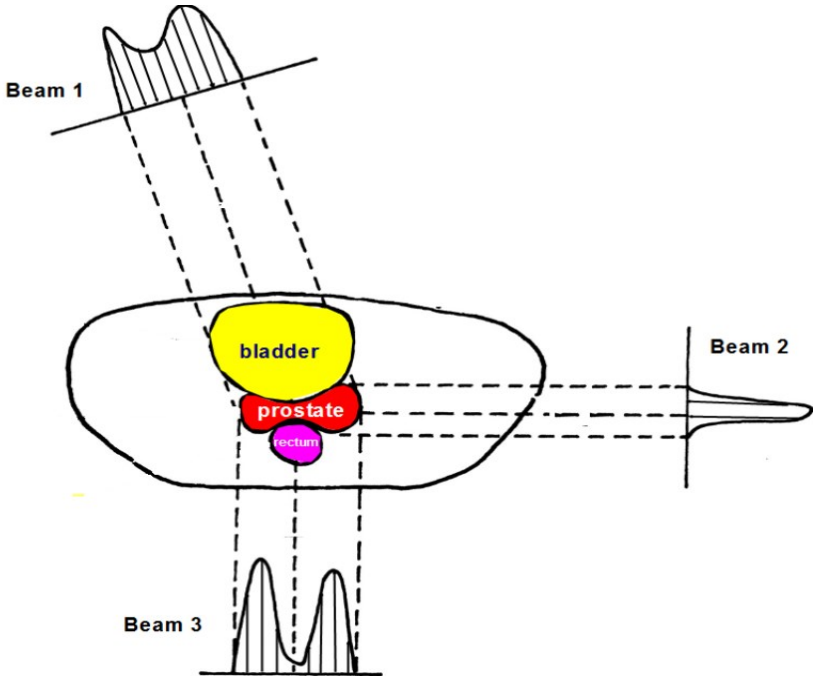

Figure 2: A sketch of fluence intensity of 3 beams in an IMRT for prostate cancer treatment. High beam intensity (and therefore high dose) is delivered to the target prostate (red) and low beam intensity (and low dose) is delivered to the surrounding bladder (yellow) and rectum (magenta).

However, like the other treatment modalities, EBRT is far from perfect even with the advanced modes. The ultimate goal of EBRT is to deliver a prescribed dose to treat targets (i.e. malignant cells) with as low as possible toxic irradiation to the surrounding normal tissues.

According to a clinical outcome review (Cahlon *et al.* 2008) on 478 prostate cancer patients treated with 86.4 Gy[2] using a 5- to 7-field IMRT technique, the 5-year actuarial PSA relapse-free survival according to the nadir plus 2 ng/mL definition was 98%, 85% and 70% for the low, intermediate, and high risk NCCN prognostic groups, respectively. The normal tissue complication, such as Grade 2 genitourinary toxicity and acute Grade 2 gastrointestinal toxicity that associated with bladder toxicity and rectal bleeding, was experienced by 22% and 8% patients. The improvement of tumor control rate is still limited by treatment complications to surrounding normal tissues.

EBRT is composed of multiple processes: problems in any process could prevent the destruction of all the cancer cells or excessively damaging normal tissues. The flow of EBRT is as follows. First, the cancer is staged and a therapeutic decision is made for the patient. When EBRT is chosen, the patient is imaged to quantify the location and volume of tumor and surrounding normal tissues. Often, to better align the target, fiducial markers are inserted into prostate before patient being imaged. Based on the imaging data, the treatment target and normal tissue structures are delineated. A computerized treatment planning system (TPS) is then used to design a treatment plan on the patient image. Treatment parameters such as treatment volume, dose prescription and external beam arrangement are determined. During the IMRT inverse planning (See chapter 2, section 2.1), the dose distribution is calculated and optimized until it satisfies a specific set of dose objectives. The treatment delivery is then simulated for quality assurance purposes prior to the treatment. During the treatment course, the prescribed dose is delivered in multiple treatment fractions on separate days. (For instance, total dose 78 Gy for a patient may be delivered in fractions of 2 Gy on each of five day per week over 8

[2] Gy is dose unit used in this dissertation. 1 Gy = absorbed energy (associated with ionizing radiation) deposited per unit mass of irradiated tissue. 1Gy = 1J/kg.

weeks.) The treatment is fractionated with the purpose of e.g., allowing repair of cellular damage for normal tissues based on radiobiological principles. (See section 3.3.1 of chapter 3 for more details of cellular response to fractionated dose.) Obviously, the uncertainties involved in each stage of the EBRT can impact the final treatment outcome. Within the scope of this dissertation, a particular attention is paid to how GUs can be addressed during the EBRT treatment planning process.

1.1.2 GUs and their models

To improve the probability of achieving the therapeutic intent of treatment, GUs should be considered adequately during the treatment planning. GUs introduce deviations between the planned (intended) and the treatment geometry, which, if inadequately accounted for, could result in undesirable target dose coverage and/or more normal tissue toxicity. This problem is especially significant for IMRT, as miss-aligned conformal dose distribution may be more likely miss the intended target. Moreover, GUs are mostly unavoidable and not easy to predict. To achieve desirable treatment outcomes, a specified knowledge of GUs caused by each process of external beam radiation therapy is essential for planning purposes (Wilkinson 2004).

The standard method of accommodating GUs is to define various treatment volumes as recommended by the International Commission on Radiation Units and Measurements report (ICRU) reports. (ICRU Report 50 1994, ICRU Report 62 2000, ICRU Report 83 2011) These volumes aid the current planning process for the consideration of GUs. A schematic representation of these volumes is shown in Figure 3.

The targets for treatment purpose are called the clinical target volume (CTV), which consists of the gross tumor volume (GTV) that is visible through the employed image modalities and suspected anatomical spread disease. In order to absorb the GUs associated with the CTV,

the planning target volume (PTV) is defined. The distance between the CTV and PTV is termed the CTV-to-PTV margin. This margin is expected to be large enough to ensure clinically acceptable probability of CTV coverage when the PTV dose distribution serves as a surrogate of the CTV dose distribution. For normal tissues, an organ at risk (OAR) is defined as "the normal tissues whose radiation sensitivity may significantly influence treatment planning and/or prescribed dose". (ICRU Report 50 1994) The critical OARs for prostate cancer patients include the bladder, the rectum, the femurs and small bowel if within the primary beam aperture. The recent ICRU 83 report (ICRU Report 83 2011) articulates that the bladder wall and rectal wall should be used to explicitly exclude the inside content for the bladder and rectum. However, use of bladder/rectal wall structures is not yet routine clinical practice. In analogy with the PTV, the concept of the planning organ at risk volume (PRV) is introduced (ICRU Report 62 2000) to take into account the GUs of the OAR by adding margins. Clinically, PRVs are rarely used.

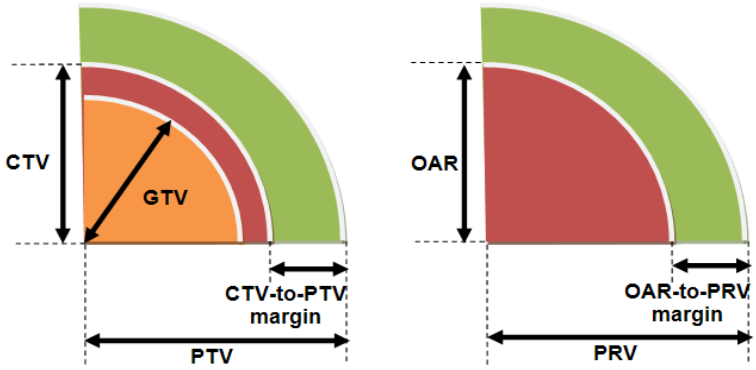

Figure 3: Schematic representations of relationship between volumes GTV, CTV, PTV for target structures and OAR, PRV for surrounding normal tissues.

GUs to be accounted for in the CTV-to-PTV margin or the OAR-to-PRV margin can be categorized as (1) setup errors, (2) delineation uncertainties, (3) interfraction and (4) intrafraction variations in structure position shape and size. Setup errors (Figure 4a) are deviations in the positioning and alignment of patient (where the coordinate system of GTV, CTV and OAR are)

with respect to therapeutic beams (the accelerator coordinate system in which PTV and PRV exist). Delineation uncertainties refer to the deviations (between different observations, or between the indicated value and the true value) on the location of the interface between target and adjacent tissues. The sources of delineation uncertainties include (i) limited image quality of employed imaging modalities (e.g. poor soft-tissue contrast in CT images), (ii) different clinical judgment of different observers (inter-observer delineation uncertainties) (Figure 4b.), and (iii) different clinical judgment of the same observer in different trials (intra-observer delineation uncertainties). Interfraction variations refer to the day-to-day (fraction-to-fraction) variations in positions and volumes (and/or shapes) of the region of interest (ROI) in different treatment fractions. Intra-fraction variations occur between the completion of setup procedure and completion of delivery of the intended radiation fraction. Both interfraction and intrafraction variations are caused by internal organ motion and deformation (Figure 4c).

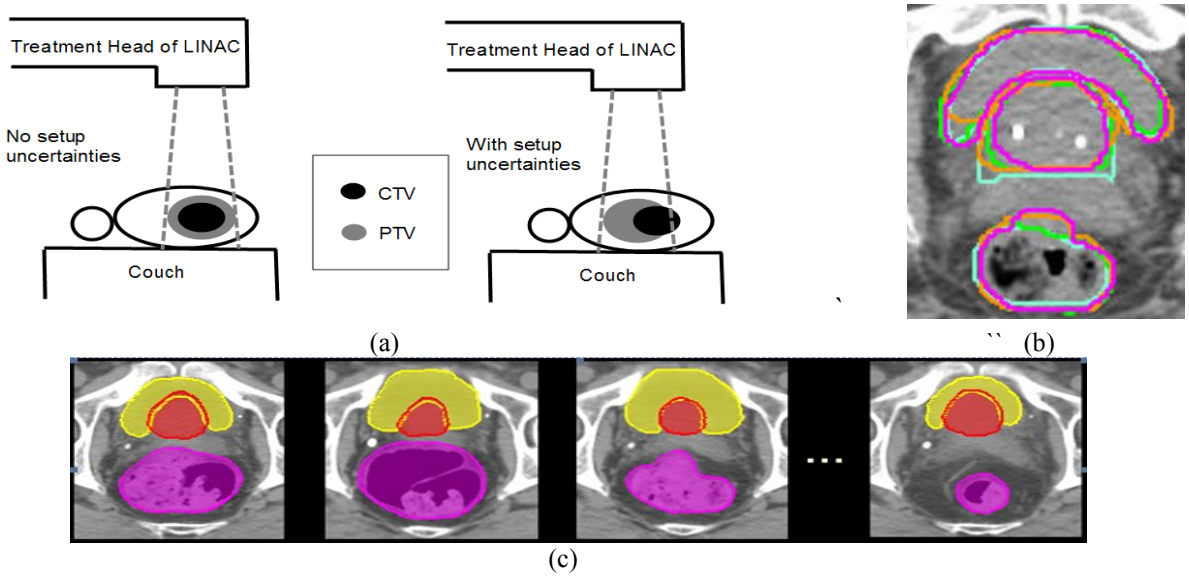

Figure 4: Illustration of different types of GUs: (a) setup errors that fail to align patient position to the beam treatment head of LINAC (linear accelerator), (b) inter-observer delineation uncertainties for the same structures, (c) organ motion and deformation that may occur between treatment fractions (interfraction organ variations) or during a single treatment fraction at different treatment fractions (intrafraction organ variations).

To incorporate GUs into treatment planning techniques, mathematical models can be very useful. The following paragraphs review the models developed for each category of GUs.

Setup errors are often modeled in terms of rigid body shifts and rotation. Methods have been proposed to describe these rigid uncertainties by six translational and rotational parameters. (Killoran *et al.* 1997, van Herk *et al.* 2002, Baum *et al.* 2004, Gordon *et al.* 2007) The probability distributions of these parameters are usually assumed to be Gaussian distributions (Stroom *et al.* 1999, Yan *et al.* 1999, Stroom and Heijmen 2002) and can be derived from a population or sometimes an estimated patient-specific level retrospectively.

Mathematical models of internal organ motions and deformations, though still evolving, show some potential in representing realistic interfraction/intrafraction variations. When it comes to prostate, building good mathematical models may not be a problem for the following reasons. Although prostate is surrounded by the rectum (Hoogeman *et al.* 2004, Adamson and Wu 2009) and bladder (Meijer *et al.* 2003), which empty and fill unpredictably to some extent, it is well known that prostate deforms less than bladder and rectum (Roeske *et al.* 1995) and prostate displacement can be reliably tracked using implanted fiducial markers or Calypso transponders (Calypso, Seattle, WA) on an interfraction (Kupelian *et al.* 2005, Peng *et al.* 2010) and an intrafraction (Langen *et al.* 2008, Santanam *et al.* 2009, Bittner *et al.* 2010) basis. In-room computed tomography (CT) (Keall 2004, Pouliot 2007, Frank *et al.* 2008) and cine-magnetic resonance imaging (cine-MRI) scans (Mah *et al.* 2002, Ghilezan *et al.* 2005) can also record anatomy motion and volumetric information. All these techniques provide information about target motion, from which dosimetric or biological effects can be estimated. Much published work (listed in Table II) has described prostate interfraction or intrafraction variations by constructing mathematical models.

Table II. Some published models of interfraction, intrafraction variations for prostate, bladder, and rectum.

reference	model	uncertainties	ROI(s)
(Fontenla *et al.* 2001)	method for reconstructing statistical distribution of organ motion	interfraction motion	Prostate/bladder/rectum (any site with serial measurement)
(Söhn *et al.* 2005a)	individual-based principal component analysis (PCA) model	interfraction deformation of structure surface	Prostate + bladder + rectum for prostate caner
(Budiarto *et al.* 2011)	population-based PCA model	interfraction motion and deformation of voxels	Prostate + seminal vesicles for prostate cancer
(Chow *et al.* 2009)	Gaussian error function for cumulative DVH for planning evaluation	interfraction motion of prostate shifting in AP direction	Prostate/bladder/rectum for prostate caner
(Jeong *et al.* 2010)	bilinear model to capture and decouple inter- and intra-patient shape variation of organ A method for reconstructing statistical distribution of organ motion	inter- and intra-patient shape variation and interfraction motion	Prostate for prostate cancer
(Lotz *et al.* 2004)	linear model to predict bladder shapes based on known urinary inflow and rectal filling	interfraction motion and deformation	Bladder for bladder cancer
(Chai *et al.* 2011)	Biomechanical model to predict short-time bladder shape with bladder volume as input	interfraction motion	Bladder + 6 surrounding pelvic organ for bladder cancer
(Hoogeman *et al.* 2002)	stochastic shape description model with population-based parameters based on dose-wall histogram	interfraction deformation	Rectum for prostate cancer

Abbreviations: ROI = region of interest; DVH = dose volume histogram; AP = anterior-posterior

Mathematical models have also been built for bladder and rectum deformable motion. Bladder and rectum are known as main drivers of pelvic organs motion (Ten Haken *et al.* 1991) and are much more likely to move and deform due to filling than prostate. As OARs, bladder

and rectum are not as well studied as target prostate, therefore many of their models may be less optimal than prostate model. For the examples listed in Table II, the linear bladder shape model (Lotz et al. 2004) is for the bladder as a tumor, not an OAR. The biomechanical model has much poorer accuracy compared with the higher degree models (Chai et al. 2011). The stochastic shape description model needs more patients for evaluation (Hoogeman *et al.* 2002). However, the principal component analysis (PCA) model (Söhn *et al.* 2005b) addresses the above challenges and provides a quantitative description of geometric variability. Therefore, interfraction and intrafraction variations can be approximated in a quasi-realistic way by models like the PCA model.

In contrast, as the "weakest link in the search for accuracy" (Njeh 2008), delineation uncertainties were rarely modeled. As there is no verifiable ground truth of the tumor locations/volume, delineation uncertainties persist even with perfect images. Delineation uncertainties are usually quantified by difference of repeatedly delineated contours. Though recent developed auto-contouring tools allows much faster with more consistent contours between trials, the tedious and time-consuming manual contours are usually still required for validations and corrections (Huyskens *et al.* 2009). Based on limited number of manual contours, most researches have been only focused on evaluation of boundary visualization (Zhou *et al.* 1998, Rasch *et al.* 1999, Weiss and Hess 2003, Gao *et al.* 2007, Weiss *et al.* 2010) or development of 3D analysis tools (Remeijer *et al.* 1999, Korporaal *et al.* 2010, Wu *et al.* 2010).

1.2 Evolution of treatment planning approaches

1.2.1 Margin-based planning

For the current practice of conventional margin-based planning approach, the PTV or PRV margin given by conventional margin formulas may be suboptimal to account for GUs. (Note, the PTV/PRV margin is the short name of CTV-to-PTV/OAR-to-PRV margin.) This is because coverage probability, the probability that desirable dose delivered to a volume is achieved, is dictated by the dose distribution, not the margins. (Gordon and Siebers 2009) An inadequate PTV margin, e.g., over-sized, may result in unnecessary irradiation to normal tissues and cause a higher risk of normal tissue toxicity. Margin size can be optimized using evolving treatment planning techniques such as the PTP approach. This actively researched approach can create anisotropic and patient-specific margins on the premise that the probability distribution function (PDF) of GUs is known. Both margin-based planning approach and PTP approach will be discussed in the following paragraphs.

While commonly practiced in the planning process for real patient treatments, the conventional margin-based planning approach faces the obstacle of defining desirable PTV and/or PRV margins in the presence of GUs. Numerous margin recipes (or guidelines) (Stroom *et al.* 1999, van Herk *et al.* 2000, McKenzie *et al.* 2002, van Herk 2004) were published to determine PTV margins, but no gold standard/consensus of recipe/guideline is clinically used for margin-based planning, whose planning objectives includes uniform dose to PTV volumes.

Two problems in the current margin recipes/guidelines are likely to be involved in the margin-based planning approach. The first problem is that the PTV margin derived from a population-based model cannot ensure patient-specific coverage in the presence of GUs. Use the most commonly used recipe — van Herk margin formula (van Herk et al. 2000) — as an

example. With the intention to guarantee that 90% of patients in a population receive a minimum cumulative CTV dose of at least 95% of the prescribed dose, this margin formula is approximately 2.5 times the total standard deviation (SD) of the systematic errors (which shift structures relative to the cumulative dose distribution) and 0.7 times the total SD of the random errors (which blur the cumulative dose distribution). The errors in convolution are assumed to follow a Gaussian distribution. The assumption of Gaussian-distributed errors may be not adequate for GUs such as prostate deformation (Deurloo *et al.* 2005), especially given that prostate is surrounded with the rectum (Hoogeman *et al.* 2004, Adamson and Wu 2009) and bladder (Meijer *et al.* 2003) which empty and fill unpredictably to some extent. Even if GUs are Gaussian distributed, the assumptions of population statistics being representative to individual patient are questionable. Setup errors are frequently believed to follow a Gaussian distribution approximately (Stroom *et al.* 1999, Yan *et al.* 1999, Stroom and Heijmen 2002). However, if one considers setup errors only, and uses margins based on population statistics (i.e. SD of setup or random errors) derived from the van Herk formula (van Herk *et al.* 2000), recent research (Gordon and Siebers 2008) showed no one-to-one relationship between PTV and target coverage. Patient-specific characteristics such as anatomy geometry (Yan *et al.* 1997) are too complicated to be summarized in a simple equation/guideline. Consequently, the patient-specific coverage probabilities for both target and OARs may vary widely between patients (e.g., 57% - 100% for prostate prescribed at minimum dose with setup SD 3mm) (Xu *et al.* 2011). (In practical cases, population statistics are still utilized, although they are necessarily approximate.) The second problem in margin recipes/guidelines is that margins are not ideally suited to balance the tradeoff of CTV coverage and OAR toxicity. During treatment planning, each voxel inside a PTV (in the accelerator coordinate system) is naively assumed equally important for CTV (in patient

coordinate system). For adjacent organs, often consideration of uncertainties yields situations where the PTV and OAR/PRV overlaps, yielding a paradox for a plan optimization algorithm. Competition between PTV and OAR criteria may end up with an unacceptable solution since shaving margins in some direction to avoid the overlap does not necessarily result in an acceptable tradeoff between target coverage and OAR sparing. These limitations potentially prevent the conventional margin-based planning approach from best accommodating GUs effect on the patient treatment plan.

1.2.2 Probabilistic treatment planning

Probabilistic treatment planning (PTP) has been studied as a potential replacement of margin-based planning approach that ameliorates the problems of margin definition. This evolving planning approach requires explicit specification of GUs (e.g., GU models and PDF) and directly incorporates GU information into planning optimization. Governed by the probabilistic planning criteria, the treatment planning system (TPS) builds a dose distribution to achieve the desired coverage probability. Therefore, PTP does not require prior specification of margin-based volumes (i.e. the PTV and the PRV) but allows direct determination of probable dose coverage in the presence of GUs. Recent publications addressed different PTP approaches. These approaches can be classified into two categories: either based on a probability weighted dose distribution (PWDD), or a probability weighted objective function (PWOF).(Gordon *et al.* 2010) The PWDD technique is to optimize dose distribution in terms of e.g., dose expectation values (Löf *et al.* 1998) alone or with dose variance together (Unkelbach and Oelfke 2004, 2005a, 2005b, Maleike *et al.* 2006), or the treatment course generated by fluence convolution (Moore *et al.* 2009). The PWOF method uses objective functions with probabilistic weights in

terms of e.g., voxel likelihood (Baum *et al.* 2006) or biological quantities[3] such as equivalent uniform dose (EUD) (Yang *et al.* 2005), TCP and NTCP (Witte *et al.* 2007). Despite the difference, most PTP studies share a common conclusion: PTP approaches can reduce dose of OARs without compromise of the highly conformal dose to targets, even though the GUs being incorporated are approximated.

1.2.3 Coverage optimized planning

The COP framework (Gordon et al. 2010) is another PTP framework. The principle of COP is described in chapter 2. Analogous to the dose volume histogram (DVH) criteria popularly used in other planning approaches, COP utilizes percentile dose volume histogram (pDVH) criteria for optimization. These criteria aim to achieve adequate target prescription dose and avoid exceeding OAR tolerance for a specified percentage of GUs. The plan optimization in COP is based on dose coverage probabilities, as opposed to static dose in conventional margin-based planning.

To date, COP has only been used to compensate setup errors of prostate cancer treatment. Like the other PTP approaches, COP demonstrated better OAR dose sparing and lower NTCP values without sacrificing target dose coverage and TCP values using the PDVH criteria for the target and the OARs. (Gordon and Siebers Unpublished) With the target pDVH criteria alone, COP can improve target coverage probability while maintaining OAR dose within the tolerance. (Gordon *et al.* 2010) To explore the application of COP, it is necessary to develop COP approach for delineation uncertainties, organ deformable motions of prostate, bladder and rectum for prostate cancer patients. Due to the fact that the treatment delivery effort of COP is not different from a margin-based planning, if COP can reduce normal tissue doses without

[3] Please refer to chapter 3.3 for details of these biological quantities.

compromising target coverage for these GUs, it should be cost beneficial to be regarded as a promising alternative of the margin-based planning.

1.2.4 COP in different clinical scenarios

The dosimetric benefit of COP may vary with different clinical strategies for target localization and adaptive replanning in EBRT. These gradually maturing advanced strategies include image-guided radiation therapy (IGRT), adaptive radiotherapy (ART) and their collaboration—image-guided adaptive radiation therapy (IGART). The purpose of these strategies is to reduce uncertainties and/or adapt radiation treatment to individual patient variations. IGRT localizes target areas during treatment by using a variety of imaging techniques in the treatment room. ART periodically adjusts the treatment to account for anticipated or observed variations (i.e., translations, rotations and deformations) of targets and critical structures. IGART uses individual patient dynamic or time-serial four-dimensional treatment history, ambitiously to allow dose evaluation and modification on a patient-specific basis with a frequency as often as treatment-day-specific.

The cost for each strategy could be (a) potentially excessive radiation exposure introduced by the IGRT imaging methods using cone-beam imaging technology with kilovoltage (kV) or megavoltage (MV) X rays for CTV positioning (Ding *et al.* 2008), (b) low efficiency of ART for plan modification due to excessive clinical work such as quality assurance (QA) effort and plan approval (Li *et al.* 2011), and (c) technical challenges of contemporary IGART including a general lack of a comprehensive QA procedure. (Timmerman and Xing 2009) Despite the cost, IGRT, ART and IGART are considered to be promising for clinical use due to their resulting benefits (de Crevoisier *et al.* 2005, Ghilezan *et al.* 2010, Lagrange and de Crevoisier 2010). Recently, the clinical evidence has been reported that adaptive IGRT "appears

to reduce the risk of geometric miss and results in good biochemical control that is independent of rectal volume at the time of simulation while maintaining low rates of toxicity." (Park *et al.* 2012) Before becoming routine procedure in the clinic, these strategies need more clinical evidence to demonstrate their benefit and cost.

Image guidance and adaptive replanning due to these strategies will reduce the magnitude of GUs and perhaps inherent uncertainties such as delineation uncertainties as well. Consequently, when IGRT, ART and IGART become clinical realities, the potential role of COP will be to account for residual uncertainties. The benefit of COP relative to margin-based planning approaches may be less pronounced because of i.e., the negligible size of residual uncertainties. As a potential intermediate solution before the widespread of the advanced clinical strategies, COP is expected to either reduce normal tissue doses for the same target coverage or enable better target coverage with same normal tissue doses with respect to margin-based planning.

1.3 Thesis Objectives and Outlines

The objectives of this dissertation are to (1) construct mathematical models for GUs including (i) interfraction organ deformable motions with prostate centroid alignment and (ii) delineation uncertainties of prostate, bladder and rectum, (2) create COP plans with GU model incorporated to accommodate these uncertainties and (3) research the clinical value of COP in the scenarios with/ without advanced strategies by comparing with plans generated by using two margin-based planning techniques.

The outline of this dissertation is described here. The principle of COP and how COP is implemented in a commercial TPS are stated in chapter 2. Treatment planning metrics utilized in this dissertation to quantify dosimetric effect of GUs and compare COP and two different PTV

plans are covered in chapter 3. Some general materials and methods used in the COP studies are described in chapter 4. For multi-fractional treatment for prostate cancer, COP plans with incorporated interfraction deformable organ motion (chapter 5) or delineation uncertainties (chapter 6) are compared with the parallel PTV plans. In chapter 7, the clinical value of COP based on results in chapter 5 and 6 is discussed and concluded and further directions of COP studies are suggested.

2 The principle of coverage optimized planning

COP is a framework of PTP and a modified IMRT approach. This chapter reviews the principle of COP and its implementation in a commercial TPS. The principle of IMRT, mathematics of different type of objective functions corresponding to different optimization criteria and how they work in a TPS are also given here.

2.1 From IMRT to COP

The idea of IMRT is to treat a patient using beams of non-uniform fluences from a number of different directions (or a continuous arc) to plan and deliver a dose distribution to enable conformal high dose to target volumes and acceptably low dose to the OARs (A simple example was shown in Figure 2, page 3.) IMRT is an advanced form of three-dimensional conformal radiotherapy (3D-CRT). As Figure 5 illustrates, both 3D-CRT and IMRT require the planner to set the beam arrangement (beam angle, energy, and etc.). In 3D-CRT, the planner also has to decide how to use beam shapers to shapes the resulting radiation. In IMRT, the planner only needs to specify the treatment criteria (such as what minimum dose delivered to target volumes) so that the radiation is inversely optimized by TPS. Each beam is automatically shaped by an MLC and divided into non-equi-weighted segments. The non-uniform beam fluence is inversely optimized by the objective function algorithm imbedded in TPS to optimally meet all the treatment criteria. With direct machine parameter optimization, MLC settings are produced

directly during the optimization process without post process like conversion or filtering which may degrade the plan quality during dose delivery. Conventionally, the objective functions used in IMRT are (static) dose-volume based.

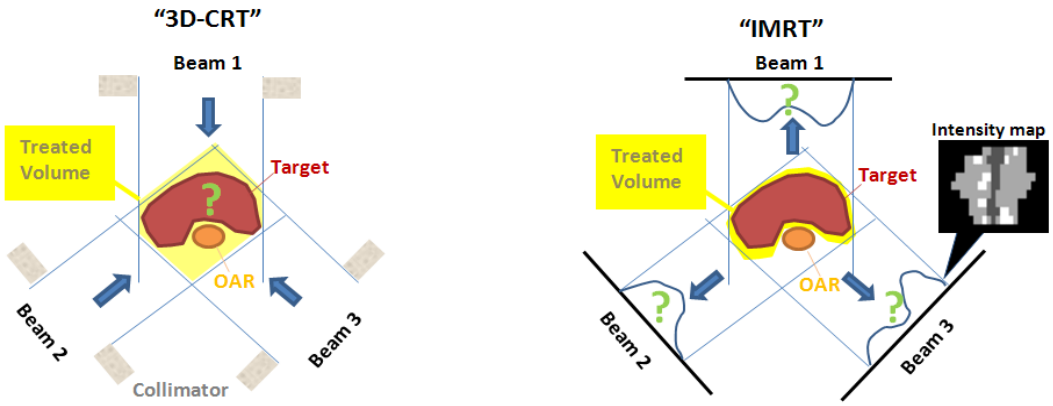

Figure 5. An illustration of 3-beam 3D-CRT (left) versus IMRT (right).

COP is an IMRT process that uses probabilistic (stochastic) dose-volume-based pDVH objective functions to adjust the beam fluence intensity profiles. Denote D_v the dose delivered to volume v of an ROI. In contrast to the static D_v in basic criteria/objective functions, COP computes and optimizes D_v at a specified coverage probability — the probability that a realized target or OAR dose metric D_v exceeds the dose of interest (Rx, tolerance or other dose) when the modeled treatment planning and delivery uncertainties are taken into account. COP seeks an optimized dose distribution for a patient to i.e., maximally achieve targets and OARs coverage probability to overcome the degraded dosimetric effect due to GUs.

The procedure of COP optimization on the patient-specific coverage probability with incorporated GUs of known PDFs is graphically illustrated in Figure 6. The deviations introduced by GUs may include shifting effects (due to systematic setup errors), blurring effects (due to random setup errors) and re-arranging dose with respect to the voxels (due to organ deformation). Different probable treatment courses (one treatment course = delivery of the

prescription dose in n_{frac} fractions) can yield different dose distribution and different patient responses. To evaluate dose incorporating uncertainties, one way is to mimic dose delivery to one of thousands of possible virtual treatment courses, each with n_{frac} fractions. Each fraction of each treatment course is associated with different GUs dependent on the parameters sampled from the known PDF(s). Dose shift invariance (Sharma *et al.* 2012) is assumed here so that dose distribution remains unchanged regardless of geometric changes of ROIs. Dose of each displaced voxel in the ROIs is calculated and accumulated over n_{frac} fractions. The consequent accumulative DVHs of each ROI for all the treatment courses can be obtained and converted into a dose volume coverage map (DVCM) – a 2D grid with many small grid squares that contain percentile values of DVHs on their D_v locations. (See section 3.2.1 for details) These percentile values, also called coverage probability, are associated each D_v on the DVCM. A pDVH of q (Gordon *et al.* 2010) is a virtual DVH created by connecting all D_v with coverage probability q. A pDVH criterion for q is D_v corresponding to q for a target/an OAR.

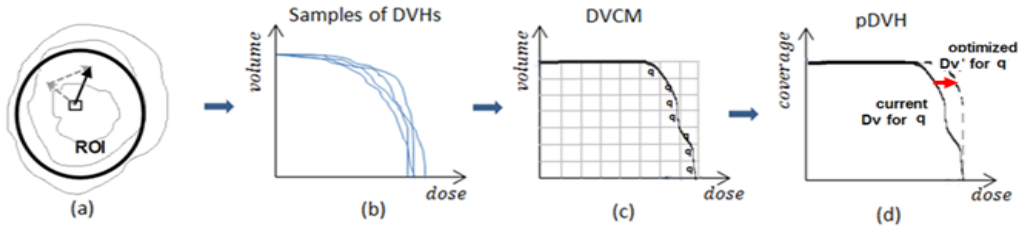

Figure 6. Workflow of how a pDVH of coverage probability q are determined (a–c) and how COP performs optimization (a-d) based on pDVH criteria by simulating n_{tx} virtual treatment courses, each with n_{frac} fractions. (a) For each fraction of a virtual treatment course, find the total offset (black arrow) for all the GUs of each voxel in the ROI (black thick circle) and get the dose for the displaced voxel, assuming shift-invariance for dose distribution (illustrated as grey thin solid isodose lines). (b) Get n_{tx} accumulative ROI DVHs over all the fractions. (c) The n_{tx} DVH samples are converted into a dose volume coverage map (DVCM), as a 2D grid built with many small grid squares. Each grid square will be assigned a probability value equivalent to the percentile value of DVHs that lie left to this grid squares, according to the distribution of DVH samples. A virtual DVH of a certain percentile value (i.e., coverage) q, namely pDVH of q, can be determined on this map. (d) pDVH criteria (such as $Pr[D_v \geq d] \geq q$) are used to optimize the dose distribution with the goal of achieving dose-volume metric D_v in the presence of q of GUs.

Note that the concept of pDVH is not unique. A similar metric called dose–volume population histogram (DVPH) related to the patient-specific coverage probability was independently and simultaneously developed before (Nguyen et al. 2009). With known SDs of the systematic and random errors for deformation-free/rotation-free structures, DVPH was the consequence of the distribution of systematic and random errors being incorporated into DVH display. Compared to DVPH, the usage of pDVH in this dissertation has been extended to plan optimization to account for GUs for both rigid and deformable structures.

2.2 The starting point — optimization criteria

As mentioned before, the planner needs to specify optimization criteria to start an IMRT/COP plan. The optimization criteria for treatment planning used in this dissertation are listed in Table IV. Based on a modified VCU protocol, these criteria are designed for a 30-fraction treatment course for high-risk prostate cancer patients. ROIs corresponding to these criteria include target structures to treat and normal tissues/organs to protect. Target structures for COP plans are the CTV volumes which include the prostate and the seminal vesicles (namely, $CTV_{prostate}$ and CTV_{SV}). Their PTV-margin-expanded volumes PTV1, PTV2 are surrogate target structures used in PTV plans. Normal tissues/organs for both COP and PTV plans are the bladder, rectum as OARs and norm_tissue_ring which is a virtual structure used to ensure a steep target dose drop-off. Three types of criteria are involved here. (1) Dose-based criteria (e.g. $D_{max} \leq 60$ Gy for norm_tissue_ring) specify the minimum or maximum dose to the whole volume of an ROI. Norm_tissue_ring $D_{max} \leq 60$ Gy means the maximum dose delivered to the norm_tissue_ring cannot be larger than 60 Gy. (2) Dose-volume-based criteria (e.g., $D_{98} \geq$ 78 Gy for prostate in PTV plans) that restrict dose to a certain percentage of ROI volume. $CTV_{prostate}$ $D_{98} \geq 78$ Gy means dose delivered to the 98% volume of the $CTV_{prostate}$ should be

above 78Gy. (3) pDVH based criteria (e.g., $D_{98,95} \geq 78$ Gy for prostate in COP plans) specify dose-volume criteria corresponding to a certain coverage probability. Prostate $D_{98,95} \geq 78$ means that the dose delivered to the 98% volume of the prostate should be no less than 78 Gy for 95% probablle treatment courses.

Table III. IMRT optimization criteria of ROIs used for COP and conventional PTV plans. Doses (D) are in the unit gray (Gy). Subscript is percentage volume +/- coverage value. Read $D_{98,95}$ as 98% of volume receiving ≥ 78 Gy for 95% of simulated treatment courses. Criterion weights are shown in square brackets. PTV1 = $CTV_{prostate}$ + PTV margin and PTV2 = CTV_{SV} + PTV margin.

Optimization criteria for COP plans[1]	
$CTV_{prostate}$	$D_{98,95} \geq 78$ [100], $D_{2,5} \leq 81$ [50]
CTV_{SV}	$D_{98,95} \geq 66$ [100]
Bladder	$D_{70,5} \leq 18$, $D_{50,5} \leq 36$, $D_{30,5} \leq 57$, $D_{20,5} \leq 66$, $D_{14,5} \leq 69$, $D_{9,5} \leq 75$, $D_{2,5} \leq 81$ [10]
Rectum	$D_{50,5} \leq 36$, $D_{30,5} \leq 51$, $D_{20,5} \leq 66$, $D_{5,5} \leq 69$, $D_{2,5} \leq 75$ [10]
norm_tissue_ring	(static) $D_{max} \leq 60$ [1]
CTV_neighborhood	(static) $D_{10} \geq 25$ [0]
Optimization criteria for PTV-based plans	
PTV1	$D_{98} \geq 78$ [100], $D_2 \leq 81$ [50]
PTV2	$D_{98} \geq 66$ [100]
Bladder	$D_{70} \leq 18$, $D_{50} \leq 36$, $D_{30} \leq 57$, $D_{20} \leq 66$, $D_{14} \leq 69$, $D_9 \leq 75$, $D_2 \leq 81$ [10]
Rectum	$D_{50} \leq 36$, $D_{30} \leq 51$, $D_{20} \leq 66$, $D_5 \leq 69$, $D_2 \leq 75$ [10]
norm_tissue_ring	$D_{max} \leq 60$ [1]

Note, margin formulation (Stroom *et al.* 1999, van Herk *et al.* 2000) are designed to dicit a population based probability (e.g., 95%) of target coverage. As used for optimized margin, the PTV margins are iterated until 95% coverage is achieved.

Once the optimization criteria are specified, an optimization altorithm is used to determine beam fluence distribution which best meet the optimization objectives. One broad category of computer algorithm to do so is called iterative methods (Khan 2003). Such methods interatively adjust beamlet weights for a given number of beams to minimize the deviation from the desired goal. Mathematically, this deviation is represented by the sum of objective functions which are transformed from the specified optimization criteria.

2.3 The central concept — objective functions

Objective functions are the central concept of IMRT inverse planning to generate a dose distribution that can maximally satisfy the specific optimization criteria. They are also termed cost functions since they represent the "costs" associated with a dose distribution of a given plan and a set of pre-determined optimization criteria. Let f denotes an individual objective function for the objective of interest o, f can also be expressed in a generalized way as

$$f = \sum_{i}^{N} c_i (\mathrm{D}_i - \mathrm{D}_{\mathrm{Rx}})^2 \qquad (1)$$

where D_i is the current dose to i^{th} voxel of o, D_{Rx} is the prescribed dose to be achieved for this objective, N is the total number of voxels and c_i is a voxel-dependent constant. c_i is zero when the voxel is not participating in the objective function.

With the aims of reducing total "cost" of all the individual objective functions, the dose distribution is iteratively optimized by adjusting treatment parameters (i.e., beamlet weight) to decrease composite objective function value. Let $f_{total,n}$ denote the total objective in n^{th} iteration of optimization. We have

$$f_{total,n} = \sum^{nObj} p \cdot f_n \qquad (2)$$

where f_n is an individual objective function for the objective of interest o in n^{th} iteration. p is weighting factor of f_n and $nObj$ is the total number of objectives of interest. $f_{total,n}$ is transformed according to the TPS algorithm and then compared with a pre-defined stopping tolerance (e.g., 0.0001) to determine if next iteration of optimization is necessary. The optimization terminates whenever the stopping tolerance has been satisfied or n exceeds the maximum iteration number (e.g., set as 50 here due to sufficient convergence).

Within the TPS optimizer, dose optimization by adjusting beamlet weight for next iteration is carried out by utilizing Newton's method. Denote beamlet weight $w_{j,n}$ for beamlet index j is the index of beamlet in n^{th} iteration. The recommended change in weight $\delta w_{j,n+1}$ in next iteration for an individual objective function f_n is defined as

$$\delta w_{j,n+1} \approx -\frac{\frac{\partial f_n}{\partial w_{j,n}}}{\frac{\partial^2 f_n}{\partial w_{j,n}^{\ 2}}} \tag{3}$$

based on Newton's method. Since the dose at voxel i is given by

$$\mathrm{D}_i = \sum_j K_{ij} w_j \tag{4}$$

where K_{ij} is the dose contribution of the j^{th} beamlet to the i^{th} voxel per unit intensity, the first derivative of equation (1) is

$$\frac{\partial f_n}{\partial w_{j,n}} = 2\sum_i^N c_i (\mathrm{D}_i - \mathrm{D}_{\mathrm{Rx}}) K_{ij} \tag{5}$$

and the second derivative of equation (1) is

$$\frac{\partial^2 f_n}{\partial w_{j,n}^{\ 2}} = 2\sum_i^N c_i K_{ij}^{\ 2} \tag{6}$$

For a composite objective function in equation (2), the derivatives are the sums of the individual derivative of each objective function:

$$\frac{\partial f_{total,n}}{\partial w_{j,n}} = \sum^{nObj} \frac{\partial f_n}{\partial w_{j,n}} \text{ and } \frac{\partial^2 f_{total,n}}{\partial w_{j,n}^{\ 2}} = \sum^{nObj} \frac{\partial^2 f_n}{\partial w_{j,n}^{\ 2}} \tag{7}$$

According to equations (3)-(7), the weight change for a given beamlet is then

$$\delta w_{j,n+1} \approx -\frac{\sum^{nObj}\left(2\sum_i^N c_i(\mathrm{D}_i - \mathrm{D}_{\mathrm{Rx}})K_{ij}\right)}{\sum^{nObj}\left(2\sum_i^N c_i K_{ij}^{\ 2}\right)} \tag{8}$$

The new beamlet weight for $n+1^{\text{th}}$ iteration is

$$w_{j,n+1} = w_{j,n} + \partial w_{j,n+1} \tag{9}$$

An example of how a composite objective value converges during the progress of an optimization is illustrated in Figure 7. The optimization is terminated in either of the following conditions: i) constraints and objectives are reasonably met as to the pre-defined stopping tolerance, ii) the maximum iteration number is reached, or iii) further iteration is determined as helpless to keep reducing the composite objective value.

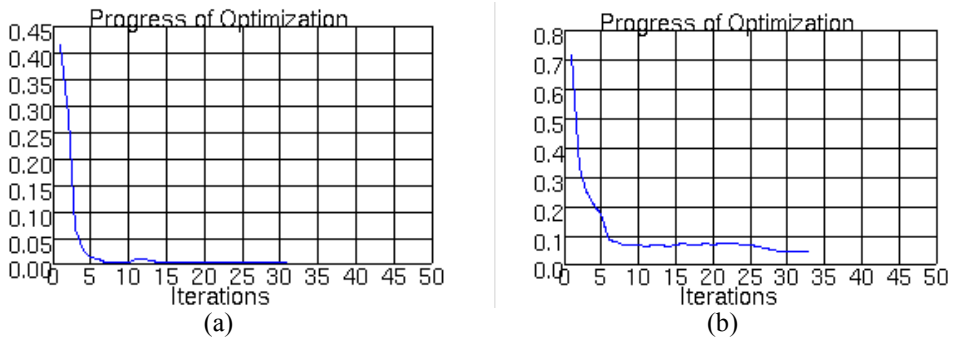

Figure 7. The converged composite objective value (vertical axis) as a function of iterations during the progress of optimization in the case that optimization terminates (a) when constraints and objectives are reasonably met as to the stopping tolerance and (b) when further iteration is determined as helpless.

2.4 Types of objective functions

Three types of objective functions will be described here in term of the three types of optimization mentioned in Table III: 1) dose based objectives for dose-based criteria, 2) dose-volume based objectives for dose-volume-based criteria and 3) pDVH objective, which is the research objectives used to achieve the aims of this dissertation. The pDVH objectives are particularly used in COP to achieve pDVH criteria. 1) and 2) are the basic format of objectives that operate on static DVH and are used in both conventional non-probabilistic optimization and COP. These basic objectives are useful for COP as they can (i) smooth the dose around target in the first several (~5) iterations for quicker convergence of composite objective value and (ii) save computation time and memory for COP implementation when an ROI that is not that critical to have pDVH objectives.

2.4.1 Dose-based objectives

Dose-based objective functions primarily build blocks for the desired DVH by penalizing dose above (or below) a specified dose to an ROI. (Here, DVH is a graphical 2D plot of dose vs. percentage volume for an ROI visualized in a cumulative way. Please refer to section 3.1 of chapter 3 for more details.) The corresponding criteria can be written in the form of $D_{max} \le D_{Rx}$ (maximum), $D_{min} \ge D_{Rx}$ (minimum) or $D_{uniform}=D_{Rx}$ (uniform), where D_{Rx} is the corresponding maximum, minimum or uniform prescription dose value.

For a minimum dose-based objective function of an ROI (with criterion $D_{min} \ge D_{Rx}$), the goal is to ensure the dose to each voxel is above a minimum prescription dose D_{Rx}. The voxels within the ROI with dose below the prescription dose are penalized proportional to the deficit squared as

$$f^{MinDose} = \frac{1}{N_{ROI}} \cdot \sum_{i}^{N_{ROI}} H(\mathrm{D_{Rx}} - \mathrm{D}_i) \cdot (\mathrm{D}_i - \mathrm{D_{Rx}})^2 \tag{10}$$

where i is the voxel index of total voxel number N_{ROI} of ROI, D_i is the dose in the i^{th} voxel of the ROI and H is Heaviside function defined as

$$H(x) = \begin{cases} 1 & (x > 0) \\ 0 & (x \le 0) \end{cases} \tag{11}$$

Note, voxels outside ROI do not contribute to the ROI objective function.

For a maximum dose-based objective function of an ROI (with criterion $\mathrm{D_{max}} \le \mathrm{D_{Rx}}$), the goal is to limit the dose to each voxel below a maximum prescription dose $\mathrm{D_{Rx}}$. The voxels within the ROI with dose above the prescription dose are penalized proportional to the excess squared as

$$f^{MaxDose} = \frac{1}{N_{ROI}} \cdot \sum_{i}^{N_{ROI}} H(\mathrm{D}_i - \mathrm{D_{Rx}}) \cdot (\mathrm{D}_i - \mathrm{D_{Rx}})^2 \tag{12}$$

For a uniform dose-based objective function of an ROI (with criterion $\mathrm{D_{uniform}} = \mathrm{D_{Rx}}$), the goal is to make the dose to each voxel equivalent to a uniform prescription dose $\mathrm{D_{Rx}}$. The voxels within the ROI with dose above or below the prescription dose are penalized proportional to the deviation from the uniform dose squared. This is equivalent to a combination of maximum and minimum dose-based objectives.

$$f^{Uniform} = \frac{1}{N_{ROI}} \cdot \sum_{i}^{N_{ROI}} (\mathrm{D}_i - \mathrm{D_{Rx}})^2 = f^{MaxDose} + f^{MinDose} \tag{13}$$

Details of dose-based objective functions are described by Wu and Mohan (Wu and Mohan 2000).

2.4.2 Dose-volume based objectives

Dose-volume based objectives corresponds a dose-volume based criterion in the form of $D_{v_{Rx}} \leq D_{Rx}$ (maximum) or $D_{v_{Rx}} \geq D_{Rx}$ (minimum), where $D_{v_{Rx}}$ is the dose computed to the prescription volume v_{Rx} of objective's ROI for a given dose distribution. Here, dose received by a proportion of voxels is constrained to be above or below a prescription dose D_{Rx}. (Note that dose-based objectives are special cases of dose-volume based objectives when v_{Rx} = 100% for maximum or v_{Rx} = 0% for minimum objectives.) Figure 8 shows an example of how a minimum and a maximum DVH objectives work on a DVH graphically. During optimization, $D_{v_{Rx}}$ is recomputed for each iteration after beamlet weight for each beam has been adjusted according to equation (9) .

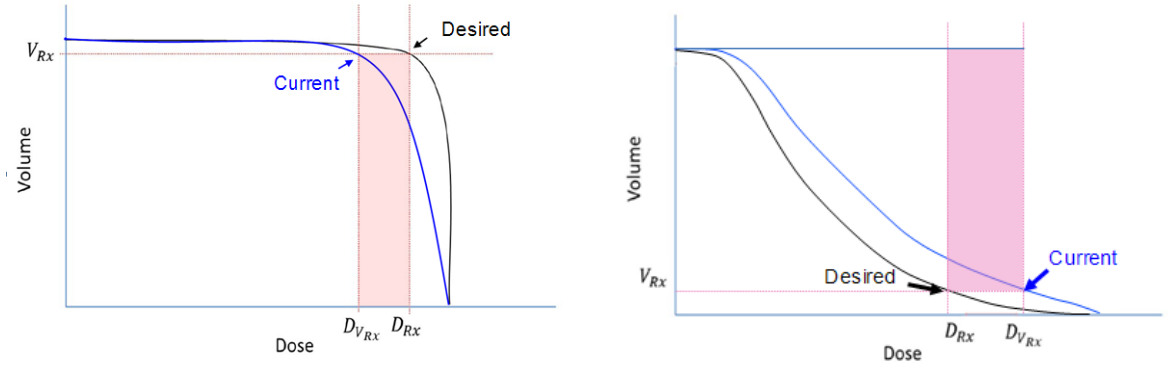

Figure 8. Graphical illustration of variables for (left) a minimum DVH objective (with goal $D_{v_{Rx}} \geq D_{Rx}$) and a maximum DVH objective (with goal $D_{v_{Rx}} \leq D_{Rx}$) The blue curve and the black curve represent desired DVH and current DVH. $D_{v_{Rx}}$ and D_{Rx} are the current and prescription dose to the prescription volume v_{Rx}. The purpose of this DVH objective is to have the DVH ($D_{v_{Rx}}$, v_{Rx}) optimized to the desirable location (D_{Rx}, v_{Rx}). The red shaded region is the penalty region.

For a minimum DVH objective (with criterion $D_{v_{Rx}} \geq D_{Rx}$), the goal is to keep the dose to the percentage of voxels ($\leq$ the prescription volume v_{Rx}) above the prescription dose D_{Rx}. Only those voxels with dose between $D_{v_{Rx}}$ and D_{Rx} are penalized. (See the pink region in

Figure 8.) The voxels with higher dose than D_{Rx} have no penalty because they meet the constraints of the objective. The voxels with lower dose than $D_{v_{Rx}}$ have no penalty because they are in the permitted percentage of the high dose volume, i.e., $D_{v_{total}-v_{Rx}} < D_{Rx}$ is allowed with respect to $D_{v_{Rx}} \geq D_{Rx}$ where v_{total} is the total percentage volume of ROI. The objective function is

$$f^{MinDVH} = \frac{1}{N_{ROI}} \cdot \sum_{i}^{N_{ROI}} H(D_{Rx} - D_i) \cdot H(D_i - D_{V_{Rx}}) \cdot (D_i - D_{Rx})^2 \qquad (14)$$

When $D_{v_{Rx}}$ is optimized above D_{Rx}, the function value is 0 as the objective has been fully satisfied.

For a maximum DVH objective (with criterion $D_{v_{Rx}} \leq D_{Rx}$), the goal is to limit the dose to the specified percentage of voxels ($\geq$ the prescription volume v_{Rx}) to be below the prescription dose. Analogous to the minimum DVH objective, only the voxels with dose below D_{Rx} and above $D_{v_{Rx}}$ are penalized. The objective function of the maximum DVH objective can be

$$f^{MaxDVH} = \frac{1}{N_{ROI}} \cdot \sum_{i}^{N_{ROI}} H(D_i - D_{Rx}) \cdot H(D_{V_{Rx}} - D_i) \cdot (D_i - D_{Rx})^2 \qquad (15)$$

When $D_{v_{Rx}}$ is optimized below D_{Rx}, the function value is 0 as the objective has been fully satisfied. Details of dose-volume-based objective functions are described by Wu and Mohan (Wu and Mohan 2000).

2.4.3 pDVH based objective

The pDVH objective functions (Gordon *et al.* 2010) serve as key functions for COP optimization. As mentioned before, pDVH is a result of "dynamic" DVHs which are different in

each virtual treatment course due to the different GUs sampled from PDFs of GU model. Unlike the previous basic objectives that operate on static DVH, pDVH-based objectives operate on pDVH with GU variability considered. These objective functions are utilized in COP to meet pDVH criteria in the format of $\Pr[D_{C_{Rx}} \geq D_{Rx}] \geq q_{Rx}$ (minimum pDVH criteria) or $\Pr[D_{C_{Rx}} \leq D_{Rx}] \geq 1 - q_{Rx}$ (maximum pDVH criteria) or where $D_{C_{Rx}}$ is dose at prescribed coverage and Pr[] denotes the probability of a DVH-based objective ($D_{C_{Rx}} \leq D_{Rx}$ or $D_{C_{Rx}} \geq D_{Rx}$) is met and q_{Rx} is the prescribed coverage probability value. A typical value of q_{Rx} is 95% for target volumes and 5% for OAR to allow 5% outlier cases. Figure 9 shows an example of how maximum pDVH objective works on a pDVH graphically. During optimization, $D_{C_{Rx}}$ must be recomputed in each iteration.

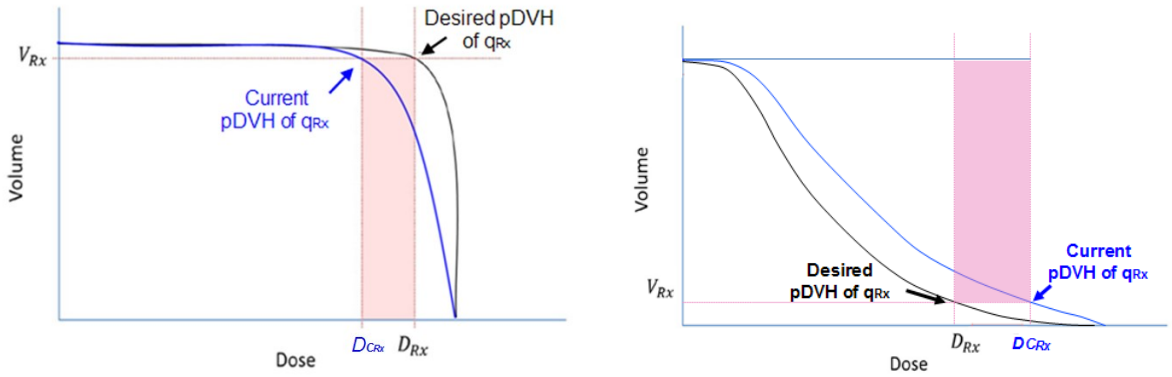

Figure 9. Graphical illustration of variables for a minimum pDVH objective (left) and a maximum pDVH objective (right) in the form of $\Pr[D_{C_{Rx}} \geq D_{Rx}] \geq q_{Rx}$ and $\Pr[D_{C_{Rx}} \leq D_{Rx}] \geq 1 - q_{Rx}$. The blue curve and the black curve represent desired pDVH and current pDVH of coverage value q_{Rx}. $D_{C_{Rx}}$ and D_{Rx} are the current and prescription dose to the prescription volume v_{Rx}. The purpose of this pDVH objective is to pull the pDVH from ($D_{C_{Rx}}$, v_{Rx}) to the desirable location (D_{Rx}, v_{Rx}) on the pDVH plot.

For a minimum pDVH objective (with criterion $\Pr[D_{C_{Rx}} \geq D_{Rx}] \geq q_{Rx}$), the goal is to ensure that dose at the prescribed coverage q_{Rx}, $D_{C_{Rx}}$, achieves the prescription dose D_{Rx}. The objective function is written as

$$f^{MinpDVH} = \frac{1}{N_{ROI\_neighborhood}} \cdot \sum_{i}^{N_{ROI\_neighborhood}} H(\mathrm{D_{Rx}} - \mathrm{D}_i) \cdot H(\mathrm{D}_i - \mathrm{D_{C_{Rx}}}) \cdot \omega_i^2 (\mathrm{D}_i - \mathrm{D_{Rx}})^2 \qquad (16)$$

where $ROI\_neighborhood$ refers to the voxels within an ROI neighborhood composed of ROI and a ring structure surrounding the ROI, and ω_i stands for a voxel-specific weighting factor. Only voxels within $ROI\_neighborhood$ with D_i between $\mathrm{D_{C_{Rx}}}$ and $\mathrm{D_{Rx}}$ are penalized.

For a maximum pDVH objective (with criterion $\Pr[\mathrm{D_{C_{Rx}}} \le \mathrm{D_{Rx}}] \ge 1 - \mathrm{q_{Rx}}$), the goal is to ensure that dose at the prescribed coverage $\mathrm{q_{Rx}}$, $\mathrm{D_{C_{Rx}}}$, is below the prescription dose $\mathrm{D_{Rx}}$ for at least $1 - \mathrm{q_{Rx}}$ chance. The objective function is

$$f^{MaxpDVH} = \frac{1}{N_{ROI\_neighborhood}} \cdot \sum_{i}^{N_{ROI\_neighborhood}} H(\mathrm{D}_i - \mathrm{D_{Rx}}) \cdot H(\mathrm{D_{C_{Rx}}} - \mathrm{D}_i) \cdot \omega_i^2 (\mathrm{D}_i - \mathrm{D_{Rx}})^2 \qquad (17)$$

When $\mathrm{D_{C_{Rx}}}$ is optimized below $\mathrm{D_{Rx}}$, the function value is 0 as the objective has been fully satisfied.

The novelty of using $ROI\_neighborhood$ and voxel-specific weight ω_i makes COP distinctive from other treatment planning techniques. $ROI\_neighborhood$ is a PTV-like structure to include all the voxels that potentially contribute the ROI coverage, and ω_i is to weight each voxel inside $ROI\_neighborhood$ based on its contribution of ROI converge. As opposed to that a PTV is determined empirically and assumed of equal importance for each voxel, both $ROI\_neighborhood$ and ω_i are determined by simulating GUs in a large number of (e.g., 1000) virtual treatment courses before optimization starts. To make sure $ROI\_neighborhood$ is large enough, ROI is first expanded by 1 voxel to include the nearest exterior surface voxels for the purpose of dose interpolation. Then possible voxel locations as a result of ROI offset in the virtual treatment courses are added to this $ROI\_neighborhood$. Let ROI_ring denote a

concentric series of *ROI _neighborhood* voxels which exclude ROI voxels. Since its location and chance of being covered by the "moving" ROI are different from others, each *ROI _ring* voxels may have different contributions to ROI coverage probability. To consider this, ω_i is used to weight the squared dose term in equation (17) for each *ROI _neighborhood* voxel. ω_i can be expressed as an empirical function below

$$\omega = \begin{cases} 5 & v_n \in ROI \\ 1 + \dfrac{4}{1 + 5(\delta - \Delta(d))} & v_n \in ROI\_ring = ROI\_neighborhood - ROI \end{cases} \quad (18)$$

The empirical weight is constantly 5 for ROI voxels and ranges from 1 to 5 for *ROI _ring* voxels. To weight a *ROI _ring* voxel, a quantity δ is used to represents a "voxel distance" in the form of

$$\delta = -\text{norminv}(prob_{ROI},\ 0,\ 0.3) \quad (19)$$

where $prob_{ROI}$ is probability that a *ROI _ring* voxel may be covered by the "moving" ROI due to GUs, norminv() is the normal inverse cumulative distribution function with parameters $prob_{ROI}$ as probability, 0 as mean, 0.3 as SD. δ decreases from ∞ to 0 as $prob_{ROI}$ increases from 0 to 1. If a *ROI _ring* voxel dose is d, $\Delta(d)$ represents the minimum δ value among all the *ROI _ring* voxels whose dose are d. The smaller $\delta - \Delta(d)$ is, the larger ω (and more important coverage contribution) of the *ROI _ring* voxel is. The mechanism of ω_i is to encourage the optimizer to optimize dose to ROI voxels first and then *ROI _ring* voxel from "near" (=more important) to "far" (=less important). Thus, more rapid convergence of optimization can be achieved to shape a desired dose distribution.

2.5 Implementation of objective functions in a commercial TPS

A base theoretical method of IMRT and COP optimization has been described in the previous sections. The commercial TPS in this dissertation is Pinnacle^3 9.0 (research version) (Philips Healthcare, Andover, MA). To implement COP to Pinnacle^3, practical modifications are required including (1) a change in the format of objective functions, (2) beam fluence initialization for the pDVH objectives used in COP.

2.5.1 Reformatted objective functions

All the objective functions mentioned before are reformatted when used in Pinnacle^3. The ROI volumes are normalized to 1, so the $\frac{1}{N_{ROI}}$ term is not necessary in the objective functions. Additionally, the weighting factor p in equation (2) is moved into each individual objective function. For example, a maximum DVH objective in equation (15) becomes

$$f^{MaxDVH} = \sum_{i}^{N_{ROI}} p \cdot V_i \cdot H(\mathrm{D}_i - \mathrm{D}_{\mathrm{Rx}}) \cdot H(\mathrm{D}_{\mathrm{v}_{\mathrm{Rx}}} - \mathrm{D}_i) \cdot (\mathrm{D}_i - \mathrm{D}_{\mathrm{Rx}})^2 \tag{20}$$

where is V_i the normalized volume of each voxel.

Also, a scaling factor $S_{\mathrm{Pinn}} = \left(\frac{1}{\mathrm{D}_{\mathrm{Rx}}}\right)^2$ to normalize scores from different prescription dose levels is used to eliminate the dose-dependent term in derivatives. In this way, the example objective in equation (20) is changed to

$$F^{MaxDVH} = \sum_{i}^{N_{ROI}} p \cdot V_i \cdot S_{\mathrm{Pinn}} \cdot H(\mathrm{D}_i - \mathrm{D}_{\mathrm{Rx}}) \cdot H(\mathrm{D}_{\mathrm{v}_{\mathrm{Rx}}} - \mathrm{D}_i) \cdot (\mathrm{D}_i - \mathrm{D}_{\mathrm{Rx}})^2 \tag{21}$$

where F denotes the Pinnacle^3 objective function for a objective of interest o. The first derivative and the second derivative of the non-zero part of equation (21) with respect to the beamlet weight w_j are

$$\frac{\partial F^{MaxDVH}}{\partial w_j} = \sum_i^{N_{ROI}} 2 \cdot p \cdot V_i \cdot S_{\text{Pinn}} \cdot H(\mathrm{D}_i - \mathrm{D}_{\text{Rx}}) \cdot H(\mathrm{D}_{v_{\text{Rx}}} - \mathrm{D}_i) \cdot (\mathrm{D}_i - \mathrm{D}_{\text{Rx}}) \cdot K_{ij} = \sum_i^{N_{ROI}} G_i^{MaxDVH} \cdot K_{ij} \quad (22)$$

and

$$\frac{\partial^2 F^{MaxDVH}}{\partial w_j^{\,2}} = \sum_i^{N_{ROI}} 2 \cdot p \cdot V_i \cdot S_{\text{Pinn}} \cdot H(\mathrm{D}_i - \mathrm{D}_{\text{Rx}}) \cdot H(\mathrm{D}_{v_{\text{Rx}}} - \mathrm{D}_i) \cdot K_{ij}^{\,2} = \sum_i^{N_{ROI}} \mathcal{H}_i^{MaxDVH} \cdot K_{ij}^{\,2} \quad (23)$$

Particularly, G_i^{MaxDVH} in equation (22) is the Pinnacle objective function gradient on a per voxel basis. G_i^{MaxDVH} is used since Pinnacle computes and stores K_{ij} independently of the first derivative matrix. The separation results in K_{ij} being dependent only on the beam and anatomy configuration and independent of objective function. For a similar reason, $\mathcal{H}_i^{MaxDVH}$ is used in equation (23). It is a constant handled internally in Pinnacle[3].

To sum up, as IMRT inverse planning is a process of iteratively computing the composite cost function and changing beamlet weight, Pinnacle[3] computes function value $F_{total} = \sum^{nObj} F$ and the gradient $G_{total,i} = \sum^{nObj} G_i$ to adjust beamlet intensity via Newton's method for each iteration.

2.5.2 Beam fluence initialization for COP

Readers may have already noticed that in Table III (page 22) a structure called CTV_neighborhood is added to the optimization criteria for COP plans. CTV_neighborhood is a virtual target expansion utilized as an initial target volume in Pinnacle[3]. The initial target volume forces Pinnacle[3] to set initial beamlet intensities, in order to permit creation of a desirable dose distribution. This volume may be not necessary in other TPS but required to be determined before COP optimization in Pinnacle[3]. At the start of an optimization, Pinnacle[3] initializes beamlet intensities to a nonzero value only for those beamlets that traverse the initial target volume. The intensities of all other beamlets are initialized to zero, and remain zero through the

optimization. For conventional PTV-based plans, the initial target volume is not required since PTV using minimum dose-based or dose-volume based criterion is regarded as the default initial target volume. However, for COP plans, the target structures $CTV_{prostate}$ and CTV_{SV} are too small to be used as the initial target volume. GUs can result in $CTV_{prostate}$ or CTV_{SV} occupying voxels outside its static contoured boundary (in the accelerator coordinate system). Dose in these "exterior" voxels affects coverage probabilities of $CTV_{prostate}$ and CTV_{SV}, too. To ensure enough voxels are occupied, the CTV_neighborhood is used in COP as the initial target volume. In this dissertation, CTV_neighborhood is empirically defined as the union volume of $CTV_{prostate}$ and CTV_{SV} on all fractions of patient database (see chapter 4.1) with a uniform expansion by 12 mm.

2.6 Summary

COP is a modified inverse planning technique of IMRT process, where beam fluence/intensity is adjusted in the goal of minimizing the composite objective function associated with the optimization criteria. The novelty of COP is using pDVH criteria and pDVH objectives to seek an optimized dose distribution to i.e., maximally achieve targets and OARs coverage probability at prescribed value to overcome the degraded dosimetric effect caused by GUs. In the pDVH objective functions, some exterior ROI voxels with potential contribution to ROI coverage probability are particularly included and weighted according to their potential contribution. To implement COP in a commercial TPS Pinnacle[3], the objective functions need to be reformatted and beam fluence initialization is required.

3 Metrics for plan evaluation

In clinical radiation therapy plan development, plan evaluation serves to judge one or inter-compare two competing treatment plans with respect to the treatment objectives. Planning metrics distill information contained in a complex patient 3D dose distribution into quantities that can be readily compared. These metrics/quantities are very useful to help determine whether COP is needed to optimize a current dose distribution and how better or worse COP plans can be relative to other PTV plans.

This chapter examines planning metrics for plan evaluation, optimization and comparison. Some are dosimetric endpoint metrics and the others are biological endpoint metrics. These metrics are used in the following chapters to investigate the potential clinical impacts of GUs and the planning methods (including COP) used to compensate these clinical impacts.

3.1 Dosimetric endpoint: dose-volume metrics

In clinical practice, dose-volume metrics of a specified structure are most commonly and routinely used metrics for plan prescription and reporting. These metrics conveniently reveal the relationship of the absorbed dose to relevant anatomic volumes. For example in Table IV, D_v represents absorbed dose to v% volume of the structure. For a target structure, D_{min} (= D_{100}) or D_{98} is often used to quantify the minimum dose to be delivered. D_{98} is used instead of D_{min} when

2% volume cold spot[4] is allowed. A typical dose-volume metric based criterion/prescription can be $D_{98} \geq d$.

Dose metrics can be read by a calculating associated dose volume histogram (DVH) which is composed of all the dose-volume metric points. A DVH summarizes a 3D dose distribution (which is a 3D dose array computed for all voxels) of a structure in a graphical 2D format. A DVH is usually visualized in a cumulative way. A cumulative DVH displays the percentage of the volume of a given region of interest which receives greater than a specified dose. Note in this dissertation, DVH elsewhere refers to cumulative DVH. Figure 10(a) demonstrates how a DVH can be used in plan comparison. DVH A lies to the right of DVH B. The dose received by a certain percentage volume of an ROI in DVH A is always higher than that in DVH B. If DVH A and DVH B are both for the same ROI, DVH A is usually preferred when the ROI is a target structure to achieve high and uniform prescribed dose. Otherwise, DVH B is better as low dose to an OAR is desired.

Table IV. Dose-volume metrics that can be obtained from a DVH curve

Metric	Meaning
D_v	Absorbed dose to v% volume of the structure. e.g., D_{avg} =Average dose D_{50} = Median dose D_{98} = Near minimum dose D_2 = Near maximum dose
V_D	volume receiving at least an absorbed dose of D

[4] A cold spot refers to an area in the target that receives a lower dose than the specified target dose. Only if its area covers at least 2 cm^2, a cold spot is considered clinically meaningful. (Khan 2003)

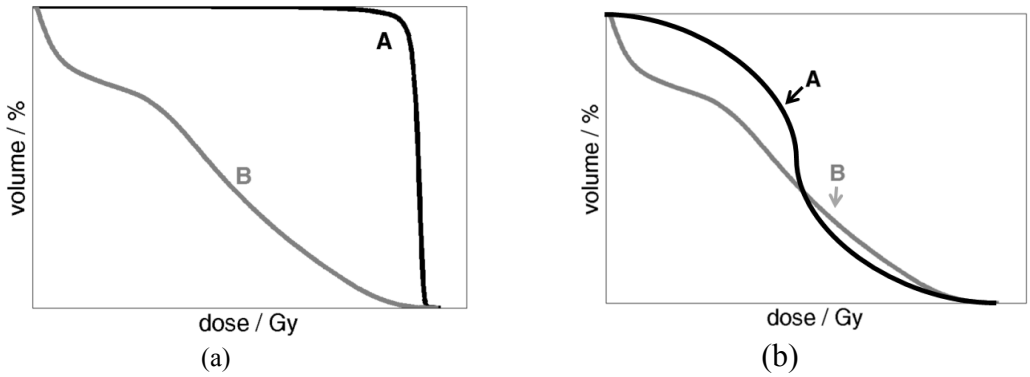

Figure 10. Two examples of (a) a simple (cumulative) DVH comparison and (b) a complex DVH comparison between A and B. Example (b) is complex because two DVHs of same ROI can have same (i.e., min, average and max) dose metrics.

However, DVH has limitations. First, the standard DVH loses spatial information of dose distribution. It is impossible to locate a specific position of an ROI voxel on a DVH in Figure 10. To augment this, many methods have been proposed i.e., to show distance between ROI voxels in DVH to either the ROI or another adjacent ROI. (Cheng and Das 1999, Chao *et al.* 2003, Bortfeld *et al.* 2008, Wu *et al.* 2008, 2009, 2011, Huang *et al.* 2010, Zhao *et al.* 2010, Zhu *et al.* 2011, Witte *et al.* 2011, Mayo *et al.* 2013) One example is to calculate vectors pointing from the voxels in one ROI DVH to the nearest points on surfaces of other ROI and add the vector information on a DVH. (Mayo *et al.* 2013) However, these methods are still proof-of-concept and cannot totally represent 3D dose distribution. They are so far only used in-house by the developers and have not been standardized. Another limitation of DVH is that DVH comparison can be very complex sometimes. It is possible that two DVHs from competing plans cross on another and may share the same average/min/max dose (e.g., Figure 10 (b)). Therefore, a thorough review of the 3D dose distribution or other metrics is still needed to judge or compare treatment plans.

3.2 Dosimetric endpoint: coverage probability

Coverage probability is an important and unique dosimetric concept that directly reveals the relationship of ROI dose and GUs. This metric is important for the evaluation/comparison of plans under the influence of GUs. A coverage probability value is the probability that a realized target or OAR dose metric D_v exceeds the dose of interest (Rx, tolerance or other dose) when treatment planning and delivery uncertainties are taken into account. (Gordon and Siebers 2008) For evaluation of a static plan (one free of GUs), coverage probability reduces to boolean (i.e., 0% or 100%) values. However, realistically, a static patient geometry is not possible in multi-fractioned radiation therapy. Coverage probability values of targets and OARs often differ considerably from the value implied by the static plans (Gordon and Siebers 2008, Xu *et al.* 2011). Therefore, coverage probability evaluations are essential for evaluating plans under the influence of GUs.

Two methods have been used to estimate coverage probability. One is using DVCM and the other is dosimetric margin distribution (DMD). The DVCM method estimates coverage probability by simulating possible treatment outcome while the DMD method calculates coverage probability by a formula under the condition that the relationship of GUs PDF and coverage probability is known. In fact, the DMD method is a simplified version of the DVCM method when a simple GUs PDF (e.g., Gaussian) is considered. Compared to the DMD method which estimates coverage probability values for only a single dose-volume metric, the DVCM method (mentioned in section 2.1) is more general and permits simultaneous analysis of multiple dose-volume metrics. Therefore, the DVCM method is used to estimate coverage probabilities for this dissertation. Both methods will be discussed in the following paragraphs.

3.2.1 Coverage probability estimation method: DVCM

One way to estimate coverage probability is by constructing a DVCM, a 2D dose volume coverage map that contains coverage probability for each dose-volume metric for an ROI. (Gordon *et al.* 2010) It has been mentioned briefly in the workflow of pDVH and COP in Figure 6 (page 20) and will be described in detail (Figure 11) here. To get a DVCM, a large number (n_{tx}) of virtual treatment courses, each with multiple fractions (n_{frac}) are simulated. For each virtual treatment course, different GUs sampled from PDF of the constructed GU model result in different ROI DVHs as a result of the accumulated dose distribution of all the n_{frac} fractions. The axes of dose and volume of DVH are divided into small increment, 0.1Gy and 1% respectively, to create a 2D grid map. For the 1st DVH of the 1st virtual treatment course, the grid squares below or left to the DVH curve are assigned value 1.0 (=100%) and the others are 0.0. Then for each DVH, increment all grid squares lying below or to the left of the DVH by 1.0. All the grid values are divided by total number of DVHs ($=n_{tx}$) to finalize this map, which is so-called DVCM. In an ROI DVCM, each grid square (corresponding dose *d* and volume v) contains the probability that, in an individual treatment course, $D_v \geq d$ can be achieved for the ROI when GU(s) are considered. For the example of a ROI DVCM in Figure 11, D_v with probability 1.0 can be achieved 100% based on the 2 simulated virtual treatment courses. The probability of each grid square is called the coverage probability corresponding to the metric D_v and can be used for plan evaluation and/or optimization.

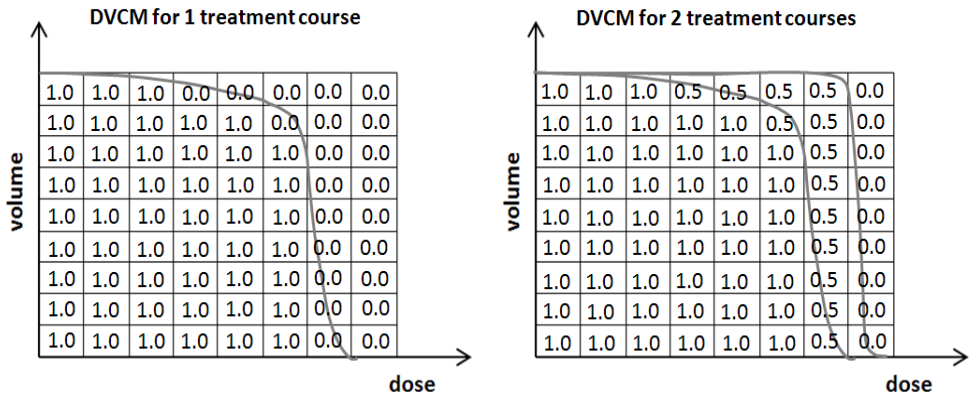

Figure 11. Example of how a ROI DVCM is generated for a simple case with only two virtual treatment courses. Get DVH (grey lines) with different GU(s) for each treatment course. For each DVH, increment all grid squares lying below or to the left of the DVH by 1.0. Then normalize the whole grid values.

3.2.2 Coverage probability estimation method: DMD

Another way to estimate coverage probability is via a DMD, the distribution of dosimetric margins (DMs) over 3D directions. DMD was inspired by the fact that ROI coverage probability with respect to dose *d* is a function of the distance between the ROI and the volume enclosed by the critical isodose surface of dose *d*. (Gordon and Siebers 2008) Such distance in a specific direction (φ, θ) is called DM and denoted as $M_{v,d}(\varphi, \theta)$. DM is the safety margin that the ROI can be offset while still satisfying a dose constraints $D_v \geq d$ for CTV or $D_v \leq d$ for OAR. For example $M_{min,70}(\varphi, \theta)$ $(=M_{100,70}(\varphi, \theta))$ denotes the maximum distance the CTV (or OAR) can be offset in the direction (φ, θ) before its D_{min} $(=D_{100})$ falls below (exceeds) 70 Gy. For an isodose surface that is within or crosses the structure, DM = 0. Examples of DMD for a target CTV and a bladder for prostate cancer treatment are shown in Figure 12. A type I (type II) ROI indicates that the static plan meets (violates) the specified dose-volume criteria. A type II ROI is non-standard and ends up with low coverage for targets and high coverage for OARs. Please refer to Appendix II.b for detailed distinction of type I and type II structures.

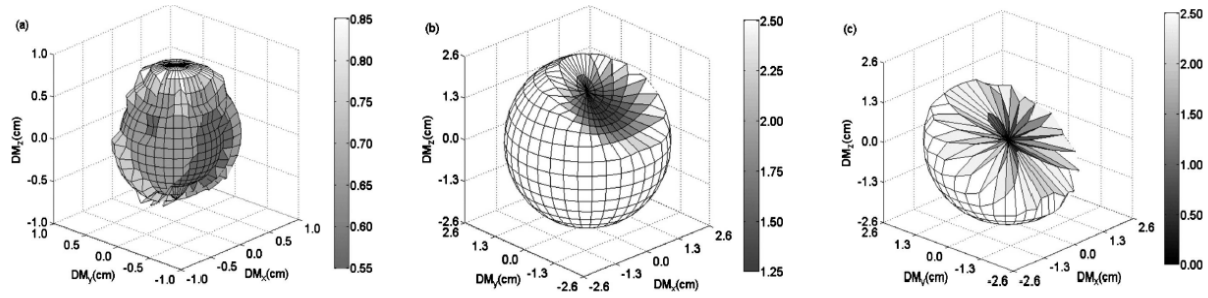

Figure 12. Examples of DMD sampled using fixed angular increment method for (a) CTV $D_{min, 79.2}$(type I), (b) bladder $D_{25, 70}$ (type I) and (d) bladder $D_{25, 70}$ (type II) (Xu *et al.* 2011)

When DM $M_{v,d}(\varphi,\theta)$ and geometric uncertainty parameter(s) such as SD of systematic setup errors Σ are known, the corresponding coverage probability $Q(\varphi,\theta,\Sigma)$ in this specific direction can be estimated using the following function,

$$Q(\varphi,\theta,\Sigma) = f(M_{v,d}(\varphi,\theta),\Sigma) \tag{24}$$

where f() denotes a coverage function whose form depends on the PDF of the geometric uncertainty. Note here we use Q (not q) to represent the coverage probability that is obtained via DMD method (not DVCM method). The overall coverage $Q(\Sigma)$ is

$$Q(\Sigma) = \sum_{\varphi,\theta} W_{\varphi,\theta} \cdot Q(\varphi,\theta,\Sigma) \tag{25}$$

where $W_{\varphi,\theta}$ is a weighting factor equal to the fraction of 4π sr covered by the ray in the direction (φ, θ). An example of how $Q(\Sigma)$ of a CTV and an OAR varies with Σ is shown in Figure 13, where random uncertainties are accounted for through fluence convolution. Each coverage curve corresponds to a single dose-volume metric D_v of the ROI.

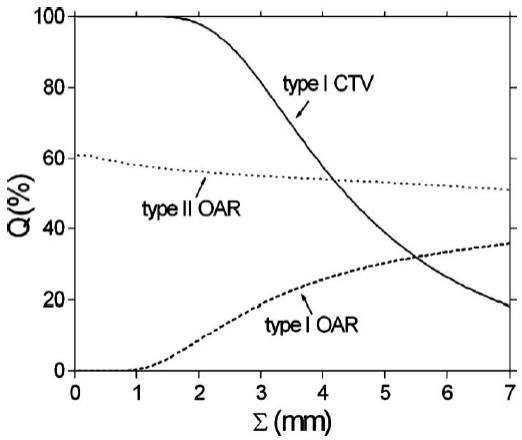

Figure 13. Qualitative dependence of coverage probability Q on systematic SD for type I targets and type I/II OAR. (Xu *et al.* 2011)

For coverage estimations using DMD method, it is important to note that a sufficient sample of DM is required to ensure a representative DMD and accurate Q. The earlier study (Xu *et al.* 2011) proved that DMD sampling with angular increment ω (fixed angular increment method) or ω_{eff} (isotropic sampling method) = 10° and δ = 0.5 mm should be adequate for planning purposes.

3.3 Biological endpoints: BED, EUD, TCP and NTCP

Biological metrics in this dissertation refers to metrics that are modeled to correlate physical dose to biological response such as cell killing and normal tissue complication. The biological metrics related to this dissertation include biological equivalent dose (BED), equivalent uniform dose (EUD), tumor control probability (TCP) and normal tissue complication probability (NTCP). Biological models used in biological metrics intend to represent complex reality (i.e., clinical observations of cell radiobiology response) by simplistic equations and a few parameters. Such models, if realistic and representative, could be considerably useful in both plan evaluation and optimization. However, uncertainty introduced by the models and their

parameters associated with the biological metrics remains a concern. (ICRU Report 83 2011) After all, the complex biology of tumors and normal tissues for each patient is unlikely to be represented by a single equation with population-based parameters. Therefore, ICRU 83 report suggests using biological metrics for secondary plan evaluation only. (ICRU Report 83 2011) Nonetheless, these metrics provide additional quantitative measures for plan comparisons.

3.3.1 Basic radiobiology: cell survival curves and fractionated dose

The biological effects of radiation lead to a certain level of DNA damage and therefore cell death in tumors and normal tissues. Damage is tissue-specific and dependent on irradiated dose and cell characteristics such as sensing and repair of damaged DNA. The cell survival curve depicts cell survival after irradiation as a function of dose, as shown in Figure 14. The linear-quadratic model is the most widely accepted way to describe the relationship of cell surviving fraction S and dose D as.

$$S = \exp(-\alpha D - \beta D^2) \tag{26}$$

where α and β are linear and quadratic component slope when equation (26) is plotted on the logarithmic scale. α/β is an important term which shows the tissue sensitivity to dose. When $D = \alpha/\beta$, linear killing and quadratic killing are equivalent.

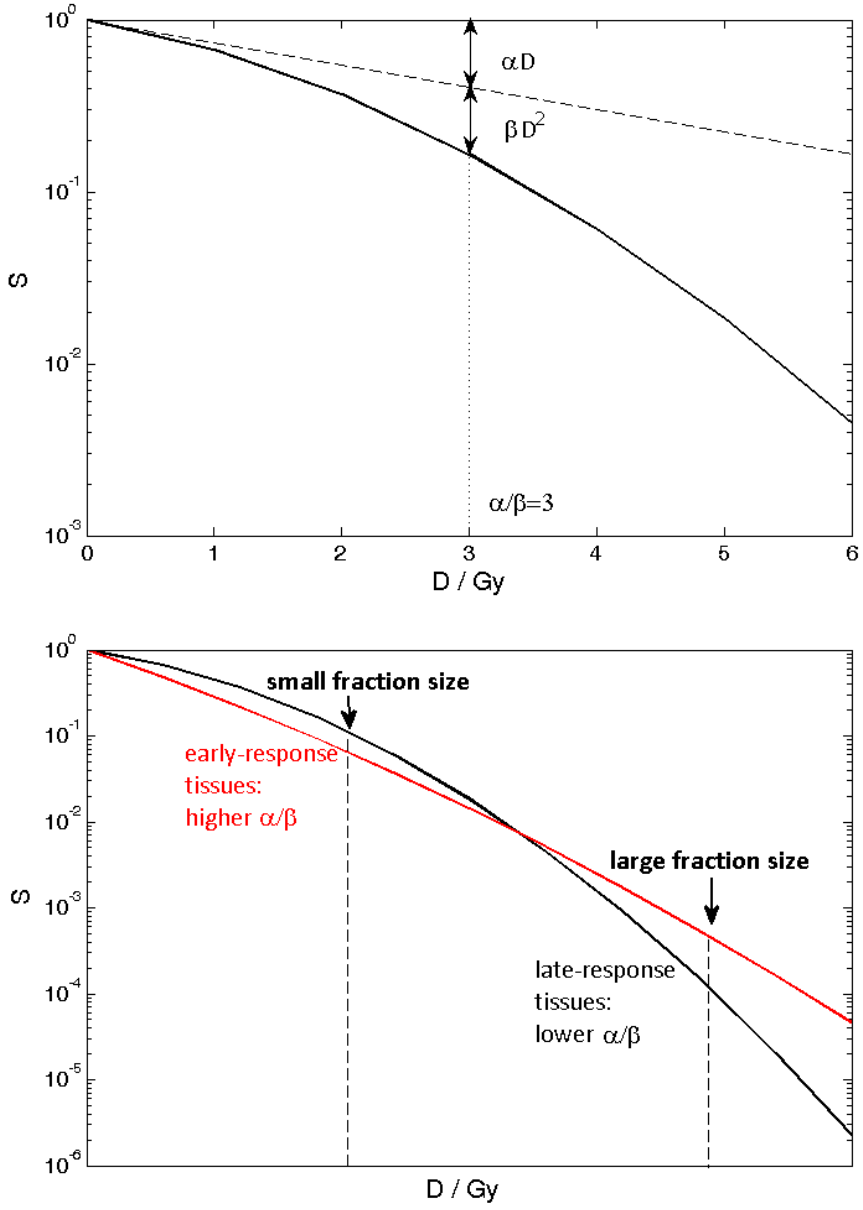

Figure 14. Illustration of (upper) cell survival curve of dose D versus survival fraction S when the α/β ratio = 3 and (lower) example of different cell survival curve of early and late response tissues.

Fractionated radiotherapy is performed in clinical treatment to take advantage of different α/β ratios between tumors and normal tissues. As Figure 14 illustrates, late-responding tissues (lower α/β) are relatively more resistant to low doses (=higher survival) and more sensitive to high doses than early-responding tissues (higher α/β). There is a growing

consensus that α/β for prostate cancer is lower than that of normal tissues. (Fowler *et al.* 2001, Bentzen and Ritter 2005, Daşu 2007, Fatyga *et al.* 2009) If this is true, theoretically, increasing the dose per fraction (and therefore larger fraction size) can result in more injury (or less repair) to the prostate cancer cells than surrounding normal tissues.

To consider α/β and fractionation scheme with respect to biological response, BED is often computed. Based on the linear quadratic model, BED_i of fraction i with dose D_i is

$$\mathrm{BED}_i = \mathrm{D}_i \cdot \left[1 + \frac{\mathrm{D}_i / n}{(\alpha/\beta)} \right] \tag{27}$$

where n is the total number of treatment fractions and α/β is the tissue-specific fractionation sensitivity. α/β introduces uncertainties of BED estimation as its value is still debated. Here, a relatively conservative α/β = 3 is selected for prostate (Fatyga *et al.* 2009). α/β = 5 is assumed for bladder and rectum.

3.3.2 Equivalent uniform dose

EUD of an ROI is the uniform dose that would give the same biological response as the non-uniform dose distribution of interest. EUD was originally introduced in a mechanistic model for tumors by employing the linear quadratic cell survival formalism. (Niemierko 1997) Later, generalized EUD (gEUD) was presented to make the concept of EUD applicable to both tumours and normal tissues (Niemierko 1999). gEUD replaces a complicated dose distribution by a single scalar dose value. This value is calculated based on the assumption that all the other conditions (e.g., patient, dose fraction, total dose) of the non-uniform dose remain unchanged. The equation of gEUD is

$$\mathrm{gEUD} = n\left(\sum_i \mathrm{v}_i \cdot \mathrm{D}_i^a\right)^{1/a} \tag{28}$$

where n is the total number of treatment fractions, v_i is the volume of the dose–volume bin with absorbed dose D_i, and the exponent a is a response-specific parameter. For tumor control in target structures (e,g., prostate), $a < 1$ so that gEUD is more sensitive to the lower doses. For a (parallel-like) normal tissue such as lung, $a = 1$ and gEUD is equivalent to the mean dose. For a (serial-like) normal tissue, $a > 1$ so that gEUD is largely affected by the higher dose. a may be determined empirically by fitting dose-volume data, but there are no universal recommendations value for a. Here $a = 0.16$ (Fatyga *et al.* 2009), 20 (Cahlon *et al.* 2008), 11.1 (QUANTEC) are used for prostate, bladder and rectum, respectively.

As an extension of concept of gEUD, general equivalent uniform biological effective dose gBEUD can be calculated by substituting D_i by biological effective dose BED_i (in equation (27)). Namely,

$$\mathrm{gBEUD} = \left(\sum_i \mathrm{v}_i \cdot \mathrm{BED}_i^a\right)^{1/a} \tag{29}$$

Both gEUD and gBEUD can be used as an independent metric or a parameter to estimate another biological metric such as normal tissue complication probability (in section 3.3.4).

3.3.3 Tumor control probability

TCP is a biological metric to predict the probability of long-term recurrence-free survival (which means the absence of a detectable or symptomatic tumor). The key assumption of all the TCP models is that a tumor is controlled when all the cells lose clonogenic viability. A TCP model based on Poisson statistics (Nahum and Tait 1992, Niemierko and Goitein 1993, Webb and Nahum 1993, Sanchez-Nieto and Nahum 1999) is used in this dissertation. This model

simply assumes that all clonogens within the tumor are uniformly distributed and have identical radio-sensitivities. TCP is estimated from a 3-D dose distribution (with uniform dose D_i for i^{th} voxel) of the tumor (CTV) of total N voxels given the dose required for a 50% probability of tumor control (D_{50}) and the normalized slope (γ_{50}) of the sigmoid-shaped dose–response curve at D_{50}. The formula is

$$\mathrm{TCP} = \begin{cases} \exp\left(-\frac{\ln 2}{N} \sum_i \exp\left[2\frac{\gamma_{50}}{\ln 2}\left(1 - \frac{\mathrm{D}_i}{D_{50}} \right) \right] \right) & \text{non-EUD Possion} \\ \exp\left(-\ln 2 \cdot \exp\left[2\frac{\gamma_{50}}{\ln 2}\left(1 - \frac{\mathrm{gEUD}}{D_{50}} \right) \right] \right) & \text{EUD Possion} \end{cases} \tag{30}$$

Parameters for TCP calculations can be obtained from studies that evaluate clinical data for dose–response relationships. The fitting parameters in (Cheung *et al.* 2005) are used here. Note D_i (or gEUD) does not have to be physical dose. It can be the BED in equation (29) as long as D_{50} is the same type of dose. In this dissertation, BED and gBEUD are used.

3.3.4 Normal tissue complication probability

NTCP is a biological metric used to predict the probability of an OAR complication, such as bladder bleeding or rectal bleeding that may occur after prostate cancer treatment. The complication is modeled as a function of the dose (or biological equivalent dose) and volume.

The classic phenomenological Lyman-Kutcher-Burman (LKB) model (Lyman 1985, Cheung *et al.* 2005) is most commonly used to calculate NTCP. This model assumes that the complication probability sigmoid curve can be described by the error function. It explicitly relates partial-volume tolerance dose through a power law in volume. LKB model can be written as

$$\mathrm{NTCP} = \frac{1}{\sqrt{2\pi}} \int_{-\infty}^{t} du \exp\left(-u^2/2\right) \tag{31}$$

where

$$\mathrm{t} = (\mathrm{gBEUD} - TD_{50}) / (\mathrm{m} \cdot TD_{50}) \tag{32}$$

where gBEUD is general equivalent uniform biological effective dose in equation (29), TD_{50} is the tolerance dose producing a 50% complication probability and m is the slope parameter of the complication sigmoid curve. Many published values of TD_{50} and m are inconsistent. Quantitative Analysis of Normal Tissue Effects in the Clinic (QUANTEC) has recommendations for the rectum but not for the bladder risk assessment, probably related to the fact that bladder wall is rarely contoured. Here, bladder parameters are obtained from other literature. (Burman *et al.* 1991, Luxton *et al.* 2004)

The TCP and NTCP models and associated parameters used in the COP studies described in chapter 5 and 6 are summarized in Table V. Note the conventional way to estimate TCP/NTCP of a CTV/OAR after treatment (under the influence of GUs) is via applying the Table V to the surrogate volumes PTV or PRV. This is based on the assumption that PTV/PRV exactly represents CTV/OAR with GUs, which is not true in reality. A novel way to incorporate GUs into TCP/NTCP estimation is by calculating the distribution of the CTV TCP values or the OAR NTCP values in a large number of virtual treatment courses. The possible TCP/NTCP distribution reveals the biological effect of GUs to CTV/OAR in a more representative way. An example of comparing TCP/NTCP distributions of two competing plan is in Figure 18. (chapter 4, page 59)

Table V. A summary of TCP and NTCP model and parameters for prostate, bladder and rectum used in this dissertation. Note conventionally TCP or NTCP value is calculated for a PTV or PRV volume. Here, TCP or NTCP distribution for a CTV or OAR volume is a novel way to account for GUs

TCP: Poisson Model	
Equation	$\mathrm{TCP} = \exp\left(-\frac{\ln 2}{N}\sum_i \exp\left[2\frac{\gamma_{50}}{\ln 2}\left(1-\frac{\mathrm{BED}_i}{D_{50}}\right)\right]\right)$ or $= \exp\left(-\ln 2 \cdot \exp\left[2\frac{\gamma_{50}}{\ln 2}\left(1-\frac{\mathrm{gBEUD}}{D_{50}}\right)\right]\right)$ where $\mathrm{BED}_i = \mathrm{D}_i \cdot \left[1+\frac{\mathrm{D}_i/n}{(\alpha/\beta)}\right]$ and $\mathrm{gBEUD} = \left(\sum_i \mathrm{v}_i \cdot \mathrm{BED}_i^a\right)^{1/a}$
Parameters	D_{50} (dose producing 50% tumor control), γ_{50} (slope parameter), a (EUD parameter), α/β (BED parameter)
Prostate	D_{50} = 67.5 Gy, γ_{50} = 2.2 , a = 0.16, α/β = 3Gy
NTCP: Lyman-Kutcher-Burman model	
Equation	$\mathrm{NTCP} = \frac{1}{\sqrt{2\pi}}\int_{-\infty}^{t} du \exp\left(-u^2/2\right)$ where t = (gBEUD – TD_{50}) / (m TD_{50}), $\mathrm{gBEUD} = \left(\sum_i \mathrm{v}_i \cdot \mathrm{BED}_i^a\right)^{1/a}$ and $\mathrm{BED}_i = \mathrm{D}_i \cdot \left[1+\frac{\mathrm{D}_i/n}{(\alpha/\beta)}\right]$
Parameters	TD_{50} (the tolerance dose producing a 50% complication probability), m (slope parameter), a (gBEUD parameter), α/β (BED parameter)
Bladder	TD_{50} = 80 Gy, m = 0.11, a = 20, α/β = 5Gy
Rectum	TD_{50} = 76.9 Gy, m = 0.13, a = 11.1, α/β = 5Gy

3.4 Summary

This chapter described the dosimetric and biological endpoint metrics used in this dissertation for plan evaluation, optimization and comparison. The pros and cons of each metric in terms of its representativeness for plan evaluation are summarized in Table VI. In the

following COP studies, multiple metrics are calculated to perform a comprehensive plan evaluation/comparison.

Table VI. Summary of metrics for plan evaluation used in this dissertation. All have the con that 3D information is lost.

Metric Name	Metric type	Pros	Cons
Dv (DVH)	Dosimetric	simple	• Static values regardless GUs • Not treatment outcome correlated
Coverage probability	Dosimetric	GUs incorporated	• Model of geometric uncertainty may not be representative • Not treatment outcome correlated
gEUD(gBEUD)	Biological	One simple value substituted from dose distribution	• Parameter is ambiguous • Model may be oversimplified
TCP (single value for PTV)	Biological	Treatment outcome (tumor control rate) correlated	• Parameters are ambiguous • Model and GUs may be oversimplified
NTCP (single value for PRV)	Biological	Treatment outcome (normal tissue complication) correlated	• Parameters are ambiguous • Model and GUs may be oversimplified
TCP (distribution for CTV)	Biological	Treatment outcome (tumor control rate) correlated and GUs incorporated	• Parameters are ambiguous • Model and GUs may be oversimplified
NTCP (distribution for OAR)	Biological	Treatment outcome (normal tissue complication) correlated	• Parameters are ambiguous • Model and GUs may be oversimplified

4 General materials and methods for COP Study

This chapter describes some general materials and methods for the following COP studies in chapter 5 and 6 to account for GUs like organ deformation and delineation uncertainties for prostate cancer treatment. In section 4.1, the patient database and the basic settings of IMRT planning are presented. In section 4.2, the software that implements the GU models in plan optimization (e.g., COP) and evaluation is given. To evaluate the clinical role of COP, the planning techniques to be compared with COP are introduced in section 4.3. The accuracy and precision tests of coverage estimates used in the plan evaluation/comparison for each COP study are discussed in section 4.4.

4.1 Patient database and IMRT planning

The patient database used in this dissertation is a 19-prostate cancer patient-cohort from the Netherlands Cancer Institute (NKI). The patient database with 8-13 CT images throughout the course of treatment per patient permits (a) reasonable confidence to do a population-based research, (b) important GU information for modeling GUs in multi-fractional treatment for prostate cancer representatively, e.g., different positions and shapes of ROI contours reveals interfraction organ motion and deformation during treatment, and (c) the convenience to perform treatment planning on any selected image to simulate virtual treatment courses with or without IGART strategies.

A brief description of this patient database is given here as more details can be found in an earlier work (Deurloo *et al.* 2005). The patient disease stages are: T1, 3 patients; T2, 4 patients; and T3, 12 patients. (Please refer Table I, page 2 for NCCN groupings of prostate cancer.) During a 7–8 week course of conformal radiotherapy, each patient received a planning fan-beam computed tomography (FBCT) scan and multiple (8-12 and 11 on average) repeat FBCT scans. The patient was instructed to empty his bladder and rectum and subsequently drink 250 ml of fluid one hour before the planning FBCT was taken and before each treatment fraction started. The repeat FBCT scans were obtained within 30 min before or after the daily treatment fraction. All FBCT scans (planning + repeat) were performed in same supine position on a flat tabletop.

The original FECTs were per-patient boney-anatomy aligned, truncated to have the scene number of slice 66–77 slices for each image set for each patient and resampled to have 3 mm slice thickness, and 512 × 512 image resolution with voxel size 0.8 × 0.8 mm^2. The scans cover the anatomical regions from the upper part of the sacroiliac joints to 4 cm below the bottom of the os pubis. For each FBCT image, the structures including prostate, seminal vesicles, rectum, bladder, left femur and right femur were delineated by a single physician. As all the patients were assumed to have high-risk prostate cancer in COP studies here, the target volumes CTVs were prostate and seminal vesicles. No associated lymph nodes are included. The remaining contoured structures (bladder, rectum, and etc.) were regarded as OARs, while the left and right femur and the small bowel were excluded since their dose limits are rarely violated due to their further distance to CTVs than the bladder and rectum.

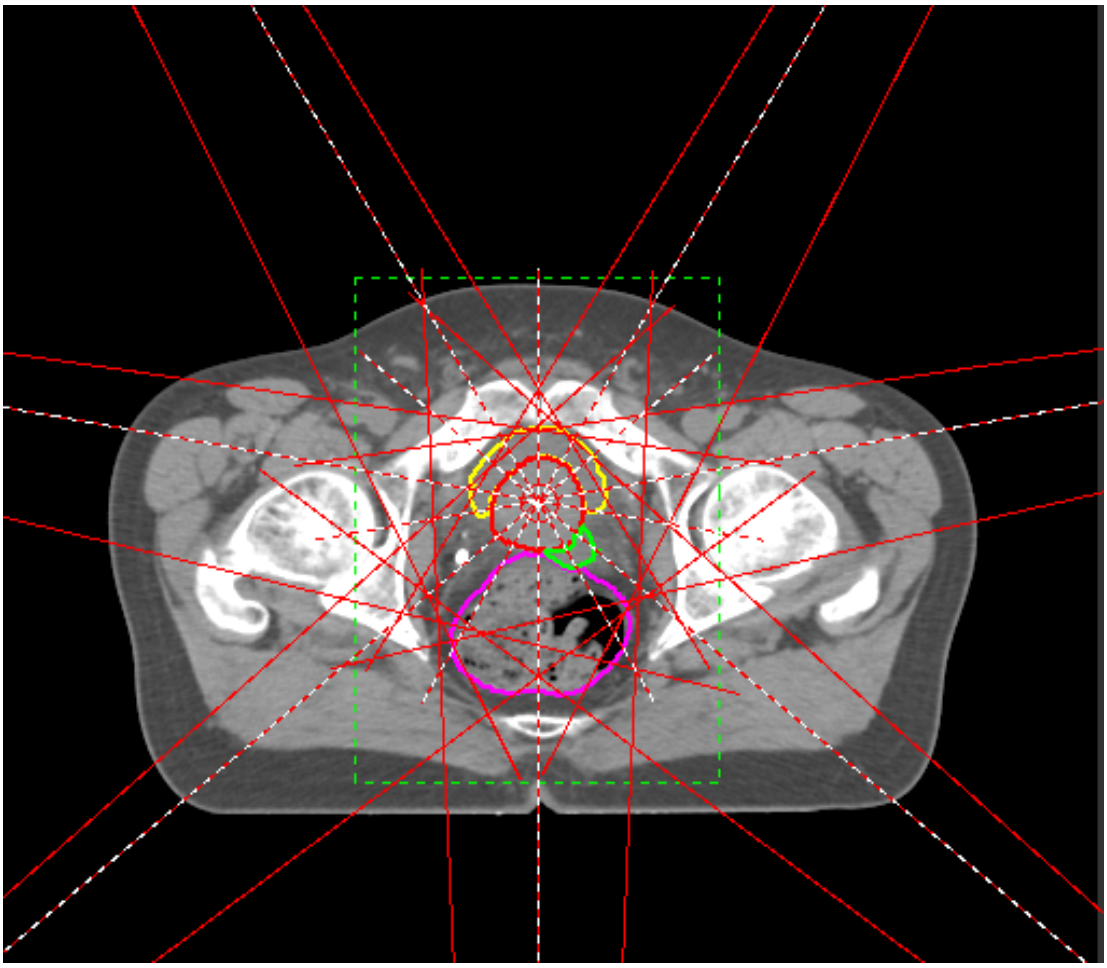

Figure 15. A transverse view of IMRT plan settings shared in COP studies: a typical seven-beam arrangement (red lines) with the beam isocenter located at prostate centroid (small red circle in the middle). The dose grid that always covers prostate (red contour), seminal vesicles (green contour), bladder (yellow contour) and rectum (magenta contour) is indicated by the dashed green box.

For IMRT planning purposes, one FBCT (usually the first image, but the second image for patient C) was selected for each patient as the reference image and the other FBCT images were called fractional images. On each reference image (e.g., Figure 15), contours of seminal vesicles, rectum and bladder were modified slightly to eliminate overlapping region with prostate and with each other. The treatment plan utilizes seven coplanar (transverse) photon beams with gantry angle 30, 80, 130, 180, 230, 280, 330º. The beam isocenter was set to the centroid of prostate (=GTV=$CTV_{prostate}$). A dose grid was created based on a volume expanded from union

ROI (prostate + seminal vesicles + rectum + bladder) by 30 mm. This dose grid size ensures all the ROIs and regions of uncertainties are covered, while excluding the unnecessary regions to reduce dose calculate time and reduce computer memory usage. The dose grid resolution is either 2×2×2 mm^3 or 3×3×3 mm^3, depending on which COP study is being performed. For planning optimization to account for interfraction deformable motion (chapter 5), the dose grid resolution is 3×3×3 mm^3. The remainder studies use 2×2×2 mm^3.

4.2 Software (GUI) for COP study

Software for the COP study refers to (i) dynamic libraries (plugins) in Pinnacle[3] which incorporate several GUs models to perform COP and related probabilistic evaluation and optimization and (ii) a graphical user interface (GUI) that allows users to interact with Pinnacle[3] via a more user-friendly interface than text. This software implements COP theory (chapter 2) in a TPS that is realistic and convenient. This section focuses on the GUI.

The dose-volume-coverage (DVC) GUI is a multi-functional tool with embedded plugins for Pinnacle[3] for the convenience of both developers and ordinary treatment planners. It serves as a bridge between the TPS and the developed plugins.

The functions of GUI have been extended. Multiple GU models have been developed to perform the COP optimization (mentioned in chapter 2) and the optional probabilistic plan evaluation based on the dosimetric/biological metrics (described in chapter 3). The results of these metrics can be displayed graphically in the GUI, allowing an efficient plan evaluation/comparison. Each function is associated with a GUI tab, whose details are listed in Table VII. How to use different GUI tabs for different purposes is illustrated in Figure 16 and the screen shots of all the functioning tabs are shown in Figure 17 and Figure 18.

Table VII. The main functions of the functioning tabs of DVC GUI

Tab 1: "Optimization" (chapter 2)
• Specify/load optimization criteria in TPS • Error check: bad weight, bad format of a research objective
Tab 2: "GU models" (II and IV are included in chapter 5 and 6 ,respectively)
• Specify geometric uncertainty model and parameters I. RigidBodyNormal (for setup errors or rigid organ motion) II. PCAdvfModel (for deformable organ motion) III. PCA+ RigidBodyNormal (a combination of the above two models) IV. DelineationModel (for delineation uncertainties) • Error check: bad parameter file that is inconsistent with the selected GU model and each structure can have only one GU model.
Tab 3: "Endpoint" (chapter 3)
• Specify endpoint model for biological metrics I. TCP_Poisson (TCP Poisson model using physical dose or BED) II. TCP_PoissonEud (TCP Poisson model using physical dose or BED-based gEUD) III. NTCP_LKB_ErfEud (NTCP LKB model using physical dose or BED-based gEUD) • Error check: bad parameter file that is inconsistent with the selected endpoint model
Tab 4: "Evaluation" (chapter 2 and 3)
• Specify DVHs/pDVHs to be plotted in the DVHs/PDVHs tab • Error check: bad DVH/pDVH metric name
Tab 5: "DVHs/PDVHs"
• Show DVHs/PDVHs of ROIs on the trials of interest
Tab 8: "Outcome"
• Show box plot of TCP/NTCP distribution of ROI on the trials of interest.

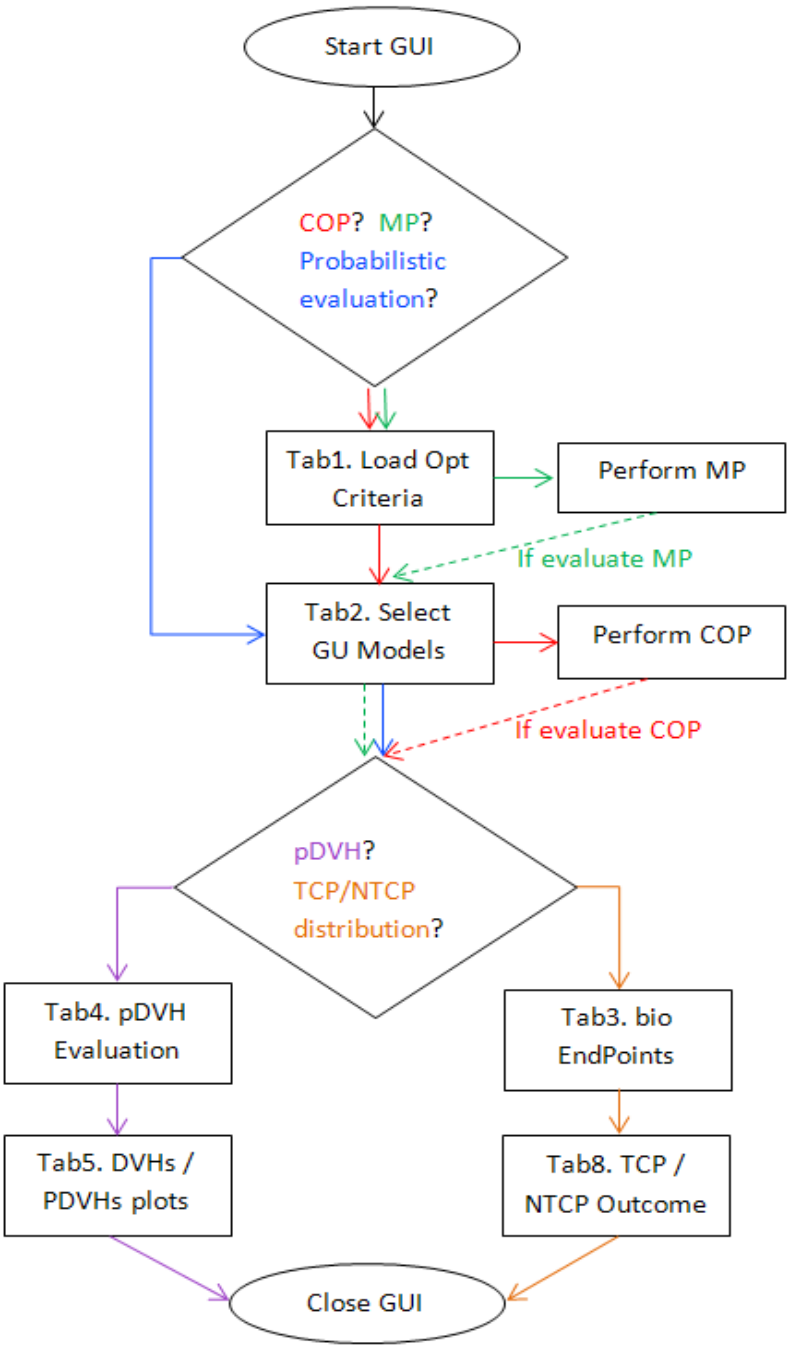

Figure 16. DVC GUI flow for performing COP or margin-based treatment planning (MP) +/- probabilistic plan evaluation by computing and plotting specified pDVHs and/or TCP/NTCP distribution. Colored arrows indicate the flow for the item listed in the same color. The details are described in the text.

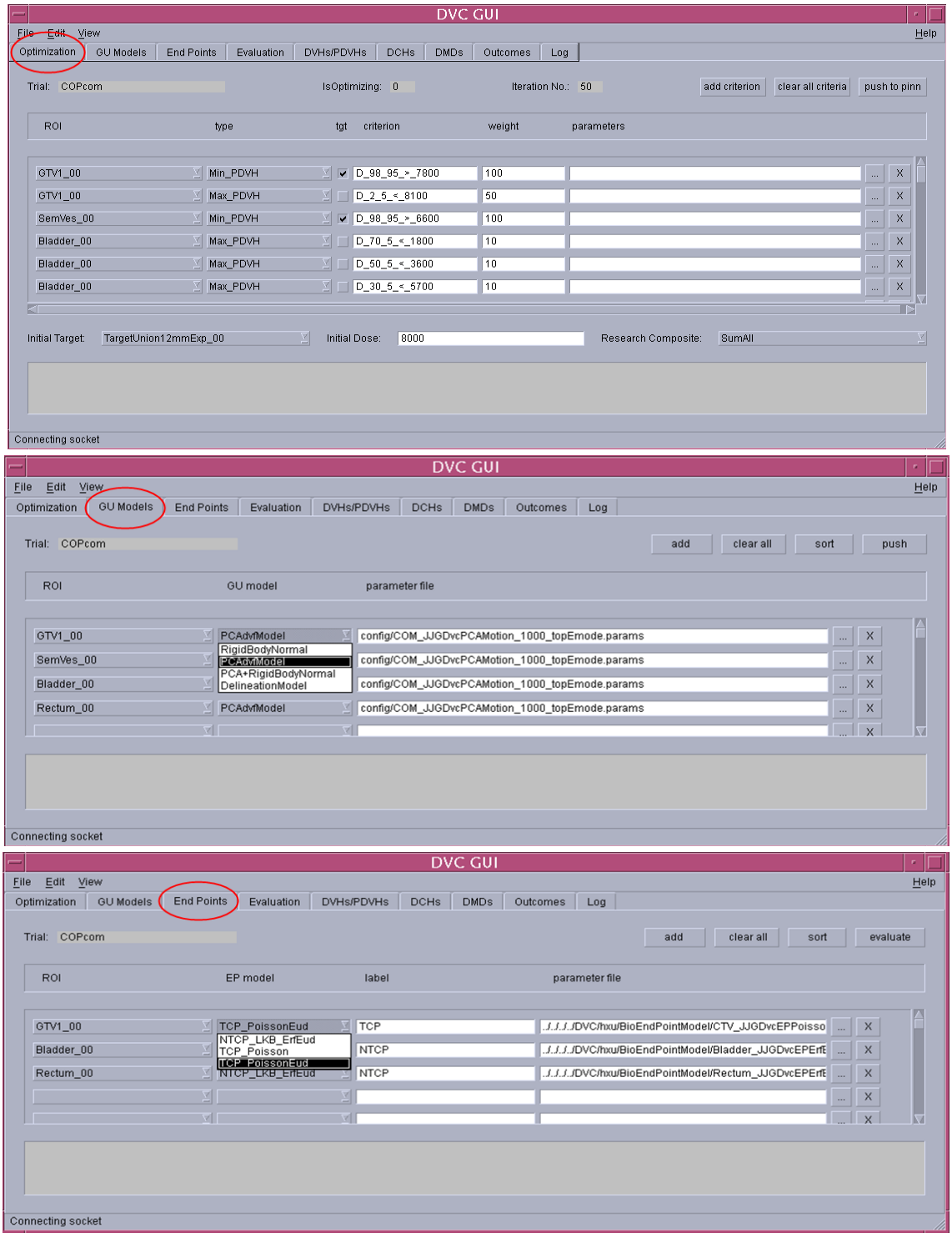

Figure 17. Interface of DVC GUI tabs: (upper) Tab 1 "Optimization" which is used to set the criteria used for optimization; (middle) Tab 2 " GU Models" used to set the GU models used for COP optimization or plan probabilistic evaluation; (lower) Tab 3 "End Points" used to set the TCP/NTCP model and parameters to calculate TCP/NTCP distribution for probabilistic evaluation and plot it in "Outcomes" tab. The primary GUI design is done by Dr. John James Gordon. (copyright JJ Gordon 2011©, copyright H Xu 2013©)

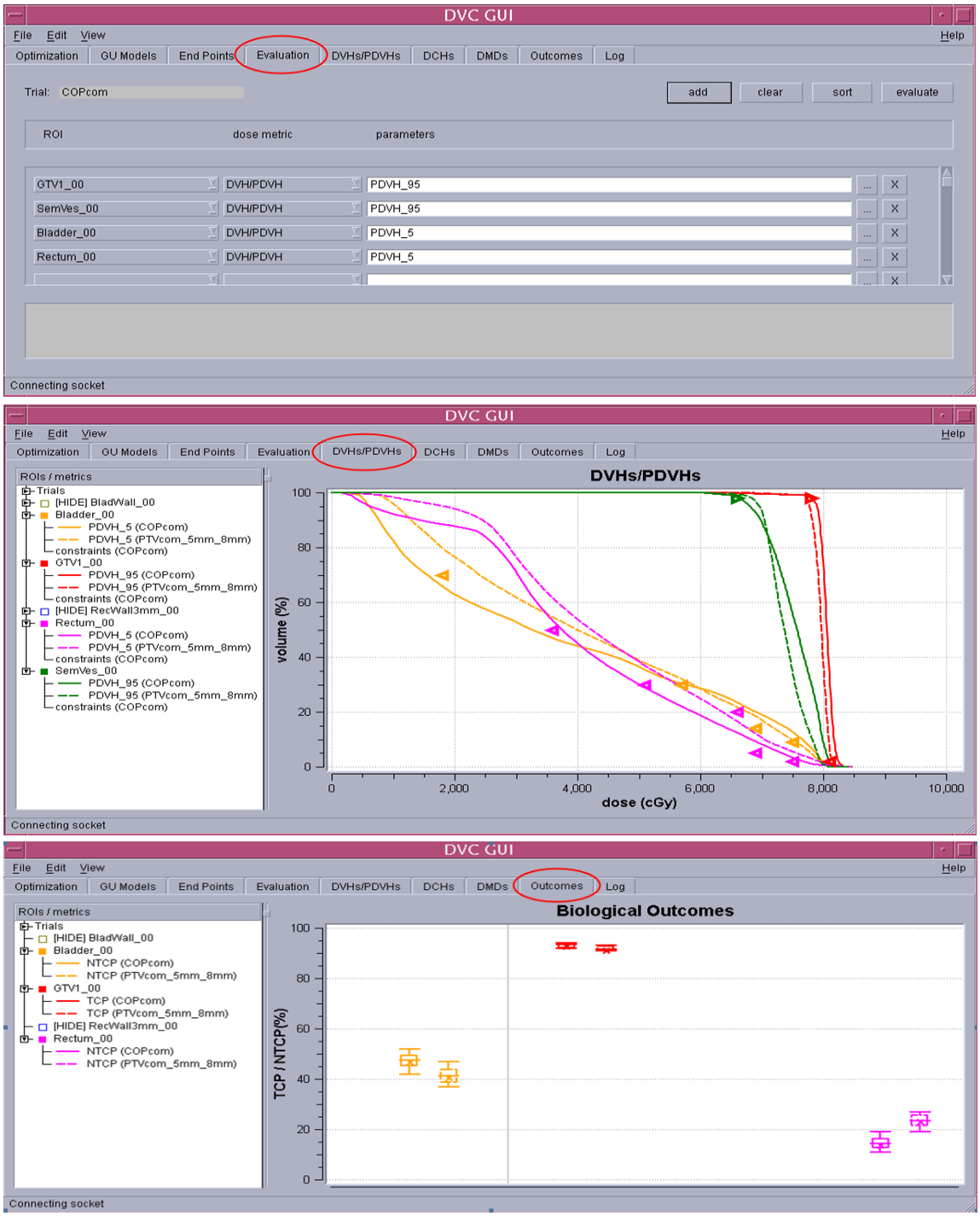

Figure 18. Interface of DVC GUI tabs: (upper) Tab 4 "Evaluation" that determines the pDVHs to be plotted in "GU Models" tab; (middle) Tab 5 " GU Models" that plots pDVHs of multiple ROIs on multiple trials (plans) with criteria highlighted as triangles. Here, dose is displayed in the unit cGy while 1 cGy = 0.01 Gy. (lower) Tab 8 "Outcomes" that plots distribution of TCP and NTCP for multiple ROIs on multiple trials (plans). For both Tab 5 and Tab 8, legends are displayed on the left showing pDVH or TCP/NTCP of different ROIs (with different color) on different trials (solid or dashed). (copyright JJ Gordon 2011©, copyright H Xu 2013©)

4.3 Planning techniques for comparison

The planning techniques to be compared with COP in this dissertation utilize PTV margins to accommodate GUs of CTVs. The PTV margins are either empirically predefined or optimized based on the target coverage evaluation. These techniques are also generally called margin-based planning techniques in the following text.

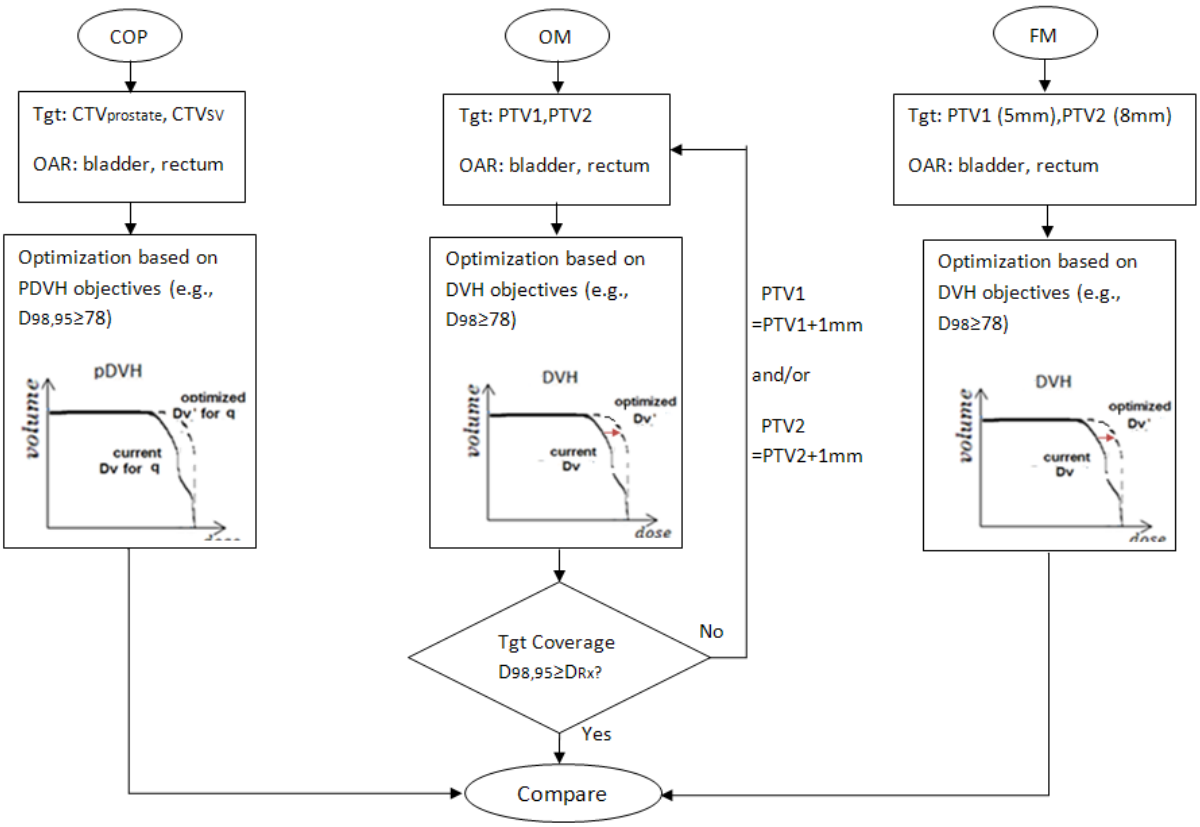

Figure 19. Workflow of COP versus OM and FM planning technique to account for GUs e.g., interfraction organ deformable motions for high-risk prostate cancer patients. Abbreviation: tgt = target, SV = seminal vesicles, PTV1 = $CTV_{prostate}$ + PTV margin of $CTV_{prostate}$ and PTV2 = CTV_{SV} + PTV margin of CTV_{SV}. The PTV margins used in FM for all the patients are empirically determined based on literature. Here, 5mm for PTV1 and 8mm for PTV2 are an example for the study to accommodate interfraction organ deformable motions.

The two margin-based planning techniques used for planning comparison with COP are called optimized-margin planning technique (OM) and fixed margin planning technique (FM). The workflow of COP, OM and FM are illustrated in Figure 19. To generate a dose distribution

intended to accommodate GUs for $CTV_{prostate}$ and CTV_{Sv}, both OM and FM rely on PTV structures (PTV1 and PTV2 for $CTV_{prostate}$ and CTV_{Sv}, respectively) and the DVH objectives. COP does away with PTVs and utilizes the pDVH objectives for dose optimization.

FM is a basic PTV-based treatment planning technique similar to the conventional margin-based planning method where pre-defined PTV margins are determined empirically. In the following studies, PTV margins for $CTV_{prostate}$ and CTV_{SV} are determined by either a published work (as shown in Figure 19) or van Herk margin formula (van Herk *et al.* 2000).

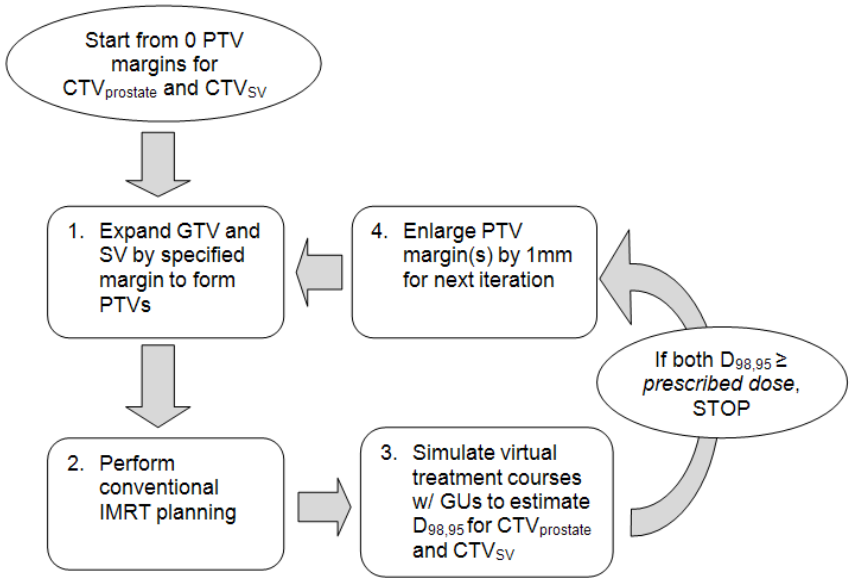

Figure 20. Flow diagram of margin iteration of the OM planning technique used in this dissertation. The PTV margins for $CTV_{prostate}$ and CTV_{SV} are initialized as 0mm and then iteratively adjusted to achieve prescribed $D_{98,95}$ for both $CTV_{prostate}$ and CTV_{SV}. PTV margin is increased by 1mm for the next iteration for any CTV whose $D_{98,95}$ is lower than the prescribed value. If one CTV achieves prescribed $D_{98,95}$ while the other fails, PTV margin for the CTV with desirable $D_{98.95}$ remains the same in the next iteration.

Compared to FM, OM is an advanced PTV-based planning technique which was proposed (Gordon and Siebers 2009) to optimize the uniform PTV margin(s) for each patient to meet the target dose at prescribed coverage $D_{98,95}$. As Figure 20 shows, OM used in this dissertation starts with 0 PTV margins for $CTV_{prostate}$ and CTV_{SV} and iteratively increases PTV margin(s) uniformly by increment 1mm until both CTVs achieves prescribed $D_{98,95}$. In each iteration,

$D_{98,95}$ values are estimated based on the dosimetric consequences of 1000 virtual treatment courses with GU model incorporated. In the contrast that COP considers OAR coverage probability and generates dosimetric margins which are often only achieved by non-uniform PTV margins, OM is less complicated and more emphasized on CTV coverage when adjusting PTV margins.

4.4 Sensitivity of coverage estimates to treatment courses sampling

In the COP studies of this dissertation, probabilistic evaluation of treatment plans are based on the 1000 virtual treatment course simulations. The inherent assumption is that the resulting pDVH and associated dose coverage metrics estimated from 1000 virtual treatment course is of acceptable accuracy and precision. This section shows the testing results to consolidate this assumption.

4.4.1 Accuracy tests

The estimation accuracy of the metric $D_{v,q}$ (dose delivered to volume v at coverage probability q) is tested via checking how $D_{v,q}$ value converges using different number of virtual treatment courses. Denote D_{v,q_Ntx} the estimated $D_{v,q}$ based on N_{tx} virtual treatment courses. $|\Delta D_{v,q\_1000}|$, the absolute percentage difference of D_{v,q_Ntx} relative to D_{v,q_1000} is calculated as

$$|\Delta D_{v,q\_1000}| = \left| \frac{D_{v,q\_1000} - D_{v,q\_N_{tx}}}{D_{v,q\_1000}} \right| \times 100\% \qquad (33)$$

The smaller $|\Delta D_{v,q\_1000}|$ is, the better D_{v,q_Ntx} converges to D_{v,q_1000}.

In terms of target structures $CTV_{prostate}$ and CTV_{SV} of two patients with ID A and S, $|\Delta D_{98,95\_1000}|$ has been calculated for the zero-PTV-margin plans and COP plans evaluated via

N_{tx} = 10, 100, 200 and 500 virtual treatment courses with PCA or ASSD model[5] incorporated. As Figure 21 illustrates, $|\Delta D_{98,95\_1000}|$ is reduced to 0.2% or lower when N_{tx} increases from 0 to 500, which reveals an acceptable convergence relative to N_{tx} = 1000.

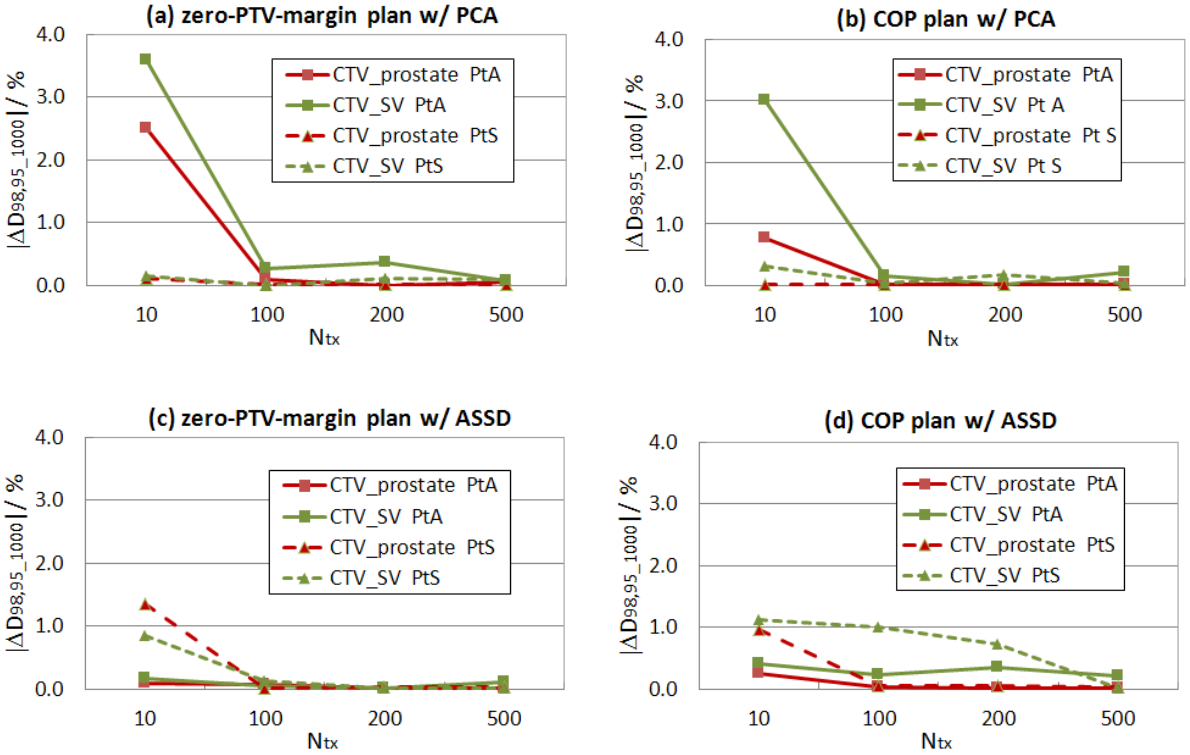

Figure 21. $|\Delta D_{98,95\_1000}|$ of $CTV_{prostate}$ (red) and CTV_{SV} (green) as a function of N_{tx} (number of simulated virtual treatment courses) for the zero-PTV margin plan ((a),(c)) and the COP ((b),(d)) plan of patient A (solid lines) and S (dashed lines). The patient-specific PCA model is incorporated to consider deformable motions in (a) and (b) while the patient-specific ASSD model in incorporated to consider delineation uncertainties.

For OAR, $|\Delta D_{v,q\_1000}|$ is plotted in Figure 22 when N_{tx} = 500 is used for the zero-PTV-margin plans and the COP plans evaluated with PCA or ASSD model incorporated for patient A and S. In the high dose region where v of $D_{v,q}$ is small, $|\Delta D_{v,q\_1000}|$ remains within 1% and mostly < 0.5%. In general, $|\Delta D_{v,q\_1000}|$ of COP plan is smaller than that of zero-PTV-margin plan. In the low dose region where v of $D_{v,q}$ is large, $|\Delta D_{v,q\_1000}|$ tends to be larger. As low dose

[5] PCA (principal component analysis) and ASSD (average-surface-of-standard-deviation) are two methods for modeling organ deformation (chapter 5) and delineation uncertainties (chapter 6). Readers are referred to section 5.2.2 and 6.1.1 for the details of these models.

region is of less interest in terms of dose sparing and OAR toxicity, OAR D_{v,q_1000} shows acceptable convergence for the test cases.

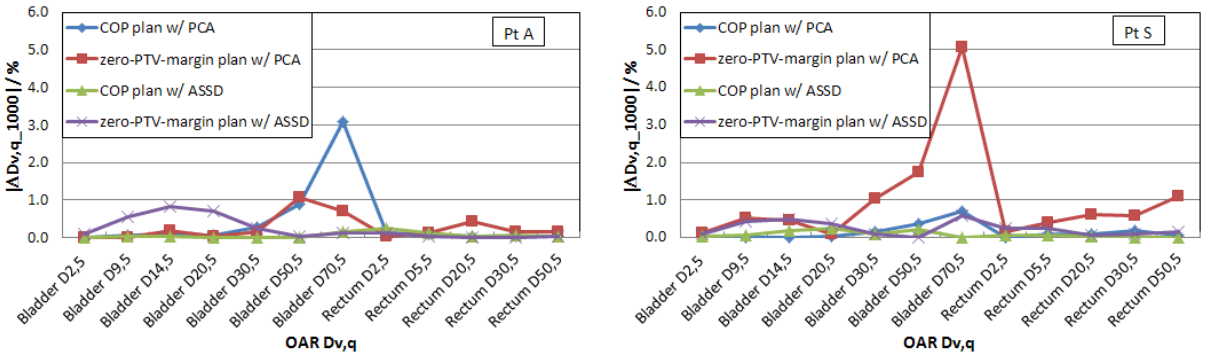

Figure 22. $|\Delta D_{v,q\_1000}|$ of OAR of Patient A (left) and S (right) when N_{tx} = 500. $|\Delta D_{v,q\_1000}|$ is obtained for COP plan (blue) and zero-PTV-margin plan (red) with the PCA model incorporated consider deformable motions, and COP plan (green) and zero-PTV-margin plan (purple) with the ASSD model incorporated to consider delineation uncertainties. $|\Delta D_{v,q\_1000}|$ is small in the high dose region and gets larger in the low dose region.

4.4.2 Precision tests

The precision of the $D_{v,q}$ value calculated previously is tested via checking the reproducibility of $D_{v,q}$ values repeatedly estimated by 1000 virtual treatment courses. Denote $D_{v,q\_No.n}$ the $D_{v,q}$ based on n^{th} repeated estimation. $|\Delta D_{v,q,precision}|$, the absolute difference of $D_{v,q\_repeat,n}$ relative to one estimated $D_{v,q}$, is calculated as

$$|\Delta D_{v,q,precision}| = \left| \frac{D_{v,q} - D_{v,q\_No.n}}{D_{v,q}} \right| \times 100\% \qquad (34)$$

The smaller $|\Delta D_{v,q,precision}|$ is, the more precise/reproducible $D_{v,q}$ is. Here, $D_{v,q} = D_{v,q\_No.1}$.

The maximum $|\Delta D_{v,q,precision}|$ ($|\Delta D_{v,q,precision}|_{max}$) among all the repeated estimated $|\Delta D_{v,q,precision}|$ is calculated for the zero-PTV-margin and COP plans with PCA or ASSD model incorporated for patient A and S in Table VIII. The $|\Delta D_{v,q,precision}|_{max}$ of $CTV_{prostate}/CTV_{SV}$ remains lower than 0.2% / 0.3% while ranges from 0.0% to 3.5% for OAR. In general, $D_{v,q}$ is

more precise in high dose regions. $D_{v,q}$ for the COP plan is more precise than that for the zero-PTV-margin plan.

Table VIII. The $|\Delta D_{v,q,precision}|_{max}$ based on repeated estimation of $D_{v,q}$ for 7-10 times for the zero-PTV-margin plan and the COP plan with PCA/ASSD model incorporated for Patient A and S.

	$\|\Delta D_{v,q,precision}\|_{max}$ (%)							
	Deformable motions (PCA)				Delineation uncertainties (ASSD)			
	zero-PTV		COP		zero-PTV		COP	
	A	S	A	S	A	S	A	S
$CTV_{prostate}$ $D_{98, 95}$	0.1	0.1	0.1	0.1	0.1	0.3	0.1	0.3
CTV_{SV} $D_{98, 95}$	0.0	0.2	0.0	0.0	0.2	0.1	0.1	0.0
Bladder $D_{2,5}$	0.2	1.0	0.1	0.0	0.8	0.2	0.1	0.1
Bladder $D_{9,5}$	0.2	1.7	0.1	0.1	1.1	0.3	0.1	0.2
Bladder $D_{14,5}$	0.3	1.8	0.2	0.1	0.3	0.4	0.1	0.2
Bladder $D_{20,5}$	0.4	1.6	0.3	0.2	0.1	0.1	0.1	0.2
Bladder $D_{30, 5}$	0.6	1.6	0.5	0.7	0.1	0.1	0.6	0.2
Bladder $D_{50, 5}$	0.6	3.5	1.0	1.4	0.3	0.6	0.5	0.0
Bladder $D_{70, 5}$	0.1	0.7	0.1	0.1	0.3	0.3	0.2	0.1
Rectum $D_{2, 5}$	0.2	0.9	0.1	0.2	0.2	0.3	0.1	0.1
Rectum $D_{5, 5}$	0.4	0.7	0.2	0.3	0.0	0.1	0.1	0.1
Rectum $D_{20, 5}$	0.2	0.9	0.3	0.9	0.0	0.1	0.1	0.0
Rectum $D_{30, 5}$	0.2	1.0	0.3	1.4	0.1	0.2	0.1	0.0
Rectum $D_{50, 5}$	0.1	0.1	0.1	0.1	0.1	0.3	0.1	0.3

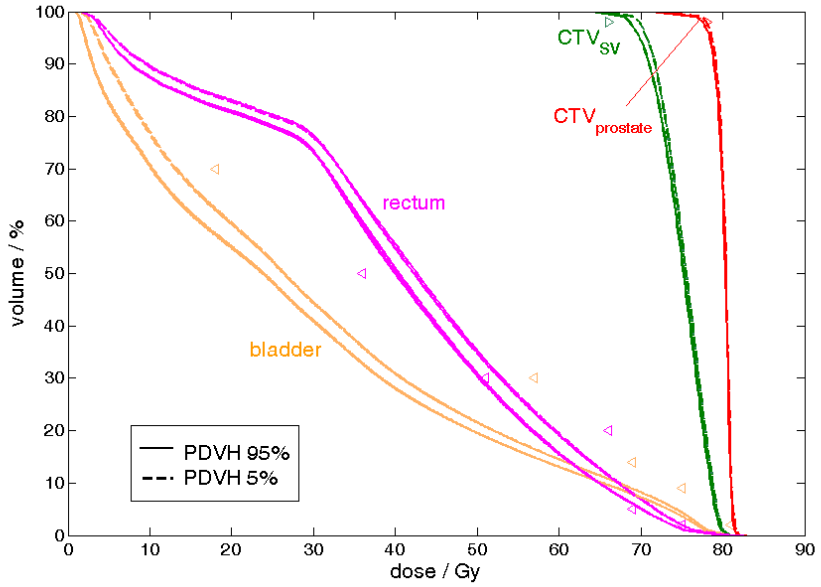

Figure 23. The repeated estimated pDVHs 95% (solid lines) and 5% (dashed lines) of $CTV_{prostate}$ (red), CTV_{SV} (green), bladder (yellow) and rectum (magenta) based on the simulations using 1000 virtual treatment courses repeated for 7 times. The differences between the repeated pDVHs are very small.

The repeated estimated pDVHs 95% and 5% with PCA model incorporated for zero-PTV-margin plan for patient S are plotted in Figure 23. Even with relatively large $|\Delta D_{v,q,precision}|_{max}$ in the low dose region, the difference between the repeated pDVHs is hardly noticeable, so the reproducibility of coverage estimation using 1000 virtual treatment courses is acceptable.

Based on the above testing results, the assumption that the pDVH and associated dose coverage metrics estimated from 1000 virtual treatment course is acceptably accurate and precise is consolidated.

5 COP to account for interfraction deformable motions

For prostate cancer, interfraction organ displacement and deformation occur due to the bladder and rectal filling and are seemingly random as no expansion/shrinkage occurs due to disease progression/regression. The uncertainties caused by interfraction deformable motion were found to be common and can be significant during the treatment course. (Mah *et al.* 2002, van Herk 2004, Byrne 2005, Kerkhof *et al.* 2008, Peng *et al.* 2010)

In conventional margin-based planning, there is not a recommended method determine the size of PTV margin to account for CTV and OAR interfraction organ variations. The commonly used margin recipes (Stroom *et al.* 1999, van Herk *et al.* 2000) derived for the assumed rigid motion are not applicable to deformable organ motion, which are of a much higher dimensionality than the six parameters of shifts and rotations. The dosimetric consequence of a margin may vary with factors such as localization and immobilization methods, patient anatomy, treatment protocol, plan quality and beam arrangement. Although CTV-to-PTV margin size for prostate and seminal vesicles has been suggested in some studies (Meijer *et al.* 2008, Mutanga *et al.* 2011), they should be used with caution.

Compared with the conventional margin-based planning, COP may have the potential to either further improve the target coverage probability by raising OAR doses within tolerance or reducing OAR normal tissue toxicity with comparable target coverage in the presence of different GUs. (Gordon and Siebers Unpublished, Gordon *et al.* 2010) This chapter concentrates

on the application of COP to account for organ interfraction deformable motion in the clinical scenario where IGRT for prostate centroid alignment is utilized. The prostate plans and GU models used for this study are described first. Then the research results of dosimetric effect and plan optimization with GU model incorporated are discussed to explore potential clinical benefit of COP.

5.1 Prostate plans

As previously mentioned, 19 NKI patients are involved in this study. For each patient, one of the bony aligned FBCT images was selected as reference image set for planning. On this image set, a series of 7-beam IMRT plans were generated either based on COP or the two margin-based techniques for comparison. Other details of patient database and IMRT plans are referred to section 4.1 (page 52).

Two CTVs, $CTV_{prostate}$ (= prostate) and CTV_{SV} (= seminal vesicles), are for treatment, since all the patients are assumed with high-risk prostate cancer. The prescription dose to the prostate is 2.6 Gy/fraction for 30 fractions, which is biologically equivalent (equation (27)) to 2 Gy/fraction for 43 fractions used in a VCU protocol. The optimization criteria are listed in (Table III, page 22). The two critical OARs are the bladder and the rectum. The norm_tissue_ring is an artificial structure extending from 7 to 30 mm from $CTV_{prostate}$ and CTV_{SV} to force a steep dose drop-off. CTV_neighborhood is another artificial structure extending by 12mm from the union volume of $CTV_{prostate}$ and CTV_{SV} on all image sets. This structure is purely used to set initial beam fluence for COP implementation in Pinnacle[3] (See section 2.5.2). During optimization, CTV_neighborhood has no contribution to the objective functions as its objective function weight is set to 0.

The statistics of the patient-specific ROI volume changes based on the delineations on the multiple image sets for each NKI patient are summarized in Table IX. Large percentage SD relative to mean (%SD) indicates large magnitude of deformable motions involved in different treatment fractions.

Table IX. The mean and the percentage SD relative to mean (%SD) of ROI volumes over all image sets for each patient with ID A-S of the patient database

	$CTV_{prostate}$		CTV_{SV}		Bladder		Rectum	
ID	mean	%SD	mean	%SD	mean	%SD	mean	%SD
A	37	12	17	22	277	45	106	24
B	69	7	14	14	287	31	132	34
C	50	9	28	14	220	34	84	22
D	29	10	10	15	230	38	71	25
E	44	6	10	11	176	54	74	37
F	27	12	11	9	110	31	54	23
G	76	14	9	16	412	18	72	32
H	39	13	17	14	224	45	103	44
I	40	10	15	15	142	29	84	30
J	97	7	19	11	127	26	67	24
K	45	8	12	10	211	35	59	29
L	46	5	7	17	212	50	78	28
M	24	6	13	6	160	56	65	25
N	33	9	13	3	174	26	104	30
O	30	6	8	9	128	46	55	29
P	46	5	8	11	109	21	83	30
Q	46	7	19	8	166	37	60	37
R	75	5	18	8	237	49	87	27
S	52	5	11	11	143	31	77	11

5.2 GU models for deformable organ motions

Two candidate models to represent deformable organ motions are studied in this work. Both models intend to predict ROI voxel positional offsets in the patient coordinates caused by deformable motion under the condition that $CTV_{prostate}$ centroid is aligned. The simpler one is called the simple surface variation (SSV) model. The more sophisticated one is based on principal component analysis (PCA). The SSV model is constructed first to see if it represents

the characteristics of variations of patient database. If not, the PCA model is then constructed for modeling.

5.2.1 Simple surface variation (SSV) model

The SSV model is intended to give a first-order estimation of ROI geometry variability using few variables as input. This rough model, dependent on a linear correlation between the ROI centroid locations and volume, is used to guide necessity of finer linear model, i.e., PCA model.

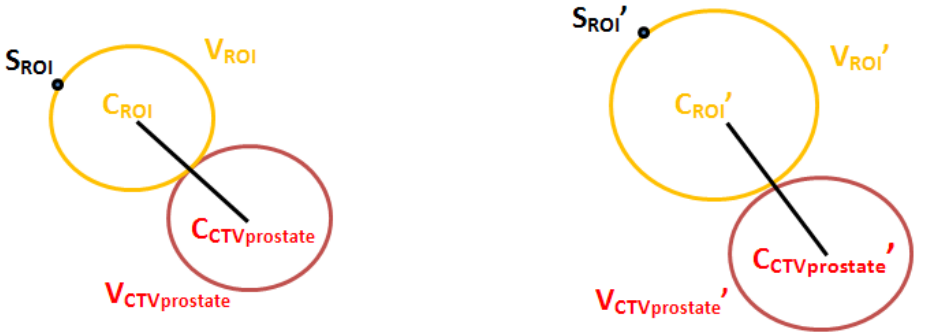

known	S_{ROI} $C_{ROI}, C_{CTVprostate}, CD_{ROI-P}(=C_{ROI}- C_{CTVprostate})$ $V_{ROI}, V_{CTVprostate}$	$C_{CTVprostate}'$
sampled	--	C_{ROI}'
calculated	--	$CD_{ROI-P}'(=C_{ROI}'- C_{CTVprostate}')$, $\Delta C_{ROI} = C_{ROI}'- C_{ROI}$ ⇨ $\Delta V_{ROI} = f(CD_{ROI-P}')$ ⇨ $S_{ROI}' = S_{ROI} + g(\Delta V_{ROI}, \Delta C_{ROI})$

Figure 24. An illustration of how to obtain a new position of surface voxel of a ROI (other than $CTV_{prostate}$) (S_{ROI}') based on a SSV model. As $CTV_{prostate}$-centroid alignment is assumed, the centroid position of $CTV_{prostate}$, old as $C_{CTVprostate}$ and new as $C_{CTVprostate}$', is always known. By sampling a new position of the ROI centroid (C_{ROI}'), the new centroid distance between ROI and $CTV_{prostate}$, (CD_{ROI-P}') and ROI centroid offset (ΔC_{ROI}) can be calculated. Assume that ROI volume change (ΔV_{ROI}) is a function of CD_{ROI-P}', ΔV_{ROI}, and ΔC_{ROI} can be used to estimate the surface point change relative to old position (S_{ROI}) so that S_{ROI}' can be therefore determined. *Abbreviation: P = $CTV_{prostate}$*

How the SSV model predicts an ROI surface position change due to deformable motions is illustrated in Figure 24. The SSV model relies on a strong correlation (and therefore a simple function) between the ROI-$CTV_{prostate}$ centroid distance (CD_{ROI-P}) and the ROI volume (V_{ROI}) as

$$V_{ROI} = a(CD_{ROI\text{-}P} - c)^b + d \tag{35}$$

where a,b,c,d are the parameters to fit using correlation and least-square fitting based on information from the patient database. On each image set for each patient, $CTV_{prostate}$ volume ($V_{CTVprostate}$), ROI volume (V_{ROI}) and the position of ROI surface voxel ($\mathbf{S_{ROI}}$), ROI centroid ($\mathbf{C_{ROI}}$), $CTV_{prostate}$ centroid ($\mathbf{C_{CTVprostate}}$) and their difference ($CD_{ROI\text{-}P}$) are known and can be used to determine a,b,c,d. Therefore, the ROI volume change between the reference and the fractional image sets becomes

$$\Delta V_{ROI} = a[(CD_{ROI\text{-}P} - c)^b - (CD_{ROI\text{-}P}' - c)^b] \tag{36}$$

where ' means a new value on the fractional image set. The SSV model also assumes that the ROI radius $r_{ROI} \propto \sqrt[3]{\Delta V_{ROI}}$, so the new ROI surface voxel position $\mathbf{S_{ROI}}'$ can be estimated by

$$\mathbf{S_{ROI}}' = \mathbf{S_{ROI}} + v(\mathbf{C_{ROI}}' - \mathbf{C_{ROI}}) + u(\sqrt[3]{\Delta V_{ROI}})\frac{\mathbf{S_{ROI}}' - \mathbf{C_{ROI}}'}{|\mathbf{S_{ROI}}' - \mathbf{C_{ROI}}'|} \tag{37}$$

where u,v are the parameters to fit based on data variation from the patient database. Equation (37) means that $\mathbf{S_{ROI}}'$ is determined by three components: (1) the old position of ROI $\mathbf{S_{ROI}}$, (2) the ROI centroid position change $\mathbf{C_{ROI}}' - \mathbf{C_{ROI}}$, and (3) the radius changes in direction pointing from $\mathbf{S_{ROI}}'$ to $\mathbf{C_{ROI}}'$. Assume the direction of $\mathbf{S_{ROI}}$ relative to $\mathbf{C_{ROI}}$ remains unchanged and substitute equation (36) into equation (37), we have

$$\mathbf{S_{ROI}}' = \mathbf{S_{ROI}} + v(\mathbf{C_{ROI}}' - \mathbf{C_{ROI}}) + u(\sqrt[3]{a[(CD_{ROI\text{-}P} - c)^b - (CD_{ROI\text{-}P}' - c)^b]})\frac{\mathbf{S_{ROI}} - \mathbf{C_{ROI}}}{|\mathbf{S_{ROI}} - \mathbf{C_{ROI}}|}) \tag{38}$$

For a $CTV_{prostate}$-centroid-aligned treatment, the new $CTV_{prostate}$ centroid position ($\mathbf{C_{CTV\text{-}centroid}}'$) is always "known". By sampling ROI centroid position ($\mathbf{C_{ROI}}'$) from a PDF based on the patient database, the new ROI surface voxel position $\mathbf{S_{ROI}}'$ can be calculated.

To test if the SSV is valid for deformable organ motion, the mean and SD of correlation coefficients of different volume and different centroid distance relative to $CTV_{prostate}$ across 19 patients are calculated in Table X. Only the bladder-$CTV_{prostate}$ centroid distance and bladder volume show strong correlation (> 0.9), when parameter $b = 1$. Similar coefficient calculations have been done for bladder wall and rectal wall, but none of them showed strong correlations. When b is replaced by 2 and 3, the correlation coefficient does not change significantly for all the structures. For example, patient E has correlation coefficients of 0.947 for bladder volume (V_B) and bladder-$CTV_{prostate}$ centroid distance ($CD_{B\text{-}P,z}$), 0.950 V_B and $CD_{B\text{-}P,z}^2$ and 0.939 V_B and $CD_{B\text{-}P,z}^3$. Based on the correlation coefficient, the SSV model has limited applications for prostate cancer modeling and is only potentially useful to predict bladder deformable motion.

Table X: The mean and SD values of the correlation coefficients between volumes and centroid distances of ROI for 19 NKI patients. Highly correlated variables are highlighted.

	mean	SD
V_B, $CD_{B\text{-}P,z}$	**0.943**	**0.039**
V_B, $CD_{B\text{-}P}$	**0.923**	**0.064**
V_R, $CD_{R\text{-}P}$	0.427	0.447
V_R, $CD_{R\text{-}P,y}$	0.183	0.461
V_B, $CD_{R\text{-}P}$	0.149	0.425
V_R, $CD_{B\text{-}R}$	0.125	0.395
V_R, $CD_{R\text{-}P,z}$	0.100	0.426
V_B, $CD_{R\text{-}P,y}$	0.075	0.374
V_R, V_B	0.029	0.454
V_B, V_P	-0.063	0.369
V_R, V_P	-0.164	0.283

Abbreviations: V_B: bladder volume; V_R: rectum volume; V_P: $CTV_{prostate}$ volume; $CD_{B\text{-}P,z}$: centroid distance between bladder and $CTV_{prostate}$ in z axis; $CD_{B\text{-}P}$: centroid distance between bladder and $CTV_{prostate}$; $CD_{R\text{-}P}$: centroid distance between rectum and $CTV_{prostate}$; $CD_{R\text{-}P,y}$: centroid distance between rectum and $CTV_{prostate}$ in y axis.

For the bladder SSV model, the residual error of bladder volume in equation (35) with fitted parameters based for an individual patient can be significant. In Figure 25 (a), the bladder volume residual error using fitted parameters specific for patient E is about 50 cc for a 200 cc V_B and therefore the surface position error, if comparable to radius difference, is approximately 3mm. For each patient, the residual error as a result of each patient-specific fitting is plotted into

a population-based histogram and fitted by a normal distribution. The SD of this fitted normal distribution is 27 cc, so the uncertainty for V_B is ±54 cc for a 95% confidence interval. Based on these numbers, the SSV model is oversimplified and not representative for modeling organ deformable surface positions for prostate cancer patients. A higher dimensional model, i.e., PCA model, is needed to represent more realistic organ deformable motions in the prostate cancer studies.

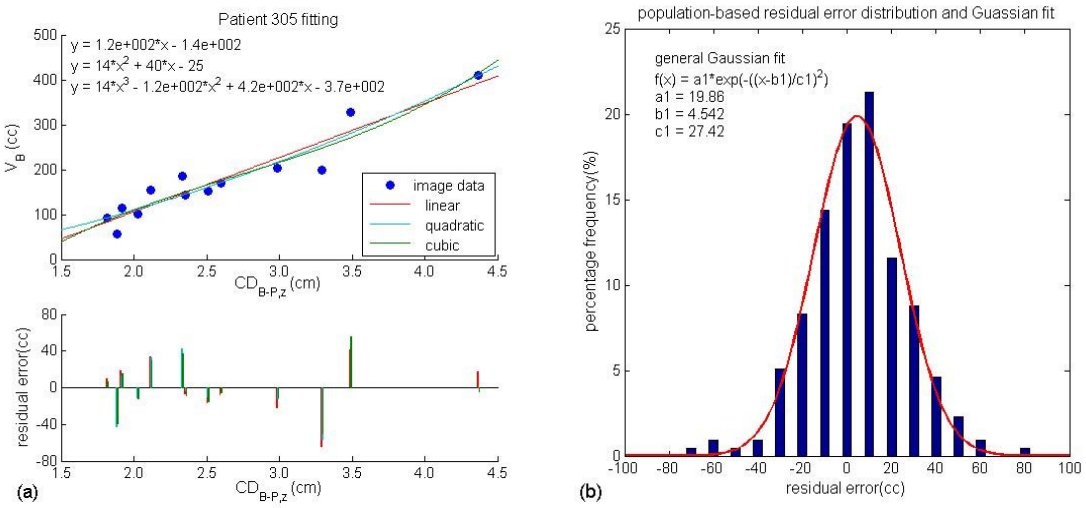

Figure 25. (a) (Upper panel) The linear, quadratic and cubic fitting of centroid distance between bladder and prostate in z axis $CD_{B\text{-}P,z}$ to bladder volume V_B. (Lower panel) The corresponding residual error for the three types of fitting. (b) Histogram of the distribution of residual error over 19 patients and its general Gaussian fit.

5.2.2 Principal component analysis (PCA) model

PCA is a mathematical procedure that uses an orthogonal transformation to convert large complex data sets of possibly correlated variables into a set of values of linearly independent variables called principal components. Based on a few deformable-registration-based displacement vector fields (DVFs) of organ geometry, PCA can create a low-dimensional parametric statistical organ deformation model to generate a synthetic DVF (Söhn *et al.* 2005b), which is representative of the possible organ deformation on a virtual treatment fraction. The

residual errors of a PCA model for prostate, bladder and rectum were small, e.g., less than 2mm when eigenmodes representing more than 86% overall variability were used. (Söhn *et al.* 2005b) As an earlier study stated (Söhn *et al.* 2012), PCA is a practical model to generate DVFs used to simulate anatomies for a large number of virtual treatment courses, thereby allowing the comprehensive assessment of dosimetric effects caused by deformable GUs (i.e., for the applications of COP or probabilistic plan evaluation in this dissertation).

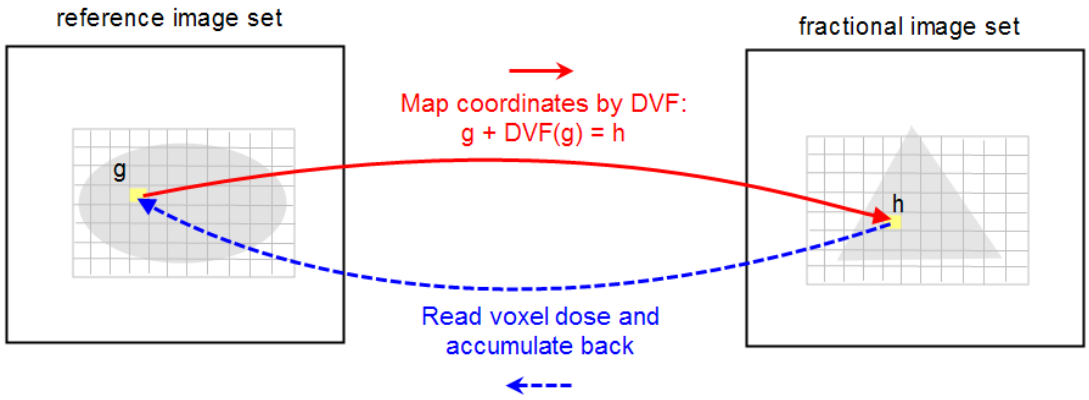

Figure 26. Illustration of a DVF between reference image set *R* and fractional image set *F* and dose mapping process. Due to the effects of GUs, the shape and position of a ROI change on different image sets (i.e., elliptical on *R* and triangle on *F*). Image *R* and *F* are not necessarily in the same domain. Denote g and h the coordinates in image *R* and *F*, respectively. The geometric transformation between g and h are represented by DVF(g) in the equation g + DVF(g) = h, which relates the intensity R(g) and F(h). For the dose mapping, dose to h is mapped back to g for i.e., dose accumulation of a multi-fractional treatment course.

The DVF created by PCA is a vector field that matches corresponding ROI voxel positions in a reference image set *R* to a synthetic fractional image set *F*. As Figure 26 shows, a DVF grid on the reference image set needs to be determined first to store a displacement vector for each DVF voxel. (The DVF grid used here is a little different from image grid and dose grid, so interpolation is required during conversion of the grids.) The DVF between *R* and *F* is computed by a deformable registration algorithm called Small Deformation Inverse Consistent Linear Elastic (SICLE) (Christensen and Johnson 2001). Based on the information of CT

intensity and ROI delineation, SICLE matches ROI coordinates in R and F, thereby determining the DVF for the whole DVF grid. Let g and h denote the coordinates of voxels on R and F. The relationship between g and h and $\mathrm{DVF}(g)$ is

$$h = g + \mathrm{DVF}(g) \tag{39}$$

The $\mathrm{DVF}(g)$ accounts for both affine and deformable transformations with respect to anatomies represented in R.

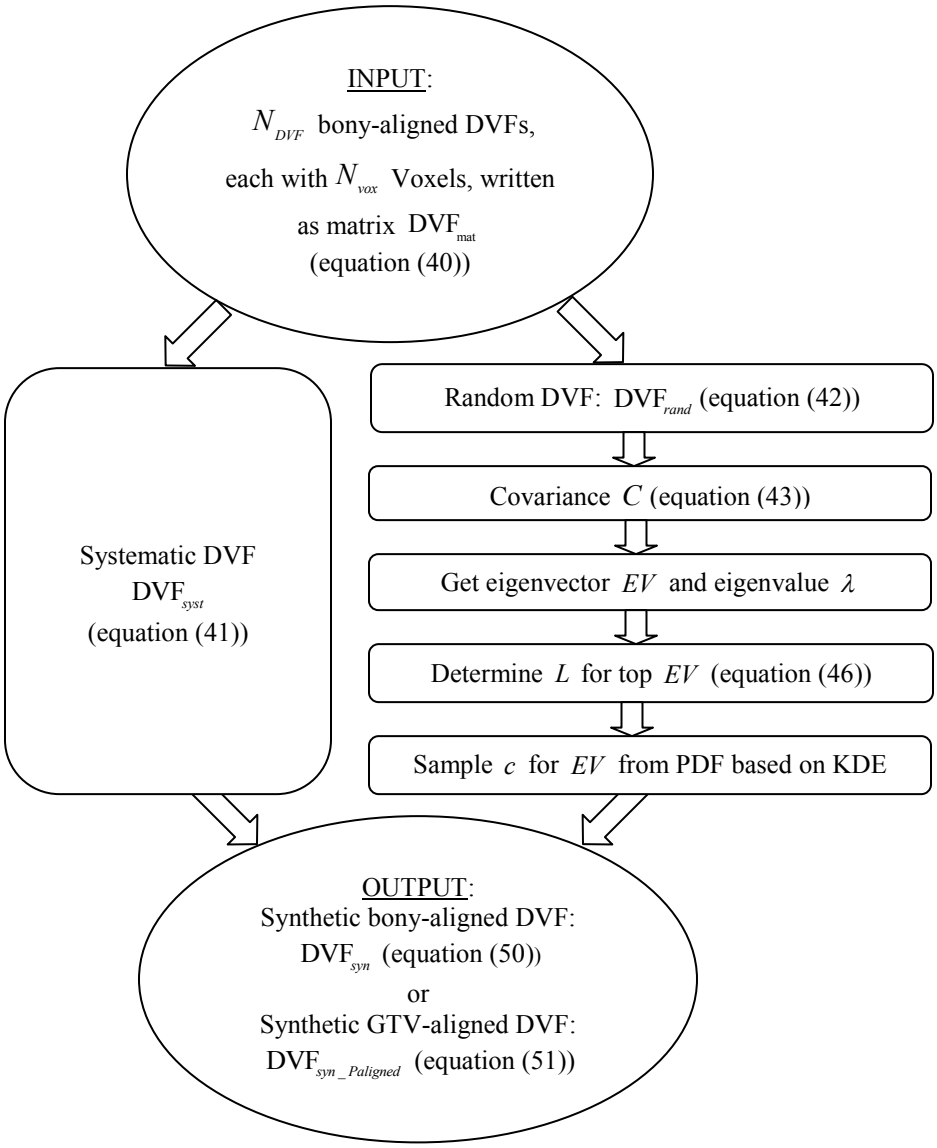

Figure 27. Workflow of construction of a patient-specific PCA model. KDE=kernel density estimator. See the following text for detailed description.

The workflow of a patient-specific PCA model is illustrated in Figure 27. The purpose of using the PCA model is to create synthetic DVFs that represent anatomical deformable motions likely to occur in virtual treatment courses. For a patient with N_{FBCT} (= 9-13) FBCT images, the number of training set DVFs is N_{DVF} ($=N_{FBCT}-1$) for ($N_{FBCT}-1$) repeat FBCT images mapping to the reference planning FBCT image. These N_{DVF} DVFs, each with N_{vox} DVF voxels, are written into a matrix $\mathrm{DVF}_{\mathrm{mat}} \in \mathbb{R}^{3N_{vox}\times N_{DVF}}$ as a practical way for coding. $\mathbb{R}^{3N_{vox}\times N_{DVF}}$ means that the size of matrix $\mathrm{DVF}_{\mathrm{mat}}$ is $3N_{vox}$ (rows) by N_{DVF} (columns) as follows,

$$\mathrm{DVF}_{\mathrm{mat}} = \begin{pmatrix} x_{1,1} & x_{1,2} & \cdots & x_{1,N_{DVF}} \\ x_{2,1} & x_{2,2} & \cdots & x_{2,N_{DVF}} \\ \cdots & \cdots & \cdots & \cdots \\ x_{N_{vox},1} & x_{N_{vox},2} & \cdots & x_{N_{vox},N_{DVF}} \\ y_{1,1} & y_{1,2} & \cdots & y_{1,N_{DVF}} \\ y_{2,1} & y_{2,2} & \cdots & y_{2,N_{DVF}} \\ \cdots & \cdots & \cdots & \cdots \\ y_{N_{vox},1} & y_{N_{vox},2} & \cdots & y_{N_{vox},N_{DVF}} \\ z_{1,1} & z_{1,2} & \cdots & z_{1,N_{DVF}} \\ z_{2,1} & z_{2,2} & \cdots & z_{2,N_{DVF}} \\ \cdots & \cdots & \cdots & \cdots \\ z_{N_{vox},1} & z_{N_{vox},2} & \cdots & z_{N_{vox},N_{DVF}} \end{pmatrix} \tag{40}$$

where x, y, z are the displacement vector field components or magnitude in the x,y,z directions for each DVF voxel. $\mathrm{DVF}_{\mathrm{mat}}$ is then divided into a systematic component $\mathrm{DVF}_{syst} \in \mathbb{R}^{3N_{vox}\times 1}$ and a random component $\mathrm{DVF}_{rand} \in \mathbb{R}^{3N_{vox}\times N_{DVF}}$. DVF_{syst} is the mean DVF of the N_{DVF} DVFs for a given voxel. DVF_{syst} represents the DVF which relates the patient's average anatomy relating to the reference image set. DVF_{rand} is obtained via subtracting DVF_{syst} from each fractional DVF

$(\mathrm{DVF}_{\mathrm{mat}}(i))$, which is i^{th} column data of $\mathrm{DVF}_{\mathrm{mat}}$. As Figure 27 illustrates, PCA manipulation is performed on DVF_{rand}. The equations to determine DVF_{syst} and DVF_{rand} are

$$\mathrm{DVF}_{syst} = \frac{1}{N_{DVF}} \sum_{i=1}^{N_{DVF}} \mathrm{DVF}_{\mathrm{mat}}(i) = \frac{1}{N_{DVF}} \begin{pmatrix} \sum_{i=1}^{N_{DVF}} x_{1,i} \\ \sum_{i=1}^{N_{DVF}} x_{2,i} \\ \cdots \\ \sum_{i=1}^{N_{DVF}} x_{N_{vox},i} \\ \sum_{i=1}^{N_{DVF}} y_{1,i} \\ \sum_{i=1}^{N_{DVF}} y_{2,i} \\ \cdots \\ \sum_{i=1}^{N_{DVF}} y_{N_{vox},i} \\ \sum_{i=1}^{N_{DVF}} z_{1,i} \\ \sum_{i=1}^{N_{DVF}} z_{2,i} \\ \cdots \\ \sum_{i=1}^{N_{DVF}} z_{N_{vox},i} \end{pmatrix} \tag{41}$$

and

$$\mathrm{DVF}_{rand} = (..., \mathrm{DVF}_{rand}(i), ...), \ \mathrm{DVF}_{rand}(i) = \mathrm{DVF}_{mat}(i) - \mathrm{DVF}_{syst} \tag{42}$$

$\mathrm{DVF}(i)$ denotes DVF in i^{th} column (for i^{th} repeat FBCT) while $i = 1, 2, ..., N_{DVF}$. For DVF_{rand}, the implicit covariance matrix $C \in \mathbb{R}^{N_{DVF} \times N_{DVF}}$ that generalizes the notion of variance to dimensions $N_{DVF} \times N_{DVF}$ (Murakami and Kumar Sept., Lorenz and Krahnstöver 2000) is

$$C = \frac{1}{N_{DVF}} \sum_{i=1}^{N_{DVF}} \mathrm{DVF}_{rand}{}^{T} \cdot \mathrm{DVF}_{rand} \tag{43}$$

where $(\,)^T$ denotes the transpose of the matrix and $(\,)^T \cdot (\,)$ represents the outer product of the two matrices. Then C is diagonalized as C_{diag}

$$C_{diag} = diag(\lambda_1, \lambda_2 ..., \lambda_{N_{DVF}}) \tag{44}$$

where $\lambda_l \in \mathbb{R}^{1\times 1}$ (with index l) is called an eigenvalue. During this diagonalization, each eigenvector $EV(l) \in \mathbb{R}^{3N_{vox}\times 1}$ corresponding to each eigenvalue is obtained. An eigenvector is also called an eigenmode as it represents a DVF of correlated displacements of N_{vox} voxels. All the eigenvectors are mutually independent vector fields and the maximum number of eigenmodes that exist is $N_{DVF} - 1$. Therefore, the whole eigenvector matrix is $EV \in \mathbb{R}^{3N_{vox}\times(N_{DVF}-1)}$. To measure the fraction of overall geometric variability (present in the input $\mathrm{DVF}_{\mathrm{mat}}$) represented by an eigenmode with index l, the relative eigenvalue $\bar{\lambda}_l$ is calculated as

$$\bar{\lambda}_l = 100\% \cdot \frac{\lambda_l}{\sum_{i=1,2,...,N_{DVF}} \lambda_i} \tag{45}$$

which means the larger the eigenvalue is, the more dominating eigenmode it is due to capturing more geometric variability in $\mathrm{DVF}_{\mathrm{mat}}$. The total fraction of geometric variability $\bar{\lambda}$ of L most "principal" eigenmodes is

$$\bar{\lambda} = \sum_{i=1,2,...,L} \bar{\lambda}_i \tag{46}$$

For each eigenvector, coefficients are found in a matrix $Coeff \in \mathbb{R}^{N_{DVF}\times(N_{DVF}-1)}$, which is the product of $\mathrm{DVF}_{rand}{}^T \in \mathbb{R}^{N_{DVF}\times 3N_{vox}}$ and $EV \in \mathbb{R}^{3N_{vox}\times(N_{DVF}-1)}$,

$$Coeff = (\mathrm{DVF}_{rand})^T (EV) = \begin{pmatrix} c_{1,1} & \cdots & c_{l,1} & \cdots & c_{N_{DVF}-1,1} \\ \vdots & \ddots & \cdots & \iddots & \vdots \\ c_{1,i} & \cdots & c_{l,i} & \cdots & c_{N_{DVF}-1,i} \\ \vdots & \iddots & \cdots & \ddots & \vdots \\ c_{1,N_{DVF}} & \cdots & c_{l,N_{DVF}} & \cdots & c_{N_{DVF}-1,N_{DVF}} \end{pmatrix} \tag{47}$$

where i and l are the row and the column index of $Coeff$ corresponding to $\mathrm{DVF}_{rand}(i)$ and $EV(l)$. Based on this finite data sample of eigenvector coefficients $Coeff$, a PDF for the l^{th} eigenvector can be estimated by kernel density estimation (KDE) (Rosenblatt 1956, Parzen 1962). With a Gaussian kernel, each coefficient sample is made into a Gaussian, of SD, σ. The PDF is a continuous function as a result of superposition (sum) of Gaussians of all the samples. An example of a KDE-based PDF and the Gaussians of samples is given in Figure 28. For l^{th} eigenvector, the PDF P_l of random variable t ranging from a to b is represented as

$$P_l[a \le t \le b] = \frac{1}{N_{DVF} \cdot \sigma_l \cdot \sqrt{2\pi}} \sum_{i=1}^{N_{DVF}} e^{\frac{-(t-c_{i,l})^2}{2\sigma_l^2}} \tag{48}$$

where $c_{i,l}$ is the matrix $Coeff$ element in the i^{th} row and the l^{th} column in equation (47), and the Gaussian SD σ_l is expressed as a rule of thumb equation (Silverman 1986)

$$\sigma_l = \frac{1.06}{N_{DVF}^{0.2}} \sqrt{\frac{\sum_{i}^{N_{DVF}} (c_{i,l} - \frac{1}{N_{DVF}} \sum_{i}^{N_{DVF}} c_{i,l})^2}{N_{DVF} - 1}} \tag{49}$$

With known eigenvectors and their PDFs of coefficients, a synthetic DVF, $\mathrm{DVF}_{syn} \in \mathbb{R}^{3N_{vox} \times 1}$, is

$$\mathrm{DVF}_{syn} = \mathrm{DVF}_{syst} + \sum_{l}^{L} c_l \cdot EV(l) \tag{50}$$

where c_l is the sampled coefficient for l^{th} eigenmode sampled from the PDF in the form of equation (48) based on rejection sampling. To create a DVF_{syn} that represent at least 90% overall geometric variability, L is determined by $\bar{\lambda} \ge 90\%$ (Figure 29 (a)) and consequently ranges from 4 to 7 for 19 NKI patients (Figure 29 (b)). Since the input DVF are calculated for bony-aligned anatomies on FBCT images, DVF_{syn} in equation (50) represents the interfraction deformable motions relative to aligned bones.

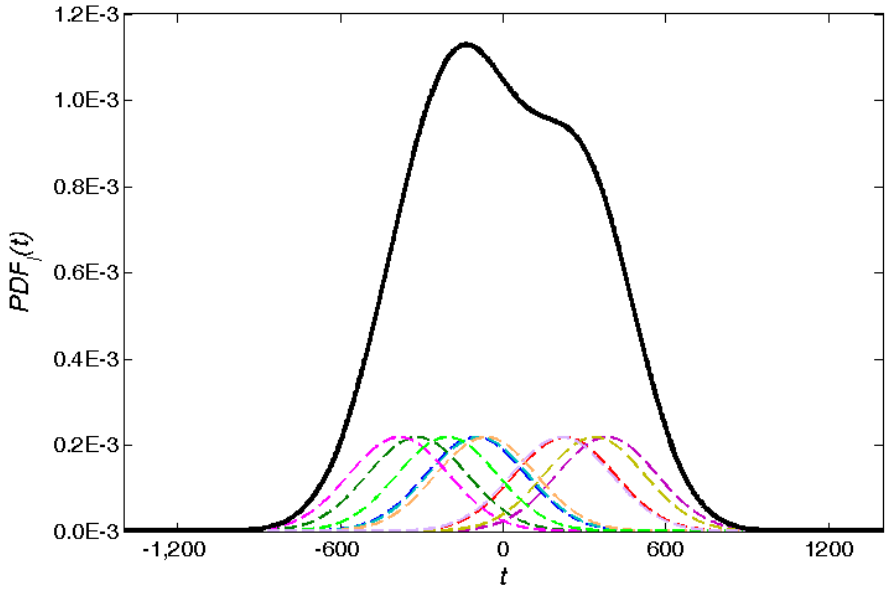

Figure 28. An example of coefficient PDF (black thicker line) for l^{th} eigenvector based on KDE using Gaussian kernels of the coefficient data samples (dashed lines). (Modified from Douglas Vile, VCU graduate student)

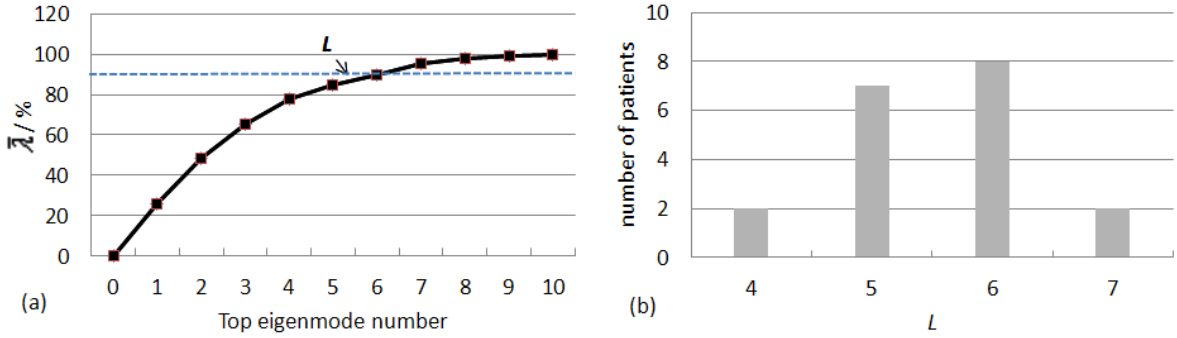

Figure 29. (a) The total fraction of geometric variability $\bar{\lambda}$ as a function of top eigenmode number with 90% threshold line to determine L. (b) Top eigenmode number L used for PCA model for 19 patients.

One concern of planning on a reference image of bony aligned anatomy is that large margin for $CTV_{prostate}$ is often required to account for prostate motion and deformation relative to bones. To effectively reduce the fractional anatomical deformation, a reference image set of the average patient anatomy is preferred for planning. However, this is unlikely to happen. It is nearly impossible to find the patient in such a state for imaging, or it requires repetitive imaging prior to therapy which is not feasible in clinic. With the development of IGRT, a prevalent

image-guided technique provides alternative solution for more precise target localization — prostate centroid alignment. This technique is clinically feasible and widely used since implanted gold markers or Calypso beacons are safe and reliable for tracking the centroid prostate on a fractional or even real-time basis. Because of this, the deformable motion to be considered during treatment planning is reduced for the prostate. As Figure 30 shows, in a $CTV_{prostate}$-centroid-alignment based plan, the dosimetric degradation and variability due to deformable motion on $CTV_{prostate}$ is smaller than the bony-aligned plan and mean geometry-based plan. This technique, however, does not necessarily reduce the dosimetric degradation or variability for CTV_{SV} or OARs.

To simulate deformable organ motions for treatment with $CTV_{prostate}$-centroid-aligned, the bony-aligned DVF_{syn} in equation (50) needs to be modified. Let the vector element of DVF_{syn} represented by $(x_{syn,i}, y_{syn,i}, z_{syn,i})$ where $i = 1,2,...,N_{vox}$ and denote synthetic $x_{syn,P}, y_{syn,P}, z_{syn,P}$ as displacement vector of $CTV_{prostate}$ centroid. The synthetic DVF for $CTV_{prostate}$-centroid-aligned anatomies $DVF_{syn\_Paligned} \in \mathbb{R}^{3N_{vox}\times 1}$ is

$$DVF_{syn\_Paligned} = \begin{pmatrix} x_{syn,1} - x_{syn,P} \\ x_{syn,2} - x_{syn,P} \\ \cdots \\ x_{syn,N_{vox}} - x_{syn,P} \\ y_{syn,1} - y_{syn,P} \\ y_{syn,2} - y_{syn,P} \\ \cdots \\ y_{syn,N_{vox}} - y_{syn,P} \\ z_{syn,1} - z_{syn,P} \\ z_{syn,2} - z_{syn,P} \\ \cdots \\ z_{syn,N_{vox}} - z_{syn,P} \end{pmatrix} \quad (51)$$

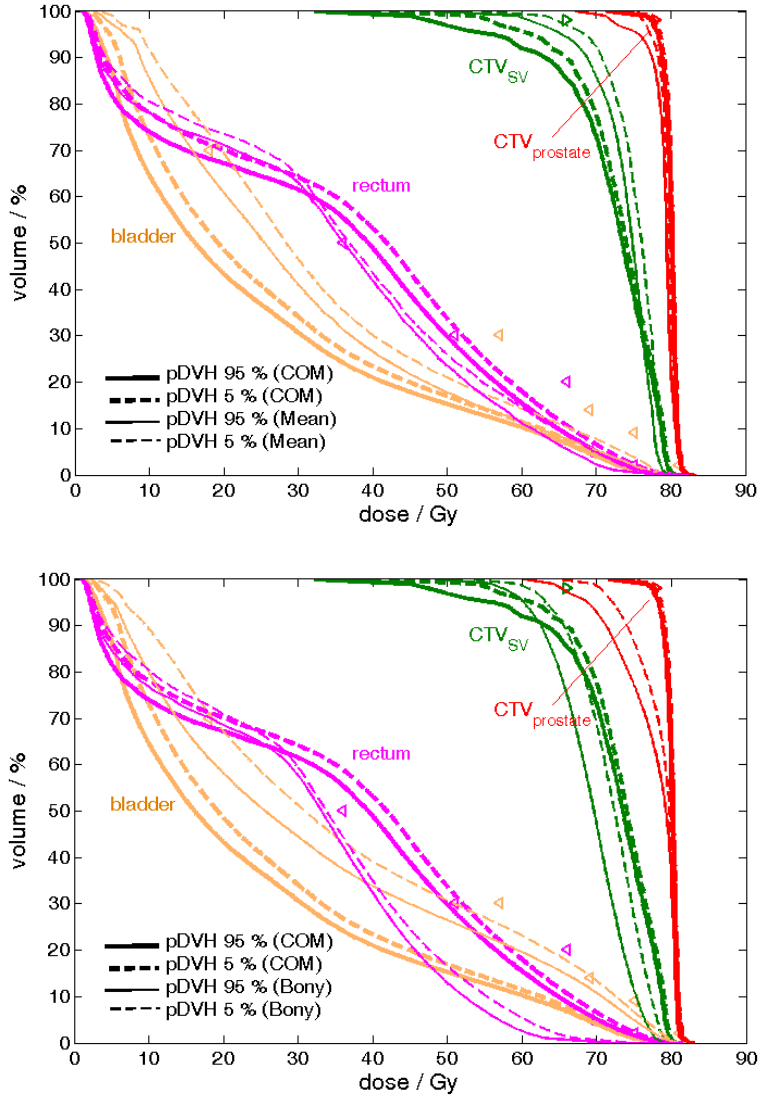

Figure 30. A patient example of pDVH comparisons of zero PTV-margin plans planned (upper) on the $CTV_{prostate}$ centroid aligned anatomy (COM: thick lines) versus on the mean geometry (Mean: thin lines), and (lower) on the $CTV_{prostate}$ centroid aligned anatomy (COM: thick lines) versus bony aligned anatomy (Bony: thin lines). pDVH is obtained from 1000 virtual treatment courses. For target structures $CTV_{prostate}$ (red) and CTV_{SV} (green), pDVH 95% is desired to lie upper or right to the objective values which are denoted by right triangle of corresponding color. For rectum (magenta) and bladder (orange), pDVH 5% is desired to lie lower or left to the objective values which are denoted as the right triangle of corresponding color. pDVH 95% and pDVH 5% are both plotted for each structure to examine the 90% confidence interval of DVH distribution with PCA model incorporated.

To highlight the effect of small versus large random DVF variations on the dose coverage probability, the dosimetric effect of using original PCA modeled DVF ($DVF_{syn\_Paligned}$) versus 5-times magnified DVF ($5DVF_{syn\_Paligned}$) is compared in Figure 31.

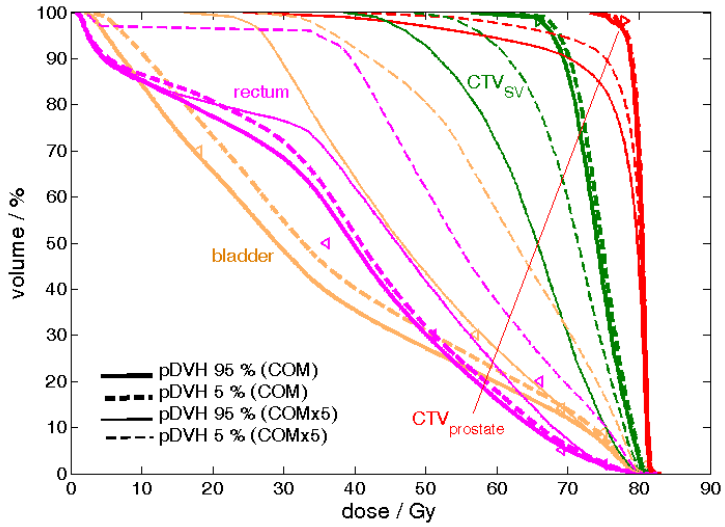

Figure 31. A patient example of pDVH 95%(solid) and pDVH 5% (dashed) of zero PTV-margin plans obtained from 1000 virtual treatment courses using 1 times (thick) versus (thin) 5 times magnitude of PCA-modeled synthetic DVF for a $CTV_{prostate}$-centroid-aligned anatomy.

In the following COP study, $DVF_{syn\_Paligned}$ is utilized to simulate the synthetic ROI voxel offset under the influence of organ deformable motions.

5.3 Decision flow to use COP

With a constructed PCA model, prostate plans can be evaluated and optimized to account for the effects of interfraction deformable organ motion. To investigate the clinical value of COP in terms of the resulting coverage probability and TCP/NTCP distribution, a treatment planning decision flow shown in Figure 32 was designed. This decision flow exists to address two concerns: (1) COP may not be necessary when dosimetric effect of GUs is insignificant and (2) how to determine the clinical advantages of a COP plan relative to the PTV-based plans using empirically determined PTV margins and optimized PTV margins based on target coverage probability.

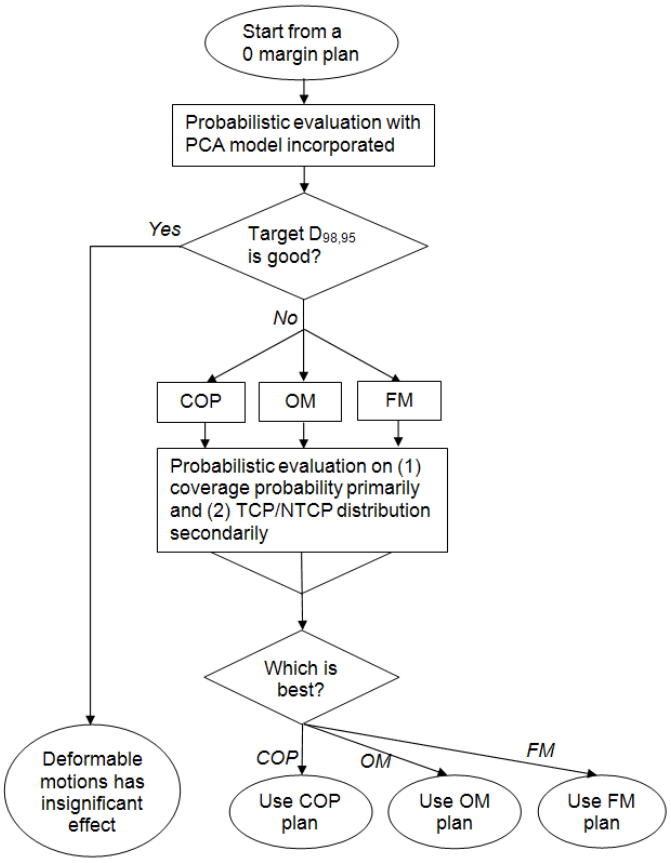

Figure 32. Decision flow of COP to optimize treatment plans to consider organ deformable motions for prostate cancer patients compared with optimized margin (OM) and fixed margin planning techniques.

Figure 32 shows the flow used for each patient. First, the dosimetric effect of PCA-modeled deformable organ motion is evaluated for the $CTV_{prostate}$-centroid-aligned daily fractions. A zero-PTV-margin IMRT plan is created based on optimization criteria for PTV-based plan in Table III (page 22) where PTV1 = $CTV_{prostate}$ and PTV2 = CTV_{SV}. By simulating 1000 [6] virtual treatment courses (30 fractions per treatment course) with PCA model incorporated, the DVCM is constructed and the target dose-volume metric D_{98} at prescribed coverage probability 95% ($D_{98,95}$) is computed for both $CTV_{prostate}$ and CTV_{SV}. Bladder and rectum are excluded in the zero-PTV-margin evaluation because they are assumed to be

[6] The analysis of accuracy and precision of ROI coverage estimated by 1000 virtual treatment courses has been presented in chapter 4, section 4.4.

maximally spared relative to the non-zero PTV or COP plans. Denote $D_{98,95,Rx}$ as the prescribed dose 78 Gy for $CTV_{prostate}$ and 66 Gy for CTV_{SV}. If $D_{98,95} \geq D_{98,95,Rx}$ for both $CTV_{prostate}$ and CTV_{SV}, the dosimetric effect of deformable organ motions for this patient will be regarded as insignificant since target coverage probability is resistant to anatomical variability. Otherwise, replanning the plan to further improve target coverage probability is required. In this case, COP, OM and FM are performed. Here, FM utilizes fixed PTV margins for all the patients — 5 mm for $CTV_{prostate}$ and 8 mm for CTV_{SV} based on a published work (Mutanga *et al.* 2011). The best plan among COP, OM and FM plans is determined by comparing their coverage probabilities primarily. If the target coverage probabilities of these plans are very close, TCP/NTCP distributions are examined for a secondary comparison.

5.4 Results

5.4.1 Dosimetric effects on zero-PTV-margin plans

The dosimetric effect of deformable organ motions reflected on the zero-PTV-margin plans for 19 patients with prostate-centroid alignment is not insignificant. For the static plans which are motion-free, the dose-volume based optimization criteria are not difficult to be satisfied by a simple IMRT optimization. For the non-static plans when deformable motions are considered and simulated in 1000 virtual treatment courses, the pDVH objective criteria for both $CTV_{prostate}$ and CTV_{SV} are not easy to achieve. The pDVH evaluation of each patient is shown in Figure 49, in Appendix I.a. In Figure 33, the average pDVHs of 19 zero-PTV-margin plans are plotted. Even with prostate centroid alignment, the mean $CTV_{prostate}$ $D_{98,95}$ (red solid line) is still lower than prescribed value (red triangle marker). Such dose degradation of CTV_{SV} is even more severe. For bladder and rectum, the pDVH 5% (orange and magenta dashed lines)

indicates some dose slack relative to OAR objective criteria can be exploited for margin expansion to improve target coverage probabilities, though a few rectal $D_{v,5}$ have reached their upper limit. According to the 90% confidence interval of the DVH (the gap between pDVH 95% and 5%), DVH variability due to deformable motion for all ROIs are not large, probably due to the blurring nature of random motions around the mean positions modeled by PCA.

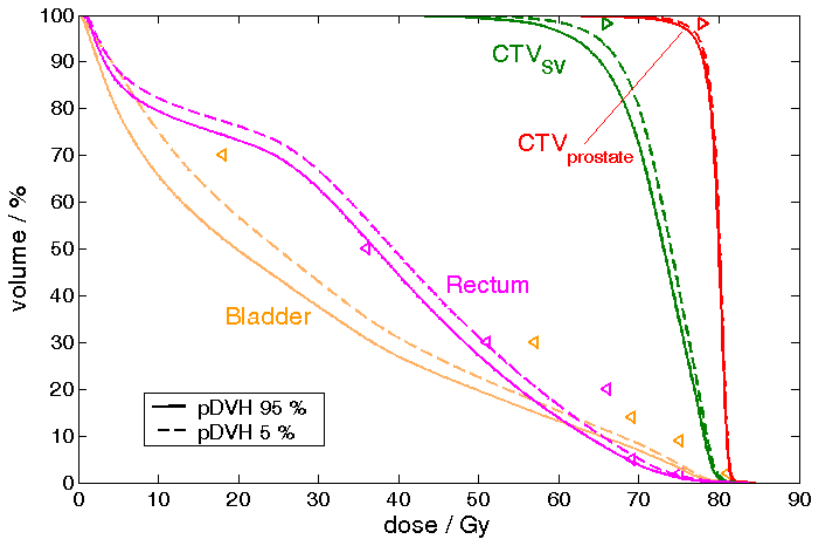

Figure 33. The average pDVHs 95% (solid) and pDVHs 5% (dashed) evaluated on zero-PTV-margin plans through 19 high-risk prostate cancer patients for anatomies $CTV_{prostate}$ (prostate) (red), CTV_{SV} (green), bladder (orange) and rectum (magenta) with optimization objectives (triangle markers). The PCA model is incorporated to show the dosimetric consequence of organ deformable motions.

To determine the necessity of replanning using COP, OM or FM for each patient, the percentage dose degradation $\%\Delta D_{98,95}$ is calculated.

$$\%\Delta D_{98,95} = \begin{cases} \dfrac{D_{98,95,Rx} - D_{98,95}}{D_{98,95,Rx}} \cdot 100\% & (D_{98,95} < D_{98,95,Rx}) \\ 0 & (Else) \end{cases} \tag{52}$$

where $D_{98,95,Rx}$ and $D_{98,95}$ represent prescribed and achieved D_{98} at 95% coverage probability. The percentage DVH variability $\%\Delta DVH_{98,5\text{-}95}$ achieved D_{98} at 95% and 5% coverage probability is

$$\%\Delta DVH_{98,5\text{-}95} = \frac{D_{98,5} - D_{98,95}}{(D_{98,5} + D_{98,95})/2} \cdot 100\% \tag{53}$$

Both $\%\Delta D_{98,95}$ and $\%\Delta DVH_{98,5\text{-}95}$ for 19 zero-PTV-margin plans are displayed in Figure 34. The $\%\Delta D_{98,95}$ and $\%\Delta DVH_{98,5\text{-}95}$ values are well correlated (Figure 35), with the correlation coefficients 0.86 for $CTV_{prostate}$ and 0.90 for CTV_{SV}.

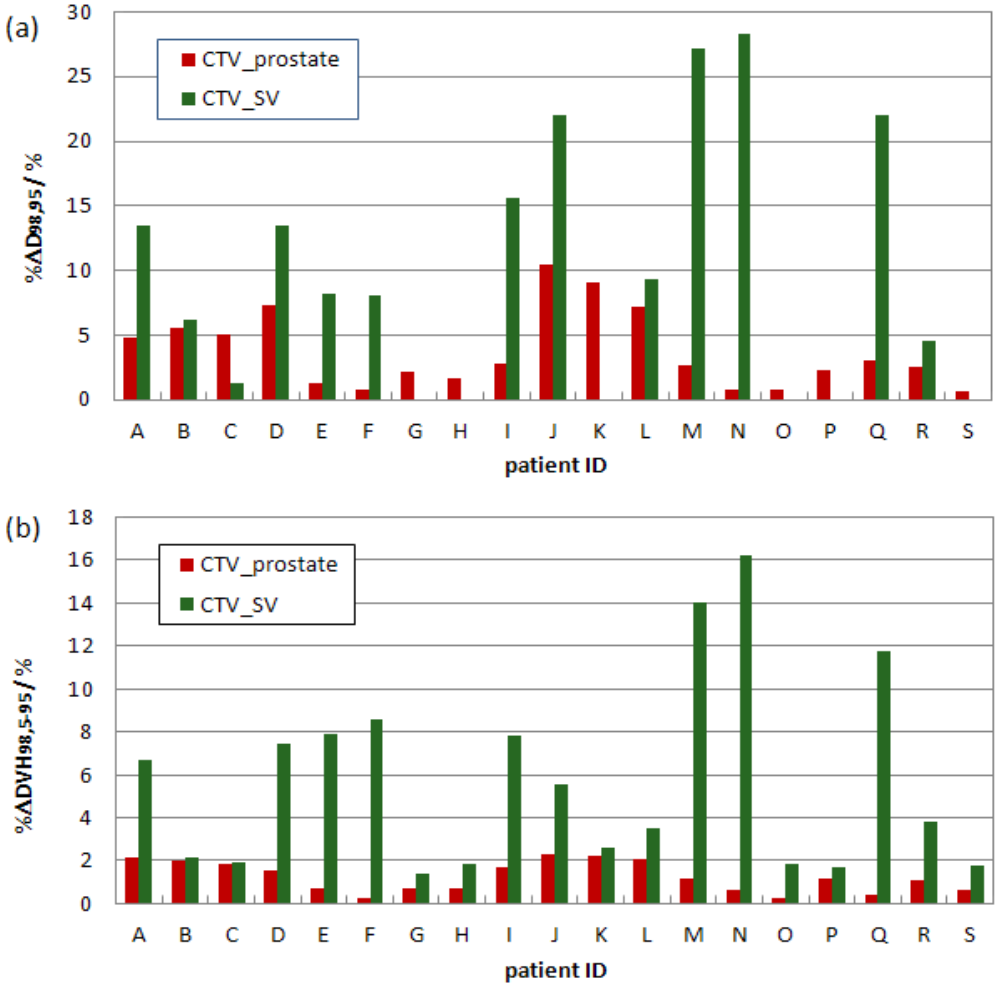

Figure 34. (a) Percentage degraded dose ($\%\Delta D_{98,95}$) and (b) DVH variability ($\%\Delta DVH_{98,5\text{-}95}$) at prescribed dose of $CTV_{prostate}$ (red bins) and CTV_{SV} (green bins) for 19 zero-PTV-margin plans with organ deformable motions considered (using PCA model).

On a patient-specific basis, the dosimetric effect of organ deformable motions is not insignificant: 0/19 patients satisfy the $D_{98,95,Rx}$ objective for both $CTV_{prostate}$ and CTV_{SV} as one or

the other $\%\Delta D_{98,95} > 0\%$. The $\%\Delta D_{98,95}$ and $\%\Delta DVH_{98,5\text{-}95}$ vary widely across the 19 patients. The range of $\%\Delta D_{98,95}$ is 0.7-10.5% for $CTV_{prostate}$ and 0.0-28.3% for CTV_{SV}. The range of $\%\Delta DVH_{98,5\text{-}95}$ is 0.2-2.3% for $CTV_{prostate}$ and 1.4-16.3% for CTV_{SV}. Based on these results, replanning using COP, OM or FM is required to achieve satisfactory $D_{98,95}$ for the patients. In other words, margins or some other accommodation must be made to account for the dosimetric effects of deformable motions.

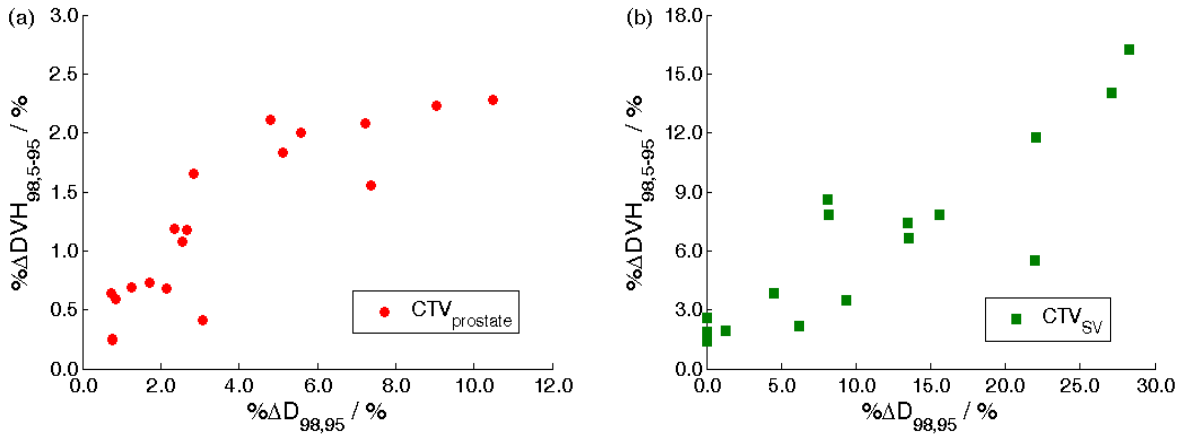

Figure 35. Scatter plot of percentage degraded dose ($\%\Delta D_{98,95}$) versus DVH variability ($\%\Delta DVH_{98,5\text{-}95}$) for (a) $CTV_{prostate}$ (red dots) and (b) CTV_{SV} (green dots) on 19 zero-PTV-margin plans evaluated with PCA model incorporated for each patient.

5.4.2 COP plans vs. OM plans vs. FM plans

Among the COP, OM, FM plans generated for each patient, either (12/19) OM plans or (7/19) COP plans are preferred, while the relative advantages between each other are patient specific. This comparison result is based on the achieved dose at specified coverage probabilities primarily and P+ (probability of complication free control) value secondarily. As a single-number substitute to represent complicated statistics of TCP/NTCP distribution, P+ is expressed as

$$P+ = E\left[TCP_{prostate}\right] \cdot \left(1 - E\left[NTCP_{rectum}\right]\right) \cdot \left(1 - E\left[NTCP_{bladder}\right]\right) \quad (54)$$

where E[] signifies the mean (i.e., expectation) value from the 1000 treatment course simulations. The details of dosimetric/biological metric comparison between COP, OM and FM are summarized in Table XI. The pDVH comparison of each individual patient is shown in Figure 50 of Appendix I.b.

Table XI. Patient ID, percentage target dose degradation $\%\Delta D_{98,95}$ for $CTV_{prostate}$ (P) and CTV_{SV} (S), the optimized PTV margins obtained by OM technique, and best planning technique and its gain relative to the other two plans in terms of target dose coverage($D_{98,95}$) , normal tissue coverage ($D_{v,5}$) and probability of complication free control P+. ID with */ † / ‡ denotes COP / OM / FM plan that fails to achieve target $D_{98,95}$

ID	$\%\Delta D_{98,95}$(%)		OM PTV (mm)		best plan	Gain relative to the other plans	
A*	P: 4.9	S: 14.5	P: 2	S: 8	OM	COP (target $D_{98,95}$)	FM (+6.5% P+)
B*†‡	P: 5.8	S: 6.4	P: 10	S: 5	OM	COP (target $D_{98,95}$)	FM (target $D_{98,95}$)
C*	P: 5.3	S: 1.3	P: 5	S: 3	OM	COP (target $D_{98,95}$)	FM (+2.8% P+)
D*‡	P: 7.7	S: 14.4	P: 5	S: 3	OM	COP (target $D_{98,95}$)	FM (target $D_{98,95}$)
E*	P: 1.3	S: 8.5	P: 2	S: 6	OM	COP (target $D_{98,95}$)	FM (+11.9% P+)
F*	P: 0.8	S: 8.5	P: 1	S: 3	OM	COP (target $D_{98,95}$)	FM (+21.5% P+)
G	P: 2.2	S: 0.0	P: 2	S: 0	COP	OM (OAR, $D_{v,5}$)	FM (+4.2% P+)
H*	P: 1.7	S: 0.0	P: 4	S: 3	OM	COP (target $D_{98,95}$)	FM (+0.9% P+)
I*†‡	P: 2.9	S: 16.9	P: 6	S: 18	OM	COP (target $D_{98,95}$)	FM (target $D_{98,95}$)
J*†‡	P: 11.1	S: 24.7	P: 7	S: 15	COP	OM (target $D_{98,95}$)	FM (target $D_{98,95}$)
K‡	P: 9.5	S: 0.0	P: 9	S: 0	COP	OM (+5.9% P+)	FM (target $D_{98,95}$)
L†‡	P: 7.5	S: 9.8	P: 9	S: 5	COP	OM (target $D_{98,95}$)	FM (target $D_{98,95}$)
M	P: 2.7	S: 31.4	P: 5	S: 4	OM	COP (+2% P+)	FM (+3.1% P+)
N	P: 0.8	S: 32.9	P: 4	S: 8	OM	COP (OAR, $D_{v,5}$)	FM (+3.3% P+)
O*	P: 0.8	S: 0.0	P: 1	S: 0	OM	COP (target $D_{98,95}$)	FM (+22.8% P+)
P‡	P: 2.4	S: 0.0	P: 2	S: 2	COP	OM (+ 1.7% P+)	FM (target $D_{98,95}$)
Q*	P: 3.1	S: 24.8	P: 3	S: 5	OM	COP (target $D_{98,95}$)	FM (+9.5% P+)
R*†‡	P: 2.6	S: 4.6	P: 4	S: 4	COP	OM (target $D_{98,95}$)	FM (target $D_{98,95}$)
S	P: 0.7	S: 0.0	P: 2	S: 0	COP	OM (OAR, $D_{v,5}$)	FM (+6.4% P+)

For the 7 best COP plans and the 12 best OM plans, the clinical benefit with respect to the other plans is patient-specific, and is due to either target coverage or OAR sparing. Relative to FM plans, 5/7 COP plans and 3/12 OM plans improve target $D_{98,95}$ value, and 2/7 COP and 9/12 OM plans achieve better OAR sparing. When COP and OM compete with each other, 3/7

COP plans versus 10/12 OM plans have better target $D_{98,95}$ values. 4/7 COP plans versus 2/12 OM plans reduce more OAR dose.

As to the primary plan comparison metric coverage probabilities, 7/19 COP plans, 14/19 OM plans and 11/19 FM plans meet the optimization criteria of target coverage probability $D_{98,95}$. COP is most likely to fail the prescribed $D_{98,95}$ because the target dosimetric margins are constrained by the bladder and rectum, whose dose tolerance is often pursued in the expense of degrading the target dose. After COP optimization using the pre-selected objective weights, the target $D_{98,95}$ is sometimes compromised at some level below $D_{98,95,Rx}$ to minimizes the composite objective value (equation (2)) when the OAR $D_{v,5}$ terms are non-zero. The $\%\Delta D_{98,95}$ of a COP plan is mostly within 1% but can be up to 4.1% for $CTV_{prostate}$ and 9.3% for CTV_{SV}. The relatively poorer target coverage probability is also reflected in the planning results using COP_{OM}, which generates COP plans starting from OM plans. In Table XII, the originally satisfied target $D_{98,95}$ values in 7 of 14 OM plans end up below $D_{98,95,Rx}$ after COP_{OM} optimization. About half of 19 COP_{OM} plans further spare bladder and rectum with a P+ gain up to 9.8%.

Table XII. Good, moderate and bad changes resulting from COP_{OM} relative to OM

Changes	Target	OAR
Good	Push $D_{98,95}$ up to $D_{98,95,Rx}$: 0/5	Satisfy more $D_{v,5}$ criteria: 8/19 P+ gain: 9/19
Moderate	$D_{98,95}$ remains $D_{98,95,Rx}$: 8/14 $D_{98,95}$ remains below $D_{98,95,Rx}$: 5/5	Minor change in $D_{v,5}$ criteria: 4/19
Bad	Degrade the achieved $D_{98,95}$: 6/14	Violate more $D_{v,5}$ criteria: 7/19 P+ loss: 10/19

It seems surprising that 5/19 OM plans (for patient ID with † in Table XI) failed to achieve target $D_{98,95}$ criteria as the termination condition of OM iteration (Figure 20 on page 61) should ensure target $D_{98,95} > D_{98,95,Rx}$. However, the result is reasonable as the large OM PTV margins result in larger overlap volume of the PTV and bladder/rectum and consequently a tough tradeoff needs to be balanced between these structures. Figure 36 shows the tendency of the competing target and OAR dose at each prescribed coverage probability using different PTV margins. Due to this challenge, increasing uniform PTV margins is not the universal solution to ensure target coverage probability.

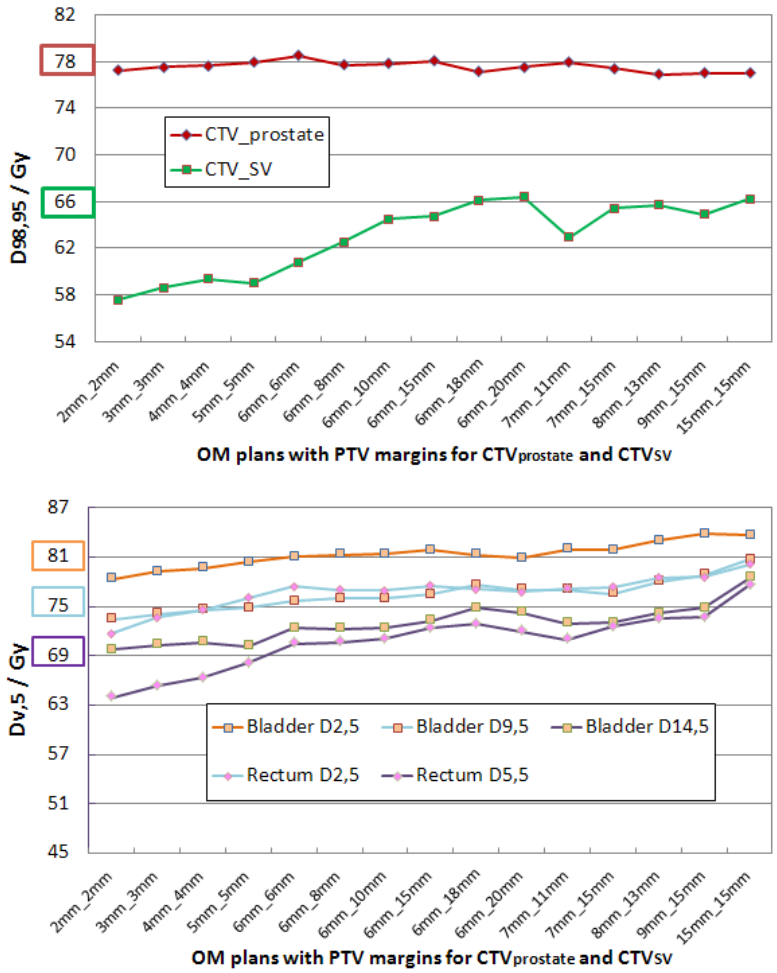

Figure 36. An example of increasing competition between target and OAR criteria with increasing PTV margins during OM optimization. The target prescribed dose or the OAR tolerance dose is highlighted in the same color as the achieved dose curve for each ROI criterion.

In FM plans, the fixed PTV margins — 5 mm and 8 mm selected for $CTV_{prostate}$ and CTV_{SV} — fails to achieve target $D_{98,95,Rx}$ for 8/19 cases. This failure is caused by the sub-optimal margin size without considering patient-specific response to GUs. To avoid undesirable target coverage probability or excessive OAR dose, a patient-specific margin is required to customize individualized characteristics of patient anatomy, deformable organ motions, plan quality, and etc.

On a population basis, COP and OM plans are comparable and both are better than FM plans. As the average pDVH 95% for $CTV_{prostate}$, CTV_{SV} and average pDVH 5% for bladder, rectum shown in Figure 37, COP spares more rectal dose while OM spares more bladder dose relative to FM. The average P+ gain of COP and OM relative to FM is 1.1% and 3.1%, respectively. This concludes that for the high-risk prostate cancer patients with prostate centroid aligned, using the pre-selected objective weights from this study, the benefit of COP in treatment planning is limited when patient-specific coverage-based uniform PTV margins can be determined (via OM). Uniform PTV margins iteratively optimized from 0 during OM optimization are preferred over COP since COP fails to achieve target coverage probability due to the concern of OAR coverage probability for deformable organ motions. The bottleneck of COP relative to OM may be overcome by more advanced IGRT strategies. These strategies effectively reduce the time scale, magnitude and effect of deformable organ motions be accounted for during treatment planning (Jaffray 2007, Bujold *et al.* 2012), thereby allowing smaller target margins, geometrically (PTV margins) or dosimetrically (DMs), to achieve desirable target coverage probability and OAR sparing.

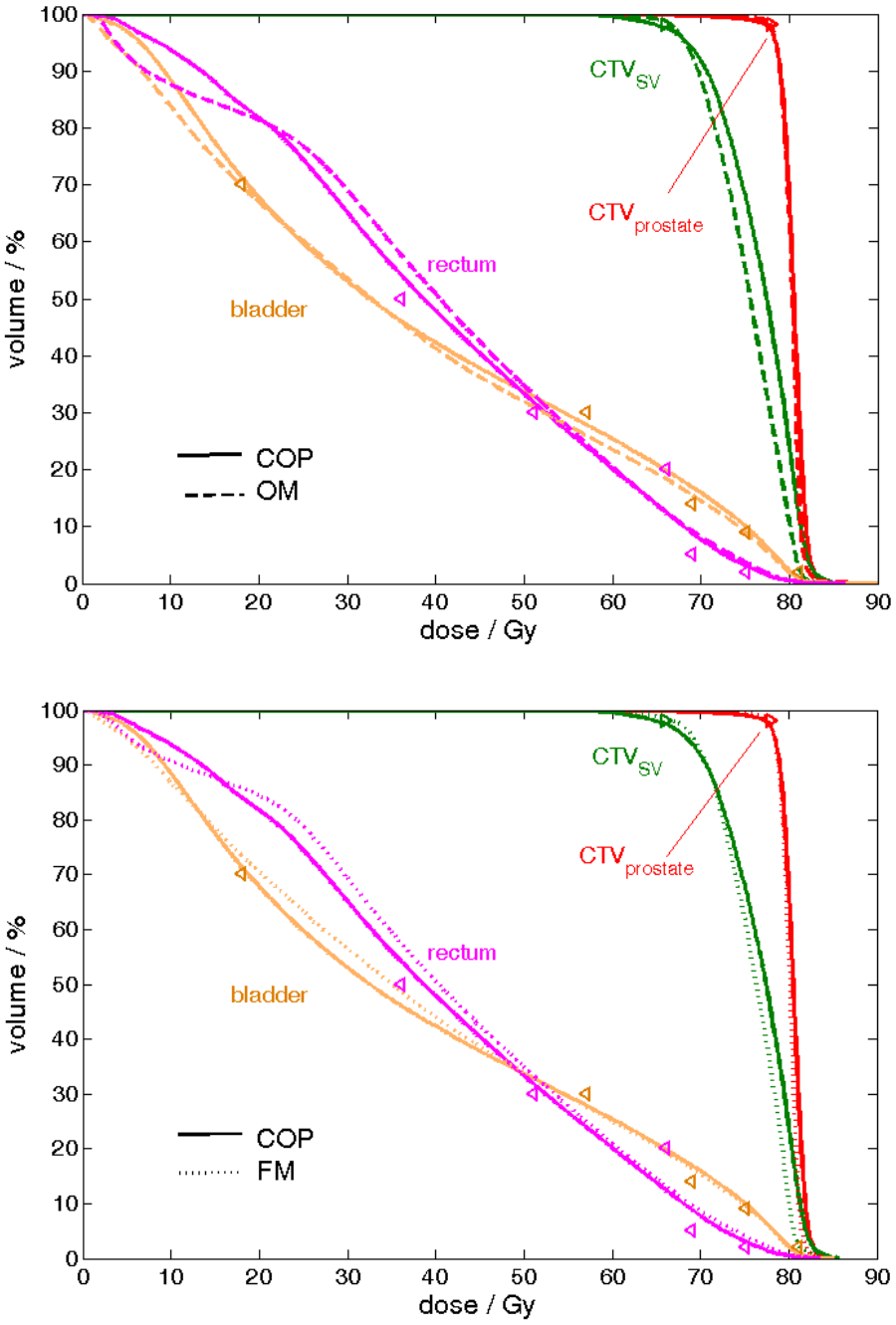

Figure 37. For a population-based comparison, the average pDVHs of (upper) COP vs. OM plans and (lower) COP vs. FM plans to account for deformable motions. For target structures $CTV_{prostate}$ and CTV_{SV}, pDVH 95% are the lower bound of target dose-volume metrics. For OAR structures bladder and rectum, pDVH 5% are the upper bound of OAR dose-volume metrics.

5.5 Conclusions

This chapter explores of dosimetric effect of patient-specific deformable organ motions (via a PCA model) on 19 patients with prostate-centroid aligned throughout the treatment course and describe the implementation of COP with the PCA model incorporated. For the purpose of evaluating the clinical benefit of COP, the PCA model is also incorporated into plan evaluation and OM technique for parallel planning comparison.

The dosimetric effect of deformable organ motions on 19 zero-PTV-margin plans are not insignificant, so treatment replanning using COP, OM and FM techniques is performed. Compared with FM technique that uses empirical fixed PTV margins for each patient, COP or OM techniques result in either better achieved target dose coverage or less toxicity of normal tissues because of using coverage-probability metrics as optimization criteria. The relative advantage between COP and OM are patient-specific. For some patients, COP has limited clinical benefit relative to OM due to poorly selected objective weights and consequently compromised target coverage probability in the presence of deformable organ motions. The bottleneck of COP may be compensated in a more advanced clinical scenario where deformable organ motions are effectively reduced.

6 COP to account for delineation uncertainties

As the "weakest link" of GUs (Njeh 2008), delineation (contouring) uncertainties can have a large impact on target coverage probabilities and protection of surrounding OAR for prostate cancer patients. Though site and application-specific, systematic tumor delineation errors cause an offset from the true target to be hit for treatment (van Herk 2004). Such effect persists during the treatment course of radiation therapy and is "for some tumor locations probability the largest factor contributing to geometric inaccuracy" (Weiss and Hess 2003). Therefore, potential delineation uncertainties should be considered adequately during treatment planning. However, this is challenging (Njeh 2008) since the magnitude of delineation uncertainties depends on many complicated factors including image quality and delineator's expertise, training experience and subjective preference.

COP is potentially very useful to account for delineation uncertainties for prostate cancer patients. It is still ambiguous whether delineation uncertainties can be reduced by advanced techniques such as IGRT (Njeh *et al.* 2013). The components of safety margins for target volumes can be reduced based on improved patient setup and organ variability information provided by IGRT, but it is inappropriate to overly reduce margins without considering delineation uncertainties. The residual errors and probabilities involved in delineation uncertainties can be compensated by using COP.

This chapter focuses on the implementation of COP for prostate cancer treatment in the presence of simulated delineation uncertainties. The so-called delineation uncertainties are referring to the difference in voxel locations between the true ROI and the delineated ROI. Like chapter 5, an introduction of prostate plans and GU model for delineation uncertainties is given first in the section 6.1 and 6.2. Then the dosimetric effect of delineation uncertainties and treatment plans using COP and OM, FM techniques will be investigated in the section 6.3 and 6.4.

6.1 Prostate plans

The NKI patient database has been described in detail in section 4.1 and 5.1. Same reference image sets used in chapter 5 are used per patient. Delineation accuracy is limited by the CT image resolution is $0.094 \times 0.094 \times 3$ mm^3. The dose grid is $2 \times 2 \times 2$ mm^3 for both plan evaluation and optimization.

With a delineated ROI contour used for treatment planning, delineation uncertainties are modeled to predict their dosimetric and biologic metric consequences to the possible true ROI in a virtual treatment course simulation. Here, an average-surface-of-standard-deviation (ASSD) model is constructed to simulate the delineation uncertainties involved in EBRT for high-risk prostate cancer.

6.1.1 ASSD model

Inspired by a population-based model of surface segmentation uncertainties for uncertainty-weighted deformable image registrations (Wu et al. 2010b), the ASSD model is developed to represent the delineation uncertainties involved in a treatment course. By using

ASSD, the true ROI volume (with no delineation uncertainties) can be estimated based on the delineated ROI location on the reference image set of patient database.

The idea of ASSD model is described as follows. In the eye of the tumor, the effect of delineation uncertainties is very similar to organ motion and setup errors — to introduce displacement of ROI voxels. The difference between these GUs in terms of voxel displacement is the voxel-to-voxel distance after displacement. This distance is the same for setup errors, magnified/demagnified equidistantly for the delineation uncertainties to be modeled here and non-equidistantly for organ deformable motion. Assume that the possible true ROI surface can be estimated by expanding or contracting the delineated surface. (The expansion or contraction corresponds to conservative or aggressive delineators who tend to delineate larger or smaller ROI contours.) The magnitude of delineation uncertainties for each voxel is scaled by a voxel-specific delineated-to-true-location displacement vector, in analogy of the vector in the DVF used for the PCA model. This displacement vector for an ROI surface voxel is assumed as a function of a population-based Gaussian distribution and an individualized variable quantified by the image intensity gradient on the location of this voxel. The mean of Gaussian distribution is zero because the delineated ROI surface is assumed to be the best available estimate of the average of the possible true ROI surfaces. The SD values of the Gaussian distribution in right-left (RL), posterior-anterior (PA) and superior-interior (SI) are determined empirically based on literature in Table XIII. The image intensity gradient, or CT gradient in this study, determines the voxel-specific component of delineation uncertainties caused by different image contrast. Lower gradient (= poor image contrast) is associated with a larger displacement vector. After the delineated-to-true-location displacement vectors of the ROI surface voxels are known, the displacement vectors for an ROI interior voxel is determined by a simple interpolation algorithm

between two nearest surface voxels to this voxel so that all ROI voxels are deformed in an equispaced way.

Table XIII: SD values in (mm) of in RL (x), PA (y) and SI (z) direction used in ASSD model for ROIs of prostate cancer patients

ROI	SD_x	SD_y	SD_z	reference
$CTV_{prostate}$	1.7	2	2.5	(van Herk 2004)
CTV_{SV}	1.7	2	3	(Fiorino *et al.* 1998) (Rasch, Steenbakkers, and Van Herk 2005)
bladder	0.7	0.7	3	(Weiss *et al.* 2010)
rectum	1.3	1.3	3	(Weiss *et al.* 2010)

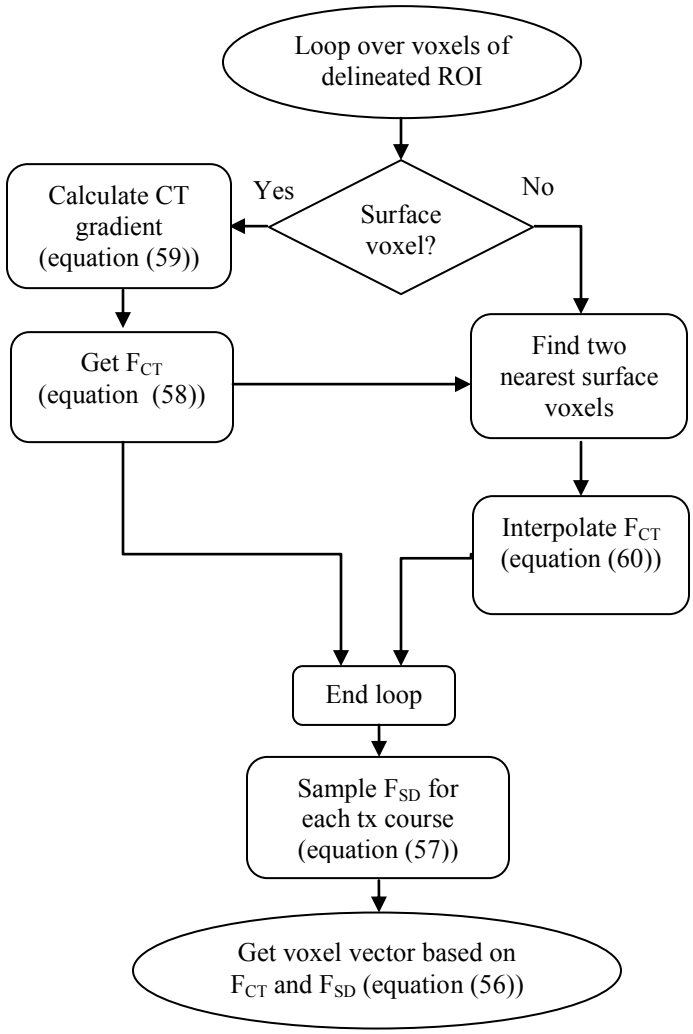

Figure 38. Flow of ASSD model to get voxel displacement due to delineation uncertainties. See text for details.

The detailed workflow of ASSD model is shown in Figure 38. Mathematically, the displacement vector **DT** from a delineated (D) to true (T) ROI for a voxel is written as

$$\mathbf{DT} = (DT_x, DT_y, DT_z) \tag{55}$$

where DT_x, DT_y, DT_z are RL(x), PA(y), SI(z) components of **DT**. Use r to represent x, y or z direction generally, then each component of **DT** is generalized as DT_r. For the ROI voxel with index i, $(DT_r)_{i,k}$ of treatment course k is assumed to be a function of factors of thw Gaussian SD $(F_{CT})_{r,k}$ and the CT gradient $(F_{SD})_{r,i}$ in the r direction

$$(DT_r)_{i,k} = (F_{SD})_{r,k} \cdot (F_{CT})_{r,i} \tag{56}$$

$(F_{SD})_{r,k}$ varies with the treatment course as

$$(F_{SD})_{r,k} = \text{norminv}\left((p_{Rand})_k, 0, SD_r\right) \tag{57}$$

where norminv() is an inverse standard normal cumulative density function (CDF). $(p_{Rand})_k$ is a random probability sampled for the treatment course k. 0 and SD_r are the Gaussian mean and the SD in r direction. (As mentioned before, the SD_r values of each ROI used in ASSD model is listed in Table XIII.) If voxel i is a surface voxel of ROI, its CT-gradient dependent factor $(F_{CT})_{r,i}$ is written as

$$(F_{CT})_{r,i} = \frac{a}{|(grad_{CT})_{r,i}| + a} \tag{58}$$

where $(grad_{CT})_{r,i}$ is the CT number gradient of voxel i in r component, $|\ |$ denotes its absolute value, and a is a normalization factor used to ensure that $(F_{CT})_{r,i}$ ranges from 0 to 1 (Figure 39).

For all the patients, $a = 50$ is arbitrarily used here. The voxel-specific $(grad_{CT})_{r,i}$ is obtained from equation

$$(grad_{CT})_{r,i} = \frac{CT_{r,i}^{+} - CT_{r,i}^{-}}{r_i^{+} - r_i^{-}} = \frac{CT_{r,i}^{+} - CT_{r,i}^{-}}{2 \cdot VoxelSize_r} \tag{59}$$

which is the ratio of CT number difference ($CT_{r,i}^{+} - CT_{r,i}^{-}$) and position difference ($r_i^{+} - r_i^{-}$) of neighboring voxels in positive (+) and (negative (-) side of voxel i in r direction. ($r_i^{+} - r_i^{-}$) is equivalent to 2 times the voxel size in the r direction. When voxel i is an interior voxel, its CT-gradient dependent factor $(F_{CT})_{r,i}$ is interpolated from its two nearest surface voxels, i_surf+ and i_surf-, in the positive and the negative r direction.

$$(F_{CT})_{r,i} = (F_{CT})_{r,i\_surf-} + \frac{((F_{CT})_{r,i\_surf+} - (F_{CT})_{r,i\_surf-})}{r_{i\_surf+} - r_{i\_surf-}} \cdot (r_i - r_{i\_surf-}) \tag{60}$$

An illustration of F_{CT}-dependent vectors on a transverse slice of rectum is shown in Figure 40. The different dosimetric effects of delineation uncertainties simulated using F_{CT}-dependent versus F_{CT}-independent vectors (with F_{CT}=1 as a result of $a \sim \infty$) are reflected in the different pDVHs (Figure 41).

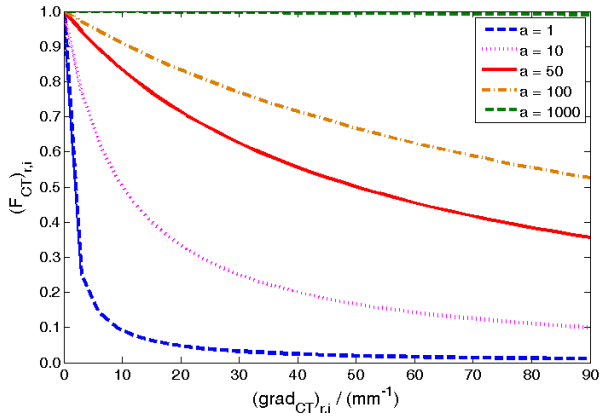

Figure 39. F_{CT} as a function of CT gradient when different parameter a is used.

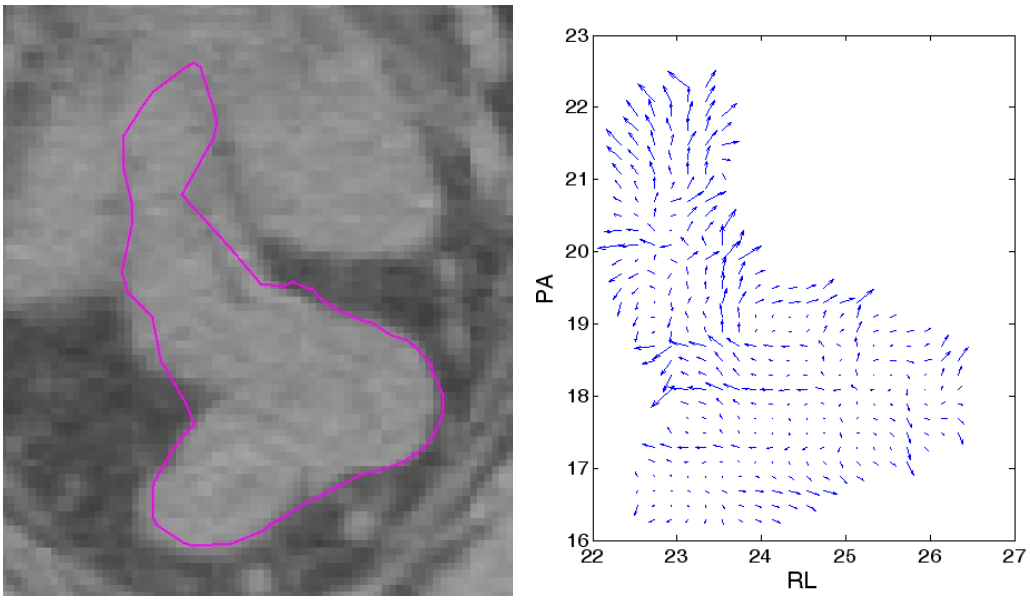

Figure 40. CT image slice in transverse plane for rectum (magenta contour) and corresponding F_{CT} vectors, using a=50.

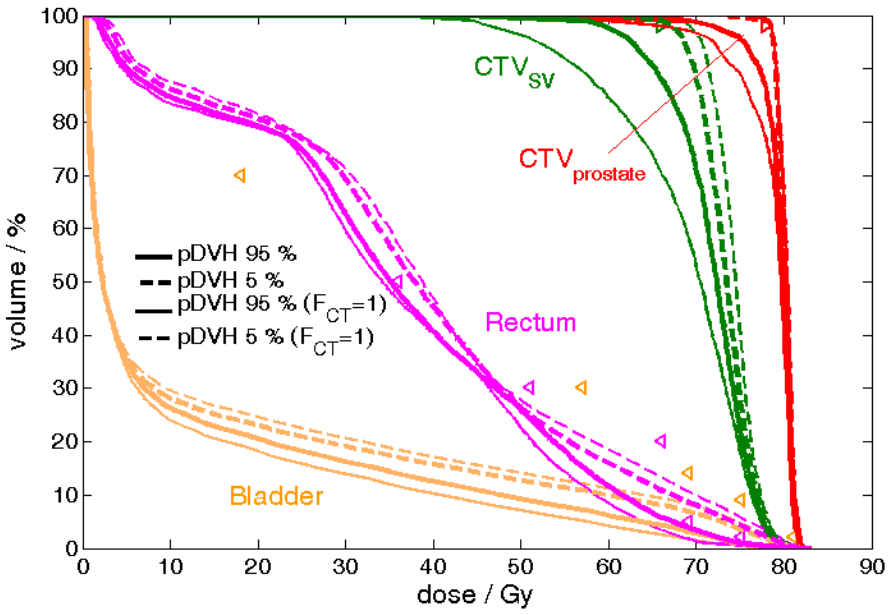

Figure 41. A patient example of pDVH 95% and 5% using ASSD model using CT-gradient factor: (thick lines) F_{CT} calculated using a = 50 versus (thin lines) F_{CT} = 1 when a is very large.

6.2 Decision flow to use COP

With an ASSD model, a prostate plan can be evaluated and optimized to account for effects of the delineation uncertainties. Like the COP study for deformable organ motions in chapter 5, a treatment planning decision flow (in Figure 32, page 84) is also used here. This decision flow is for two concerns: (1) COP may be not essential when dosimetric effect of GUs is insignificant and (2) how clinically advantageous a COP plan is relative to the PTV-based plans using empirically determined PTV (FM) and optimized PTV based on target coverage probability (OM).

The first concern is investigated by calculating the target dose-volume D_{98} at prescribed coverage probability 95% ($D_{98,95}$) on a zero-PTV margin IMRT plan with ASSD model incorporated. Denote D_{Rx} as the prescribed dose 78 Gy for prostate and 66 Gy for seminal vesicles. By simulating 1000 virtual treatment courses, $D_{98,95}$ is compared with $D_{98,95,Rx}$ to determine whether dosimetric effect of modeled delineation uncertainties is insignificant (i.e., $D_{98,95} \geq D_{98,95,Rx}$). The second concern is researched by optimizing the prostate plans using COP, OM, FM techniques (whose workflows are shown in Figure 19, page 60). The best plan among COP, OM and FM plans is determined by comparing their coverage probabilities and P+ values in the presence of modeled delineation uncertainties.

The PTV margins used in the FM plans to account for delineation uncertainties are different as noted in Figure 19. Here, PTV margins are based on van Herk margin formula (VHMF): a PTV margin is equivalent to 2.5 SD of systematic errors plus 0.7 SD of random errors. As delineation uncertainties introduce systematic errors only, the PTV margins M_r in direction r for $CTV_{prostate}$ and CTV_{SV} are simply expressed as

$$M_r = 2.5 \cdot SD_r \quad (61)$$

where SD_r values are listed in Table XIII. Accordingly, PTV margins in RL, PA, SI directions are 4, 5, 6 mm for $CTV_{prostate}$ and 4, 5, 7 mm CTV_{SV}. (The precision of margin setting in Pinnacle[3] is mm.) Therefore, FM uses fixed but non-uniform PTV margins while OM still optimizes uniform PTV margins based on target coverage probability.

6.3 Results

6.3.1 Dosimetric effects on zero-PTV-margin plans

The dosimetric impact of delineation uncertainties modeled by ASSD model is non-negligible on target coverage probability for zero-PTV-margin IMRT plans. Therefore, replanning using COP, OM or FM is determined as needed to achieve better target coverage probability. In Figure 42, with 1000 virtual treatment courses simulated, 0/19 zero-PTV-margin plans achieves D_{Rx} for both the $CTV_{prostate}$ and the CTV_{SV}. The resulting dose degradation $\%\Delta D_{98,95}$ calculated based on equation (52) ranges from 3.2-12.2% for $CTV_{prostate}$ and 0-12.9% for CTV_{SV}. The consequential $\%\Delta DVH_{98,5-95}$ is 2.9-13.6% for $CTV_{prostate}$ and 3.8-13.8% for CTV_{SV}. The $\%\Delta D_{98,95}$ and $\%\Delta DVH_{98,5-95}$ values are well correlated (Figure 43) with high correlation coefficients 0.96 for $CTV_{prostate}$ and 0.83 for CTV_{SV}.

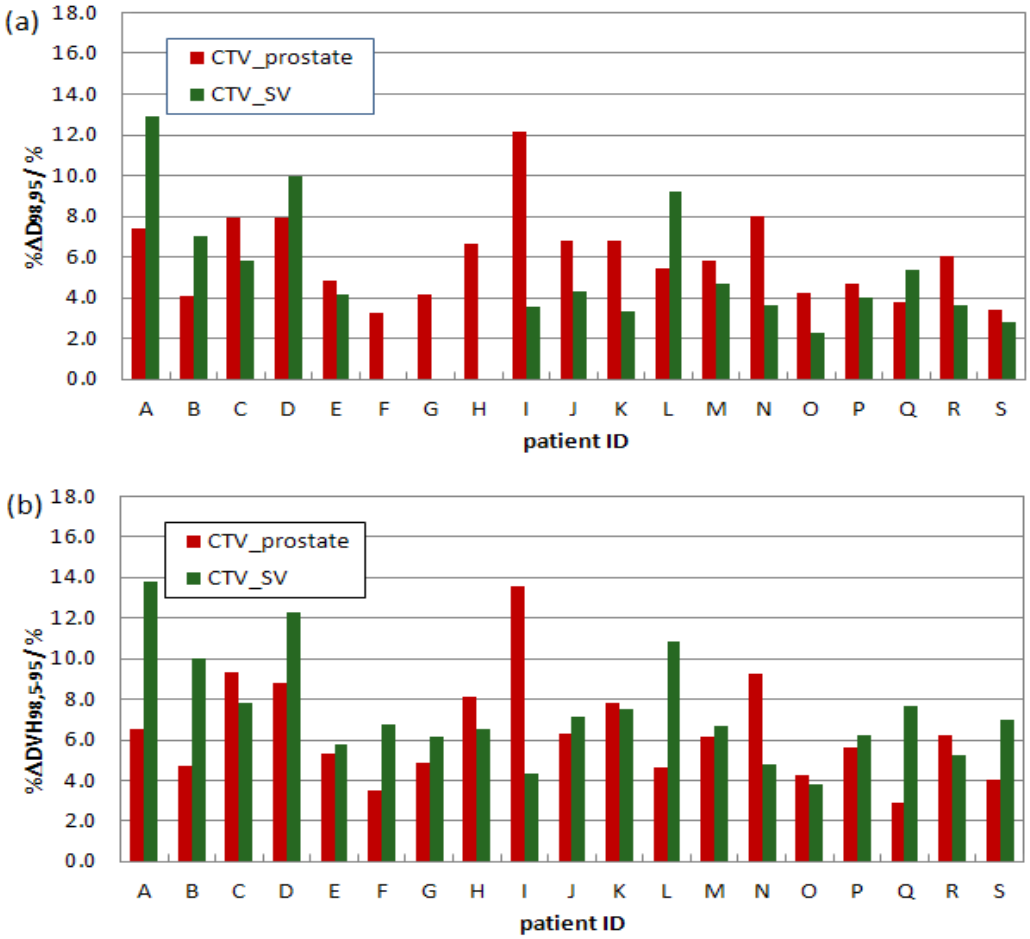

Figure 42. (a) Percentage degraded dose ($\%\Delta D_{98,95}$) and (b) DVH variability ($\%\Delta DVH_{98,5-95}$) at prescribed dose of $CTV_{prostate}$ (red bins) and CTV_{SV} (green bins) for 19 zero-PTV-margin plans with delineation uncertainties considered (using ASSD model).

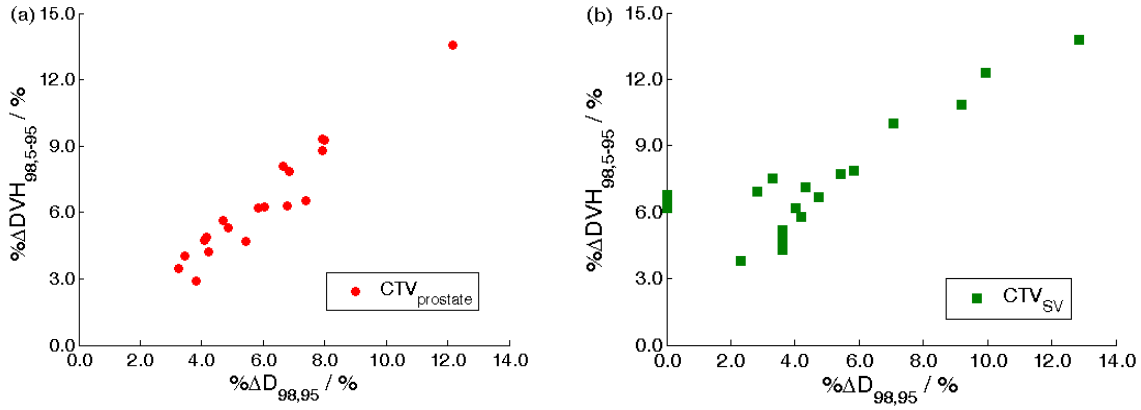

Figure 43. Scatter plot of percentage degraded dose ($\%\Delta D_{98,95}$) versus DVH variability ($\%\Delta DVH_{98,5-95}$) for (a) $CTV_{prostate}$ (red dots) and (b) CTV_{SV} (green dots) on 19 zero-PTV-margin plans evaluated with ASSD model incorporated for each patient.

The evaluation of zero-PTV-margin plans shows the potential benefit in target coverage probability by using COP, OM or FM technique. The individual patient pDVH evaluation results are shown in Figure 51 of **Appendix** I.c. Based on the average pDVHs shown in Figure 44, the average impact of delineation uncertainties on OAR volumes are smaller than target volumes. The $D_{v,5}$ criteria are mostly satisfied for OAR volumes. The slack between $D_{v,5}$ values and their objective values, large for bladder and small for rectum, provides room to be exploited for the increase of target coverage probability.

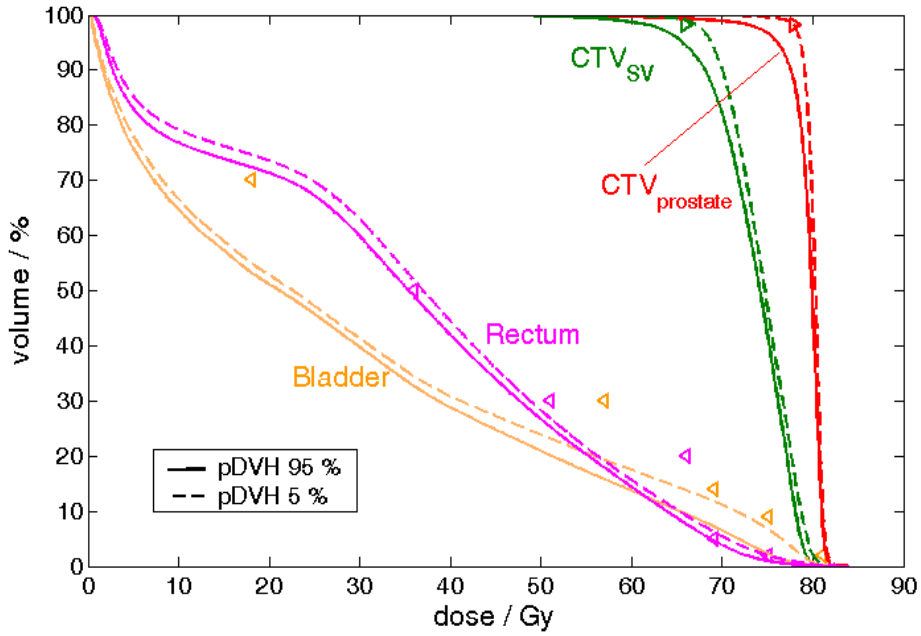

Figure 44. The average pDVHs 95% (solid) and pDVHs 5% (dashed) evaluated on zero-PTV-margin plans for 19 high-risk prostate cancer patients for anatomies $CTV_{prostate}$ (prostate) (red), CTV_{SV} (green), bladder (orange) and rectum (magenta) with optimization objectives (triangle markers). The ASSD model is incorporated to show the dosimetric consequence of delineation uncertainties for prostate cancer patients.

6.3.2 COP plans vs. OM plans vs. FM plans

Among the COP, OM, FM plans generated for each patient, either (11/19) OM plan or (8/19) COP plans are preferred, as Table XIV shows. For the 8 preferred COP plans and the 11

best OM plans, the clinical benefit relative to FM plans are mostly in OAR sparing: 2/8 COP plans and 3/11 OM plans improve target $D_{98,95}$ value while 6/8 COP and 8/11 OM plans achieve better OAR sparing. When COP and OM compete with each other, COP is more likely to compromise the target $D_{98,95}$ value as a result of balancing the weighted OAR objectives. Only 2/8 COP plans (in contrast of 9/11 OM plans) have better target coverage probability while 6/8 COP plans (compared with 2/11 OM plans) gain P+ values. The relative advantages between three plans are patient-specific. The pDVH comparison of each individual patient is shown in Figure 52 of Appendix **I**.d.

Table XIV . Patient ID, percentage target dose degradation $\%\Delta D_{98,95}$ for prostate (P) and seminal vesicles (S), the optimized PTV margins obtained by OM technique, and best planning technique and its gain relative to the other two plans in terms of target dose coverage($D_{98,95}$) and probability of complication free control P+. Patient with */ † / ‡ are those COP / OM / FM plans that fails to achieve target $D_{98,95}$

ID	$\%\Delta D_{98,95}$(%)		OM PTV (mm)		best plan	Gain relative to the other plans	
A*	P: 7.4	S:12.9	P: 3	S: 2	OM	COP (target $D_{98,95}$)	FM (+6.4% P+)
B†‡	P: 4.1	S:7.1	P: 5	S: 2	COP	OM (target $D_{98,95}$)	FM (target $D_{98,95}$)
C	P: 7.9	S: 5.8	P: 4	S: 3	COP	OM (+4.8% P+)	FM (+9.2% P+)
D*‡	P: 7.9	S: 10.0	P: 3	S: 2	OM	COP (target $D_{98,95}$)	FM (target $D_{98,95}$)
E	P: 4.9	S: 4.2	P: 3	S: 2	OM	COP (+1% P+)	FM (+7.1% P+)
F*	P: 3.2	S: 0.0	P: 2	S: 2	OM	COP (target $D_{98,95}$)	FM (+19.6% P+)
G*	P: 4.2	S: 0.0	P: 3	S: 0	OM	COP (target $D_{98,95}$)	FM (+10.8% P+)
H	P: 6.7	S: 0.0	P: 3	S: 2	COP	OM (+6.5% P+)	FM (+12.6% P+)
I*‡	P: 12.2	S: 3.6	P: 5	S: 2	OM	COP (target $D_{98,95}$)	FM (target $D_{98,95}$)
J*	P: 6.8	S: 4.3	P: 5	S: 2	OM	COP (target $D_{98,95}$)	FM (+1.9% P+)
K*	P: 6.8	S: 3.3	P: 3	S: 3	OM	COP (target $D_{98,95}$)	FM (+7.9% P+)
L*†‡	P: 5.4	S: 9.2	P: 5	S: 2	COP	OM (target $D_{98,95}$)	FM (target $D_{98,95}$)
M	P: 5.8	S: 4.7	P: 5	S: 2	COP	OM (+13.4 P+)	FM (+14.4% P+)
N	P: 8.0	S: 3.6	P: 3	S: 2	COP	OM (+5.0 P+)	FM (+16.1% P+)
O	P: 4.2	S: 2.3	P: 4	S: 3	COP	OM (+5.7% P+)	FM (+8.6% P+)
P	P: 4.7	S: 4.0	P: 3	S: 2	COP	OM (+7.0% P+)	FM (+16.4% P+)
Q	P: 3.8	S: 5.4	P: 3	S: 2	OM	COP (+0.2% P+)	FM (+10.4% P+)
R*‡	P: 6.0	S: 3.6	P: 5	S: 4	OM	COP (target $D_{98,95}$)	FM (target $D_{98,95}$)
S*	P: 3.4	S: 2.8	P: 2	S: 2	OM	COP (target $D_{98,95}$)	FM (+5.8% P+)

As to the target coverage probabilities, 9/19 COP plans, 17/19 OM plans and 14/19 FM plans meet the optimization criteria at $D_{98,95,Rx}$, but the dose degradation $\%\Delta D_{98,95}$ values for $CTV_{prostate}$ and CTV_{SV} are small. For the $CTV_{prostate}$ of COP plans, the maximum $\%\Delta D_{98,95}$ is less

than 3% and $\%\Delta D_{98,95}$ of 7/10 COP plans is smaller than 0.3%. For CTV_{SV}, only 2/10 COP plans fail to achieve the prescribed $D_{98,95.}$ For 2/19 OM plans with a degraded target $D_{98,95}$, one has $CTV_{prostate}$ $\%\Delta D_{98,95}$ = 0.3% and the other has CTV_{SV} $\%\Delta D_{98,95}$ = 0.8%. For FM plans using VHMF-based margins, $CTV_{prostate}$ $D_{98,95}$ fails to meet the criterion in 5/19 plans, with $\%\Delta D_{98,95}$ less than 0.9% , while CTV_{SV} $D_{98,95}$ on all FM plans is larger than $D_{98,95,Rx}$.

For $CTV_{prostate,}$ the VHMF-based margin does not guarantee that 90% (here, > 17/19) of patients in the population receive a minimum cumulative CTV dose of at least the prescribed dose at 95% coverage probability.

On a population-based comparison between COP, OM and FM plans in Figure 45, COP maximally satisfies bladder and rectum 5% coverage probability-based limits while ensuring target coverage probability comparable to plans using OM and FM. The comparable target coverage probability is achieved by taking advantages of OAR $D_{v,5}$ slack in lower dose region (e.g., <65 Gy for bladder and <45 Gy for rectum). Therefore, the target dose at prescribed coverage that is compromised in the high dose region of an OAR is reasonably increased in the low dose region within the OAR tolerance. As to PTV margin-based planning, OM is better than FM in terms of sparing more bladder and rectal dose and achieving more desirable target coverage probability. The fixed PTV margin based on van Herk formula is often oversized for CTV_{SV} and suboptimal for $CTV_{prostate}$, which causes excessive dose delivered to OARs, as indicated by higher $D_{v,5}$ values of FM plans in the high dose region (e.g., > 70 Gy) . To sum up these results, even in the simplest uniform style, the patient-specific margins optimized using OM are helpful to create more robust plans than those developed with VHMF-based margins. Relative to the OM-based margins, the dosimetric margins generated by COP can further reduce

excessive OAR dose in the high dose region to efficiently achieving acceptable target coverage probability.

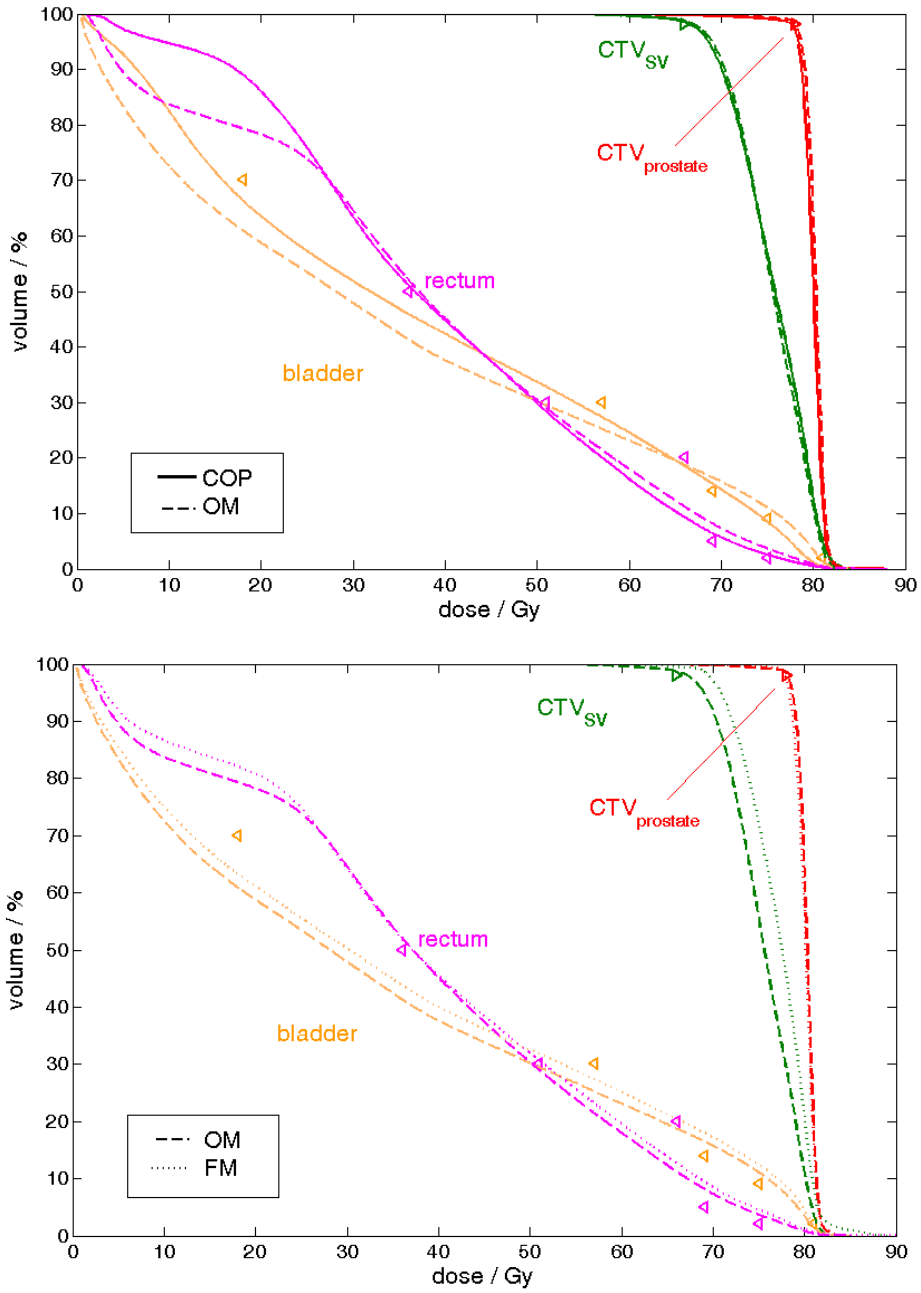

Figure 45. For a population-based comparison, the average PDVHs of (upper) COP vs. OM plans and (lower) OM vs. FM plans to account for delineation uncertainties. For target structures $CTV_{prostate}$ and CTV_{SV}, pDVH are of 95% to show the lower bound of target dose-volume metric values of 95% chances. For OAR structures bladder and rectum, pDVH are of 5% to show the upper bound of OAR dose-volume metric values of 95% chances.

6.4 Conclusions

This chapter described the dosimetric effect of patient-specific delineation uncertainties (via an ASSD model) on 19 patients and the implementation of COP with the ASSD model incorporated. For the purpose of evaluating the clinical benefit of COP, the ASSD model is also incorporated into plan evaluation and OM technique for planning comparison.

The dosimetric effect of delineation uncertainties on 19 zero-PTV-margin plans are not insignificant, so the treatment replanning using COP, OM and FM techniques is performed. Compared with FM technique that uses empirical fixed PTV margins for each patient, COP or OM techniques result in either better achieved target dose coverage or less toxicity of normal tissues because of using coverage-probability metrics as optimization criteria. The relative advantage between COP and OM are patient-specific. In general, COP shows a clinical benefit relative to OM in efficiently reducing excessive OAR dose in the high dose region while maintaining acceptable target coverage probability.

7 Discussion, conclusions and future directions

This chapter serves a summary of the clinical value of COP in terms of multi-fractional EBRT treatment for high-risk prostate cancer (7.1) and future directions to further extend usage of COP, especially for clinical application (7.2).

7.1 Discussion and Conclusions of COP studies

7.1.1 Discussion

For multi-fractional EBRT treatment of high-risk prostate cancer, COP has been studied to account for two GUs, deformable organ motions (chapter 5) and delineation uncertainties (chapter 6), respectively. Because of the non-negligible dosimetric consequences, each of the two GUs has been modeled and incorporated into the probabilistic optimization/evaluation process to perform/compare treatment techniques — COP and two margin-based treatment planning techniques, OM and FM. The results show that the beneficial dosimetric consequences gained from COP is limited for deformable motions but promising for delineation uncertianties.

The goal of COP, OM and FM is to achieve a desirable treatment outcome by creating a treatment plan dose distribution that can absorb ROI GUs through the whole treatment course. COP directly optimizes the dose distribution based on the dosimetric margin incorporating GU models evaluated in possible virtual treatment courses, while both OM and FM are based on a pre-defined surrogate volume PTV. PTV size in FM is empirally determined and in OM is

optimized based on target coverage probabiltiy. FM represents the conventional clinical method which is convenient to be practiced clinically but faces a fundamental problem of how to determine the optimal PTV margins tailored to each patient's characteristics. OM represents a simple form of coverage-probability based treatment planning to optimize patient-specific PTV margins. The optimized PTV margins are uniform, without being shaved for OARs. OM and FM are "lower-level" treatment planning techiniques compared with COP and are designed to determine the relative benefit and cost of COP. The monitor unit perfraction after plan optimization using COP, OM or FM techinqiue when accomodating deformable motions or delineation uncertainties is listed in Table XV. Larger number indicate an increased number of segments neededfor delivery. In most cases, OM plan is least complex among the three.

Table XV. Monitor unit per fraction for COP, OM or FM plan for patients with ID A to S when accommodating deformable motions (modeled by PCA) or delineation uncertainties (modeled by ASSD).

	w/ PCA			w/ ASSD		
ID	COP	OM	FM	COP	OM	FM
A	483	422	444	572	412	444
B	448	580	536	662	524	550
C	636	594	631	601	559	629
D	531	491	515	552	473	505
E	489	487	503	589	458	500
F	401	376	417	442	379	459
G	406	385	430	401	386	412
H	361	398	464	400	377	421
I	440	746	476	477	449	460
J	537	563	501	498	481	503
K	478	637	634	544	524	600
L	565	537	579	559	534	508
M	555	500	592	601	489	500
N	541	485	515	461	442	505
O	434	398	480	441	442	448
P	441	421	503	451	435	441
Q	552	537	579	600	503	577
R	476	505	587	567	536	543
S	405	410	445	417	404	432

It is inappropriate to state for granted that OM and FM are a subset of COP as implemented in this dissertation. The dose distribution of COP can be very different from OM and FM. As Figure 46 shows, the 0 Gy isodose difference surface between OM and FM plans are around $CTV_{prostate}$ volume while this is not the case for the dose distribution difference between COP and FM plans. In this example, COP tends to increase dose to the non-OAR region adjacent to the target to ensure target coverage and OAR sparing. The biggest difference between OM, FM and COP is that COP considers coverage probaiblity for both the CTVs and the OARs during optimization, while the PTV margin sizes in OM and FM techniques are determined without considering the OAR criteria. The modification of the DM during COP optimization is constrained by the OAR probablistic critera while PTV in OM can be continuously enlarged to meet the target coverage constraint. It is very normal that the DMs of COP can only be expanded within a limited range due to the competing target and OAR objectives. (One example is illustrated in Figure 47, where COP result in smaller DM between $CTV_{prostate}$ and TV 78Gy in the region of bladder.) Starting from a zero-PTV-margin plan where no PTV-OAR-overlapping volume is involved, COP may face the dilemma that how to expand dosimetric margins for the low target $D_{98,95}$ in the presence of some high OAR $D_{v,5}$ values. (See rectal pDVH 5% and $CTV_{prostate}$ or CTV_{SV} pDVH 95% in Figure 33 on page 86 and Figure 44 on page 105). As a result, to spare more OAR dose, COP often has to compromise a certain level of target coverage probability in order to minimize the composite objective value. This is why $CTV_{prostate}$ or CTV_{SV} in COP often fails the $D_{98,95,Rx}$ criteria after balancing the conflicts of CTV and OAR coverage. In contrast, thanks to the large range of PTV margin size in OM and FM, target $D_{98,95,Rx}$ of OM and FM plans are much easier to achieve. As long as no tough

competition between PTV and OAR involved (illustrated in Figure 36, page 91), the target $D_{98,95} \geq D_{98,95,Rx}$ as a result of resonably large PTV margins is possible.

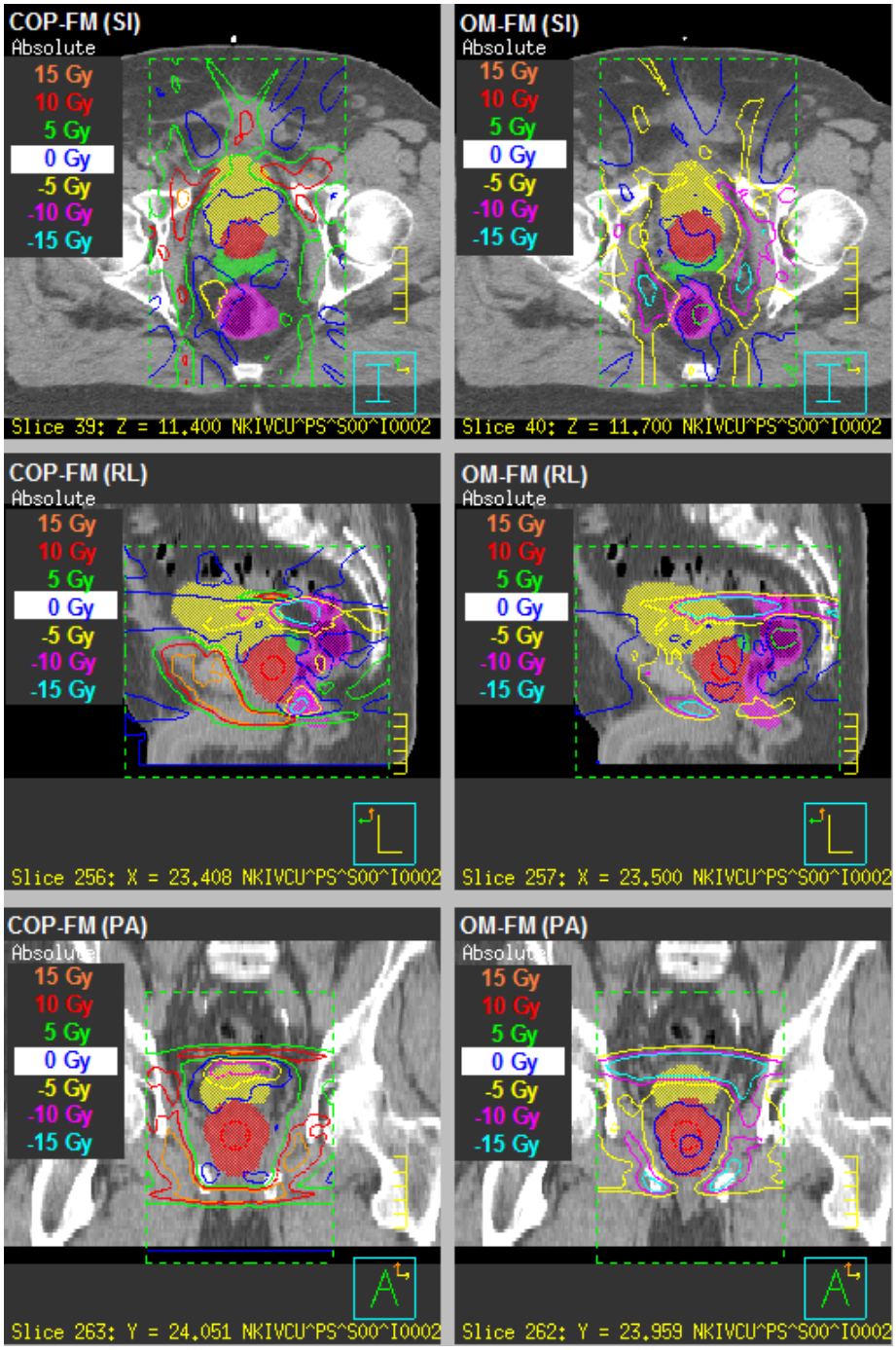

Figure 46. The dose distribution difference as COP minus FM (left column) and OM minus FM (right column) in SI, RL and PA slice for patient S when deformable motions are accommodated. ROIs displayed as colorwash are $CTV_{prostate}$ (red), CTV_{SV} (green), bladder (yellow) and rectum (magenta). The dose distribution around $CTV_{prostate}$ in COP plan is quite different from that on OM and FM plans.

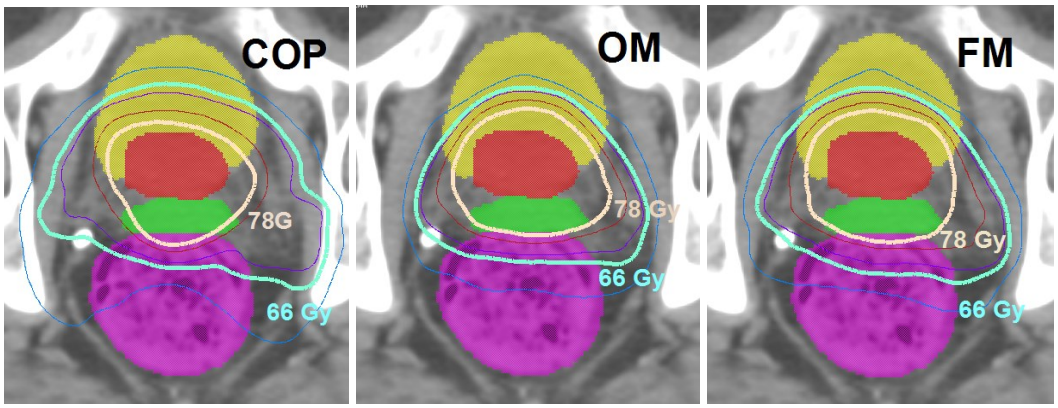

Figure 47. Dose distribution of COP versus OM versus FM plans on one slice for patient H when delineation uncertainties are considered. The thick isodose surface are TVs for of 78Gy (seashell) for $CTV_{prostate}$ (red colorwash) and of 66Gy (aquamarine) for CTV_{SV} (green colorwash). The yellow and magenta colorwash are bladder and rectum. The other isodose surfaces are 75 Gy (maroon), 69 Gy (slateblue) and 57 Gy (lightblue). The smaller DMs of COP plan in some directions due to the compromise of OAR are sometimes more likely to fail to achieve the target coverage.

When treatment for a high-risk prostate cancer patient is planned, it is inadequate to use empirical PTV margins without considering the patient-specific response to coverage probability. This has been proved for setup errors (Gordon *et al.* 2007, Gordon and Siebers 2009, Xu *et al.* 2011). The intrafraction motions can be excluded due to their insignificant dosimetric effect. (Langen *et al.* 2012) For interfraction deformable motion and delineation uncertainties in this dissertation, the PTV margins determined by a published work (Mutanga *et al.* 2011) or VHMF fail to generate desirable plans that are immune to the influence of GUs.

Coverage probability is a useful metric for treatment plan optimization. In general, the planning techinques that considers coverage probability (COP or OM) are more beneficial to account for GUs than FM. For setup errors, the advantages of COP and OM relative to VHMF-based FM have been investigated via two published works. (Gordon and Siebers 2009, Gordon *et al.* 2010) The improved target dose and/or reduced OAR dose at specified coverage probability were pronouced compared with the corresponding VHMF-FM plans for intermiediate-risk prostate cancer patients. Using OM for translation setup errors following Gaussian distribution with systematic and random SD 2 mm, the total volume of normal tissue

receiving dose higher than 65 Gy was reduced on average by 19.3% or about 48 cc.(Gordon and Siebers 2009) Using COP for translation setup errors following Gaussian distribution with systematic and random SD 3mm, rectal NTCP got reduced by 10%. In this dissertation, COP/OM also present dosimetric advantages relative to FM when compensating PCA modeled interfraction deformable organ motion and ASSD-modeled delineation uncertainties (Table XI and Table XIV). These relative advantages reveal the inadequacy of using population-based empirical margins and emphasize the the necessity and potential of coverage-based treatment planning to account for all types of GUs.

For the parameters used in this study, the benefit of COP relative to OM is patient-specific and varies with different GUs. In the study to account for deformable motions, OM is more likely to be preferrable than COP in most patient cases because the better achieved target coverage probability with comparable OAR sparing. (Table XI, page 89) In at least half of these cases, COP compromises target $D_{98,95}$ (with dose degradation more than 2%) to ensure OAR (especially rectal) dose sparing. Whether COP is advantageous over OM for these cases when COP target coverage is given a higher priority (weight) is the subject of future study. The neccessity for COP and OM plans may be reduced by advanced IGART strategies, where the reduced alignment errors and accomodation for deformable motions via adaptive corrections result in less stringent target-OAR tradeoff and better treatment outcomes. In the study to account for delineation uncertainties, COP shows promising potential in efficiently sparing both bladder and rectal dose. (Table XIV, page 106) The p+ gain is 5.5% on average and up to 18.7% relative to OM plans. (If little compromise of target coverage probability (e.g., 1%) is acceptable, at least 3 more COP plans other than OM plans become the best plans.) This clinical benefit of

COP in terms of delineation uncertainties is probably significant since the advanced IGART strategies are of limited usefulness for reducing delineation uncertainites. (Njeh *et al.* 2013)

Dose delivered to lymph nodes (as treatment target) and small bowel (as dose limiting OAR) may show more benefit of COP related to OM and FM, though these two structures are not included in the prostate cancer studies of this dissertation. To date, a growing body of data have suggested that IMRT provides greater advantages over conventional and 3DCRT for pelvic nodes irradiation than localized prostate irradiation, when attempting sparing surrounding normal tissues. (Shih *et al.* 2005, Wang-Chesebro *et al.* 2006) This reveals the complex geometry of lymph nodes and the necessity of more conformal radiation, which indiates the greater sensitivity of lymph nodes to GUs. For the small bowel, the risk of irradiated toxicity may be boosted when some dose limits (Kavanagh *et al.* 2010) are exceeded as a result of large PTV margins of $CTV_{prostate}$ or CTV_{SV} used in OM or FM. COP may result in more desirable lymph nodes coverage or small bowel sparing by savvily creating an optimized DM.

The clnical value of COP may also change with many factors. COP is expected to be more beneficial when e.g., using proton therapy and/or treating cites of some stage that are more likely to require non-uniform margins, like the findings for the PTP techniques reported by the researchers in Massachusetts General Hospital and Harvard Medical School.(Unkelbach *et al.* 2007, 2009) The advantage of COP may be reduced by e.g., implementing more advanced IGART strategies and/or planning on structures which are less senstive to dose. Different treatment protocols with loose or tight criteria may affect the outcome of COP too. Some of these factors will be discussed later for the future COP studies.

7.1.2 Conclusions

In order to ensure if a treatment plan is immune to the degraded effects of GUs, coverage probability is a critical metric to be calculated and compared during planning optimization and evaluation process. The dosimetric effects of deformable organ motion and delineation uncertainties involved in high-risk prostate cancer treatment are not insignificant in terms of the specified target coverage probability 95%.

For high-risk prostate cancer patients treated by multi-fractional EBRT, treatment planning techniques (COP and OM) based on coverage probability metrics shows dosimetric advantages relative to conventional margin-based techniques — FM. Empirical PTV margins face the risk of undesirable target coverage probability and/or excessive dose to surrounding OAR.

In this dissertation, the clinical value of COP is limited to compensate deformable organ motions due to the frequently compromised target coverage probabilities for the concern of normal tissue dose sparing. (caveat page 115) For the objective weights and criteria used here, the OM technique and more advanced clinical strategies can provide preferred solutions to compensate and/or reduce the dosimetric effect of deformable organ motions for high-risk prostate cancer patients.

The clinical role of COP is potentially significant in terms of delineation uncertainties. COP spares excessive OAR dose in high dose regions while exploiting the slack in low dose regions within the tolerance to maintain acceptable target coverage probability. (caveat page 115) Compared to less decent OM plans and IGART strategies, COP offers a good solution to adequately consider delineation uncertainties for treatment planning.

7.2 Future directions of COP studies

7.2.1 Realistic clinical implementation issues

COP still has hurdles to overcome before being implemented in clinical practice. These hurdles can be investigated in the future to improve the clinical feasibility of COP.

First, COP may fail to achieve target coverage probability due to the OAR dose-limiting criteria. It may be helpful to solve this potential problem by increasing the objective weights for the target criteria. One possible way is to utilize the "constraint" function in Pinnacle[3] to make the target objective weight effectively infinitely large. Another possible way is to reduce the relative OAR objective weights in the hope that the target dose is less tightened. How to specify appropriate OAR objective weights adaptive to each patient is an interesting topic for future research. Inappropriate weight reduction may result in undesirable OAR toxicity, as Figure 48 illustrates.

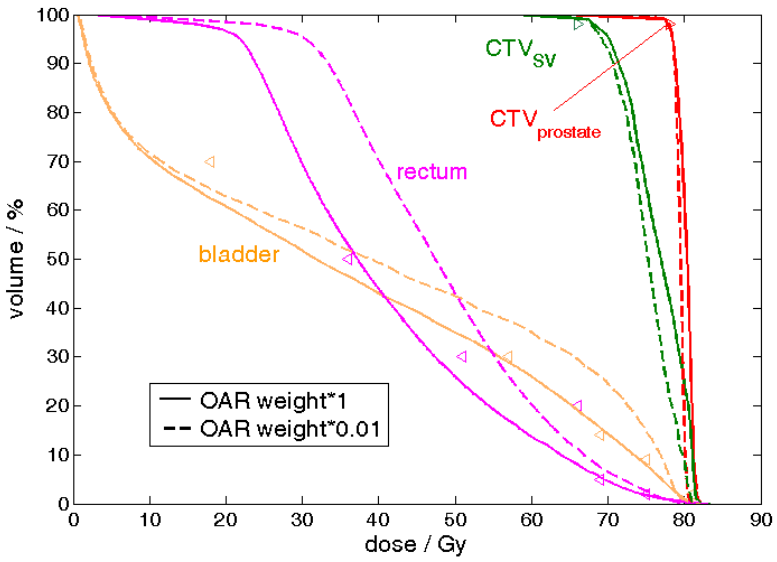

Figure 48. An example of the pDVHs of the COP plan that uses inappropriately reduced OAR objective weights (dashed) in the contrast to that uses original OAR objective weights (solid). The pDVHs are of 95% for $CTV_{prostate}$ (red) and CTV_{SV} (green) and 5% for bladder (orange) and rectum (magenta). Inappropriately reduced OAR objective weights may result in high OAR dose beyond the tolerance.

Second, GU models used in COP and the probabilistic planning optimization need verification and improvement of their representativeness for realistic patient cases. Though the modeling uncertainties can be absorbed to some extent in the large number of simulated virtual treatment course, the inadequate GU models may affect COP and probabilistic evaluation. The PCA model and ASSD model can be tested on a large sample of patient image sets and differently delineated ROI contours.

Third, for organ anatomical/contour variability between treatment fractions, it is almost impossible to obtain sufficient patient-specific GU information before treatment planning is performed. Thus, without known GU PDFs, COP cannot be used in the initial treatment planning process. A possible solution is to build a reasonably representative patient-specific GU model after several (e.g., 5) fractions. With this model, COP can be performed in sequential fractions and compensate GUs that occur in these fractions.

Fourth, COP is still too slow to be executed in the clinic. For a 50-iteration optimization, the run time for COP on a 2.93 GHz Quad Core Processor Core i7-870 is 3-4 hours for deformable organ motions and delineation uncertainties. The run times are based on simulating 100 * 30 virtual treatment fractions on a $3\times3\times3$ mm^3 dose grid (for deformable organ motions) or 1000* 1 virtual treatment fractions for COP on a $2\times2\times2$ mm^3 dose grid (for delineation uncertainties). It is necessary to optimize/parallelize COP code and/ or use more efficient COP parameters (e.g., fewer treatment course number) to speed up COP.

7.2.2 COP in different IGART strategies

The advanced clinical strategies, such as IGART utilizing daily re-planning (Sharma *et al.* Unpublished), may have dosimetric advantages over conventional IMRT for critical structures without compromising target coverage. When these strategies are clinically practical,

the future role of COP will become to compensate their residual uncertainties. Some Pinnacle[3] plugins have been developed (Appendix II.a) and may be used to simulate different frequencies of IGART. Therefore, the residual benefit of COP in different clinical scenarios can be investigated.

7.2.3 Bladder and rectal wall as OAR for prostate cancer

According to the recommendation of ICRU report 83 (ICRU Report 83 2011), bladder wall and rectal wall instead their whole volume should be used as the critical OARs for prostate cancer study. However, delineation of bladder wall and rectal wall is complicated due to poor image quality for real patient cases, which is limited by the realistic concerns such as imaging dose constraints, image data size and medical cost. Inappropriate delineation or image registration of bladder wall during planning and treatment of EBRT may result in incorrect OAR dose evaluation. This may lead to suboptimal OAR sparing or missed opportunities for target coverage due to overrepresentation of the OAR dose during the planning process. As there is no guidance on how to delineate deformed walls as the filling of hollow organs changes, the base characteristics of the bladder wall changes as a function of bladder filling was studied using pig bladders. (See Appendix II.d.) That study concludes that it is adequate to assume a constant bladder wall volume as the bladder fills/empties (and wall thins/thickens). This assumption can be used to assist and test wall delineations as well as image registration for multi-fraction EBRT. For the future prostate cancer studies, wall structures should be involved.

7.2.4 Different treatment sites

The benefit of COP may be more pronounced for the treatment cites other than prostate cancer. Due to quasi-isotropic anatomical shape of $CTV_{prostate}$ and its quasi-isotropic pattern of

GUs, uniform PTV margins (e.g., optimized by OM technique) are often good enough to ensure target coverage probabilities as well as excessive OAR dose sparing. The potential advantages of dosimetric margins derived in COP equivalent to using non-uniform PTV margins are limited in prostate cancer cases. Treatment sites with complex tumor shape (e.g., head and neck cancer) and/or irregular GU pattern (e.g., lung cancer) may have more clinical benefit from COP techniques.

List of References

Adamson, J. and Wu, Q., 2009. Inferences about prostate intrafraction motion from pre- and posttreatment volumetric imaging. *International Journal of Radiation Oncology, Biology, Physics*, 75 (1), 260–267.

Baum, C., Alber, M., Birkner, M., and Nüsslin, F., 2004. Treatment simulation approaches for the estimation of the distributions of treatment quality parameters generated by geometrical uncertainties. *Physics in Medicine and Biology*, 49 (24), 5475–5488.

Baum, C., Alber, M., Birkner, M., and Nüsslin, F., 2006. Robust treatment planning for intensity modulated radiotherapy of prostate cancer based on coverage probabilities. *Radiotherapy and Oncology: Journal of the European Society for Therapeutic Radiology and Oncology*, 78 (1), 27–35.

Bentzen, S.M. and Ritter, M.A., 2005. The alpha/beta ratio for prostate cancer: what is it, really? *Radiotherapy and oncology: journal of the European Society for Therapeutic Radiology and Oncology*, 76 (1), 1–3.

Bittner, N., Butler, W.M., Reed, J.L., Murray, B.C., Kurko, B.S., Wallner, K.E., and Merrick, G.S., 2010. Electromagnetic tracking of intrafraction prostate displacement in patients externally immobilized in the prone position. *International Journal of Radiation Oncology, Biology, Physics*, 77 (2), 490–495.

Bortfeld, T., Craft, D., Dempsey, J.F., Halabi, T., and Romeijn, H.E., 2008. Evaluating Target Cold Spots By the use of Tail EUDs. *International Journal of Radiation Oncology*Biology*Physics*, 71 (3), 880–889.

Budiarto, E., Keijzer, M., Storchi, P.R., Hoogeman, M.S., Bondar, L., Mutanga, T.F., de Boer, H.C.J., and Heemink, A.W., 2011. A population-based model to describe geometrical uncertainties in radiotherapy: applied to prostate cases. *Physics in Medicine and Biology*, 56 (4), 1045–1061.

Bujold, A., Craig, T., Jaffray, D., and Dawson, L.A., 2012. Image-Guided Radiotherapy: Has It Influenced Patient Outcomes? *Seminars in Radiation Oncology*, 22 (1), 50–61.

Burman, C., Kutcher, G.J., Emami, B., and Goitein, M., 1991. Fitting of normal tissue tolerance data to an analytic function. *International Journal of Radiation Oncology Biology Physics*, 21 (1), 123–135.

Byrne, T.E., 2005. A review of prostate motion with considerations for the treatment of prostate cancer. *Medical Dosimetry*, 30 (3), 155–161.

Cahlon, O., Zelefsky, M.J., Shippy, A., Chan, H., Fuks, Z., Yamada, Y., Hunt, M., Greenstein, S., and Amols, H., 2008. Ultra-high dose (86.4 Gy) IMRT for localized prostate cancer: toxicity and biochemical outcomes. *International Journal of Radiation Oncology, Biology, Physics*, 71 (2), 330–337.

Chai, X., van Herk, M., van de Kamer, J.B., Hulshof, M.C.C.M., Remeijer, P., Lotz, H.T., and Bel, A., 2011. Finite element based bladder modeling for image-guided radiotherapy of bladder cancer. *Medical Physics*, 38 (1), 142.

Chao, K.S.C., Blanco, A.I., and Dempsey, J.F., 2003. A conceptual model integrating spatial information to assess target volume coverage for IMRT treatment planning. *International Journal of Radiation Oncology*Biology*Physics*, 56 (5), 1438–1449.

Cheng, C.-W. and Das, I.J., 1999. Treatment plan evaluation using dose–volume histogram (DVH) and spatial dose–volume histogram (zDVH). *International Journal of Radiation Oncology*Biology*Physics*, 43 (5), 1143–1150.

Cheung, R., Tucker, S.L., Lee, A.K., de Crevoisier, R., Dong, L., Kamat, A., Pisters, L., and Kuban, D., 2005. Dose-response characteristics of low- and intermediate-risk prostate cancer treated with external beam radiotherapy. *International Journal of Radiation Oncology, Biology, Physics*, 61 (4), 993–1002.

Chow, J.C.L., Jiang, R., and Markel, D., 2009. The effect of interfraction prostate motion on IMRT plans: a dose-volume histogram analysis using a Gaussian error function model. *Journal of Applied Clinical Medical Physics / American College of Medical Physics*, 10 (4), 3055.

Christensen, G.E. and Johnson, H.J., 2001. Consistent image registration. *IEEE transactions on medical imaging*, 20 (7), 568–582.

De Crevoisier, R., Tucker, S.L., Dong, L., Mohan, R., Cheung, R., Cox, J.D., and Kuban, D.A., 2005. Increased risk of biochemical and local failure in patients with distended rectum on the planning CT for prostate cancer radiotherapy. *International Journal of Radiation Oncology, Biology, Physics*, 62 (4), 965–973.

Daşu, A., 2007. Is the alpha/beta value for prostate tumours low enough to be safely used in clinical trials? *Clinical oncology (Royal College of Radiologists (Great Britain))*, 19 (5), 289–301.

Deurloo, K.E.I., Steenbakkers, R.J.H.M., Zijp, L.J., de Bois, J.A., Nowak, P.J.C.M., Rasch, C.R.N., and van Herk, M., 2005. Quantification of shape variation of prostate and seminal vesicles during external beam radiotherapy. *International Journal of Radiation Oncology, Biology, Physics*, 61 (1), 228–238.

Ding, G.X., Duggan, D.M., and Coffey, C.W., 2008. Accurate patient dosimetry of kilovoltage cone-beam CT in radiation therapy. *Medical Physics*, 35 (3), 1135–1144.

Fatyga, M., Williamson, J.F., Dogan, N., Todor, D., Siebers, J.V., George, R., Barani, I., and Hagan, M., 2009. A comparison of HDR brachytherapy and IMRT techniques for dose escalation in prostate cancer: A radiobiological modeling study. *Medical Physics*, 36 (9), 3995.

Fiorino, C., Reni, M., Bolognesi, A., Cattaneo, G.M., and Calandrino, R., 1998. Intra- and inter-observer variability in contouring prostate and seminal vesicles: implications for conformal treatment planning. *Radiotherapy and oncology: journal of the European Society for Therapeutic Radiology and Oncology*, 47 (3), 285–292.

Fontenla, E., Pelizzari, C.A., Roeske, J.C., and Chen, G.T., 2001. Using serial imaging data to model variabilities in organ position and shape during radiotherapy. *Physics in Medicine and Biology*, 46 (9), 2317–2336.

Fowler, J., Chappell, R., and Ritter, M., 2001. Is alpha/beta for prostate tumors really low? *International journal of radiation oncology, biology, physics*, 50 (4), 1021–1031.

Frank, S.J., Dong, L., Kudchadker, R.J., De Crevoisier, R., Lee, A.K., Cheung, R., Choi, S., O'Daniel, J., Tucker, S.L., Wang, H., and Kuban, D.A., 2008. Quantification of prostate and seminal vesicle interfraction variation during IMRT. *International Journal of Radiation Oncology, Biology, Physics*, 71 (3), 813–820.

Gao, Z., Wilkins, D., Eapen, L., Morash, C., Wassef, Y., and Gerig, L., 2007. A study of prostate delineation referenced against a gold standard created from the visible human data. *Radiotherapy and Oncology*, 85 (2), 239–246.

Ghilezan, M., Yan, D., and Martinez, A., 2010. Adaptive radiation therapy for prostate cancer. *Seminars in Radiation Oncology*, 20 (2), 130–137.

Ghilezan, M.J., Jaffray, D.A., Siewerdsen, J.H., Van Herk, M., Shetty, A., Sharpe, M.B., Zafar Jafri, S., Vicini, F.A., Matter, R.C., Brabbins, D.S., and Martinez, A.A., 2005. Prostate gland motion assessed with cine-magnetic resonance imaging (cine-MRI). *International Journal of Radiation Oncology, Biology, Physics*, 62 (2), 406–417.

Gordon, J.J., Crimaldi, A.J., Hagan, M., Moore, J., and Siebers, J.V., 2007. Evaluation of clinical margins via simulation of patient setup errors in prostate IMRT treatment plans. *Medical Physics*, 34 (1), 202–214.

Gordon, J.J., Sayah, N., Weiss, E., and Siebers, J.V., 2010. Coverage optimized planning: Probabilistic treatment planning based on dose coverage histogram criteria. *Medical Physics*, 37 (2), 550–563.

Gordon, J.J. and Siebers, J.V., Unpublished. Coverage Optimized Planning Can Reduce Normal Tissue Doses.

Gordon, J.J. and Siebers, J.V., 2008. Evaluation of dosimetric margins in prostate IMRT treatment plans. *Medical physics*, 35 (2), 569–575.

Gordon, J.J. and Siebers, J.V., 2009. Coverage-based treatment planning: Optimizing the IMRT PTV to meet a CTV coverage criterion. *Medical Physics*, 36 (3), 961–973.

Van Herk, M., 2004. Errors and margins in radiotherapy. *Semin Radiat Oncol*, 14 (1), 52–64.

Van Herk, M., Remeijer, P., and Lebesque, J.V., 2002. Inclusion of geometric uncertainties in treatment plan evaluation. *International journal of radiation oncology, biology, physics*, 52 (5), 1407–1422.

Van Herk, M., Remeijer, P., Rasch, C., and Lebesque, J.V., 2000. The probability of correct target dosage: dose-population histograms for deriving treatment margins in radiotherapy. *Int J Radiat Oncol Biol Phys*, 47 (4), 1121–35.

Hoogeman, M.S., van Herk, M., de Bois, J., Muller-Timmermans, P., Koper, P.C.M., and Lebesque, J.V., 2004. Quantification of local rectal wall displacements by virtual rectum unfolding. *Radiotherapy and Oncology: Journal of the European Society for Therapeutic Radiology and Oncology*, 70 (1), 21–30.

Hoogeman, M.S., van Herk, M., Yan, D., Boersma, L.J., Koper, P.C.M., and Lebesque, J.V., 2002. A model to simulate day-to-day variations in rectum shape. *International Journal of Radiation Oncology, Biology, Physics*, 54 (2), 615–625.

Huang, Y., Joiner, M., Zhao, B., Liao, Y., and Burmeister, J., 2010. Dose convolution filter: Incorporating spatial dose information into tissue response modeling. *Medical Physics*, 37 (3), 1068–1074.

Huyskens, D.P., Maingon, P., Vanuytsel, L., Remouchamps, V., Roques, T., Dubray, B., Haas, B., Kunz, P., Coradi, T., Bühlman, R., Reddick, R., Esch, A.V., and Salamon, E., 2009. A qualitative and a quantitative analysis of an auto-segmentation module for prostate

cancer. *Radiotherapy and Oncology: Journal of the European Society for Therapeutic Radiology and Oncology*, 90 (3), 337–345.

ICRU Report 50, 1994. *Prescribing, recording and reporting photon beam therapy*. Bethesda MD: ICRU Publications.

ICRU Report 62, 2000. *Prescribing, recording and reporting photon beam therapy (Supplement to ICRU Report 50)*. Bethesda MD: ICRU Publications.

ICRU Report 83, 2011. *Prescribing, Recording, and Reporting Intensity-Modulated Photon-Beam Therapy (IMRT)*. Bethesda MD: ICRU Publications.

Jaffray, D.A., 2007. Image-Guided Radiation Therapy: From Concept to Practice. *Seminars in Radiation Oncology*, 17 (4), 243–244.

Jeong, Y., Radke, R.J., and Lovelock, D.M., 2010. Bilinear models for inter- and intra-patient variation of the prostate. *Physics in Medicine and Biology*, 55 (13), 3725–3739.

Kavanagh, B.D., Pan, C.C., Dawson, L.A., Das, S.K., Li, X.A., Ten Haken, R.K., and Miften, M., 2010. Radiation Dose-Volume Effects in the Stomach and Small Bowel. *International Journal of Radiation Oncology*Biology*Physics*, 76 (3, Supplement 1), S101–S107.

Keall, P., 2004. 4-dimensional computed tomography imaging and treatment planning. *Seminars in Radiation Oncology*, 14 (1), 81–90.

Kerkhof, E.M., van der Put, R.W., Raaymakers, B.W., van der Heide, U.A., van Vulpen, M., and Lagendijk, J.J.W., 2008. Variation in target and rectum dose due to prostate deformation: an assessment by repeated MR imaging and treatment planning. *Physics in medicine and biology*, 53 (20), 5623–5634.

Khan, F.M., 2003. *The Physics of Radiation Therapy*. Williams & Wilkins.

Killoran, J.H., Kooy, H.M., Gladstone, D.J., Welte, F.J., and Beard, C.J., 1997. A numerical simulation of organ motion and daily setup uncertainties: implications for radiation therapy. *International journal of radiation oncology, biology, physics*, 37 (1), 213–221.

Korporaal, J.G., van den Berg, C.A.T., Groenendaal, G., Moman, M.R., van Vulpen, M., and van der Heide, U.A., 2010. The use of probability maps to deal with the uncertainties in prostate cancer delineation. *Radiotherapy and Oncology*, 94 (2), 168–172.

Kupelian, P.A., Willoughby, T.R., Meeks, S.L., Forbes, A., Wagner, T., Maach, M., and Langen, K.M., 2005. Intraprostatic fiducials for localization of the prostate gland: monitoring intermarker distances during radiation therapy to test for marker stability. *International Journal of Radiation Oncology, Biology, Physics*, 62 (5), 1291–1296.

Lagrange, J.-L. and de Crevoisier, R., 2010. [Image guided radiation therapy (IGRT)]. *Bulletin Du Cancer*, 97 (7), 857–865.

Langen, K.M., Chauhan, B., Siebers, J.V., Moore, J., and Kupelian, P.A., 2012. The Dosimetric Effect of Intrafraction Prostate Motion on Step-and-Shoot Intensity-Modulated Radiation Therapy Plans: Magnitude, Correlation With Motion Parameters, and Comparison With Helical Tomotherapy Plans. *International Journal of Radiation Oncology*Biology*Physics*, 84 (5), 1220–1225.

Langen, K.M., Willoughby, T.R., Meeks, S.L., Santhanam, A., Cunningham, A., Levine, L., and Kupelian, P.A., 2008. Observations on real-time prostate gland motion using electromagnetic tracking. *International Journal of Radiation Oncology, Biology, Physics*, 71 (4), 1084–1090.

Li, T., Thongphiew, D., Zhu, X., Lee, W.R., Vujaskovic, Z., Yin, F.-F., and Wu, Q.J., 2011. Adaptive prostate IGRT combining online re-optimization and re-positioning: a feasibility study. *Physics in Medicine and Biology*, 56 (5), 1243–1258.

Löf, J., Lind, B.K., and Brahme, A., 1998. An adaptive control algorithm for optimization of intensity modulated radiotherapy considering uncertainties in beam profiles, patient set-up and internal organ motion. *Physics in Medicine and Biology*, 43 (6), 1605–1628.

Lorenz, C. and Krahnstöver, N., 2000. Generation of Point-Based 3D Statistical Shape Models for Anatomical Objects. *Computer Vision and Image Understanding*, 77 (2), 175–191.

Lotz, H.T., Remeijer, P., van Herk, M., Lebesque, J.V., de Bois, J.A., Zijp, L.J., and Moonen, L.M., 2004. A model to predict bladder shapes from changes in bladder and rectal filling. *Medical Physics*, 31 (6), 1415–1423.

Luxton, G., Hancock, S.L., and Boyer, A.L., 2004. Dosimetry and radiobiologic model comparison of IMRT and 3D conformal radiotherapy in treatment of carcinoma of the prostate. *International Journal of Radiation Oncology, Biology, Physics*, 59 (1), 267–284.

Lyman, J.T., 1985. Complication Probability as Assessed from Dose-Volume Histograms. *Radiation Research Supplement*, 8, S13–S19.

Mah, D., Freedman, G., Milestone, B., Hanlon, A., Palacio, E., Richardson, T., Movsas, B., Mitra, R., Horwitz, E., and Hanks, G.E., 2002. Measurement of intrafractional prostate motion using magnetic resonance imaging. *International Journal of Radiation Oncology*Biology*Physics*, 54 (2), 568–575.

Maleike, D., Unkelbach, J., and Oelfke, U., 2006. Simulation and visualization of dose uncertainties due to interfractional organ motion. *Physics in Medicine and Biology*, 51 (9), 2237–2252.

Mayo, C.S., Zankowski, C., Herman, M., Miller, R., Olivier, K., Vincent, A., and Suominen, J., 2013. A method to vectorize the dose distribution, the dose volume histogram and create a dose vector histogram. *Medical physics*, 40 (1), 011717.

McKenzie, A., van Herk, M., and Mijnheer, B., 2002. Margins for geometric uncertainty around organs at risk in radiotherapy. *Radiotherapy and Oncology*, 62 (3), 299–307.

McKenzie, A.L., van Herk, M., and Mijnheer, B., 2000. The width of margins in radiotherapy treatment plans. *Physics in Medicine and Biology*, 45 (11), 3331–3342.

Meijer, G., Rasch, C., Remeijer, P., and Lebesque, J., 2003. Three-dimensional analysis of delineation errors, setup errors, and organ motion during radiotherapy of bladder cancer. *International Journal of Radiation OncologyBiologyPhysics*, 55 (5), 1277–1287.

Meijer, G.J., de Klerk, J., Bzdusek, K., van den Berg, H.A., Janssen, R., Kaus, M.R., Rodrigus, P., and van der Toorn, P.-P., 2008. What CTV-to-PTV Margins Should Be Applied for Prostate Irradiation? Four-Dimensional Quantitative Assessment Using Model-Based Deformable Image Registration Techniques. *International Journal of Radiation Oncology*Biology*Physics*, 72 (5), 1416–1425.

Moore, J.A., Gordon, J.J., Anscher, M.S., and Siebers, J.V., 2009. Comparisons of treatment optimization directly incorporating random patient setup uncertainty with a margin-based approach. *Medical Physics*, 36 (9), 3880–3890.

Murakami, H. and Kumar, B.V.K.V., Sept. Efficient Calculation of Primary Images from a Set of Images. *IEEE Transactions on Pattern Analysis and Machine Intelligence*, PAMI-4 (5), 511–515.

Mutanga, T.F., de Boer, H.C.J., van der Wielen, G.J., Hoogeman, M.S., Incrocci, L., and Heijmen, B.J.M., 2011. Margin Evaluation in the Presence of Deformation, Rotation, and

Translation in Prostate and Entire Seminal Vesicle Irradiation With Daily Marker-Based Setup Corrections. *International Journal of Radiation Oncology*Biology*Physics*, 81 (4), 1160–1167.

Nahum, A.E. and Tait, D., 1992. Maximising local control by customised dose prescription for pelvic tumours. *In*: *Advanced radiation therapy tumour response monitoring and treatment planning*. Heidelberg: Springer-Verlag, 425–431.

Niemierko, A., 1997. Reporting and analyzing dose distributions: A concept of equivalent uniform dose. *Medical Physics*, 24 (1), 103.

Niemierko, A. and Goitein, M., 1993. Implementation of a model for estimating tumor control probability for an inhomogeneously irradiated tumor. *Radiotherapy and oncology: journal of the European Society for Therapeutic Radiology and Oncology*, 29 (2), 140–147.

Njeh, C., 2008. Tumor delineation: The weakest link in the search for accuracy in radiotherapy. *Journal of Medical Physics*, 33 (4), 136.

Njeh, C.F., Dong, L., and Orton, C.G., 2013. IGRT has limited clinical value due to lack of accurate tumor delineation. *Medical Physics*, 40 (4), 040601.

Park, S.S., Yan, D., McGrath, S., Dilworth, J.T., Liang, J., Ye, H., Krauss, D.J., Martinez, A.A., and Kestin, L.L., 2012. Adaptive Image-Guided Radiotherapy (IGRT) Eliminates the Risk of Biochemical Failure Caused by the Bias of Rectal Distension in Prostate Cancer Treatment Planning: Clinical Evidence. *International Journal of Radiation Oncology*Biology*Physics*, 83 (3), 947–952.

Parzen, E., 1962. On Estimation of a Probability Density Function and Mode. *The Annals of Mathematical Statistics*, 33 (3), 1065–1076.

Peng, C., Ahunbay, E., Chen, G., Anderson, S., Lawton, C., and Li, X.A., 2010. Characterizing Interfraction Variations and Their Dosimetric Effects in Prostate Cancer Radiotherapy. *International Journal of Radiation Oncology, Biology, Physics*.

Pouliot, J., 2007. Megavoltage imaging, megavoltage cone beam CT and dose-guided radiation therapy. *Frontiers of Radiation Therapy and Oncology*, 40, 132–142.

Rasch, C., Barillot, I., Remeijer, P., Touw, A., van Herk, M., and Lebesque, J.V., 1999. Definition of the prostate in CT and MRI: a multi-observer study. *International Journal of Radiation Oncology, Biology, Physics*, 43 (1), 57–66.

Rasch, C., Steenbakkers, R., and van Herk, M., 2005. Target definition in prostate, head, and neck. *Seminars in Radiation Oncology*, 15 (3), 136–145.

Remeijer, P., Rasch, C., Lebesque, J.V., and van Herk, M., 1999. A general methodology for three-dimensional analysis of variation in target volume delineation. *Medical Physics*, 26 (6), 931–940.

Roeske, J.C., Forman, J.D., Mesina, C.F., He, T., Pelizzari, C.A., Fontenla, E., Vijayakumar, S., and Chen, G.T., 1995. Evaluation of changes in the size and location of the prostate, seminal vesicles, bladder, and rectum during a course of external beam radiation therapy. *International Journal of Radiation Oncology, Biology, Physics*, 33 (5), 1321–1329.

Rosenblatt, M., 1956. Remarks on Some Nonparametric Estimates of a Density Function. *The Annals of Mathematical Statistics*, 27 (3), 832–837.

Sanchez-Nieto, B. and Nahum, A.E., 1999. The delta-TCP concept: a clinically useful measure of tumor control probability. *International journal of radiation oncology, biology, physics*, 44 (2), 369–380.

Santanam, L., Noel, C., Willoughby, T.R., Esthappan, J., Mutic, S., Klein, E.E., Low, D.A., and Parikh, P.J., 2009. Quality assurance for clinical implementation of an electromagnetic tracking system. *Medical Physics*, 36 (8), 3477–3486.

Schultheiss, T.E., Tomé, W.A., and Orton, C.G., 2012. It is not appropriate to 'deform' dose along with deformable image registration in adaptive radiotherapy. *Medical Physics*, 39 (11), 6531.

Sharma, M., Weiss, E., and Siebers, J.V., 2012. Dose deformation-invariance in adaptive prostate radiation therapy: Implication for treatment simulations. *Radiotherapy and Oncology*, 105 (2), 207–213.

Sharma, M., Williamson, J.F., and Siebers, J.V., Unpublished. Determine efficacy of different image-guided adaptive treatment strategies for prostate radiation therapy.

Shih, H.A., Harisinghani, M., Zietman, A.L., Wolfgang, J.A., Saksena, M., and Weissleder, R., 2005. Mapping of nodal disease in locally advanced prostate cancer: rethinking the clinical target volume for pelvic nodal irradiation based on vascular rather than bony anatomy. *International journal of radiation oncology, biology, physics*, 63 (4), 1262–1269.

Silverman, B.W., 1986. *Density Estimation for Statistics and Data Analysis*. CRC Press.

Söhn, M., Birkner, M., Yan, D., and Alber, M., 2005a. Modelling individual geometric variation based on dominant eigenmodes of organ deformation: implementation and evaluation. *Physics in Medicine and Biology*, 50 (24), 5893–5908.

Söhn, M., Birkner, M., Yan, D., and Alber, M., 2005b. Modelling individual geometric variation based on dominant eigenmodes of organ deformation: implementation and evaluation. *Physics in Medicine and Biology*, 50 (24), 5893–5908.

Söhn, M., Sobotta, B., and Alber, M., 2012. Dosimetric treatment course simulation based on a statistical model of deformable organ motion. *Physics in medicine and biology*, 57 (12), 3693–3709.

Stroom, J.C., de Boer, H.C., Huizenga, H., and Visser, A.G., 1999. Inclusion of geometrical uncertainties in radiotherapy treatment planning by means of coverage probability. *International Journal of Radiation Oncology, Biology, Physics*, 43 (4), 905–919.

Stroom, J.C. and Heijmen, B.J.M., 2002. Geometrical uncertainties, radiotherapy planning margins, and the ICRU-62 report. *Radiotherapy and Oncology: Journal of the European Society for Therapeutic Radiology and Oncology*, 64 (1), 75–83.

Ten Haken, R.K., Forman, J.D., Heimburger, D.K., Gerhardsson, A., McShan, D.L., Perez-Tamayo, C., Schoeppel, S.L., and Lichter, A.S., 1991. Treatment planning issues related to prostate movement in response to differential filling of the rectum and bladder. *International Journal of Radiation Oncology, Biology, Physics*, 20 (6), 1317–1324.

Timmerman, R.D. and Xing, L., 2009. *Image-Guided and Adaptive Radiation Therapy*. Lippincott Williams & Wilkins.

Unkelbach, J., Bortfeld, T., Martin, B.C., and Soukup, M., 2009. Reducing the sensitivity of IMPT treatment plans to setup errors and range uncertainties via probabilistic treatment planning. *Medical Physics*, 36 (1), 149–163.

Unkelbach, J., Chan, T.C.Y., and Bortfeld, T., 2007. Accounting for range uncertainties in the optimization of intensity modulated proton therapy. *Physics in medicine and biology*, 52 (10), 2755–2773.

Unkelbach, J. and Oelfke, U., 2004. Inclusion of organ movements in IMRT treatment planning via inverse planning based on probability distributions. *Physics in Medicine and Biology*, 49 (17), 4005–4029.

Unkelbach, J. and Oelfke, U., 2005a. Incorporating organ movements in inverse planning: assessing dose uncertainties by Bayesian inference. *Physics in Medicine and Biology*, 50 (1), 121–139.

Unkelbach, J. and Oelfke, U., 2005b. Incorporating organ movements in IMRT treatment planning for prostate cancer: minimizing uncertainties in the inverse planning process. *Medical Physics*, 32 (8), 2471–2483.

Wang-Chesebro, A., Xia, P., Coleman, J., Akazawa, C., and Roach, M., 3rd, 2006. Intensity-modulated radiotherapy improves lymph node coverage and dose to critical structures compared with three-dimensional conformal radiation therapy in clinically localized prostate cancer. *International journal of radiation oncology, biology, physics*, 66 (3), 654–662.

Webb, S. and Nahum, A.E., 1993. A model for calculating tumour control probability in radiotherapy including the effects of inhomogeneous distributions of dose and clonogenic cell density. *Physics in Medicine and Biology*, 38 (6), 653–666.

Weiss, E. and Hess, C.F., 2003. The impact of gross tumor volume (GTV) and clinical target volume (CTV) definition on the total accuracy in radiotherapy theoretical aspects and practical experiences. *Strahlentherapie Und Onkologie: Organ Der Deutschen Röntgengesellschaft ... [et Al*, 179 (1), 21–30.

Weiss, E., Wu, J., Sleeman, W., Bryant, J., Mitra, P., Myers, M., Ivanova, T., Mukhopadhyay, N., Ramakrishnan, V., Murphy, M., and Williamson, J., 2010. Clinical evaluation of soft tissue organ boundary visualization on cone-beam computed tomographic imaging. *International Journal of Radiation Oncology, Biology, Physics*, 78 (3), 929–936.

Wilkinson, J.M., 2004. Geometric uncertainties in radiotherapy. *Br J Radiol*, 77 (914), 86–87.

Witte, M., Shakirin, G., Houweling, A., Peulen, H., and van Herk, M., 2011. Dealing with geometric uncertainties in dose painting by numbers: Introducing the ΔVH. *Radiotherapy and Oncology*, 100 (3), 402–406.

Witte, M.G., van der Geer, J., Schneider, C., Lebesque, J.V., Alber, M., and van Herk, M., 2007. IMRT optimization including random and systematic geometric errors based on the expectation of TCP and NTCP. *Medical Physics*, 34 (9), 3544.

Wu, B., Ricchetti, F., Sanguineti, G., Kazhdan, M., Simari, P., Chuang, M., Taylor, R., Jacques, R., and McNutt, T., 2009. Patient geometry-driven information retrieval for IMRT treatment plan quality control. *Medical Physics*, 36 (12), 5497–5505.

Wu, B., Ricchetti, F., Sanguineti, G., Kazhdan, M., Simari, P., Jacques, R., Taylor, R., and McNutt, T., 2011. Data-Driven Approach to Generating Achievable Dose–Volume Histogram Objectives in Intensity-Modulated Radiotherapy Planning. *International Journal of Radiation Oncology*Biology*Physics*, 79 (4), 1241–1247.

Wu, J., Murphy, M.J., Weiss, E., Sleeman, W.C., and Williamson, J., 2010. Development of a population-based model of surface segmentation uncertainties for uncertainty-weighted deformable image registrations. *Medical Physics*, 37 (2), 607.

Wu, Q. and Mohan, R., 2000. Algorithms and functionality of an intensity modulated radiotherapy optimization system. *Medical physics*, 27 (4), 701–711.

Wu, Q.J., Thongphiew, D., Wang, Z., Mathayomchan, B., Chankong, V., Yoo, S., Lee, W.R., and Yin, F.-F., 2008. On-line re-optimization of prostate IMRT plans for adaptive radiation therapy. *Physics in medicine and biology*, 53 (3), 673–691.

Xu, H., Gordon, J.J., and Siebers, J.V., 2011. Sensitivity of postplanning target and OAR coverage estimates to dosimetric margin distribution sampling parameters. *Medical Physics*, 38 (2), 1018.

Yan, D., Jaffray, D.A., and Wong, J.W., 1999. A model to accumulate fractionated dose in a deforming organ. *International Journal of Radiation Oncology, Biology, Physics*, 44 (3), 665–675.

Yan, D., Vicini, F., Wong, J., and Martinez, A., 1997. Adaptive radiation therapy. *Physics in Medicine and Biology*, 42 (1), 123–132.

Yang, J., Mageras, G.S., Spirou, S.V., Jackson, A., Yorke, E., Ling, C.C., and Chui, C.-S., 2005. A new method of incorporating systematic uncertainties in intensity-modulated radiotherapy optimization. *Medical Physics*, 32 (8), 2567–2579.

Zhao, B., Joiner, M.C., Orton, C.G., and Burmeister, J., 2010. 'SABER': A new software tool for radiotherapy treatment plan evaluation. *Medical Physics*, 37 (11), 5586–5592.

Zhou, S.M., Bentel, G.C., Lee, C.G., and Anscher, M.S., 1998. Differences in gross target volumes on contrast vs. noncontrast CT scans utilized for conformal radiation therapy treatment planning for prostate carcinoma. *International Journal of Radiation Oncology, Biology, Physics*, 42 (1), 73–78.

Zhu, X., Ge, Y., Li, T., Thongphiew, D., Yin, F.-F., and Wu, Q.J., 2011. A planning quality evaluation tool for prostate adaptive IMRT based on machine learning. *Medical Physics*, 38 (2), 719–726.

Appendix I. Patient-specific pDVH results of COP studies

a. pDVH evaluation with deformable motion model (PCA) incorporated

For each one of the 19 patients, pDVH 95% and 5% for $CTV_{prostate}$, CTV_{SV}, bladder and rectum on a zero-PTV-margin plan are plotted below. The dosimetric effect of deformable organ motions reflected on the plot is patient-specific.

Though the $CTV_{prostate}$-centroid is always aligned, none of the patients is immune to the degradation effect of target coverage due to deformable organ motions. The target dose deviation from the objective values at 95% coverage probability can be relatively small (e.g., patient G, H, O, P and S) or large (e.g., patient A, D, I, J, L, M and N), but all indicate the necessity of larger PTV margin or DM to improve the target coverage.

When it comes to the OARs, the rectum is more likely to be overdosed than the bladder. The rectal dose at 5% coverage probability of more than half patient cases already exceeds the dose limits before larger margin is used, which shows the potential conflict of rectal sparing and target coverage improvement. In contrast, the bladder dose at 5% coverage probability is mostly within the dose tolerance for most patients, except patient B, E, J, O, R whose bladder dose is a little beyond one or two objective values. The slack between the current bladder dose and the corresponding bladder dose limits, which is large for more than half of patients, provides room for margin expansion.

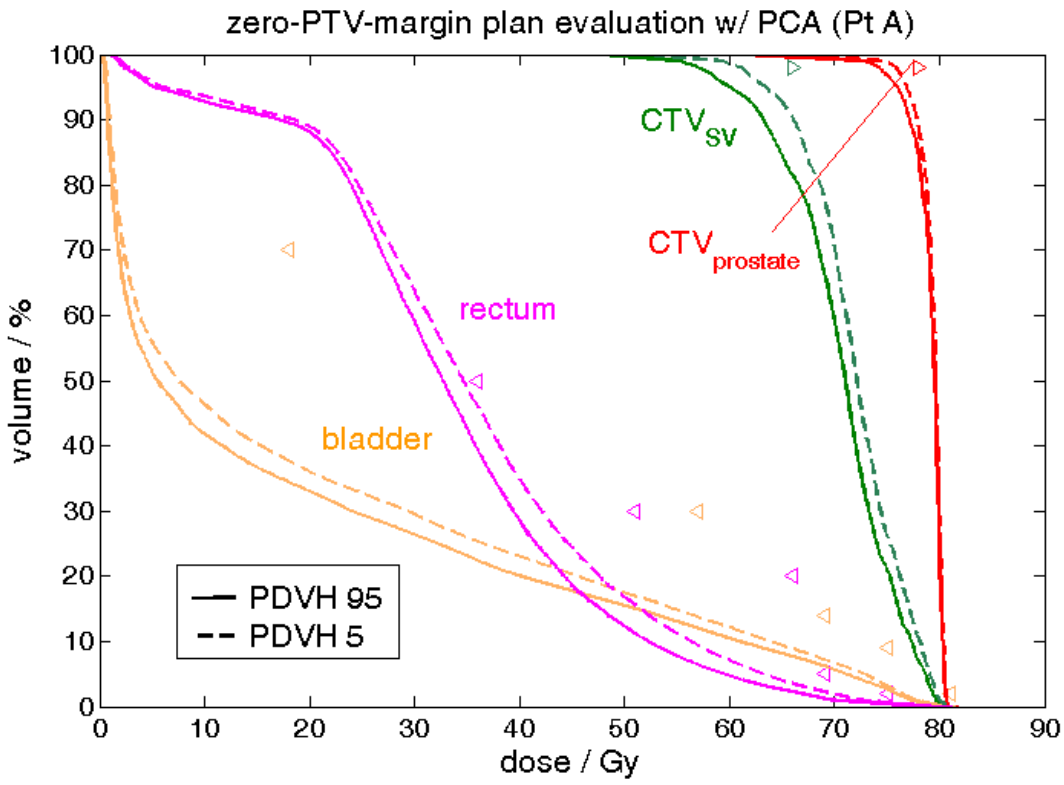

Figure 49. The patient-specific pDVHs 95% (solid) and pDVHs 5% (dashed) evaluated on zero-PTV-margin plans for patient with ID A to S(continued below) for anatomies CTVprostate (prostate) (red), CTVSV (green), bladder (orange) and rectum (magenta) with optimization objectives (triangle markers). The PCA model is incorporated to show the dosimetric consequence of organ deformable motions.

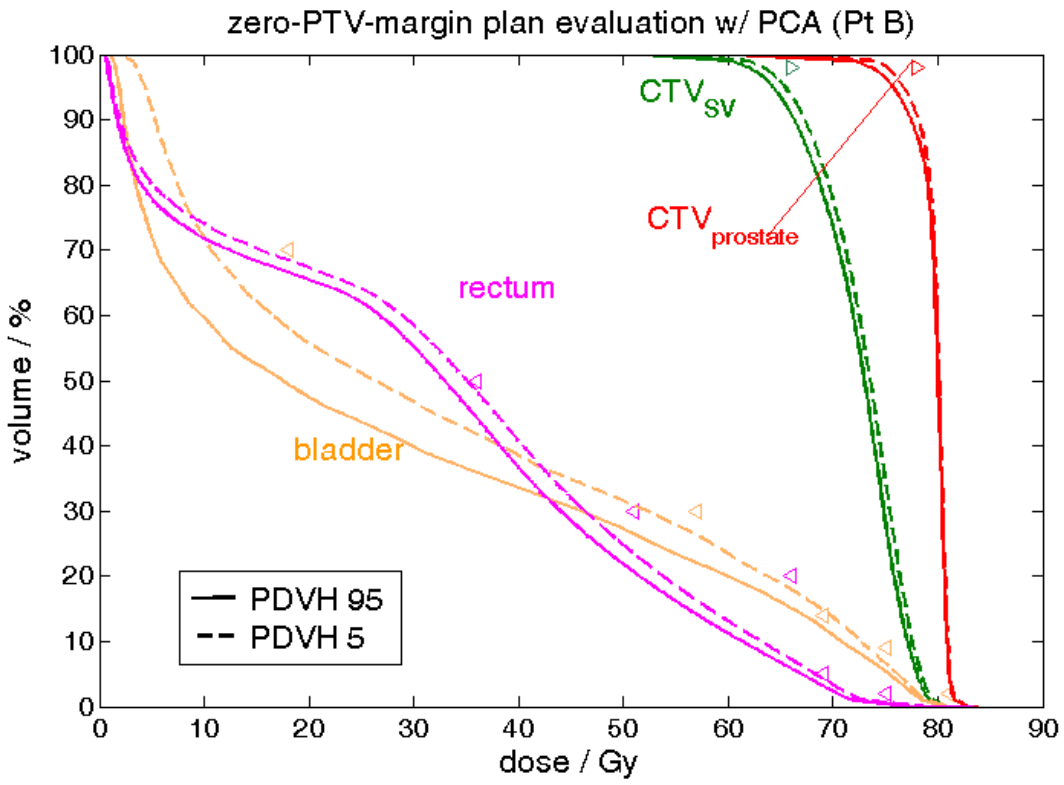

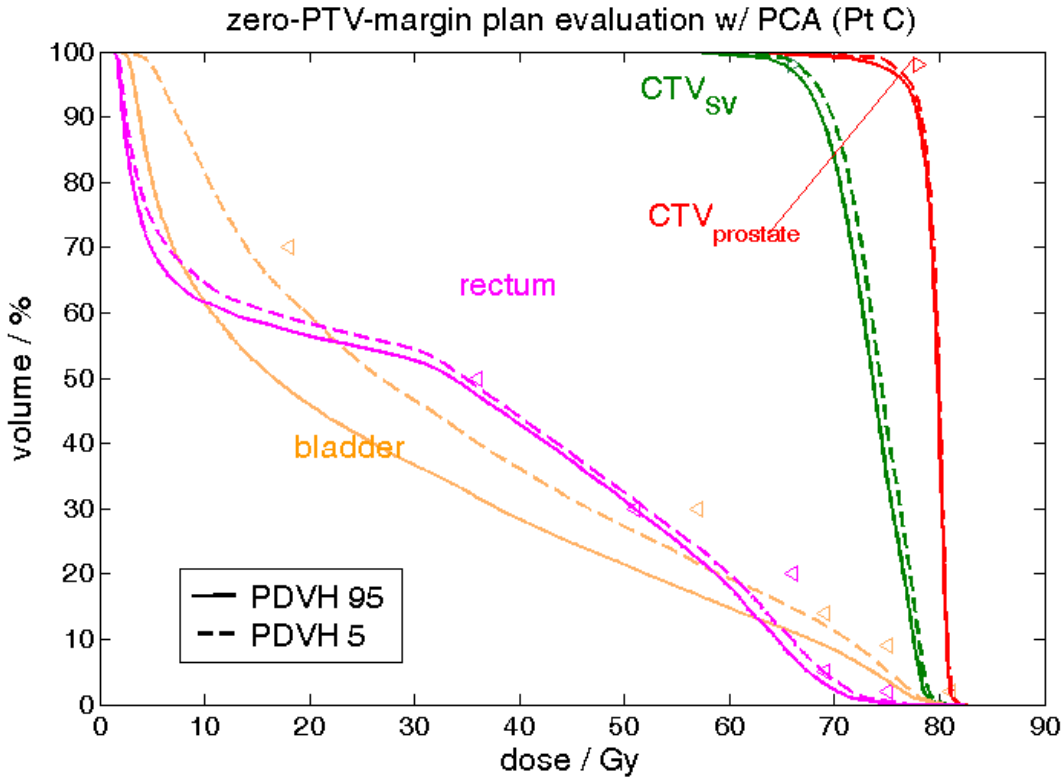

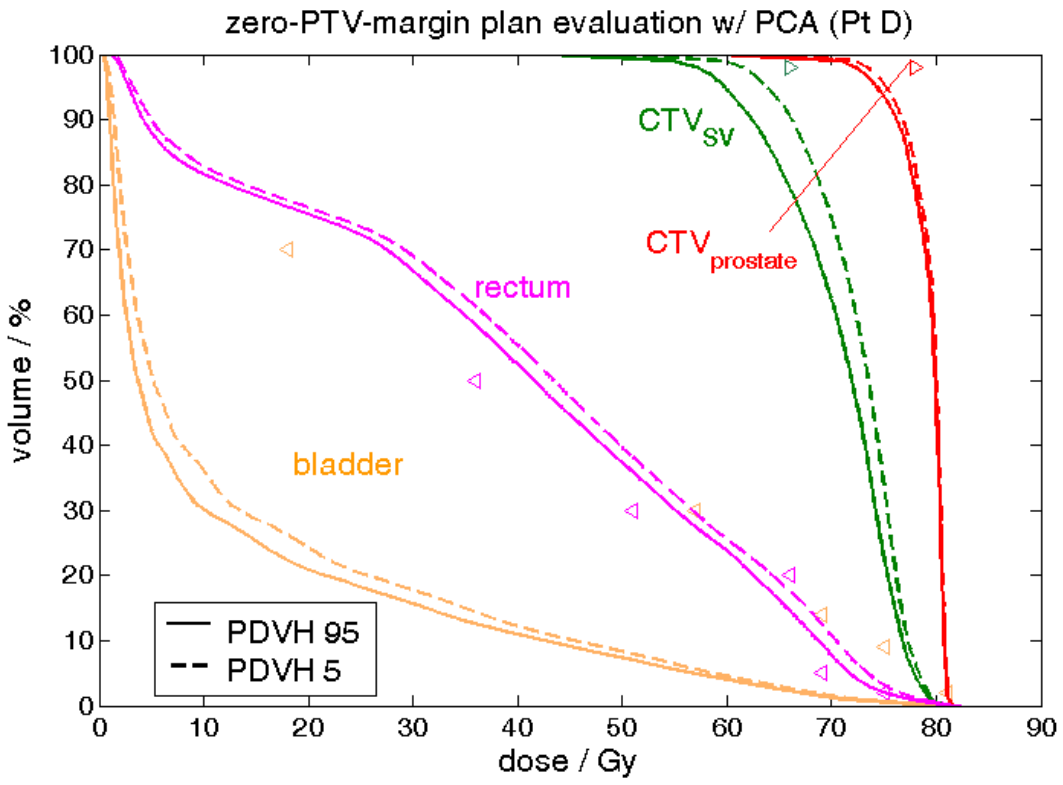

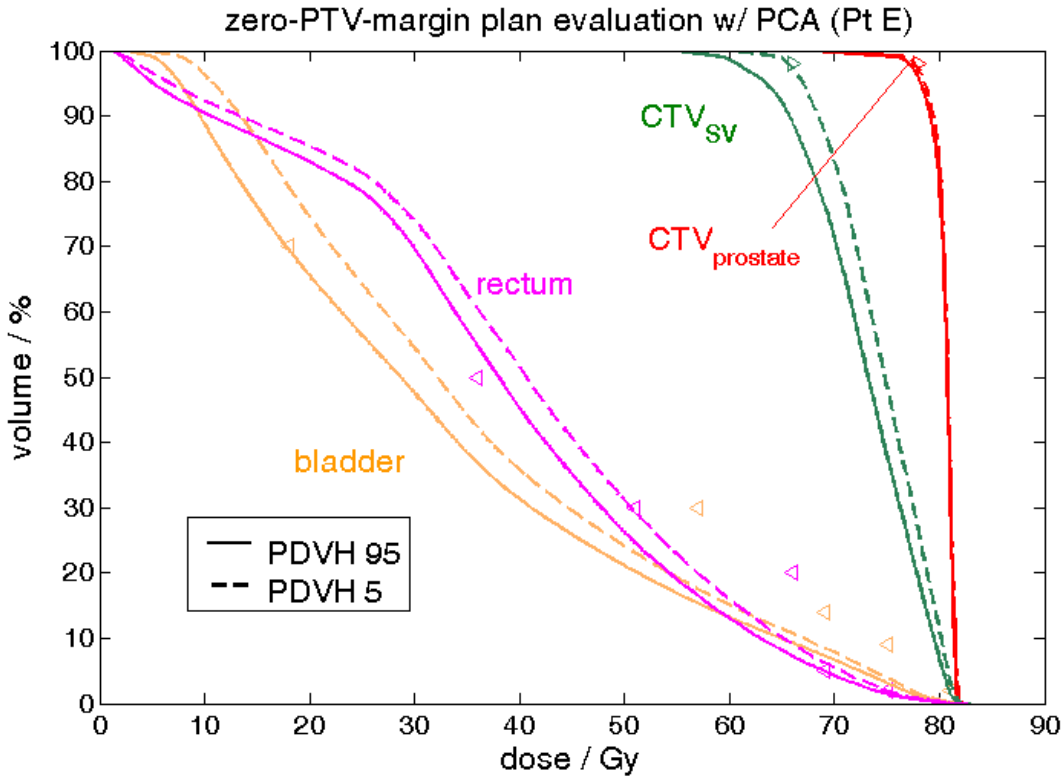

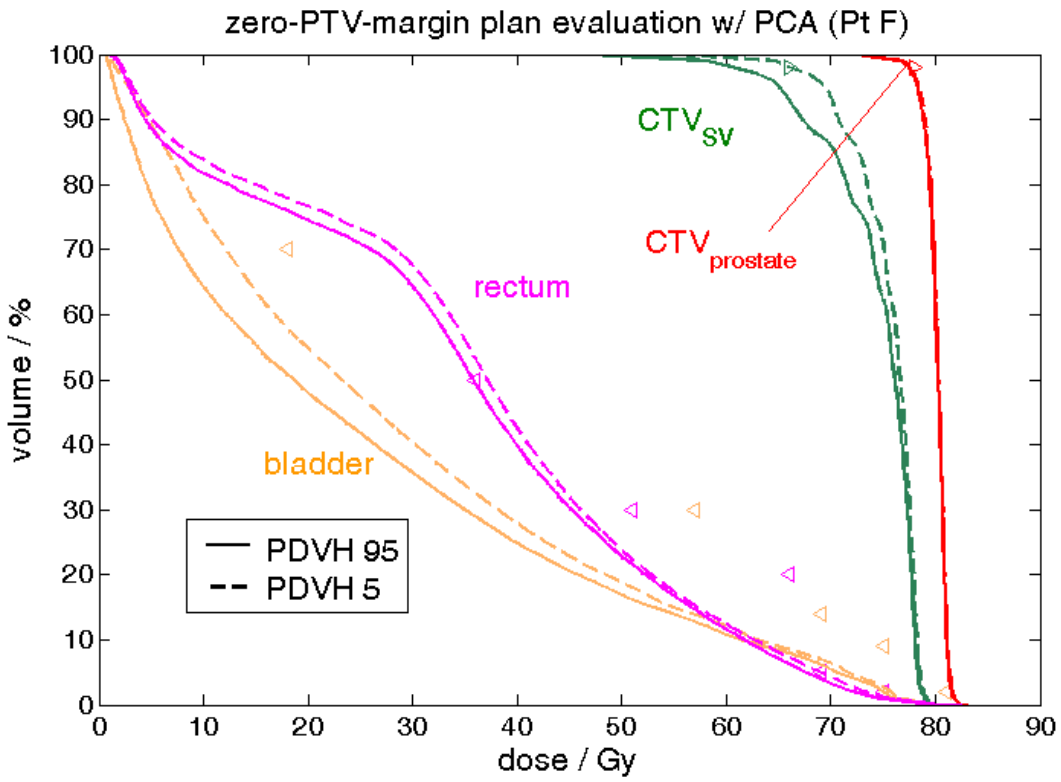

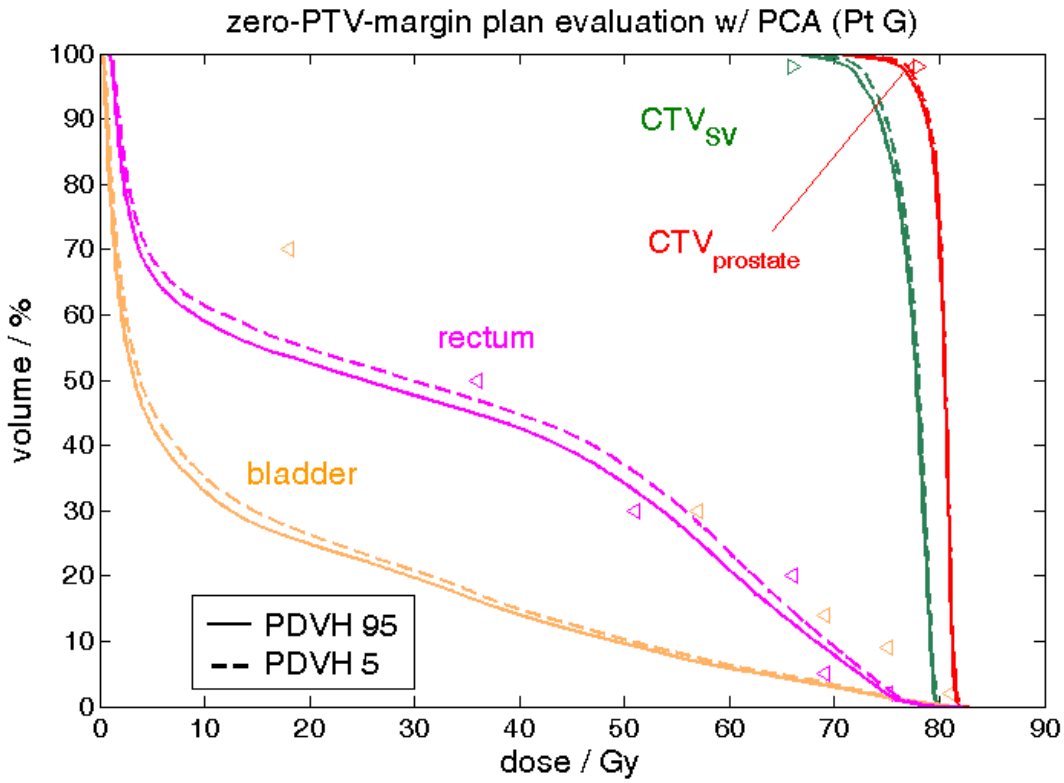

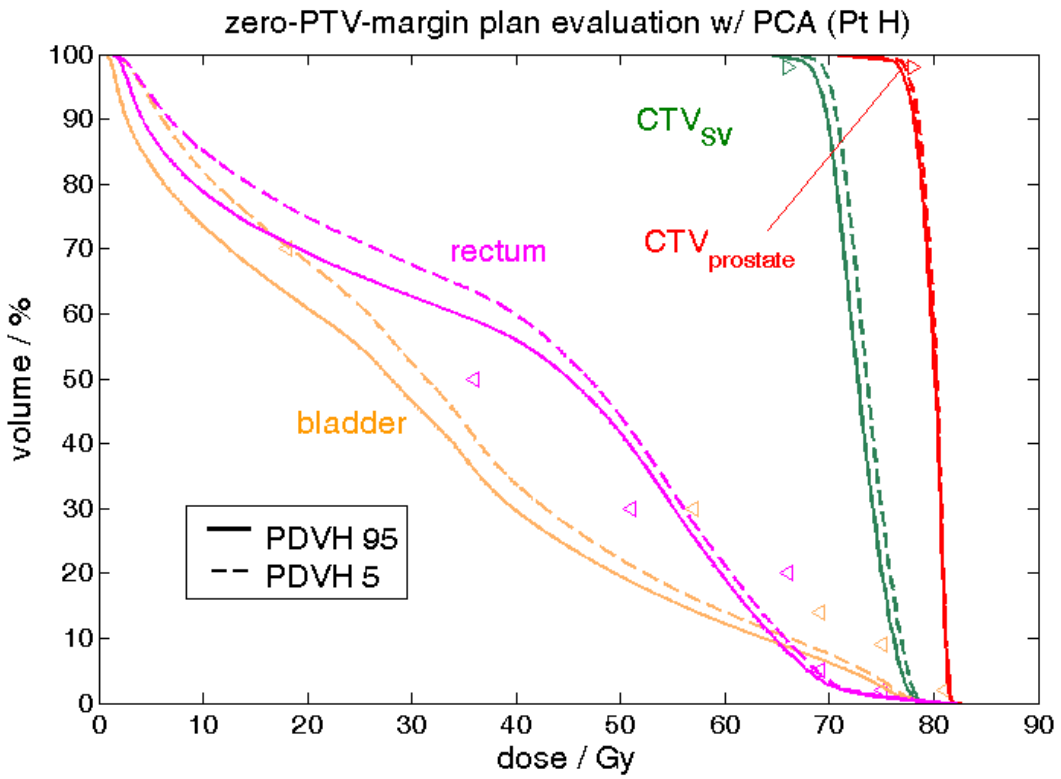

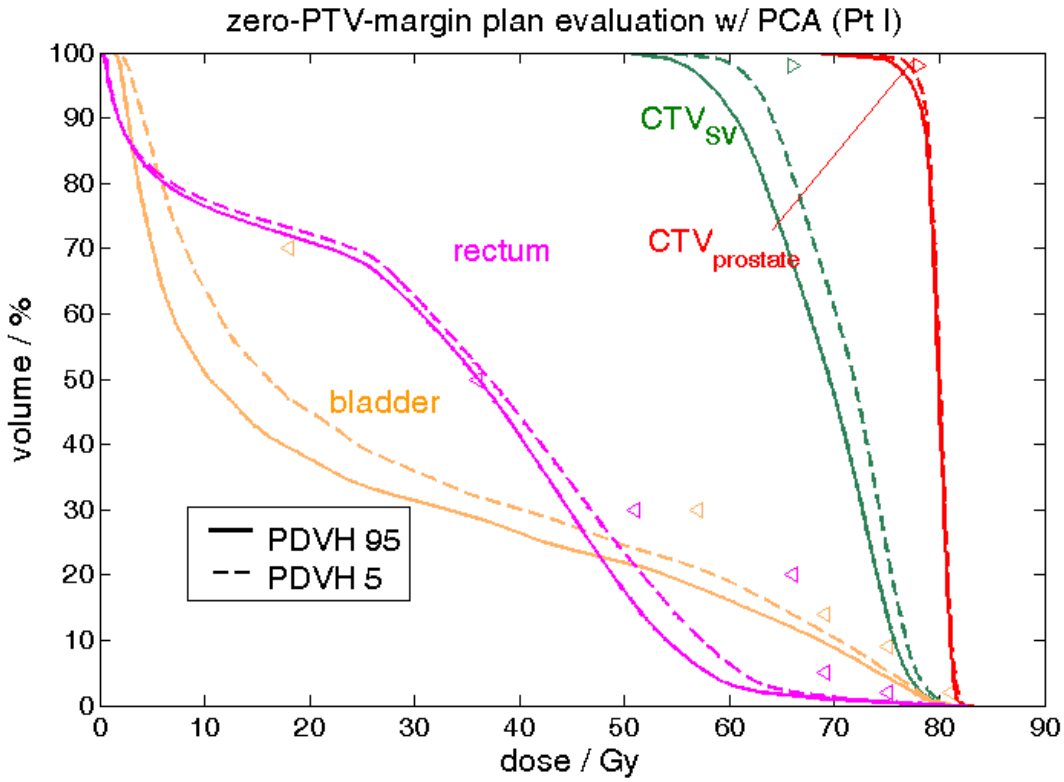

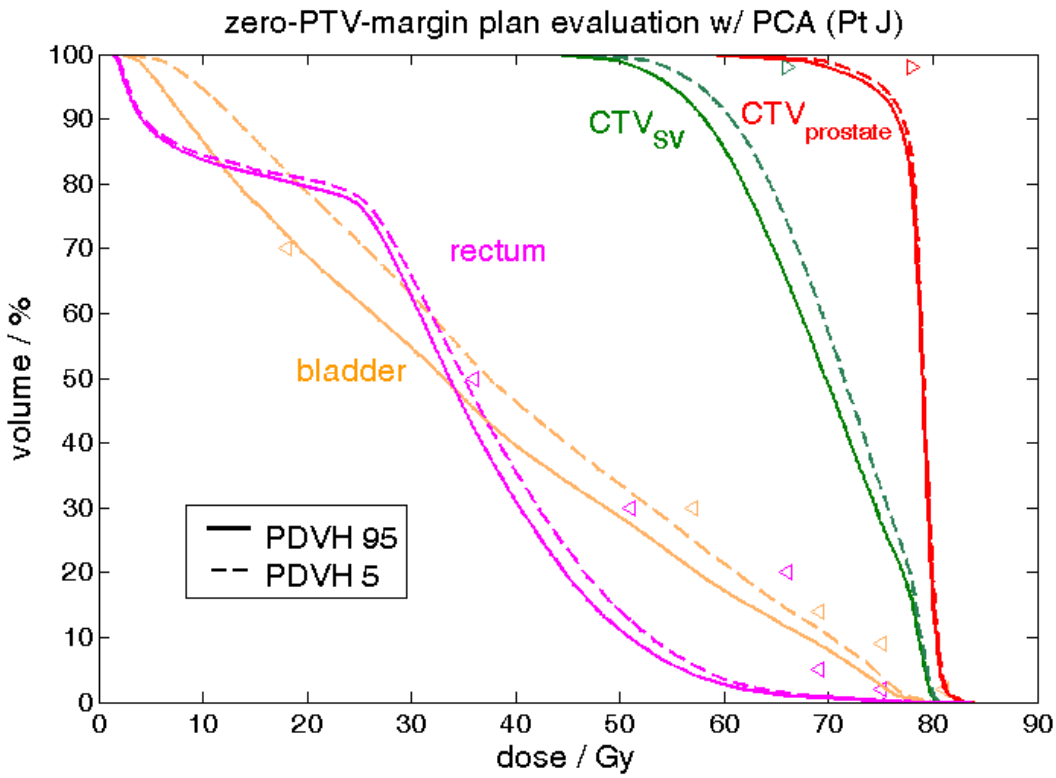

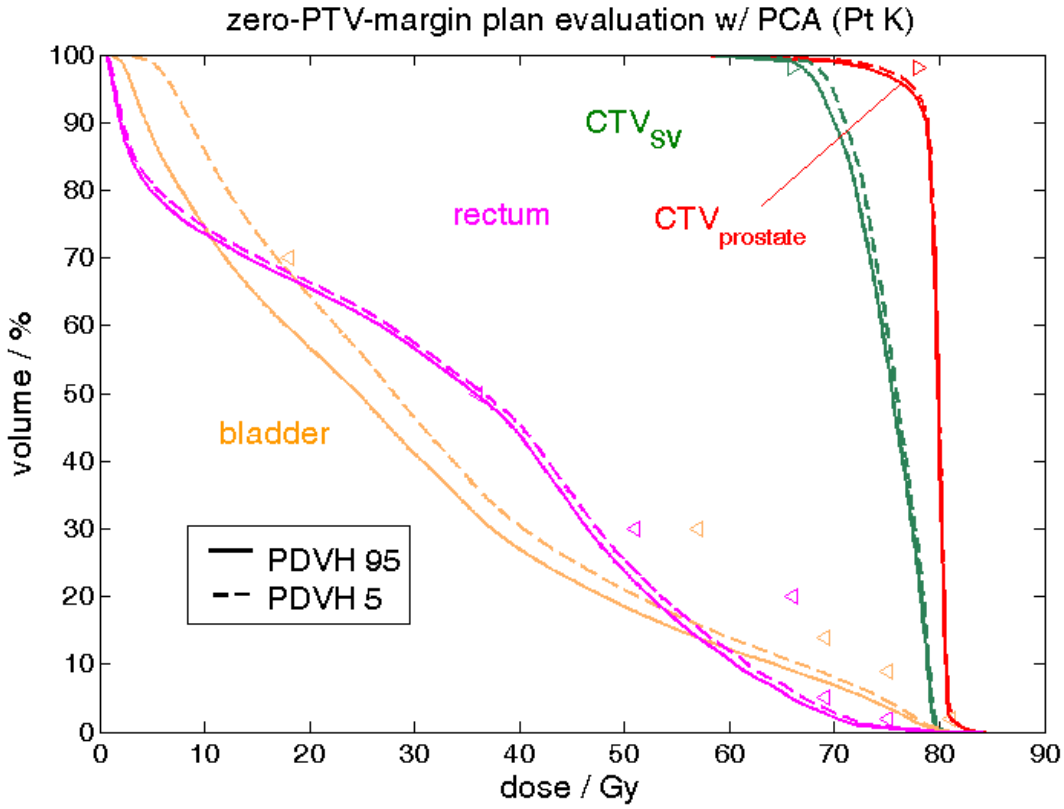

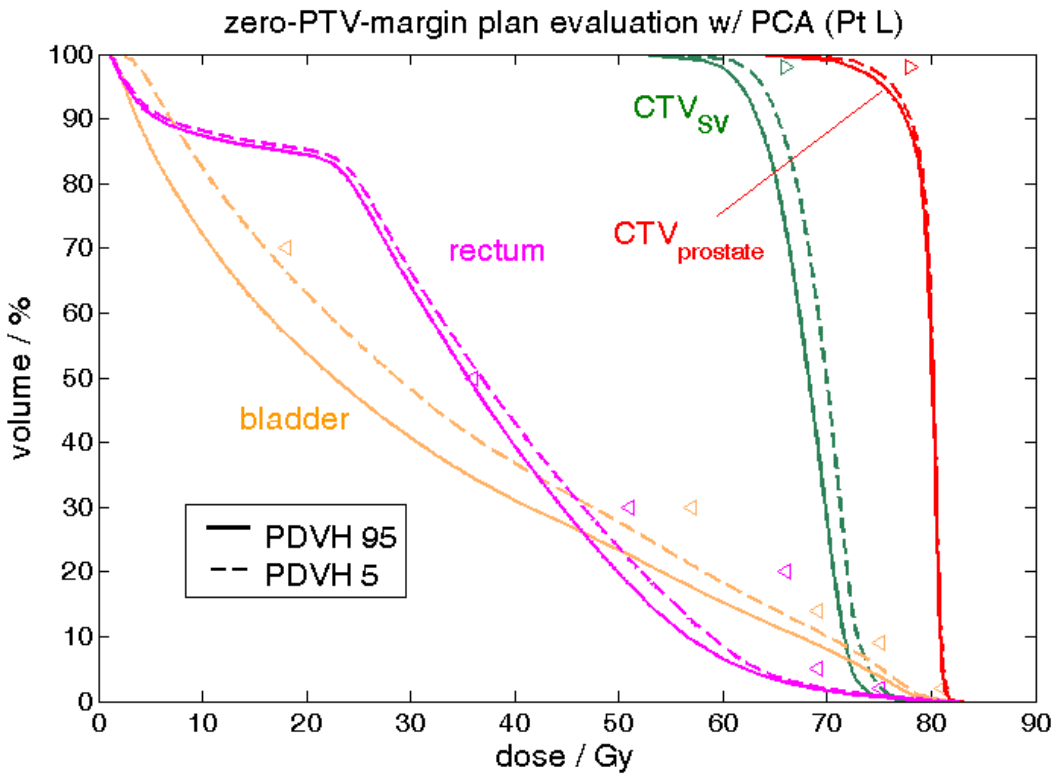

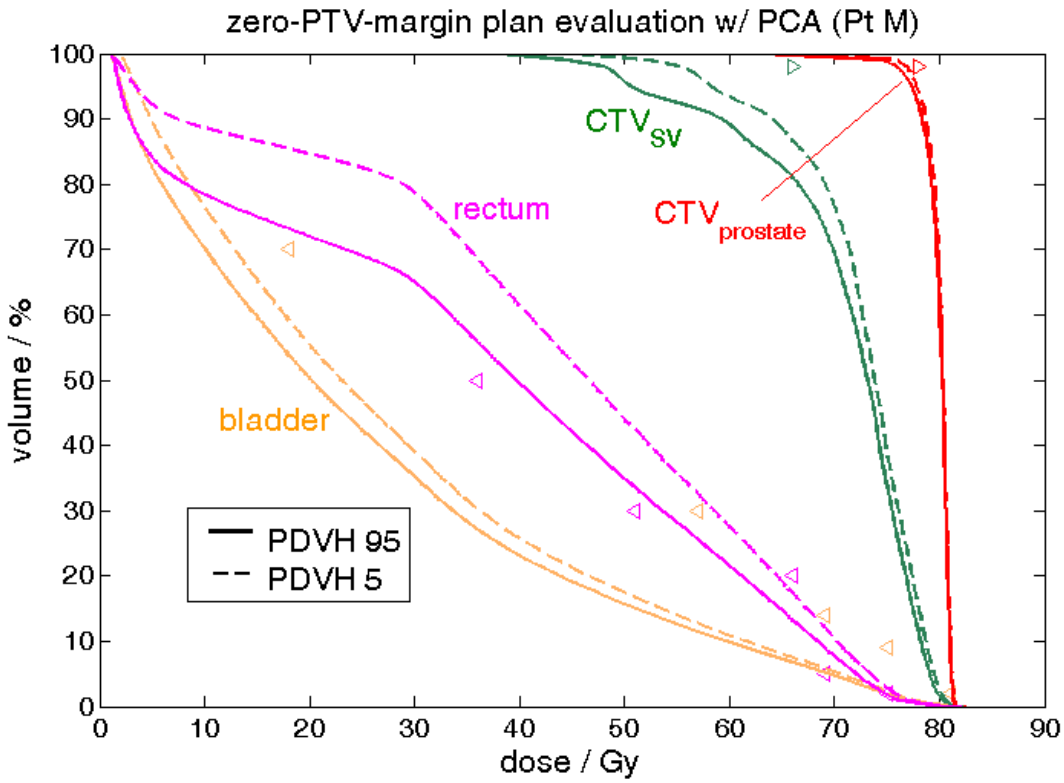

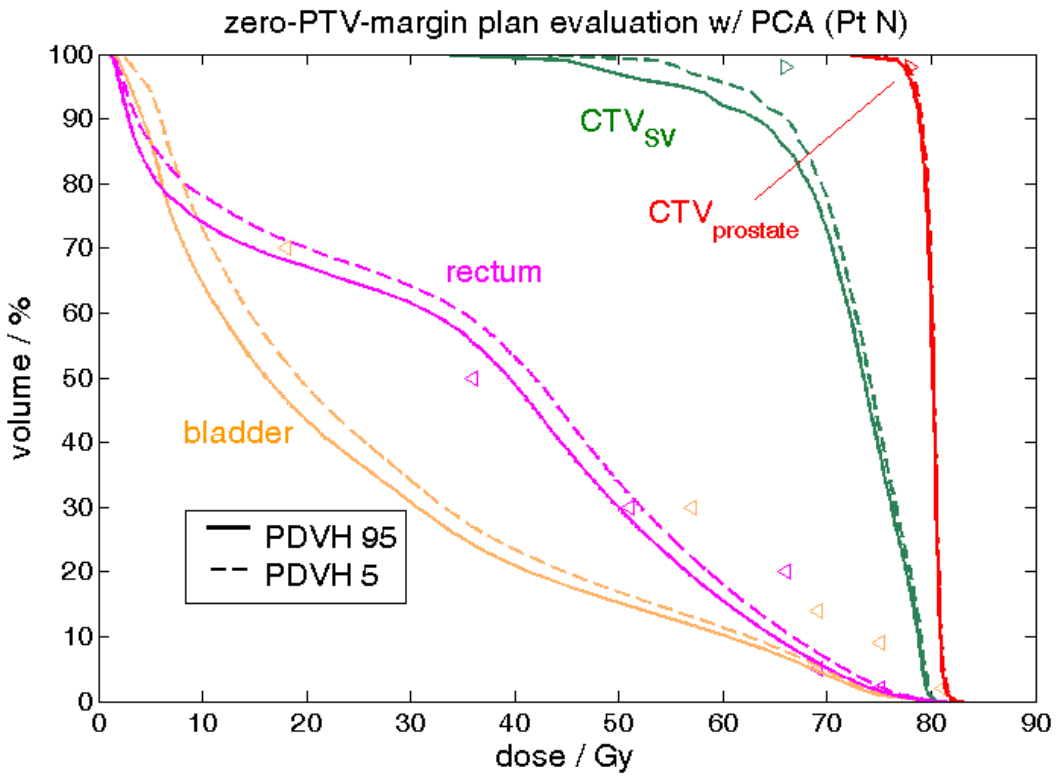

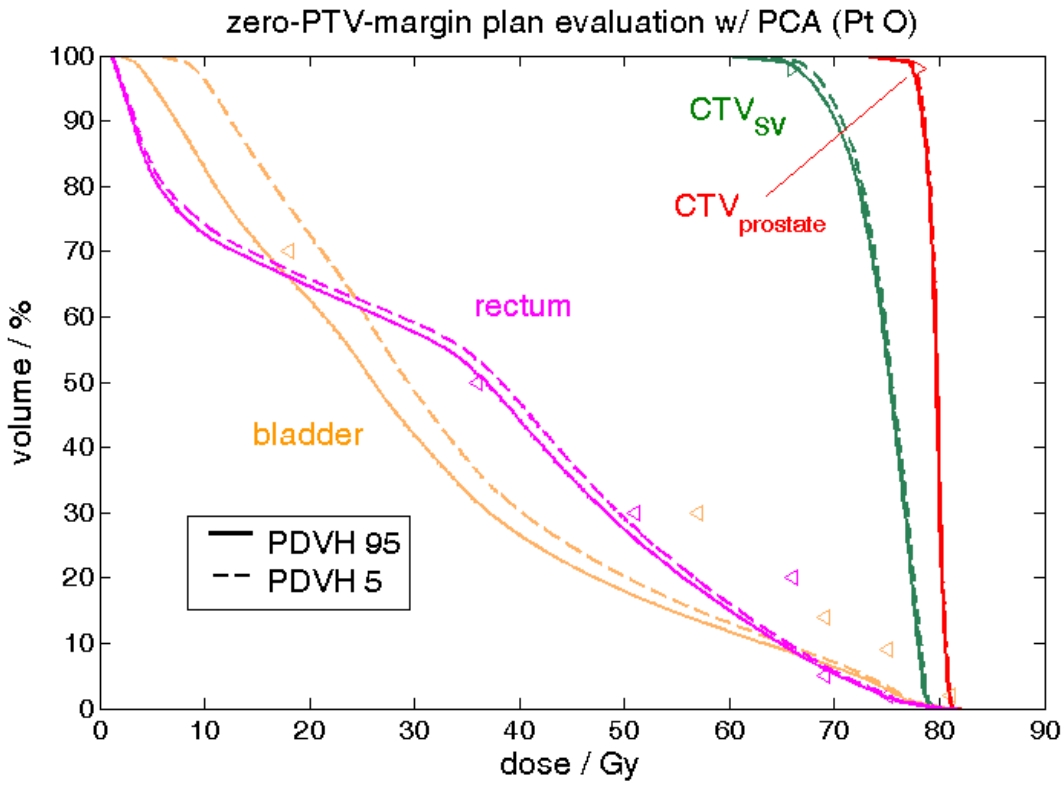

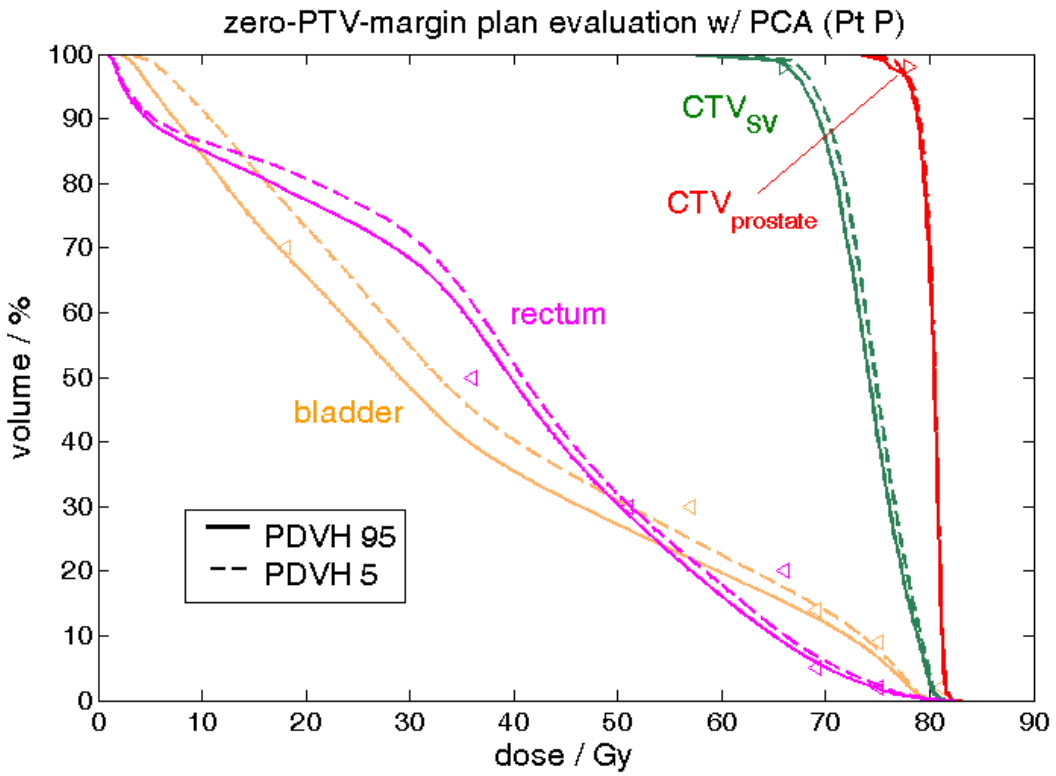

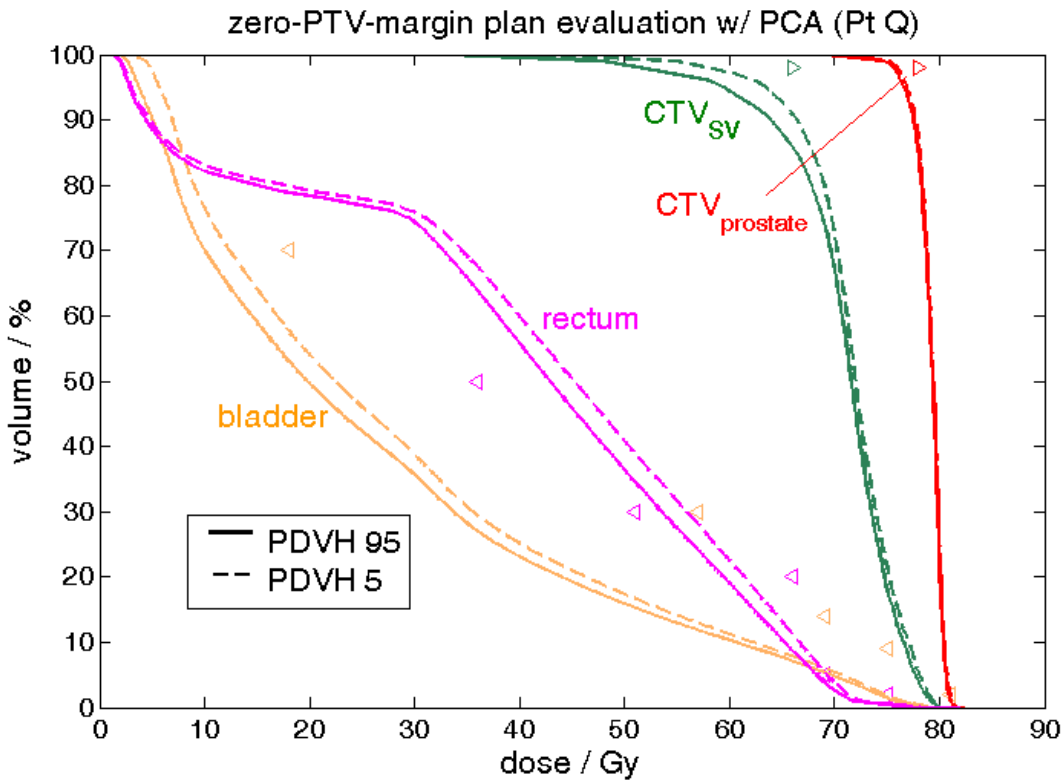

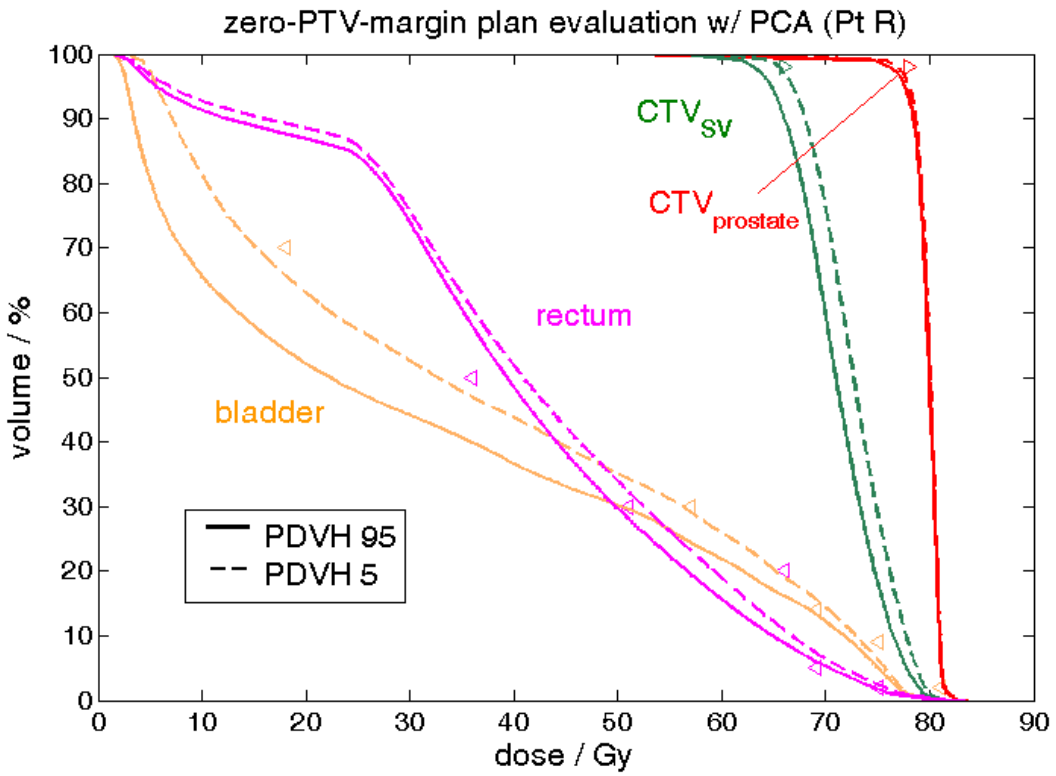

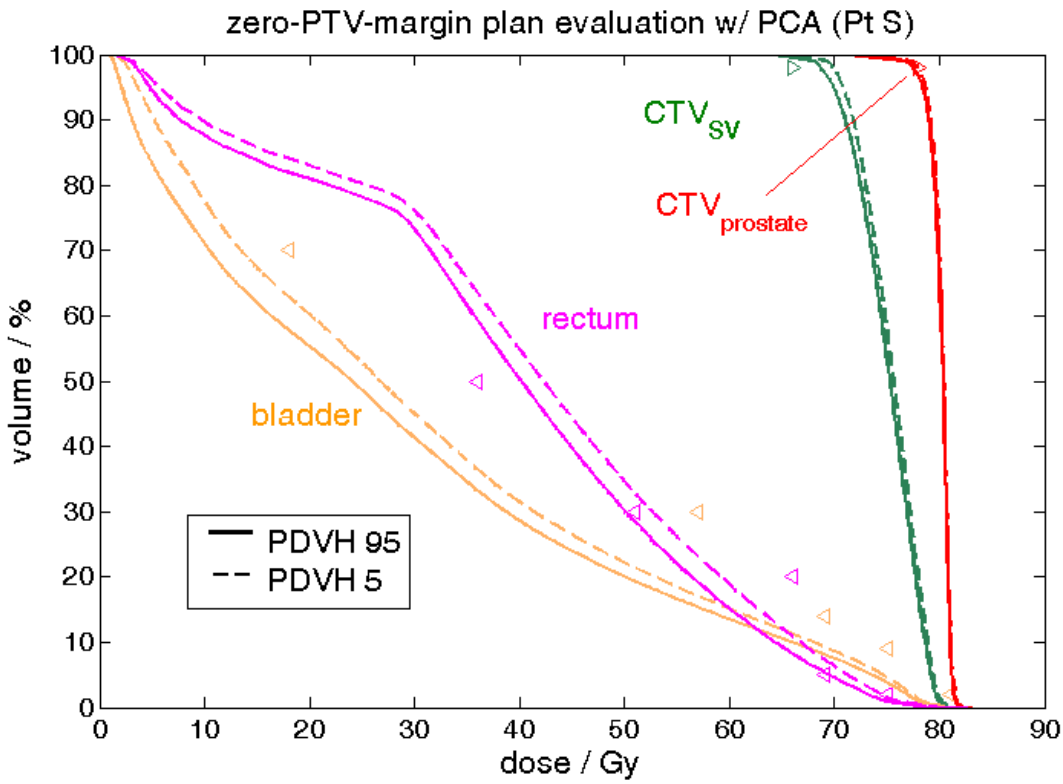

b. Optimized plan comparison with deformable motion model (PCA) incorporated

For each one of the 19 patients, pDVH 95% for $CTV_{prostate}$ and CTV_{SV}, and pDVH 5% for bladder and rectum on COP, OM and FM plans are plotted below. The benefit of COP relative to the other two margin-based planning techniques when accommodating organ deformable motions is patient-specific. For the patient cases (G, J, K, L, P, R, S) whose COP plan is preferred, some show the improved target coverage and the others get more decent OAR sparing. The best case for COP pDVH is patient P, as both target coverage and OAR sparing get effectively improved. However, advantages brought from COP are more limited for the other patients. When the COP plan fails to meet the target coverage criteria due to the competing OAR coverage criteria, the OM plan is more likely to be preferred.

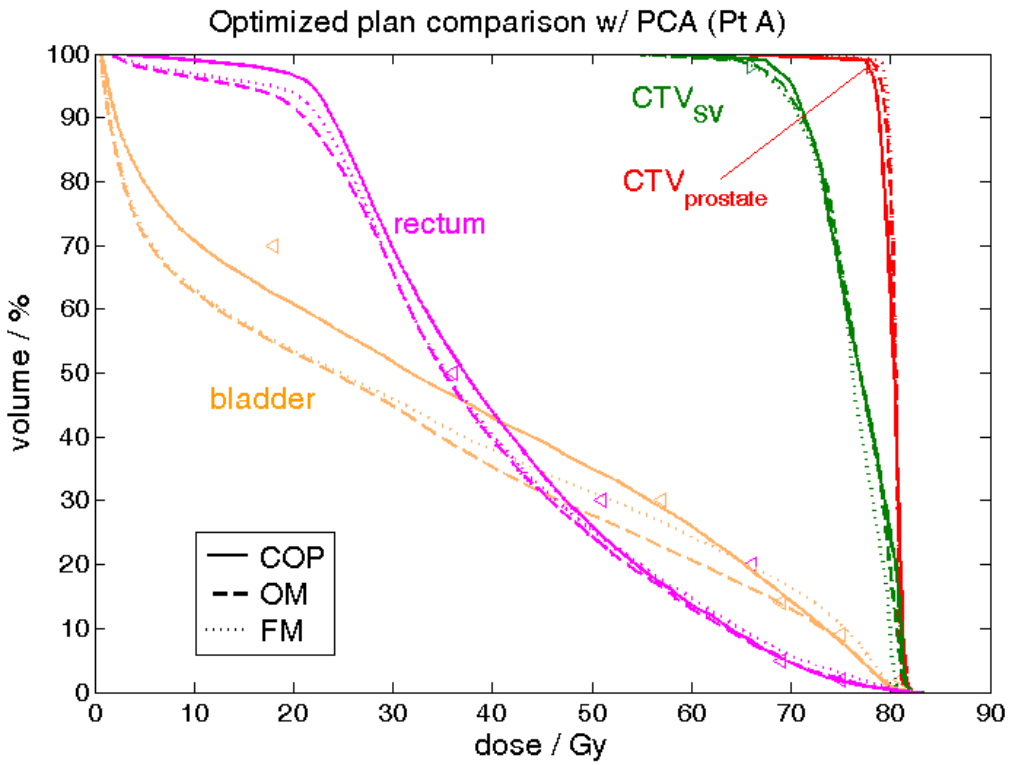

Figure 50. The pDVHs 95% of $CTV_{prostate}$ (red) and CTV_{SV} (green) and the pDVHs 5% bladder (orange) and rectum (magenta) for the patient-specific comparison of COP(solid), OM (dashed) and FM (dot) plans for the patient with ID A to S (continued below), with optimization objectives (triangle markers). The PCA model is incorporated to show the dosimetric consequence of organ deformable motions.

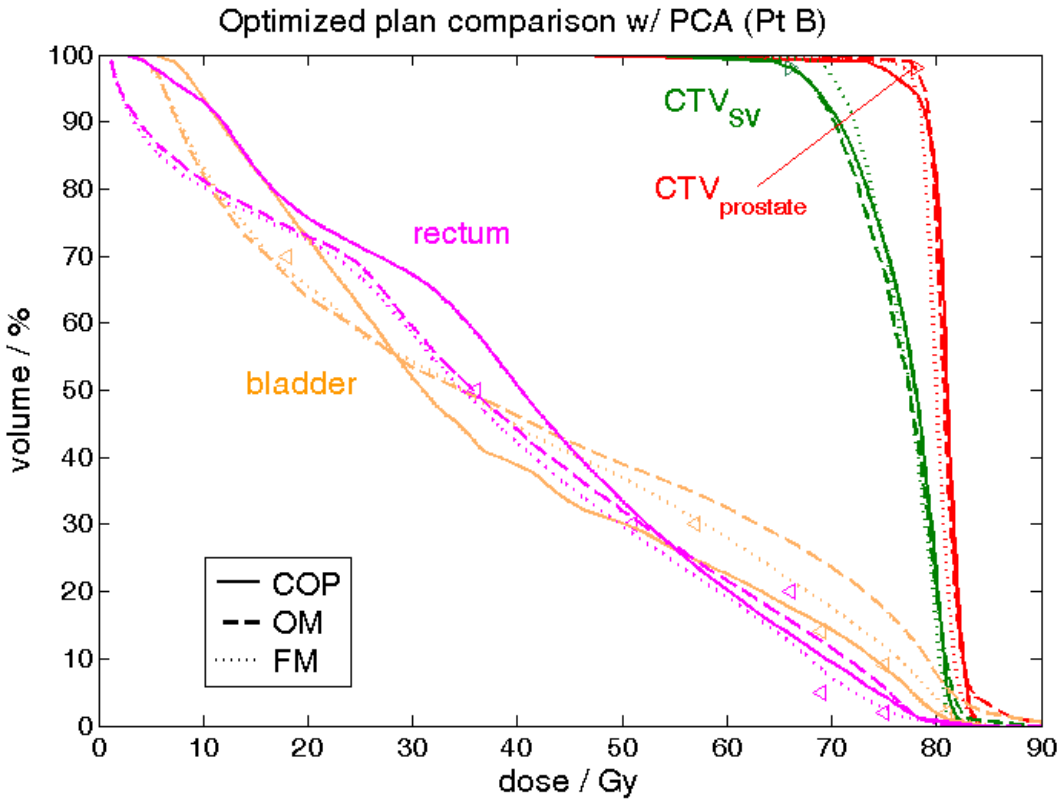

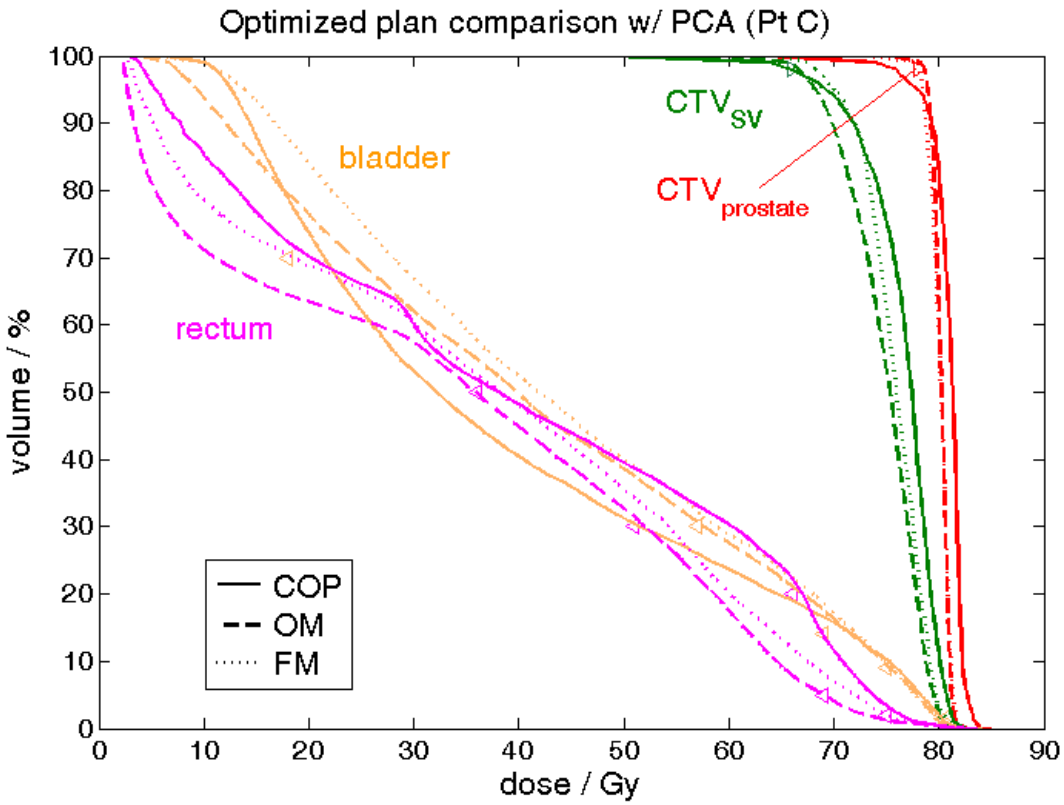

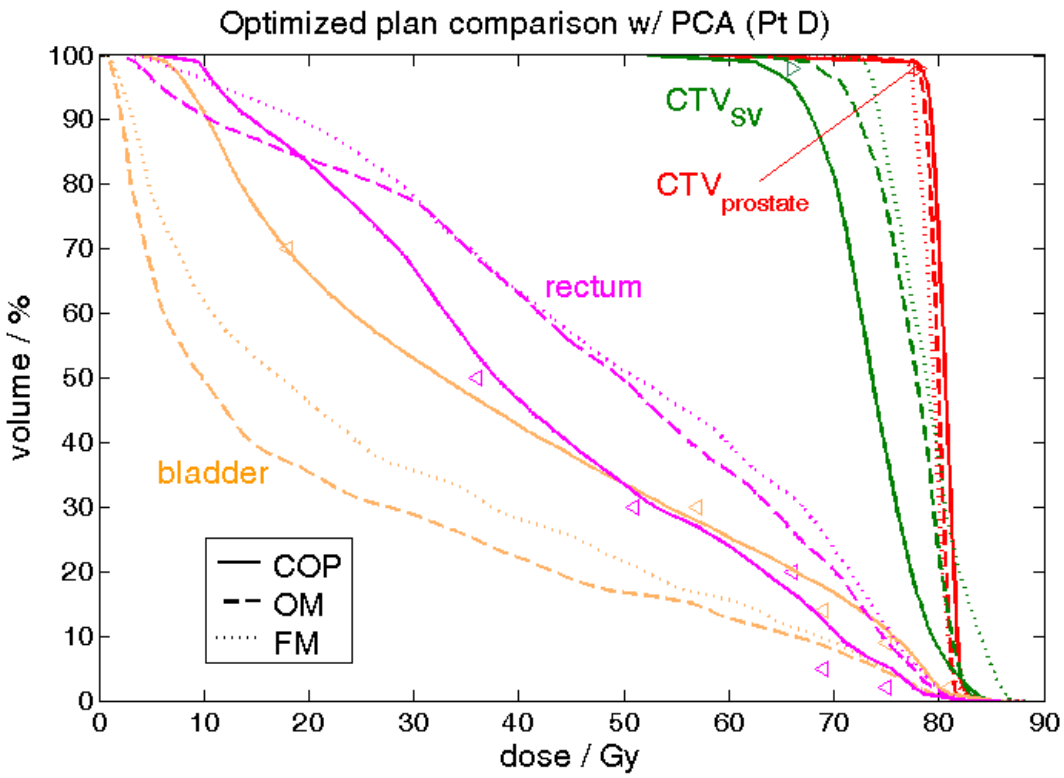

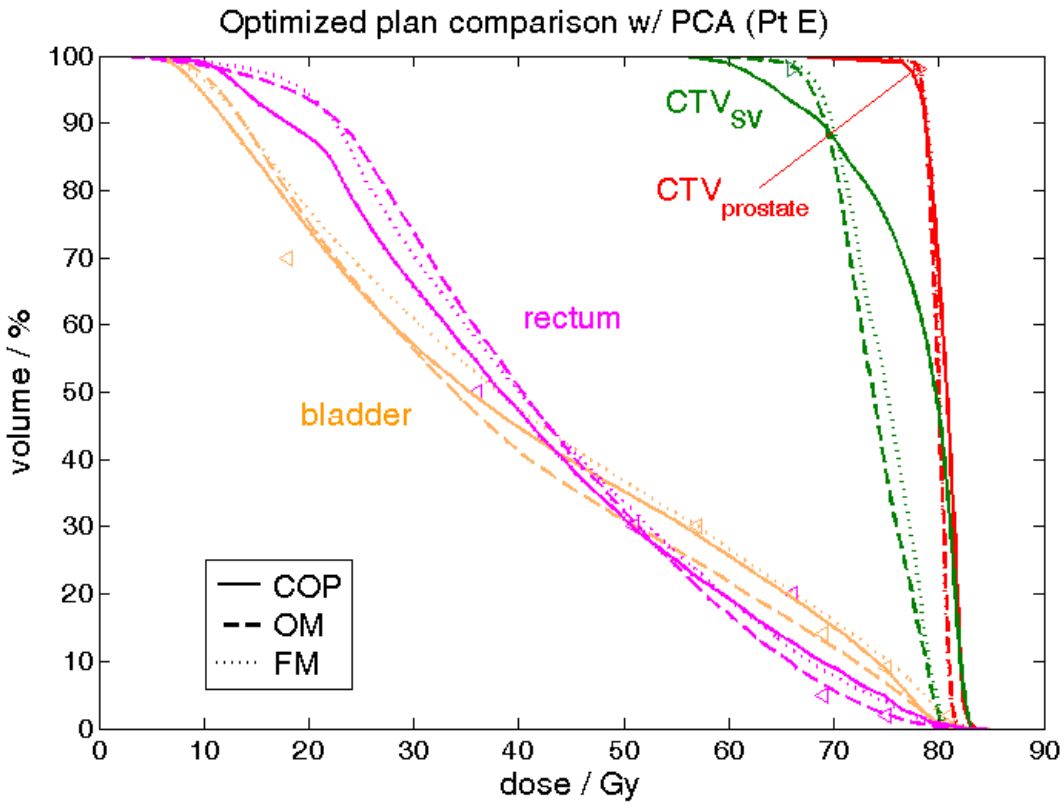

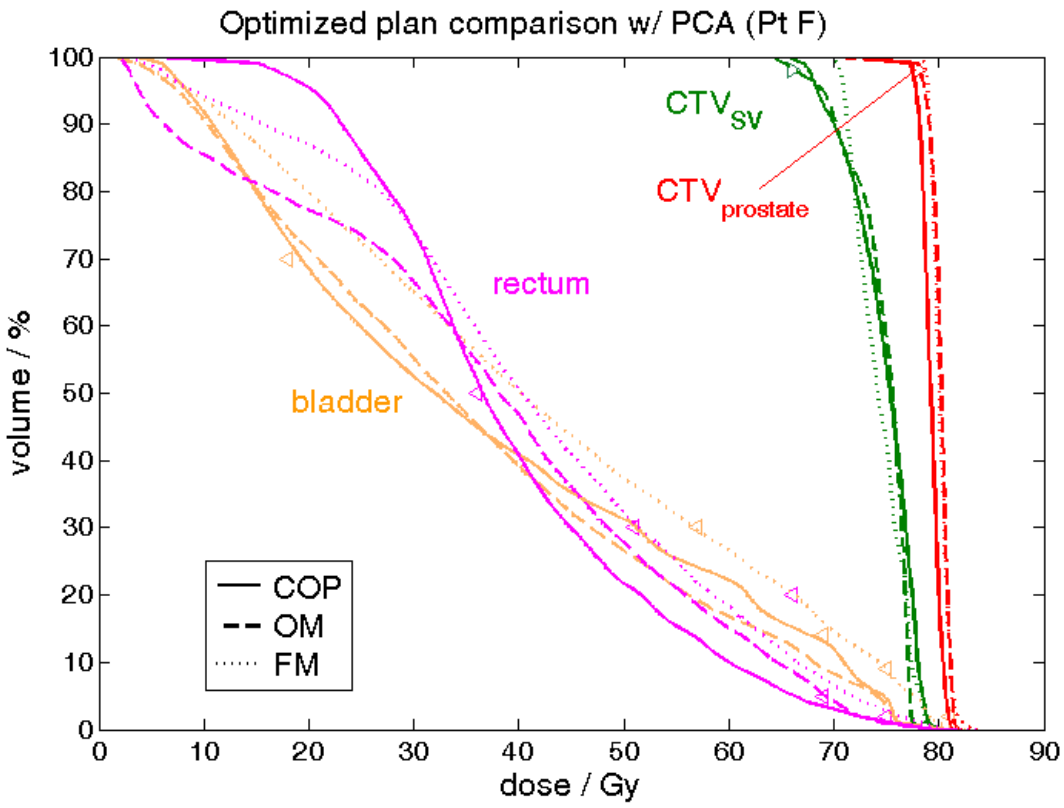

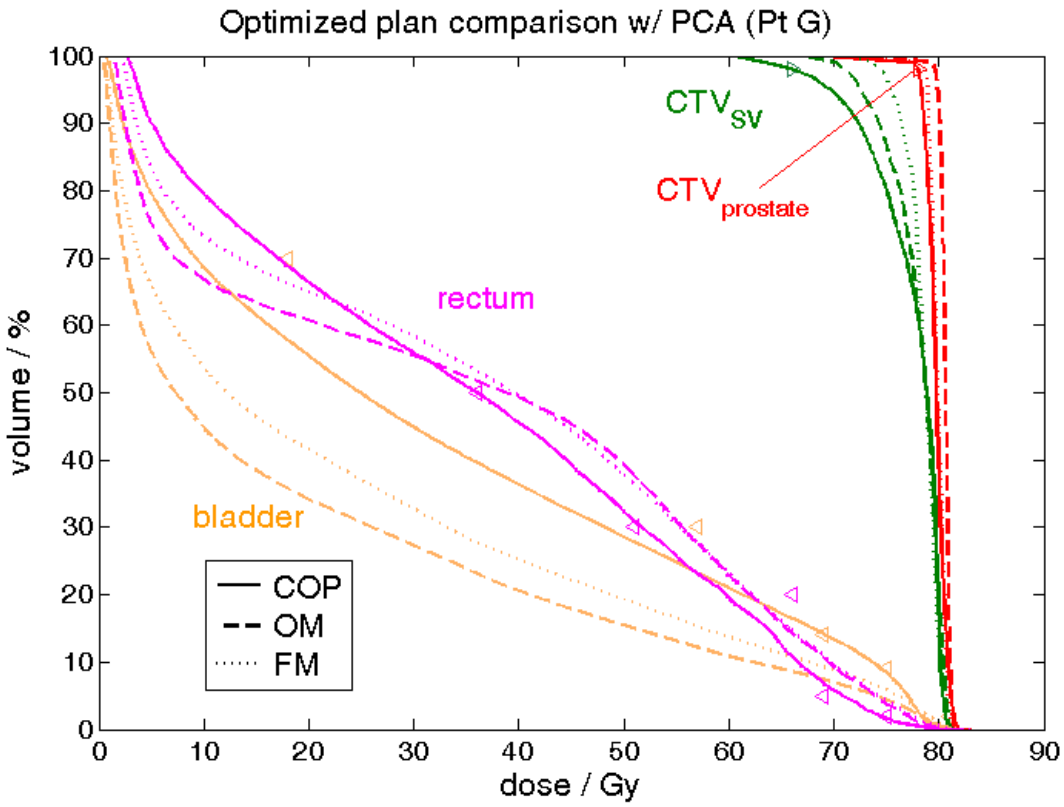

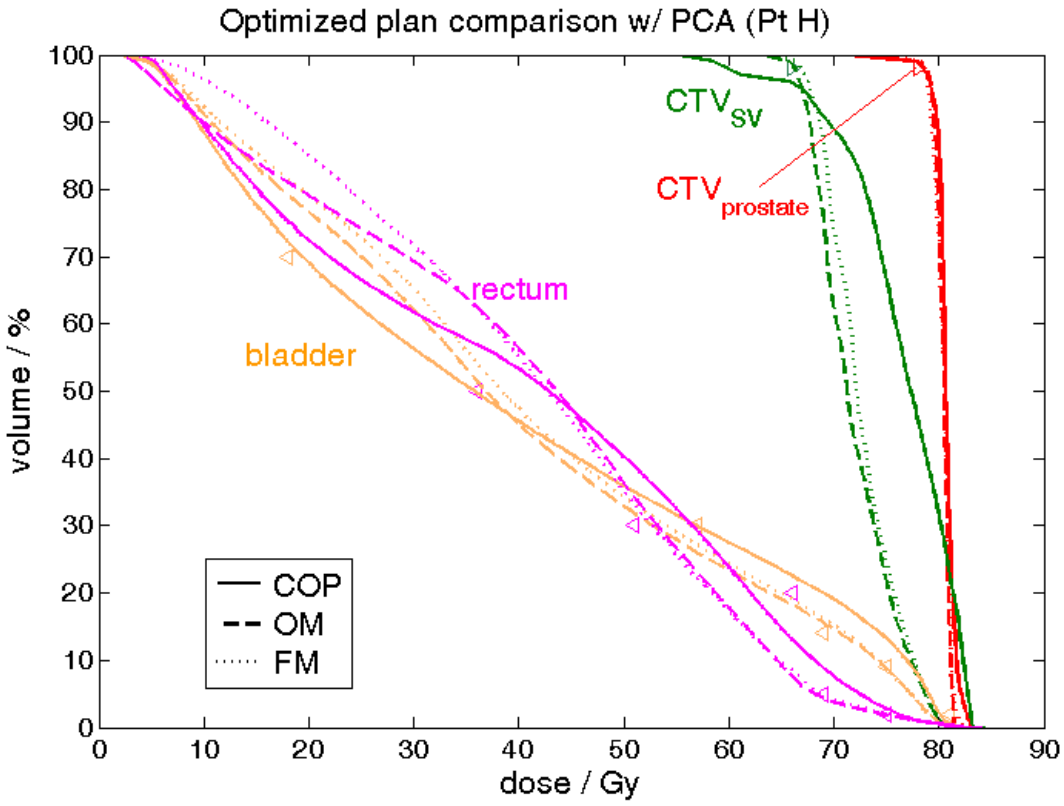

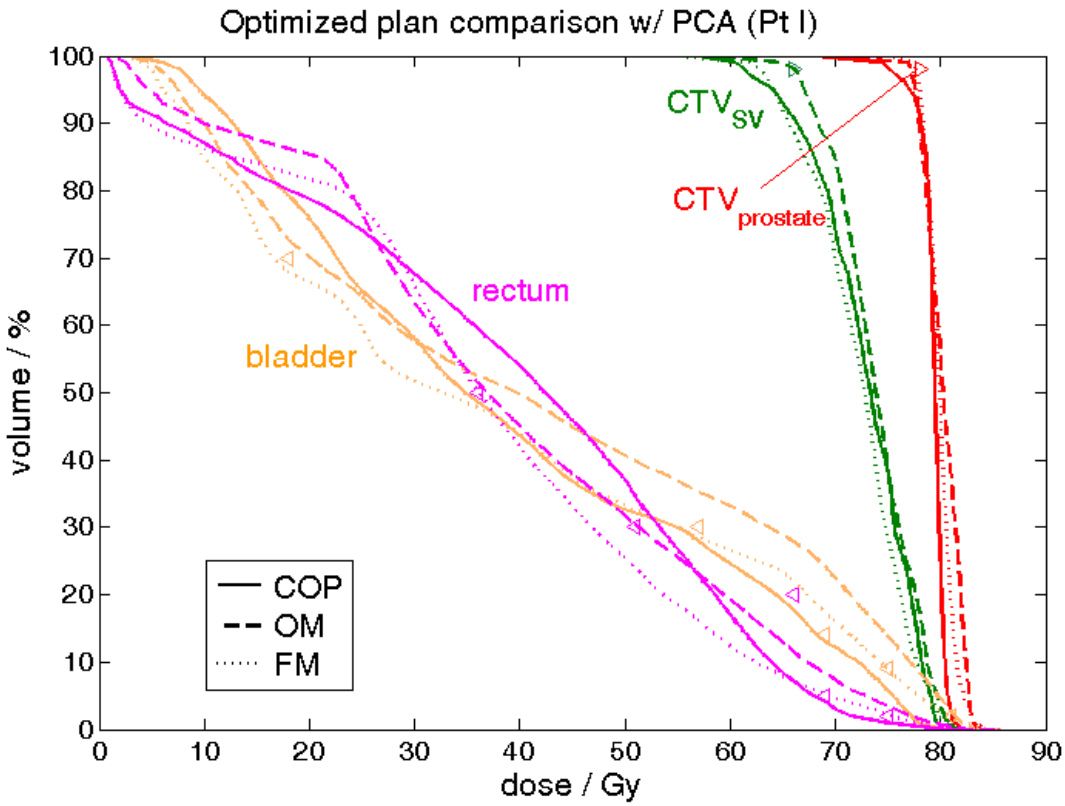

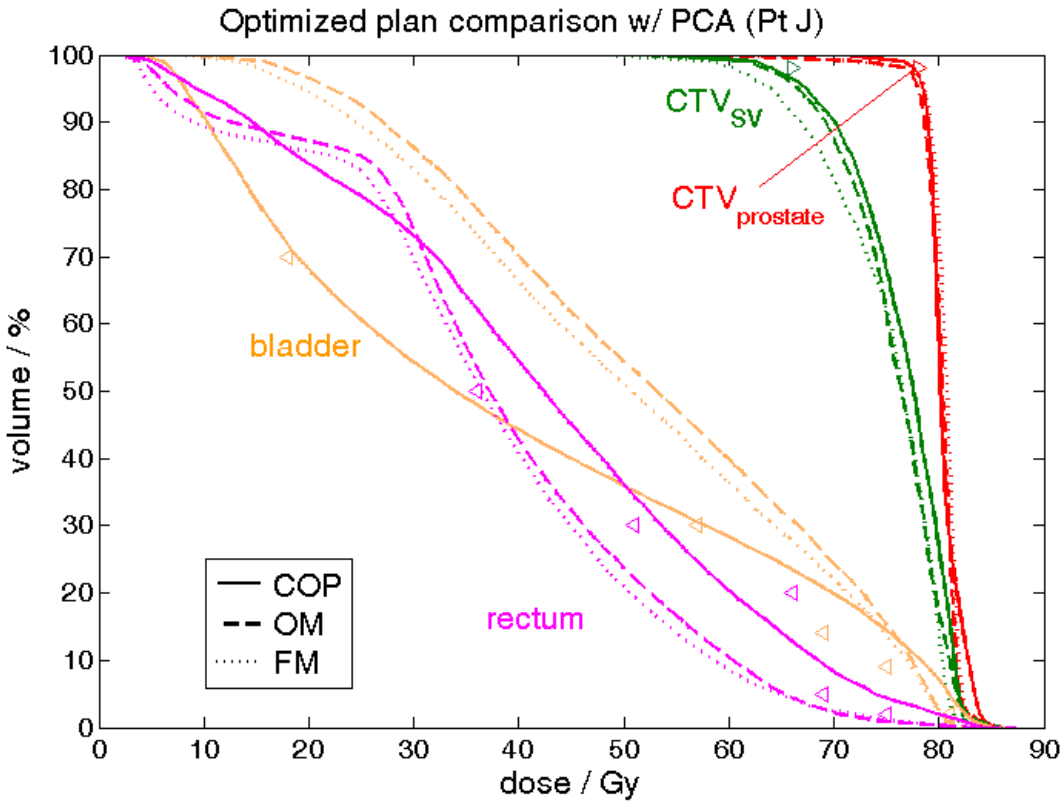

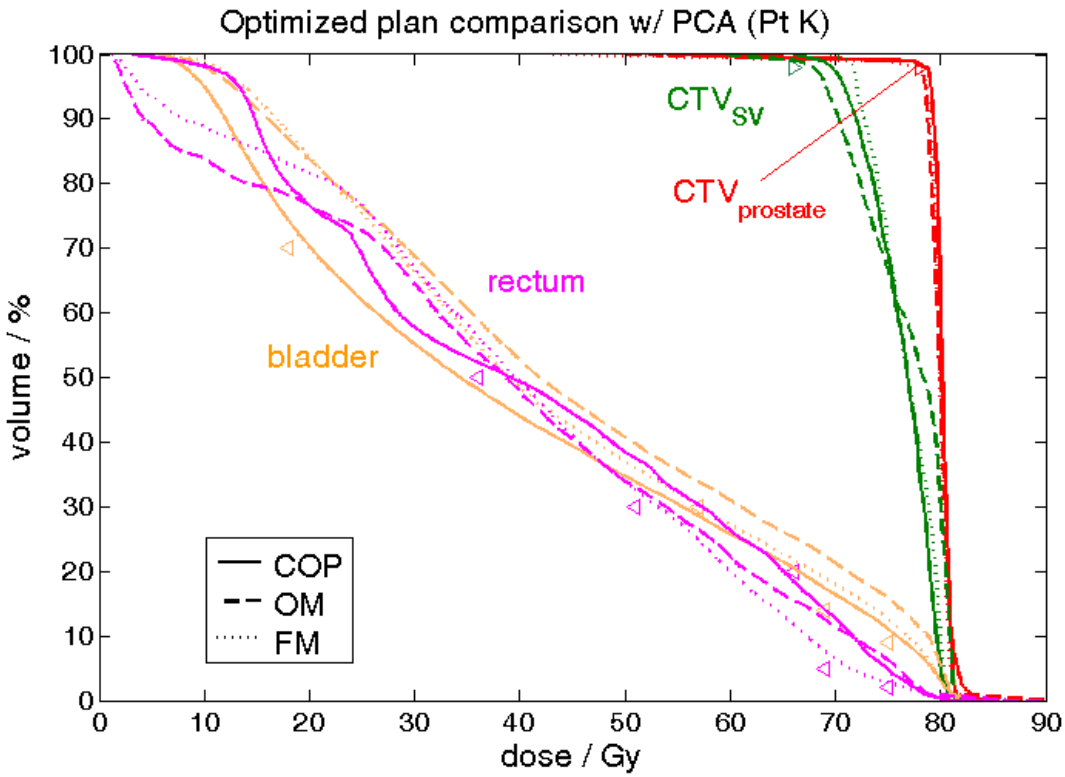

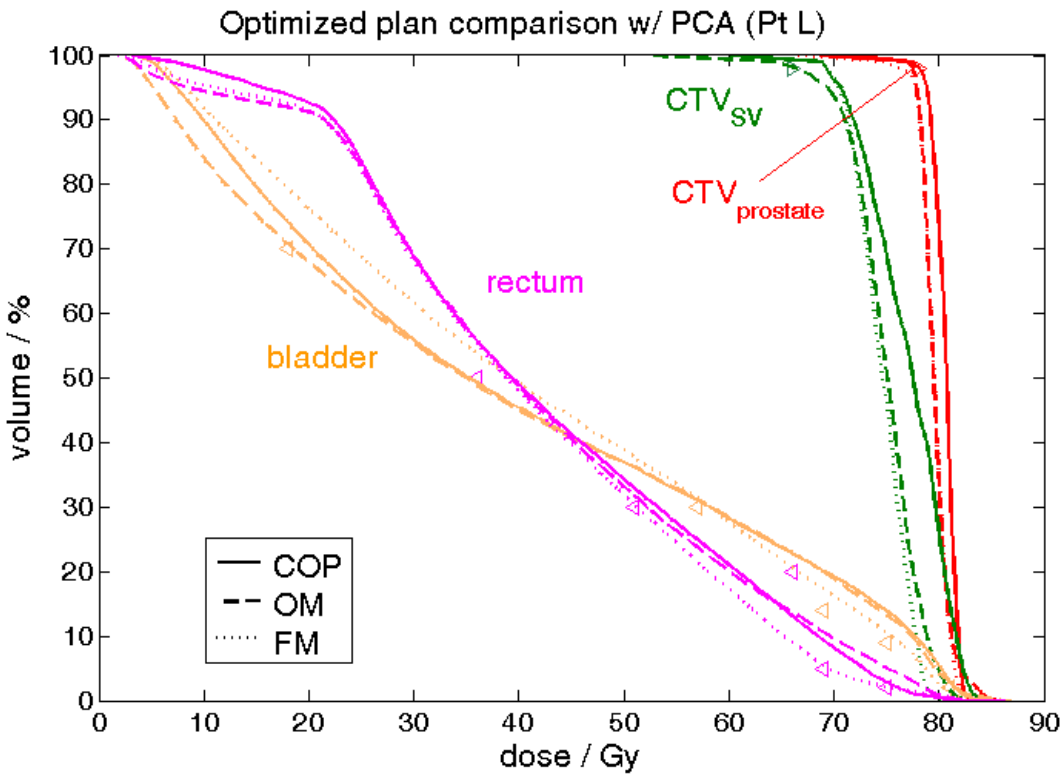

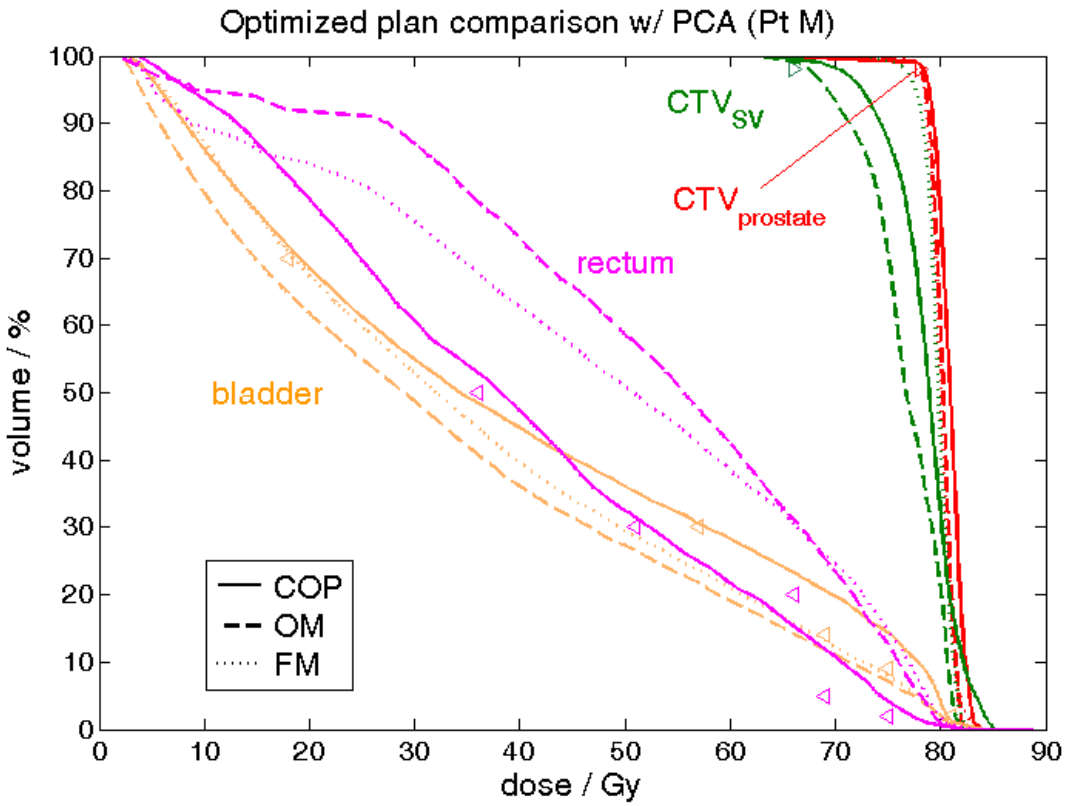

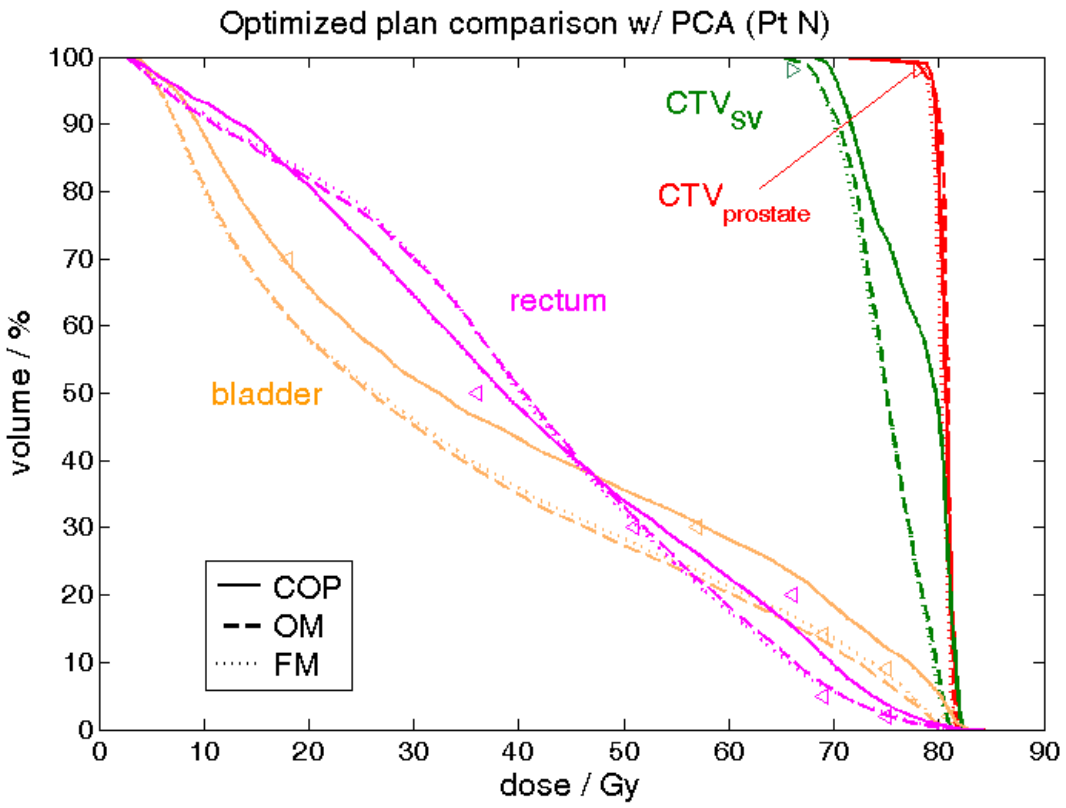

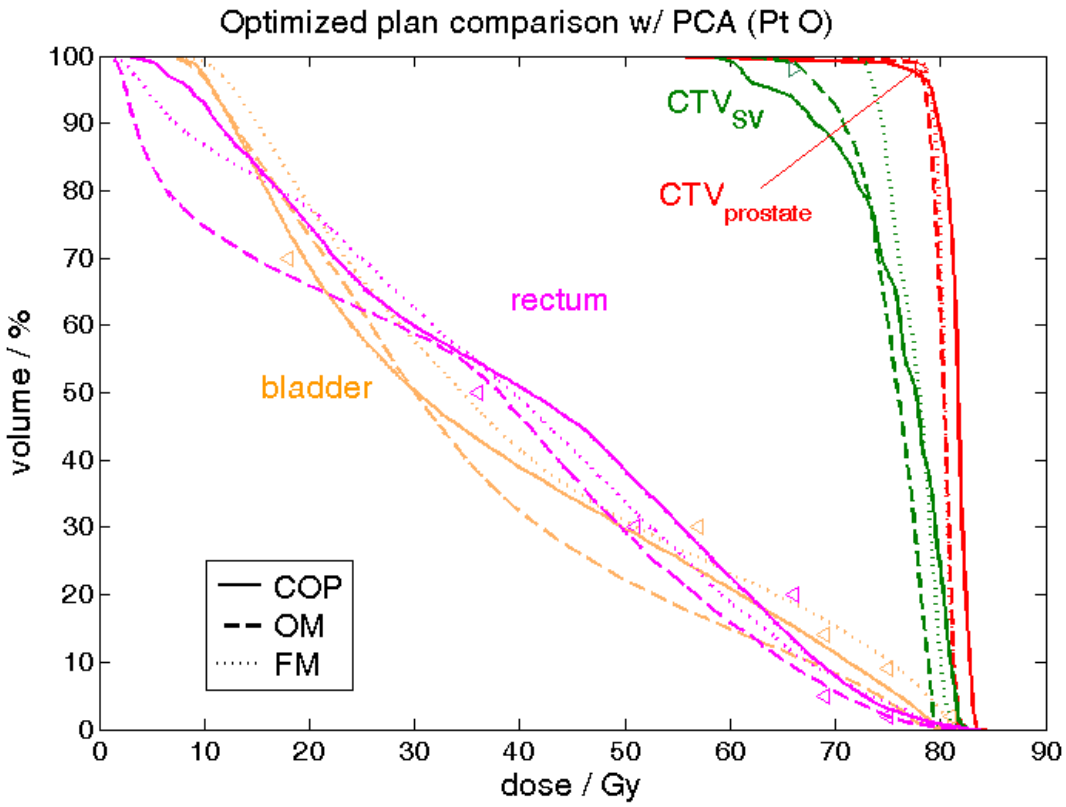

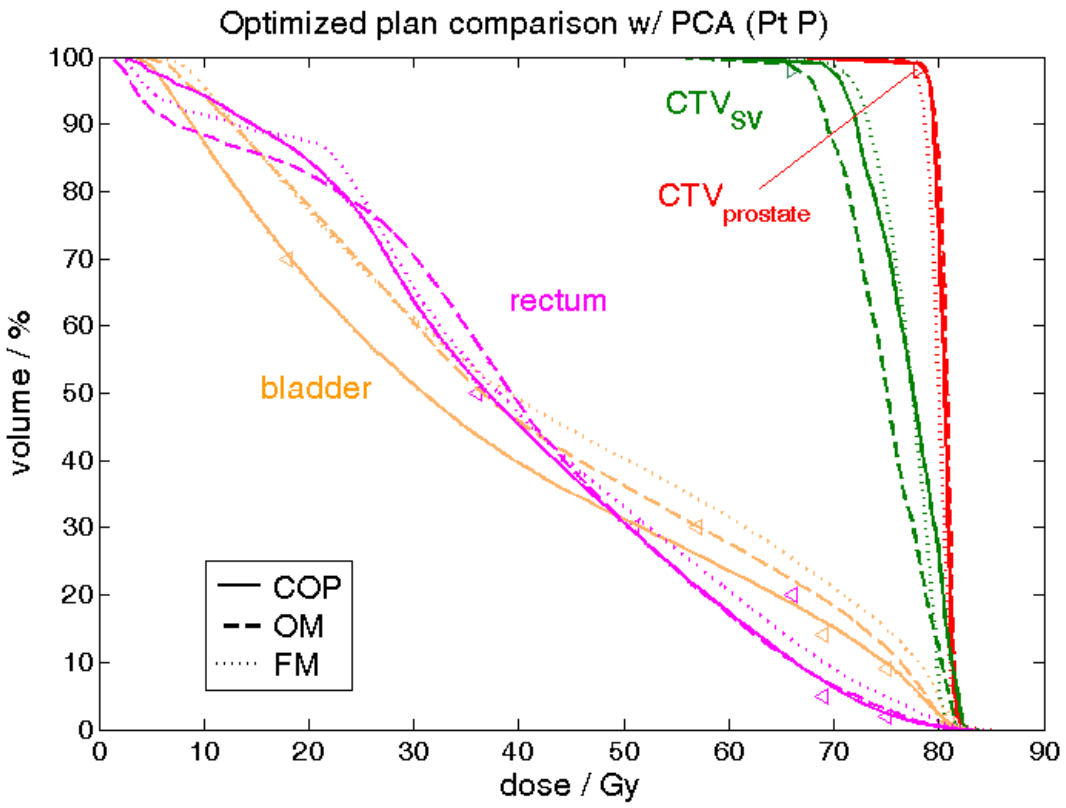

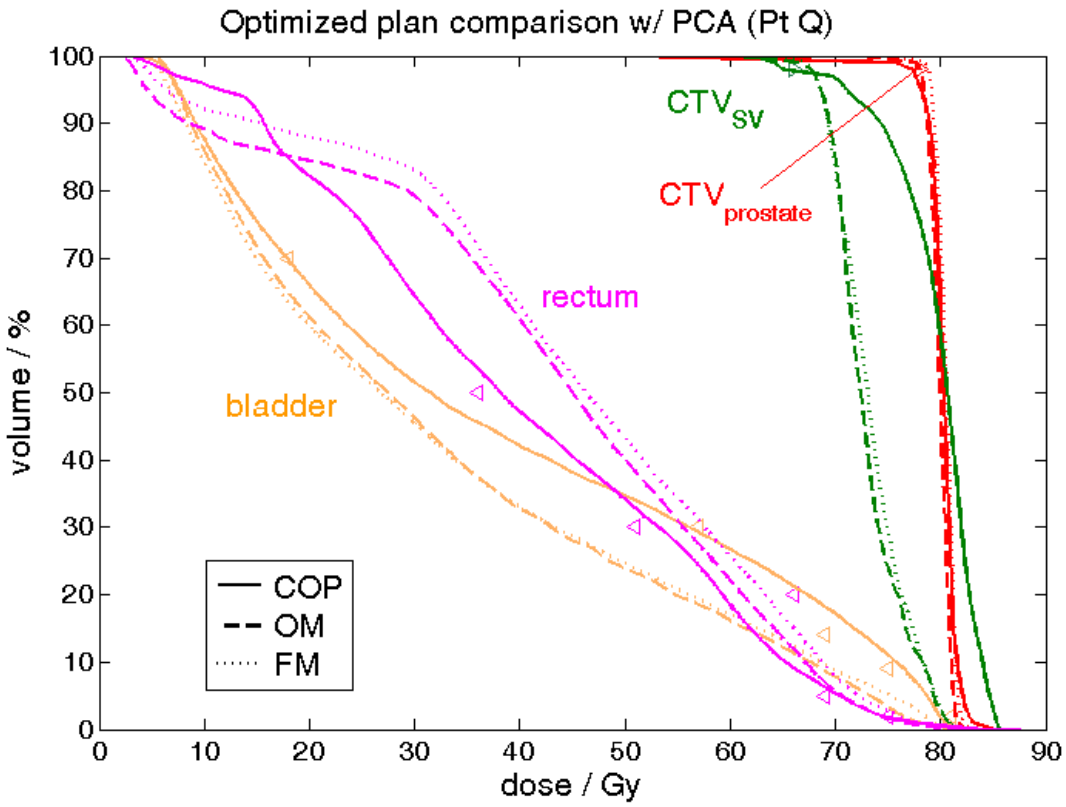

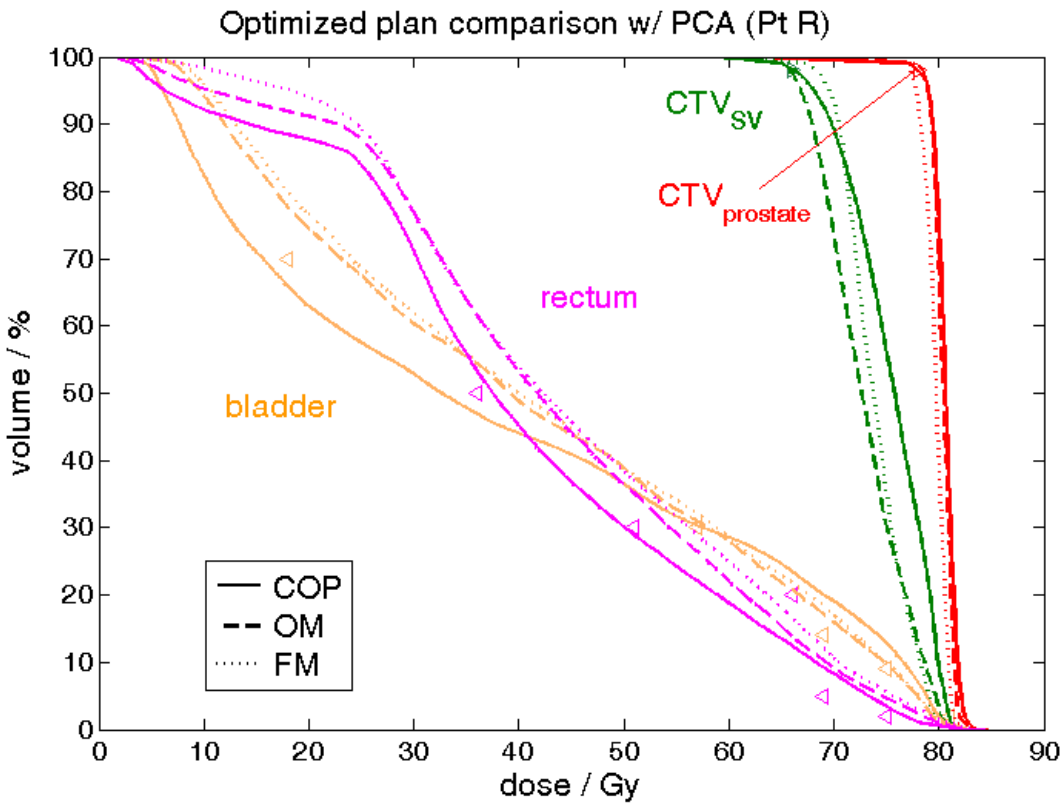

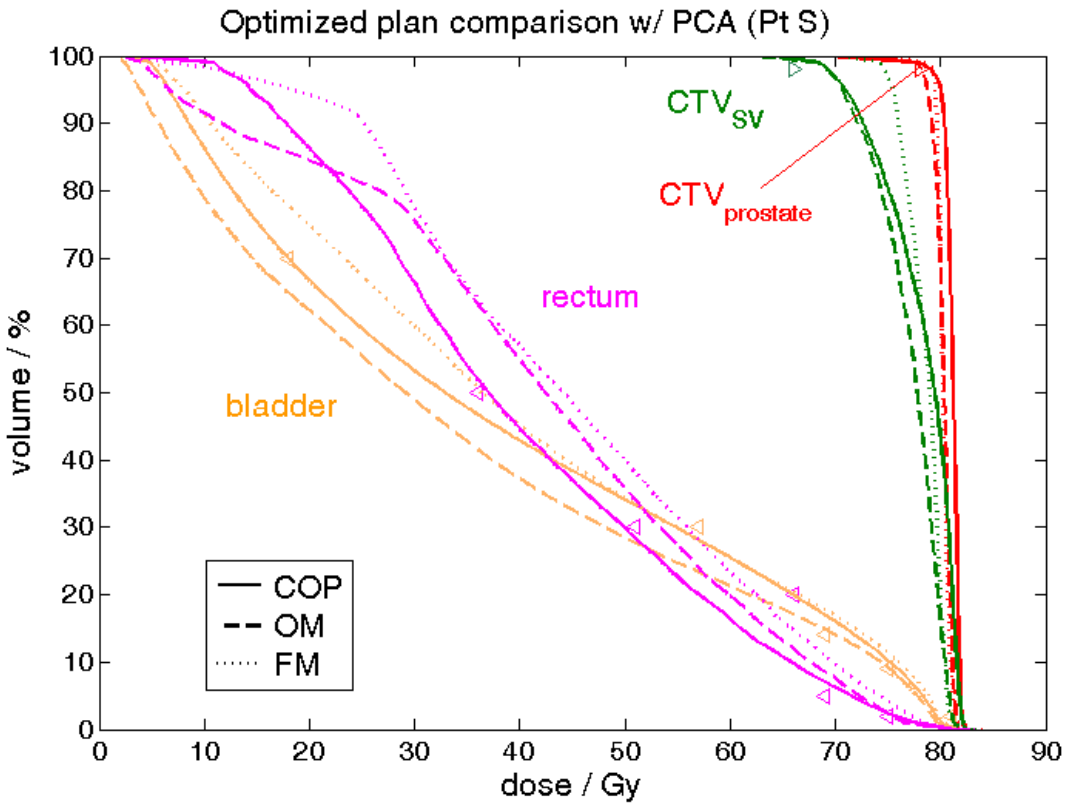

c. pDVH evaluation with delineation uncertainties model (ASSD) incorporated

For each one of the 19 patients, pDVH 95% and 5% for $CTV_{prostate}$, CTV_{SV}, bladder and rectum on a zero-PTV-margin plan are plotted below. The dosimetric effect of delineation uncertainties is patient-specific and non-negligible.

As the target dose at 95% coverage probability is more or less degraded from the objective values, larger PTV margin or DM is needed to improve the target coverage. For OARs, the rectum is more likely to be overdosed than the bladder. The rectal dose of each patient at 5% coverage probability exceeds at least one dose limits before margin is used, which shows the potential conflict of rectal sparing and target coverage improvement. In contrast, the bladder dose at 5% coverage probability is mostly within the dose tolerance for most patients, except patient B, I, L, N, R. The slack between the current bladder dose and the corresponding bladder dose limits, which is large for most patients, provides room for margin expansion.

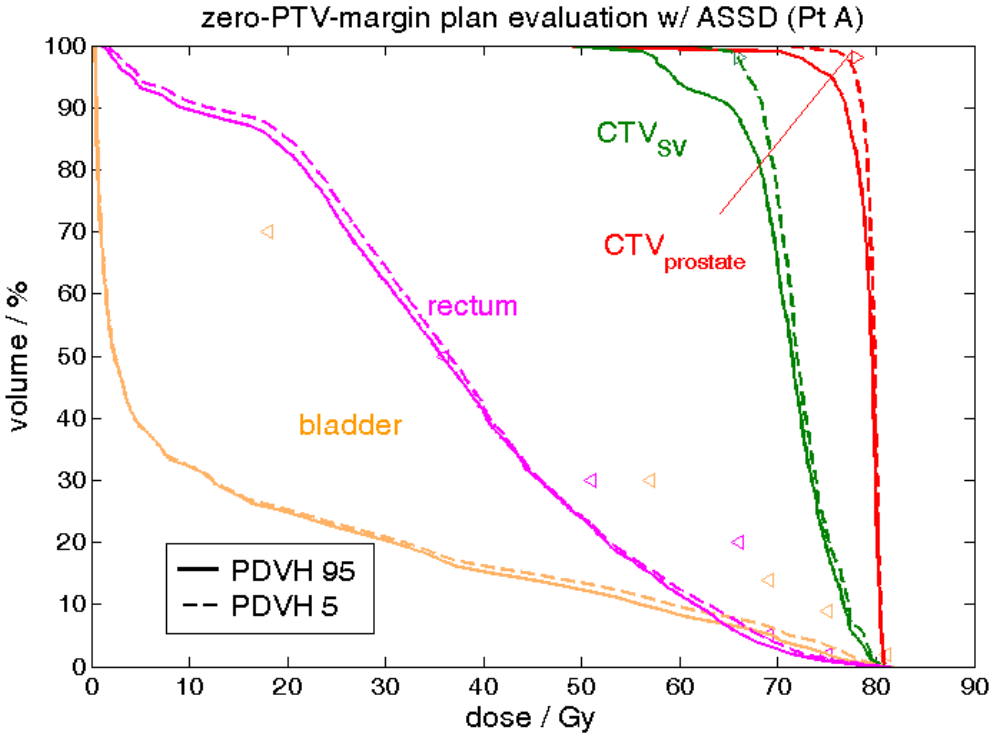

Figure 51. The patient-specific pDVHs 95% (solid) and pDVHs 5% (dashed) evaluated on zero-PTV-margin plans for patient with ID A to S(continued below) for anatomies $CTV_{prostate}$ (red), CTV_{SV} (green), bladder (orange) and rectum (magenta) with optimization objectives (triangle markers). The PCA model is incorporated to show the dosimetric consequence of organ deformable motions.

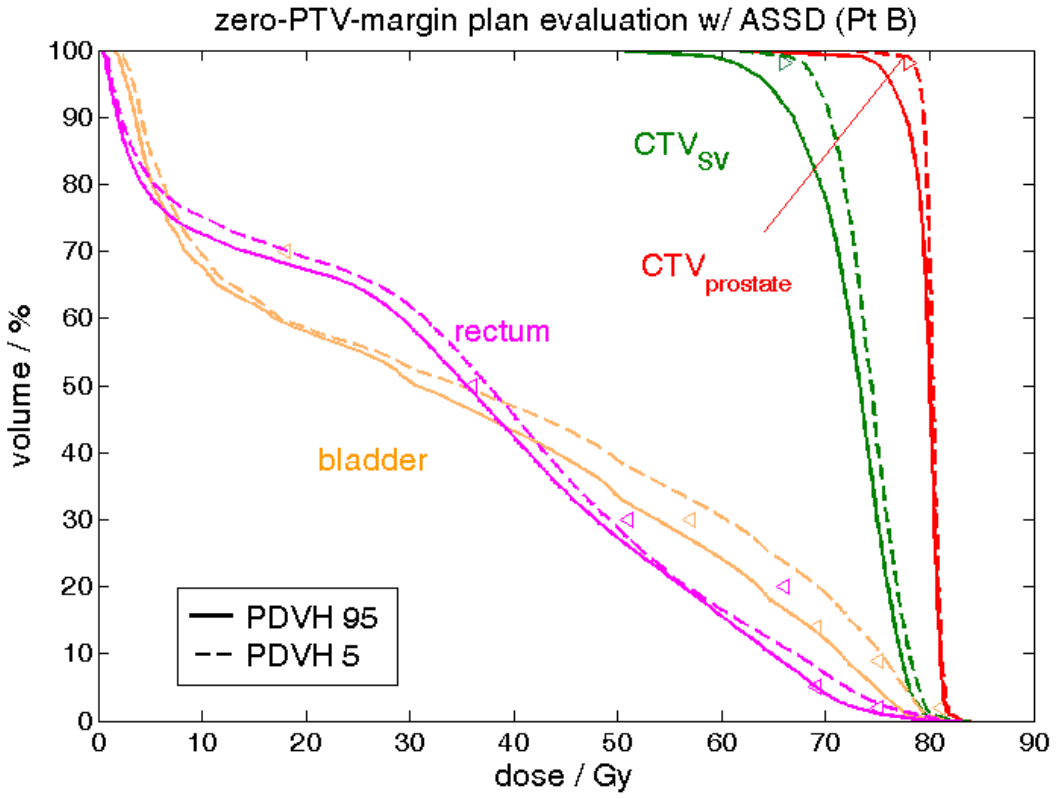

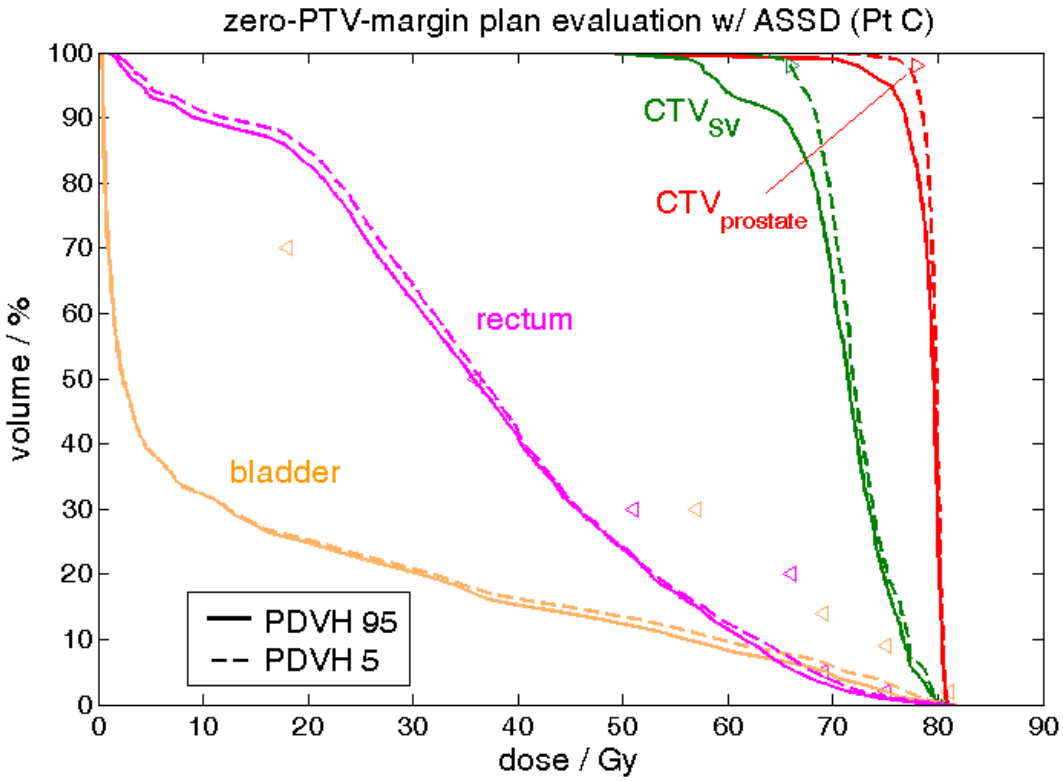

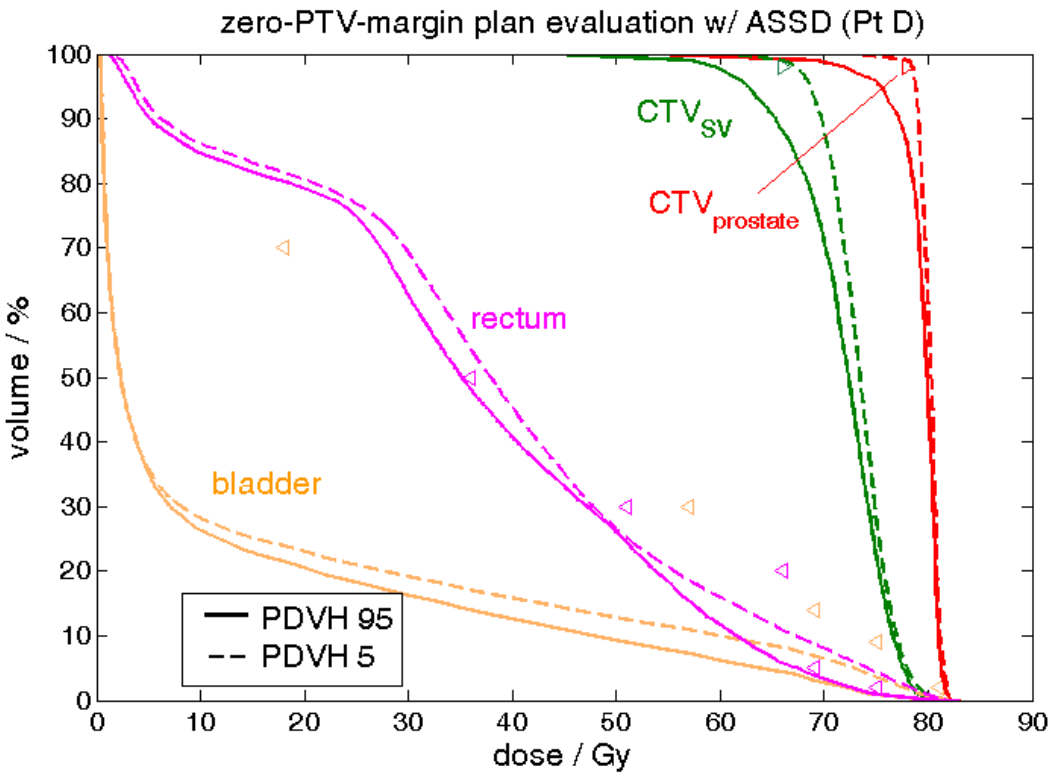

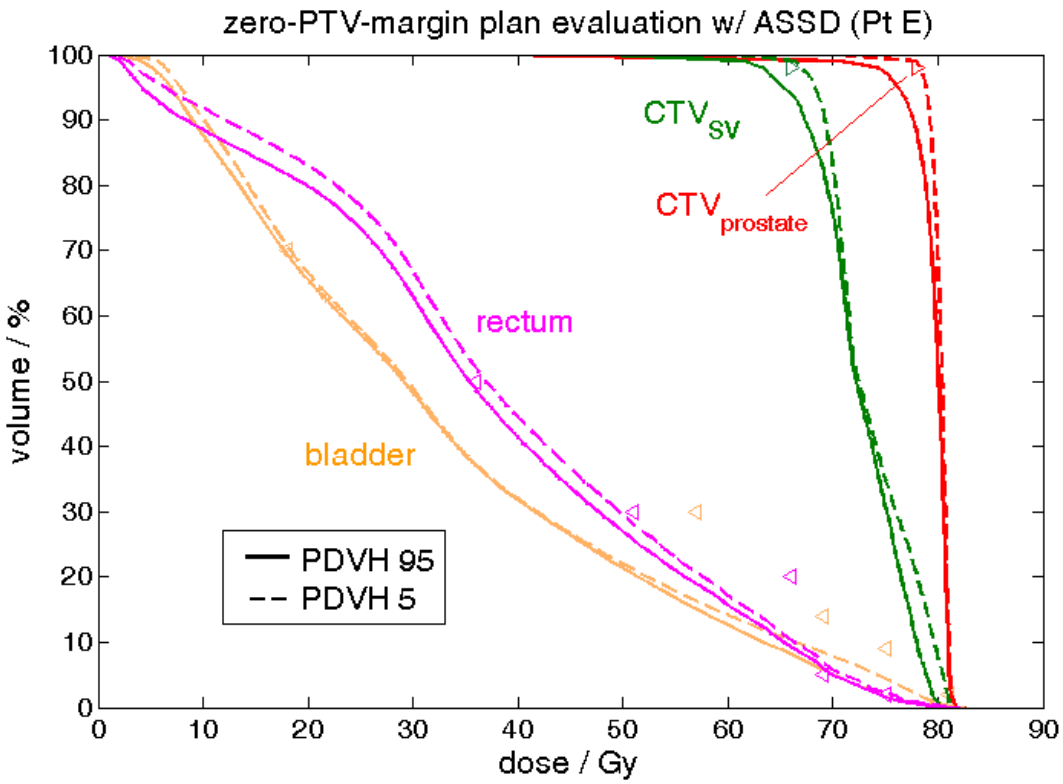

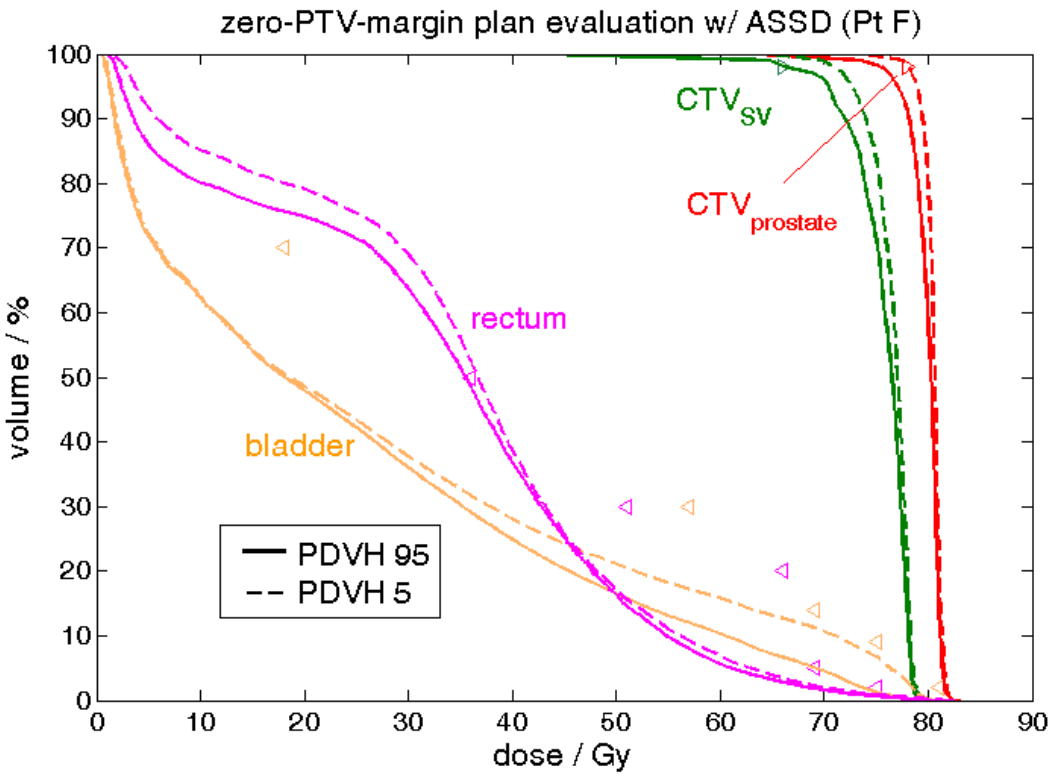

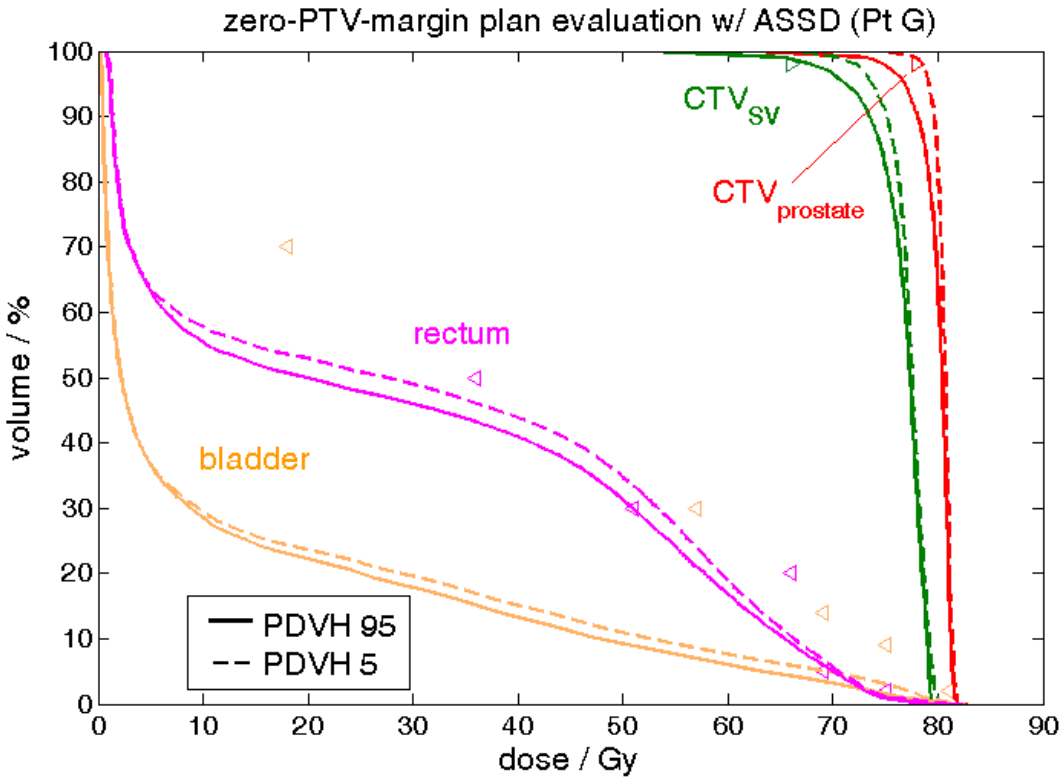

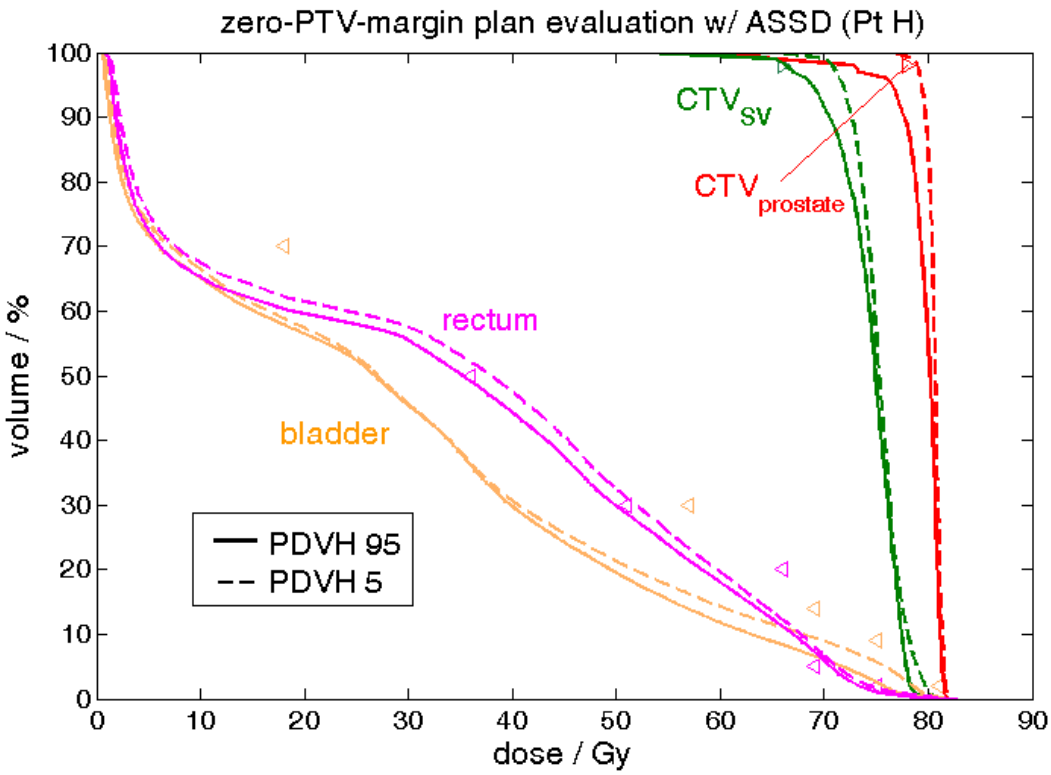

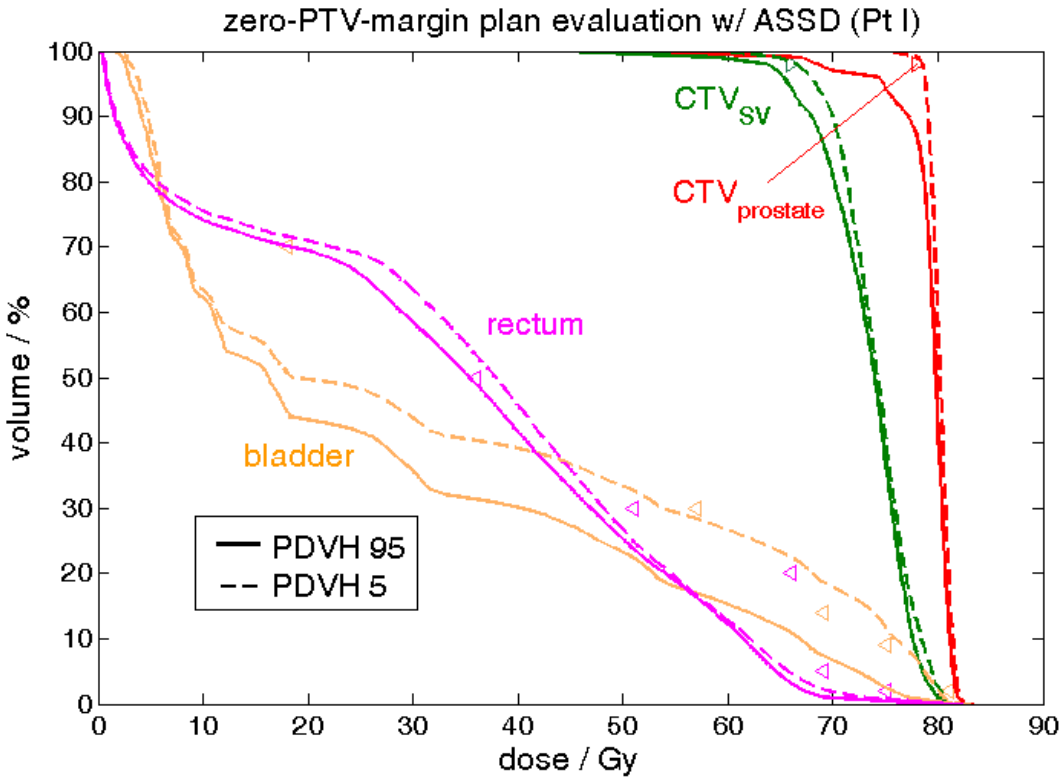

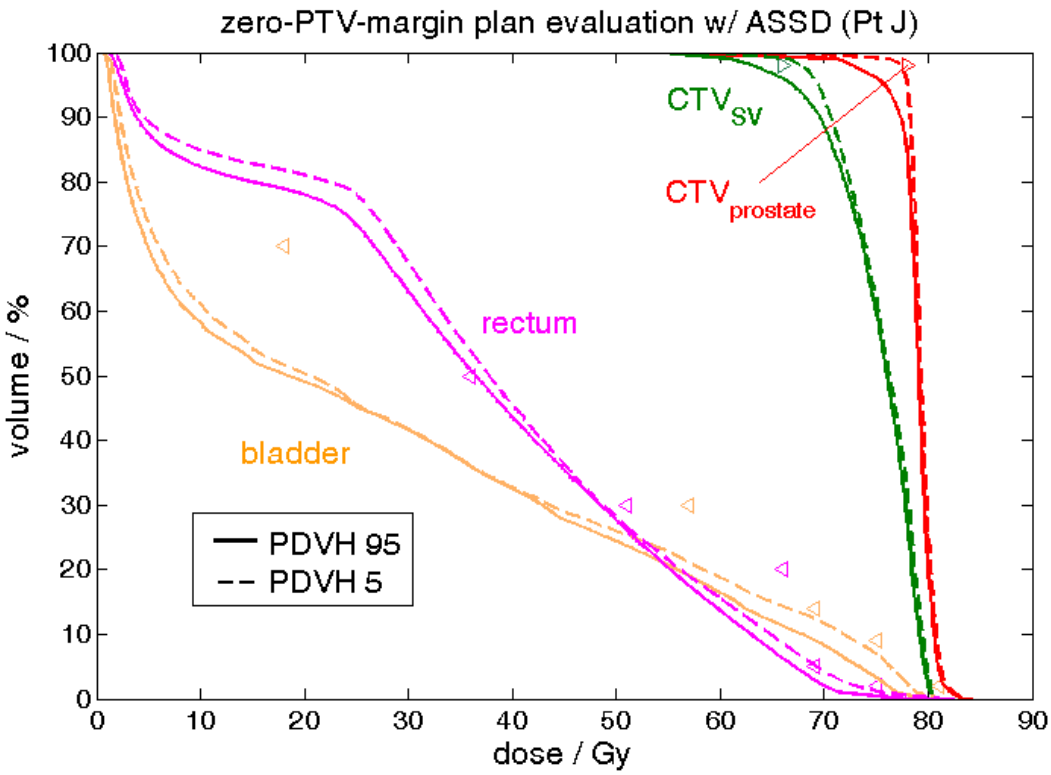

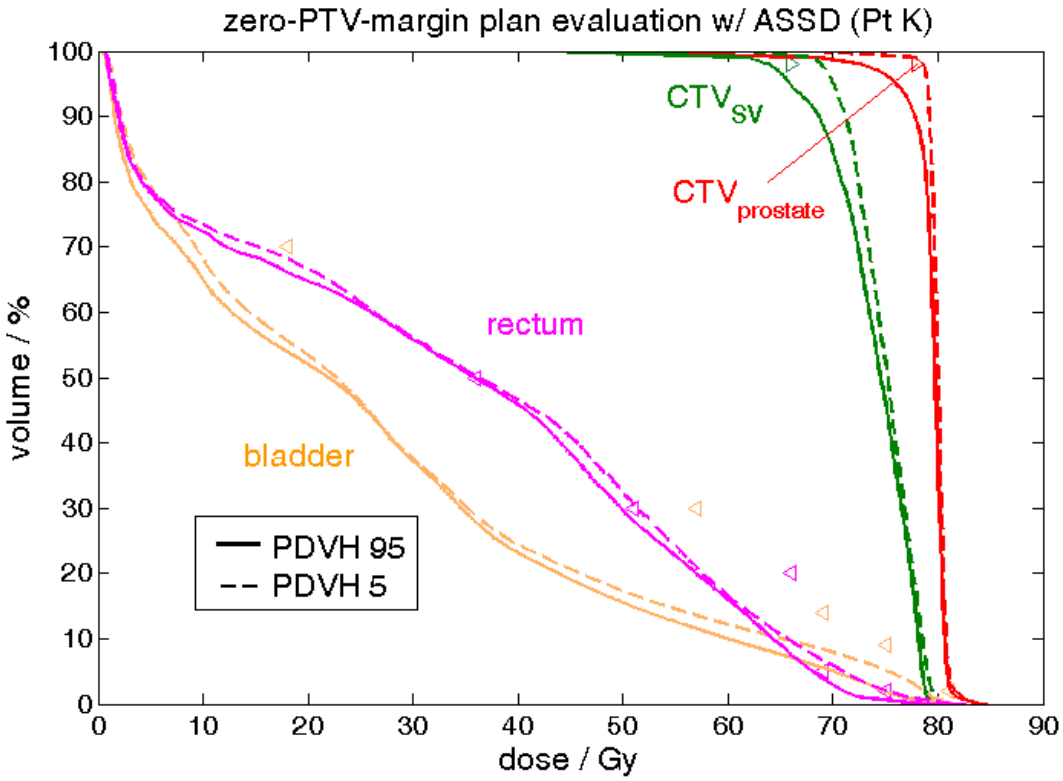

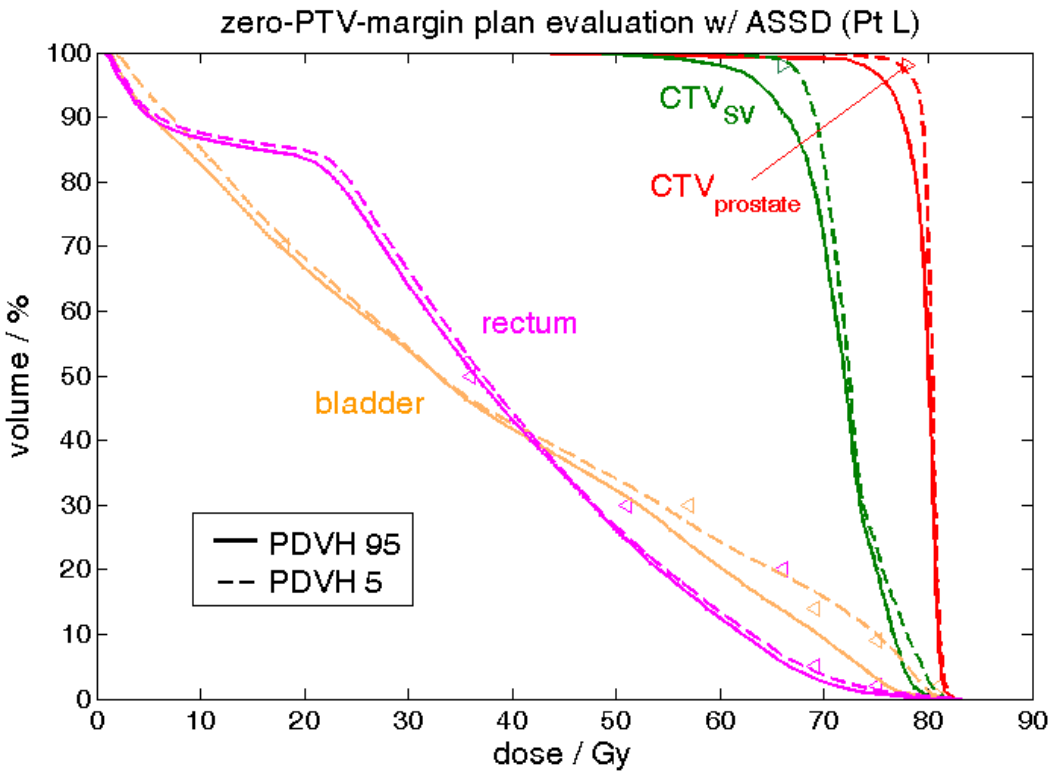

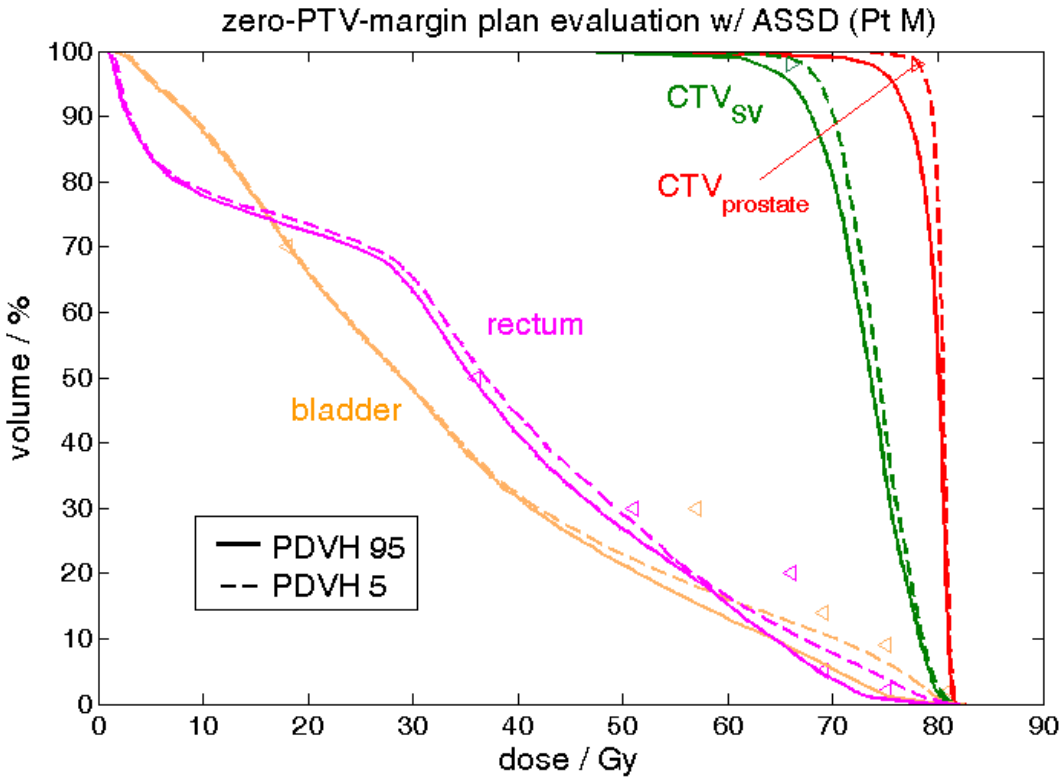

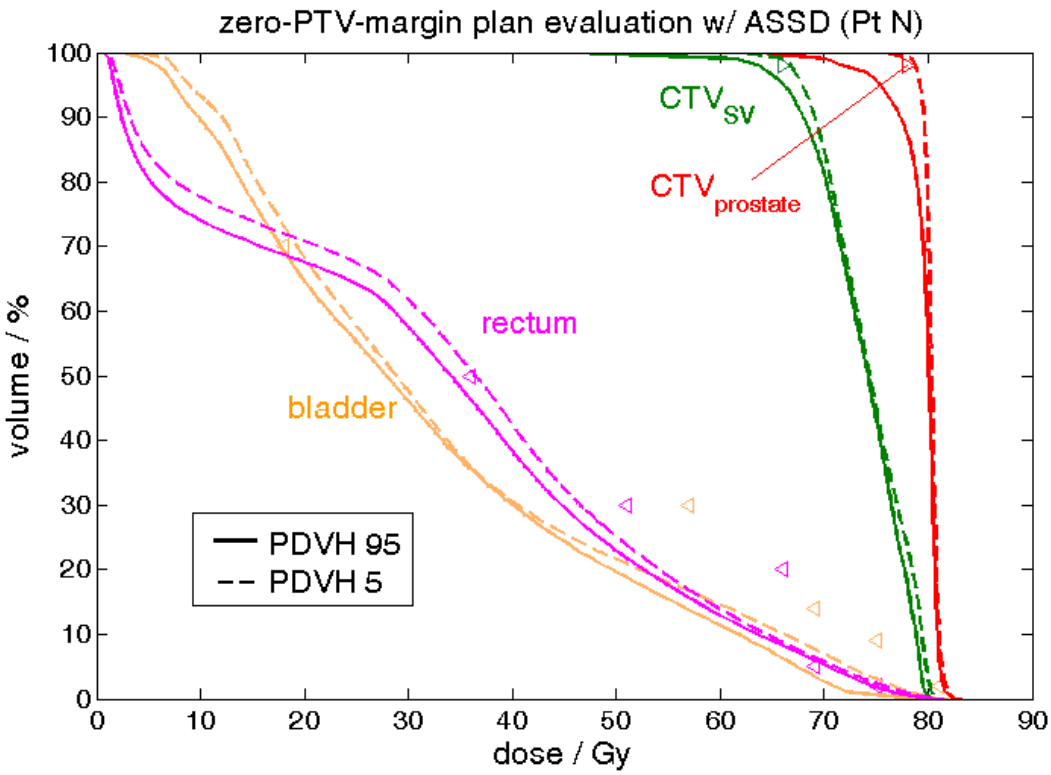

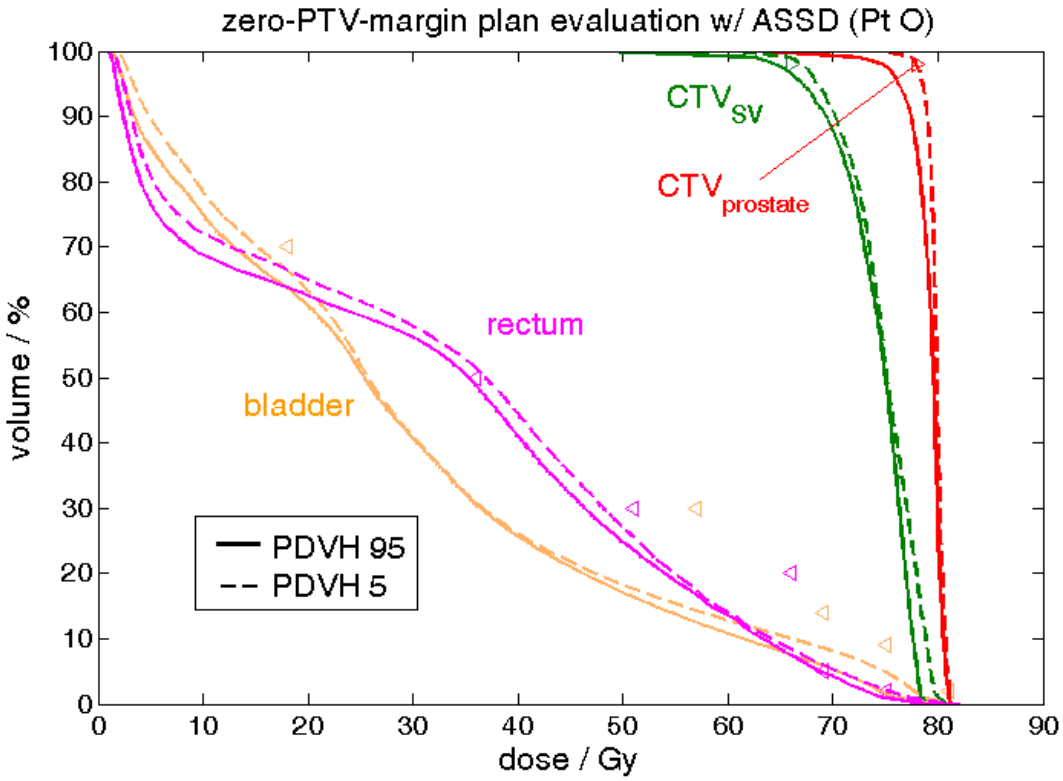

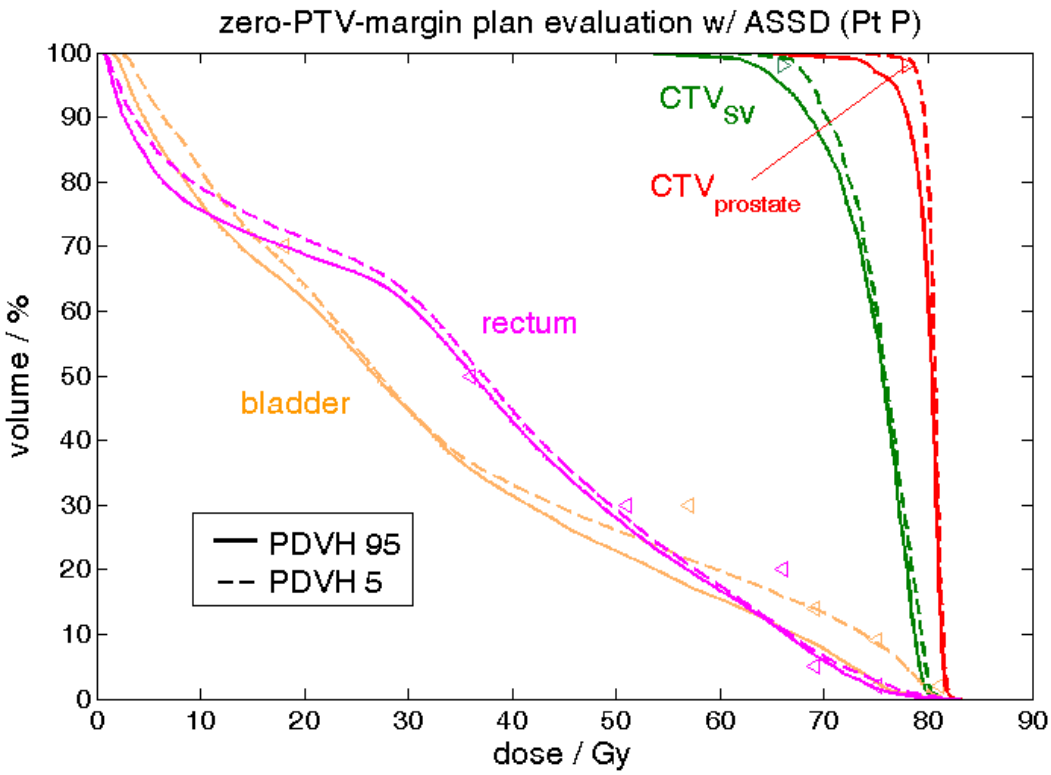

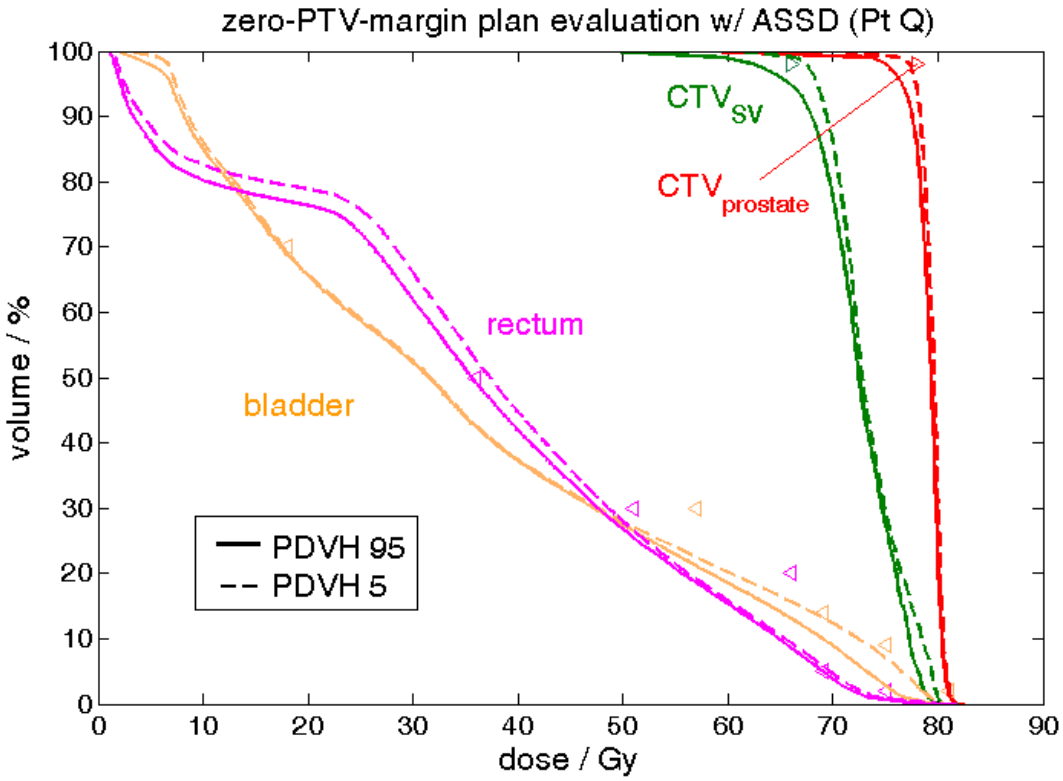

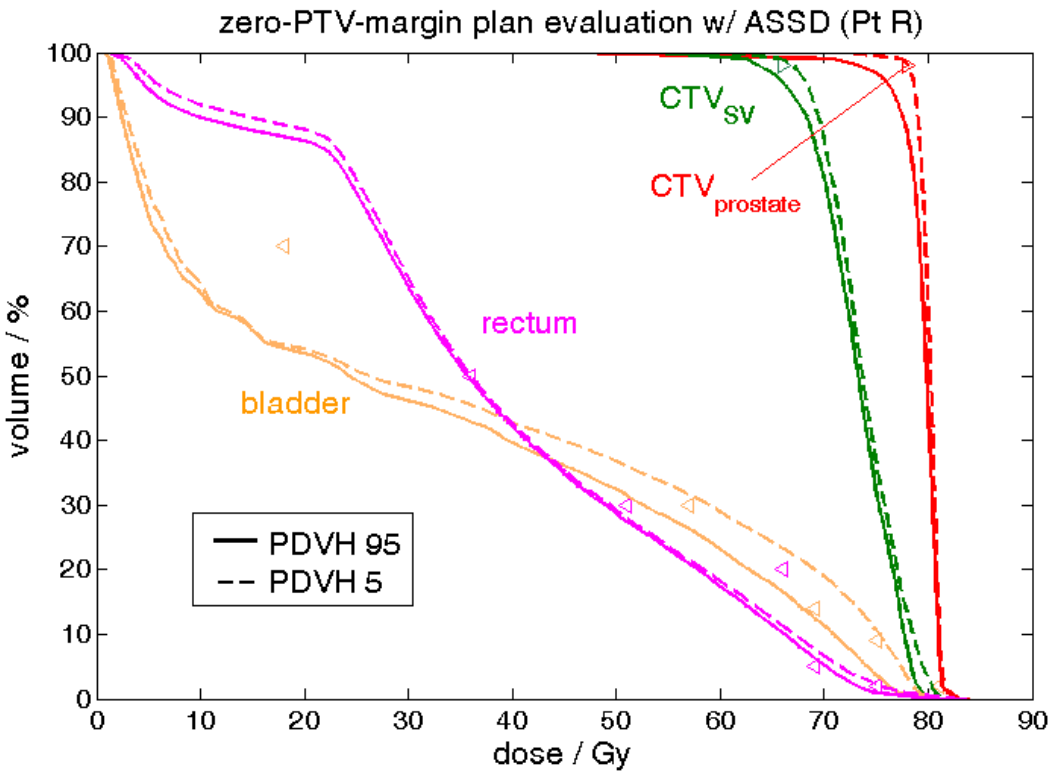

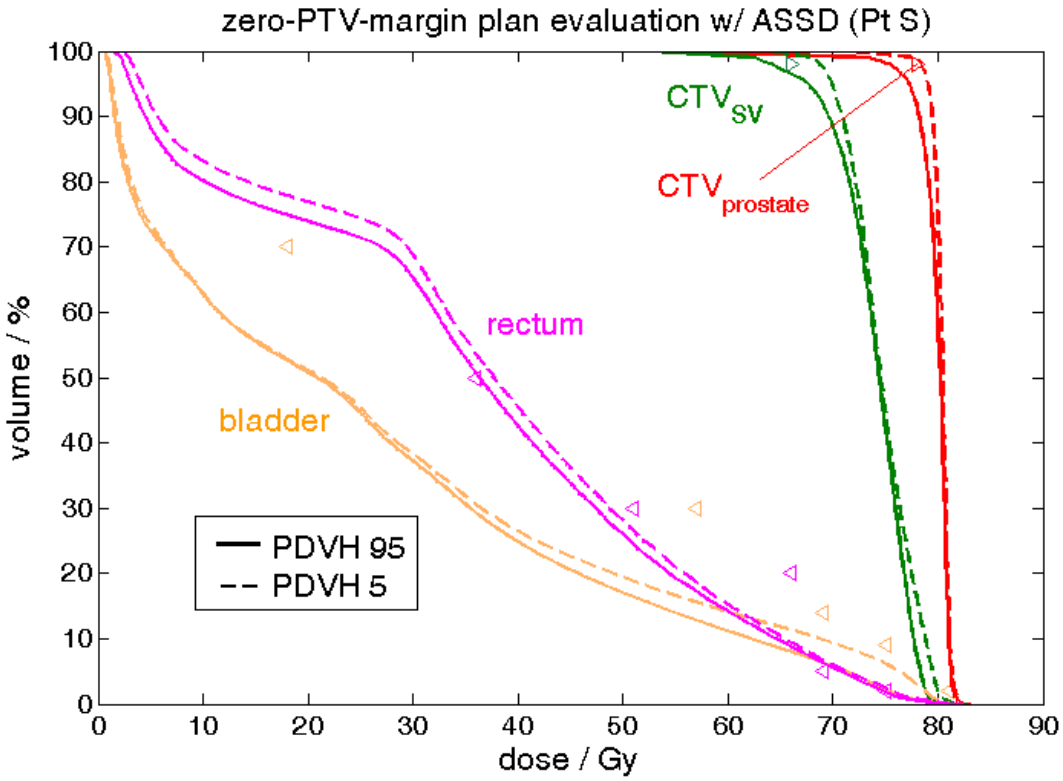

d. Optimized plan comparison with delineation uncertainties model (ASSD) incorporated

For each one of the 19 patients, pDVH 95% for $CTV_{prostate}$ and CTV_{SV}, and pDVH 5% for bladder and rectum on COP, OM and FM plans are plotted below. When delineation uncertainties are accommodated, the benefit of COP relative to the other two margin-based planning techniques is patient-specific. For the patient cases (B, C, H, L, M, N, O, P) whose COP plan is preferred, most show more decent OAR sparing. The best case for COP pDVH is patient C, whose dose sparing for bladder and rectum relative to OM and FM pDVHs is most pronounced. Compared to the study for deformable motions, COP plan is more beneficial when delineation uncertainties are accommodated.

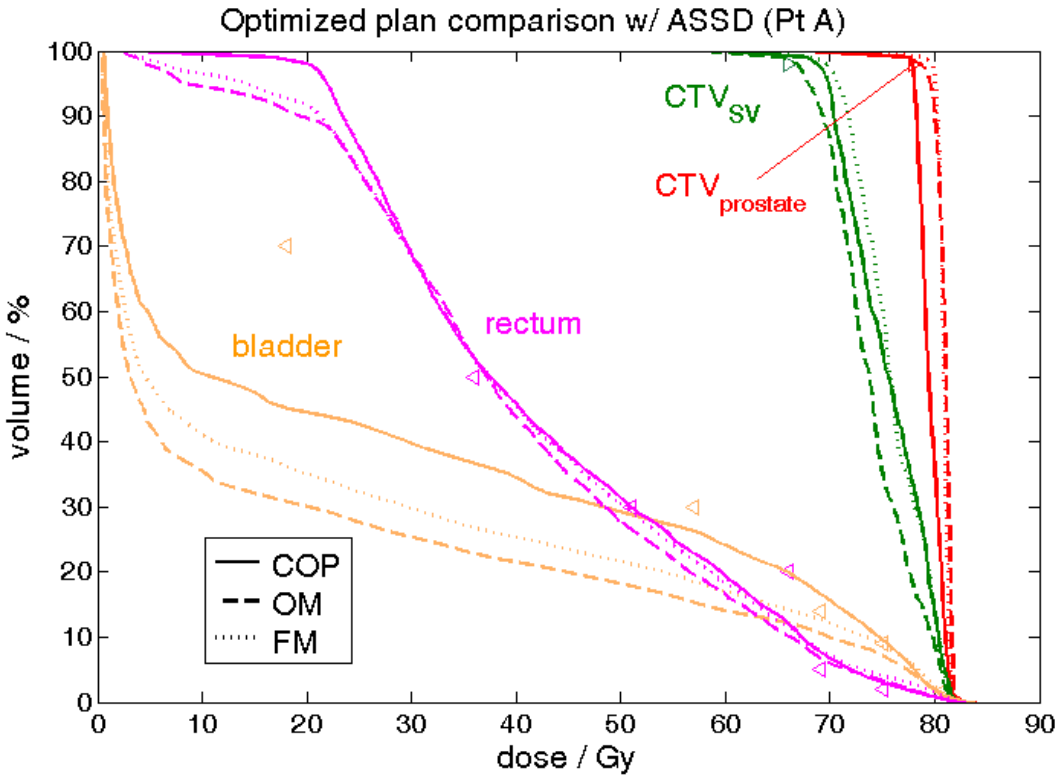

Figure 52. The pDVHs 95% of $CTV_{prostate}$ (red) and CTV_{SV} (green) and the pDVHs 5% bladder (orange) and rectum (magenta) for the patient-specific comparison of COP(solid), OM (dashed) and FM (dot) plans for the patient with ID A to S (continued below), with optimization objectives (triangle markers). The ASSD model is incorporated to show the dosimetric consequence of delineation uncertainties.

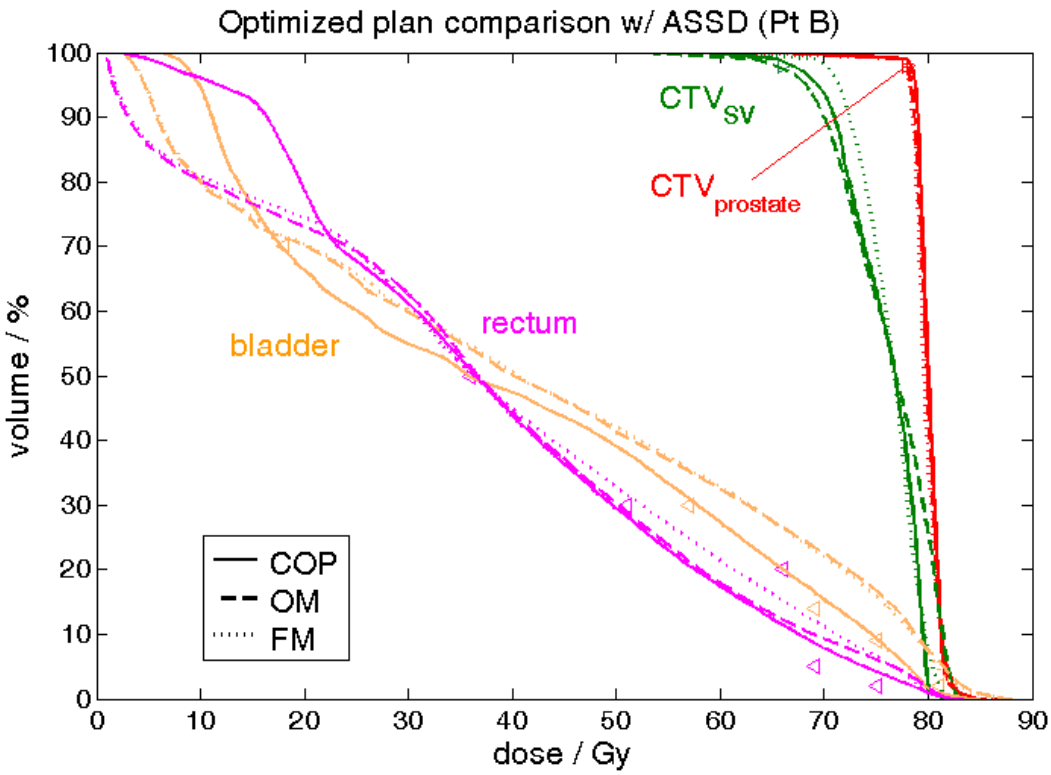

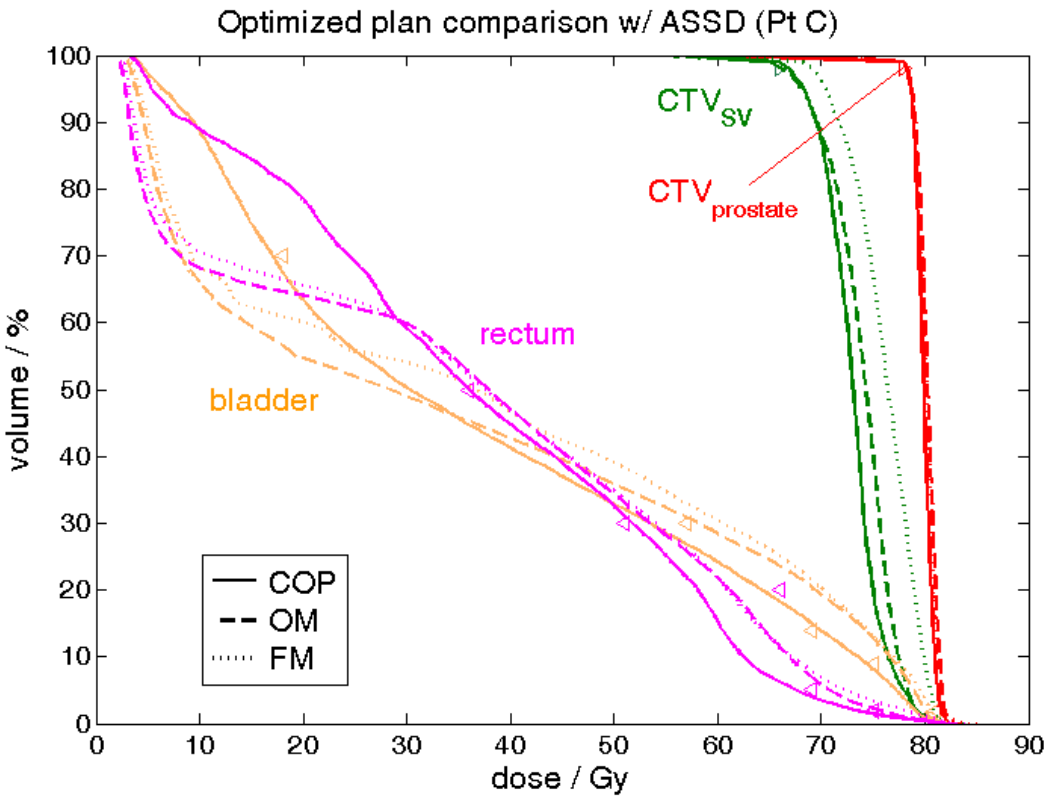

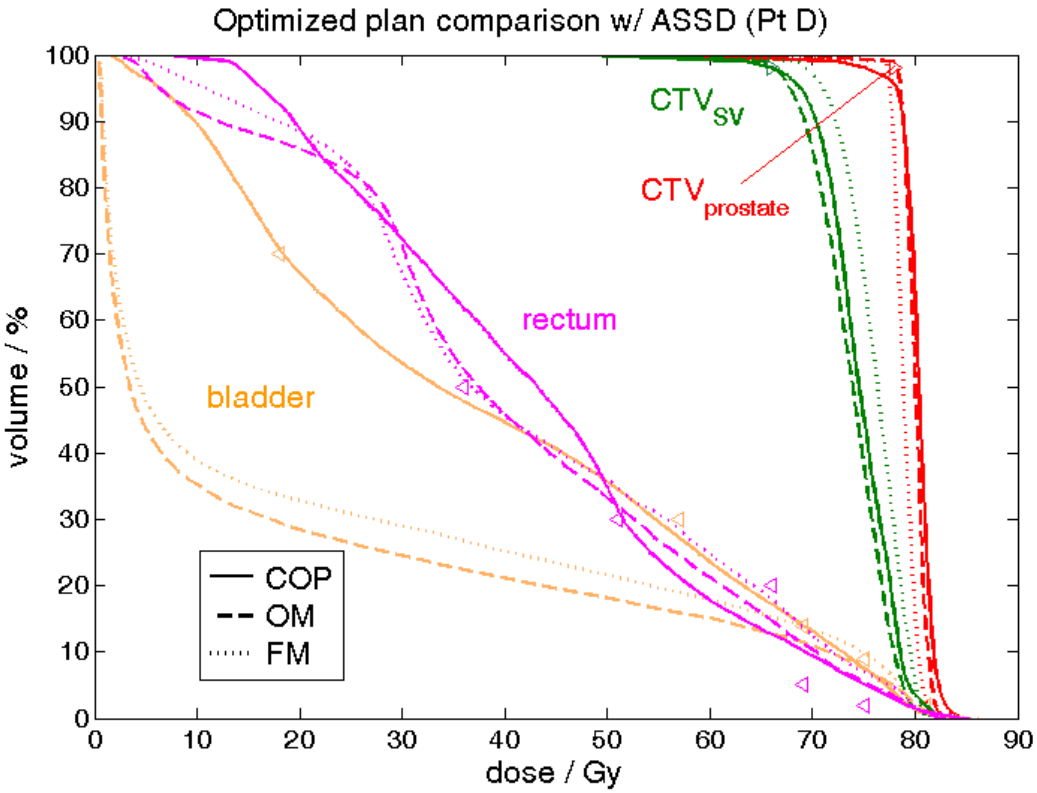

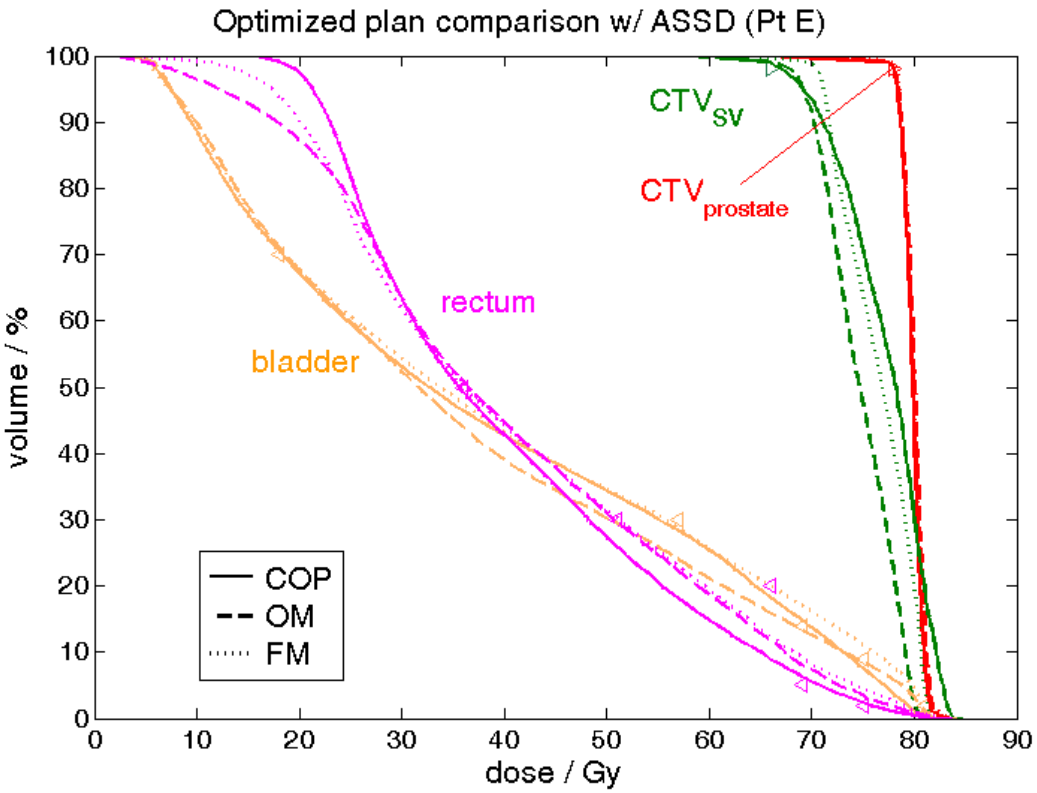

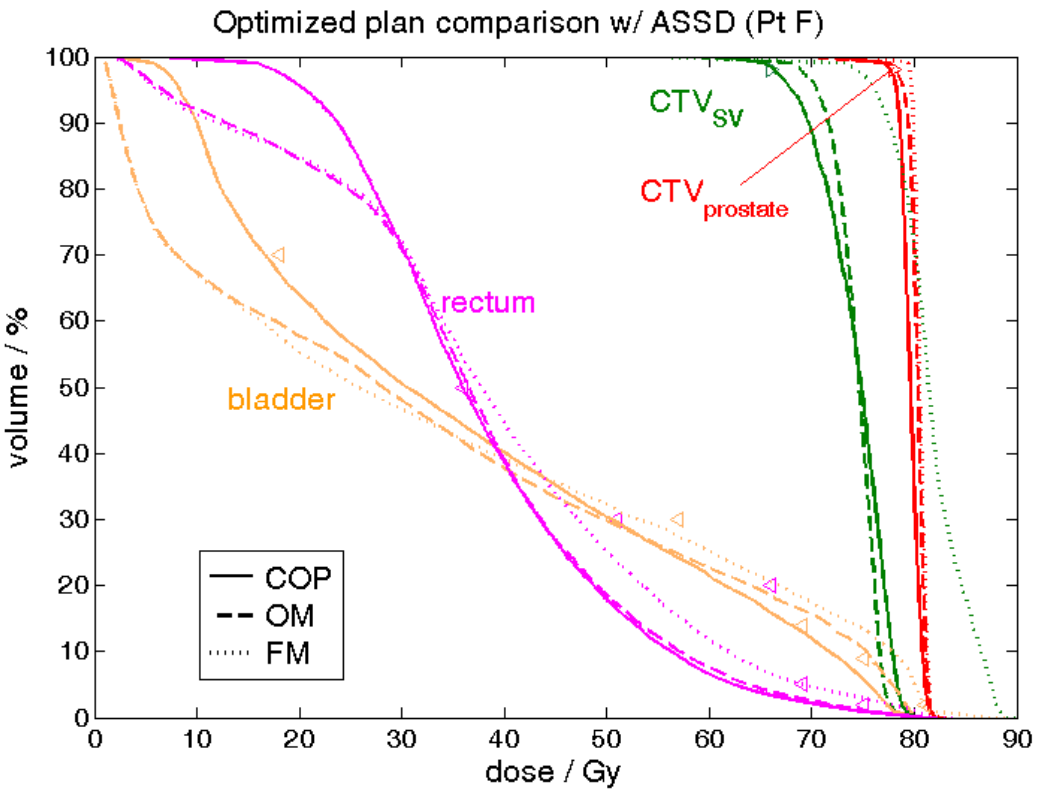

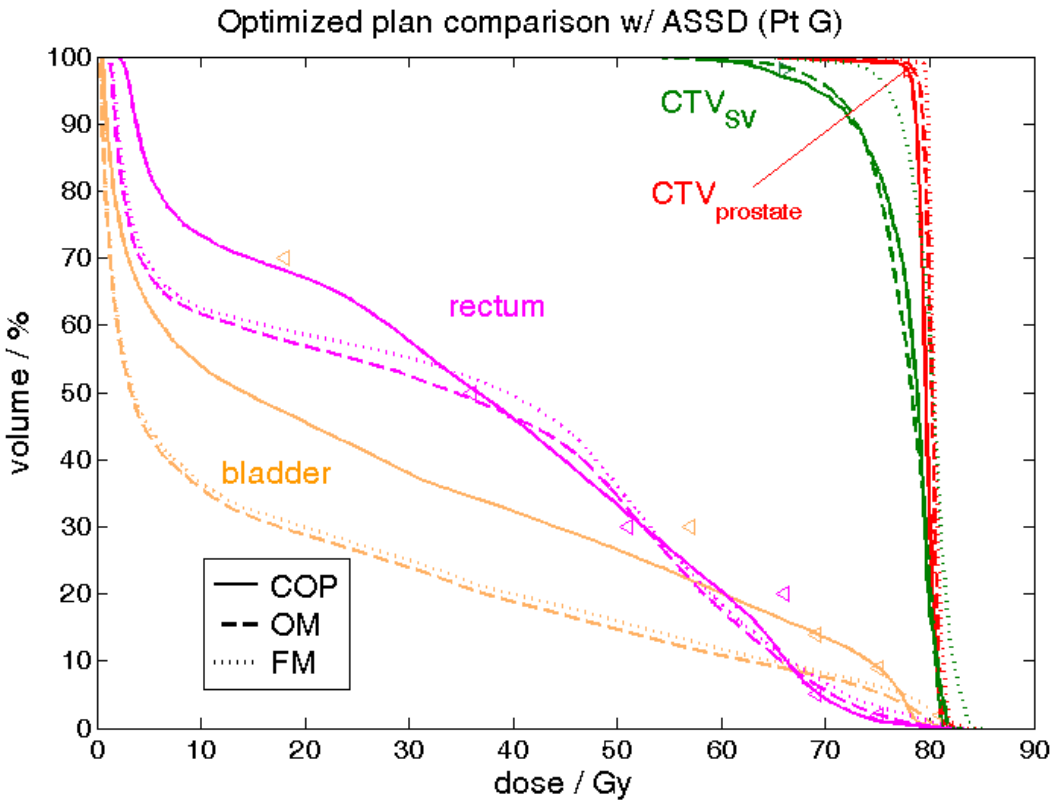

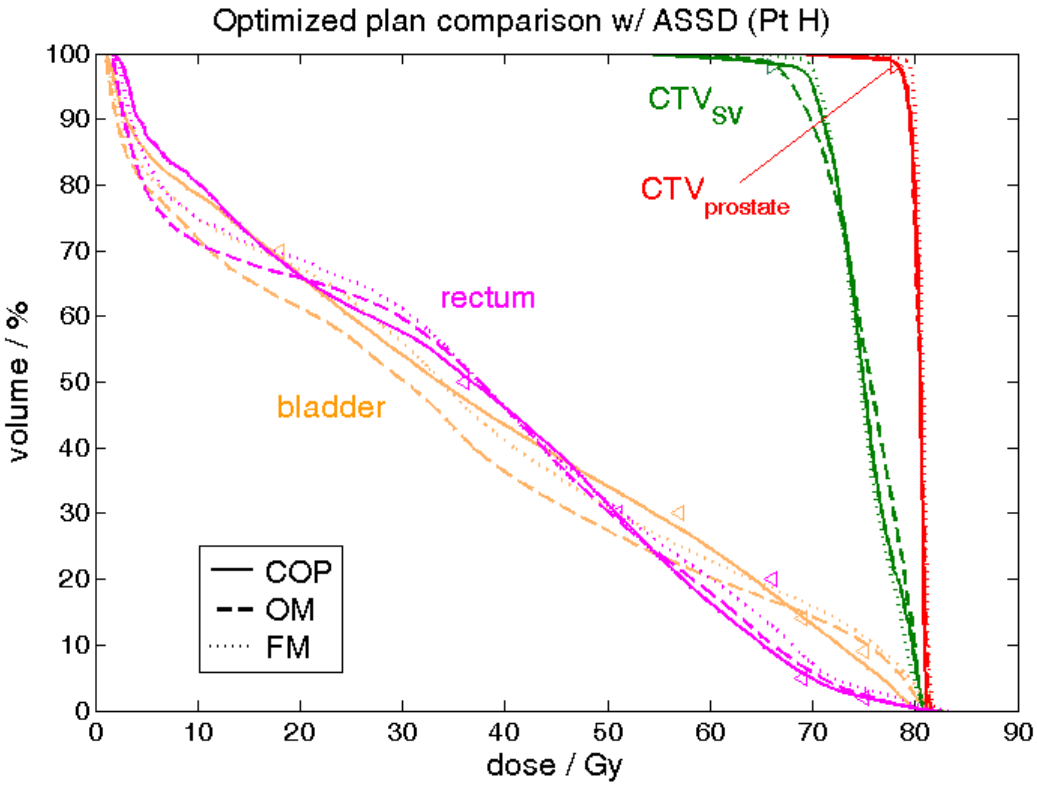

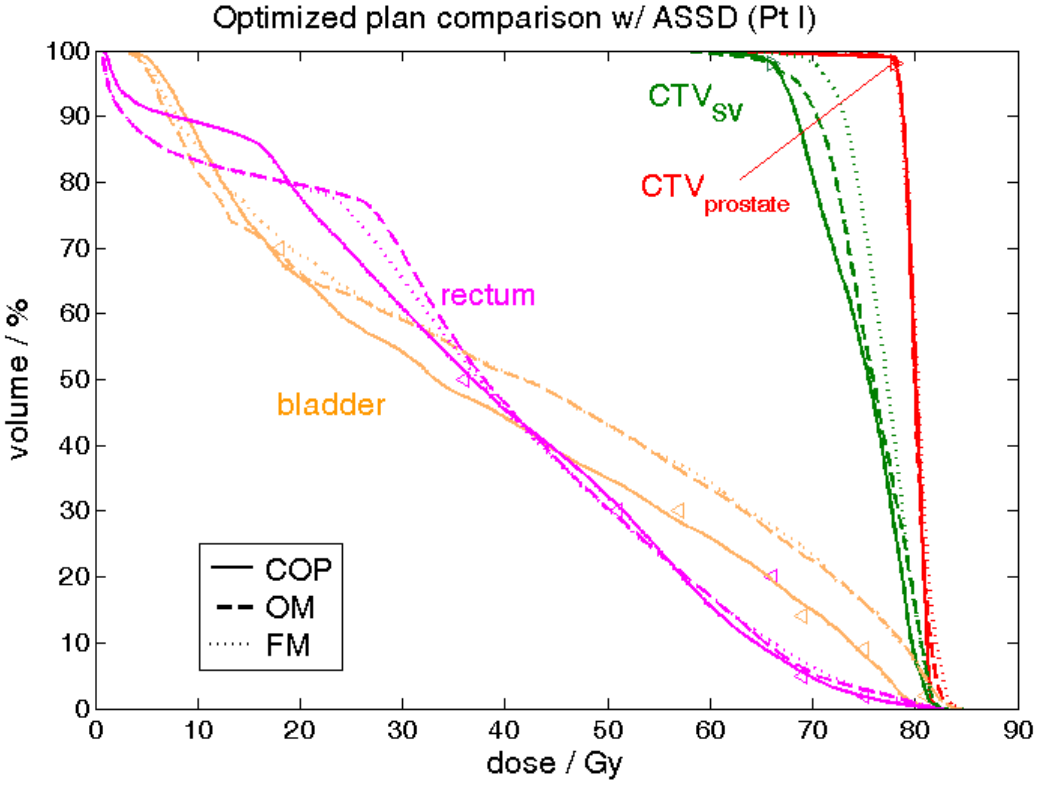

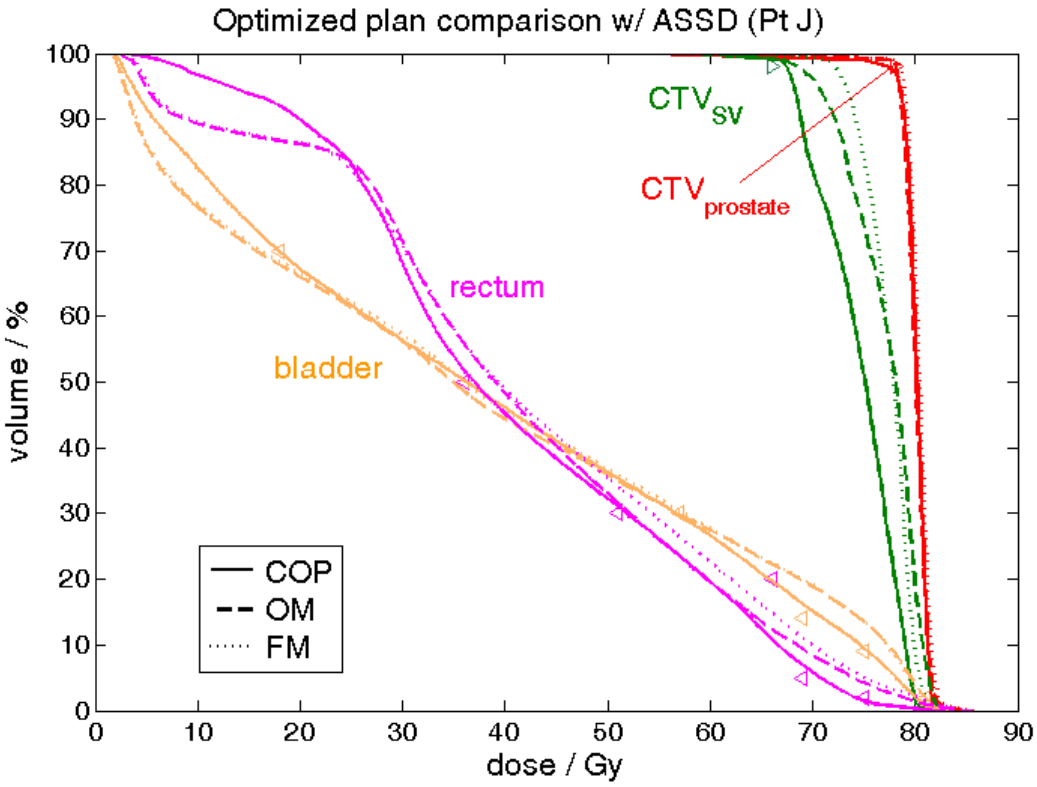

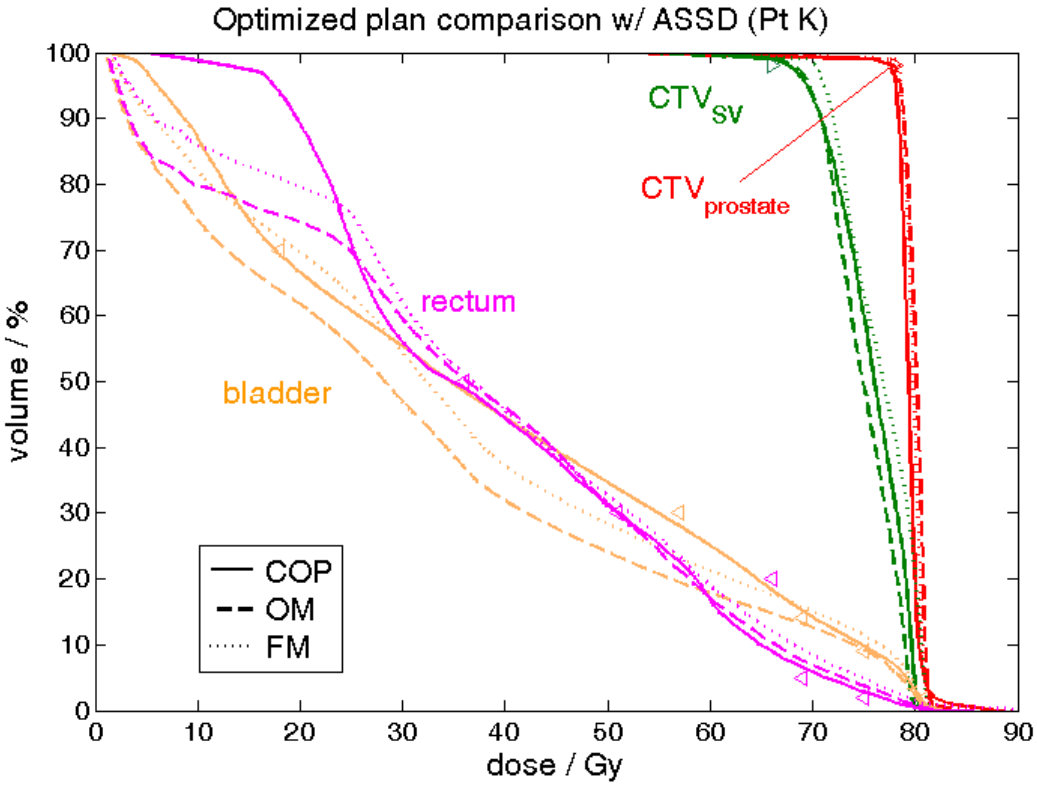

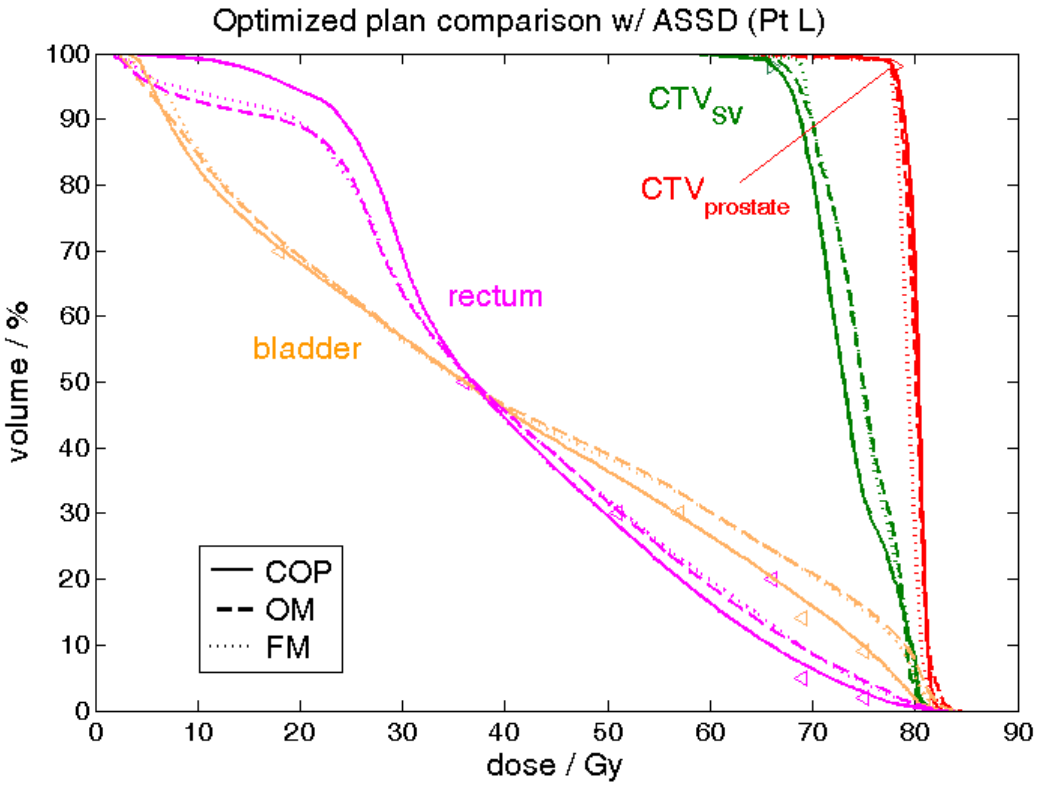

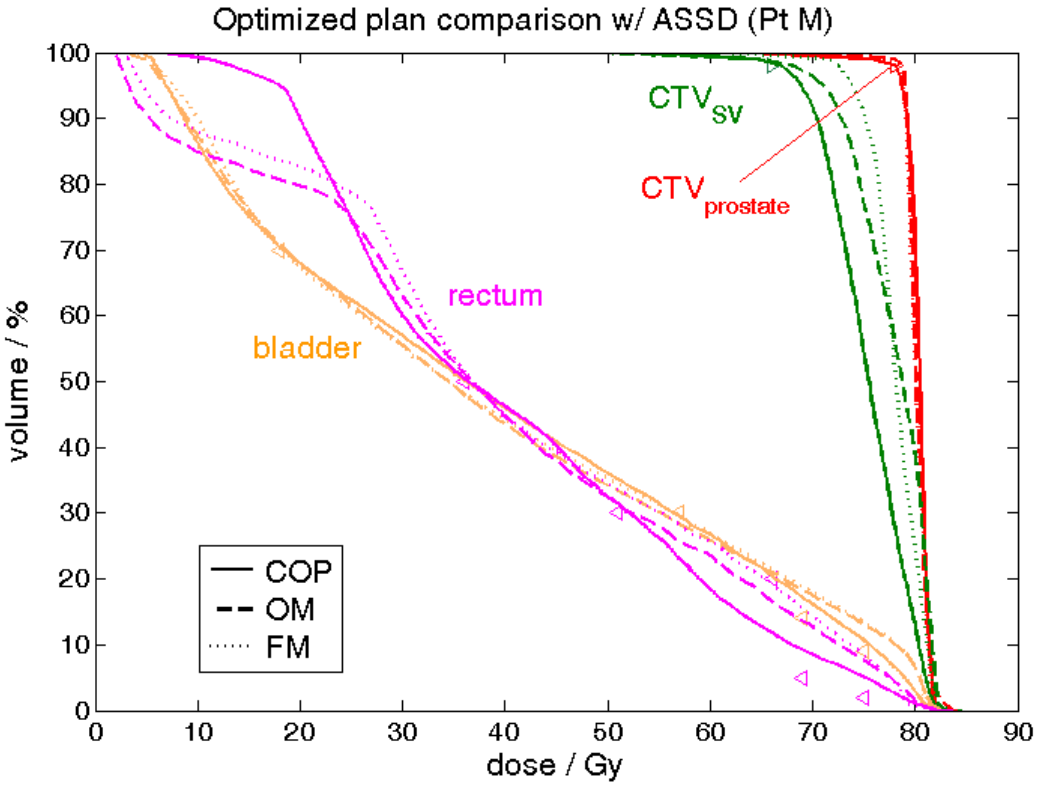

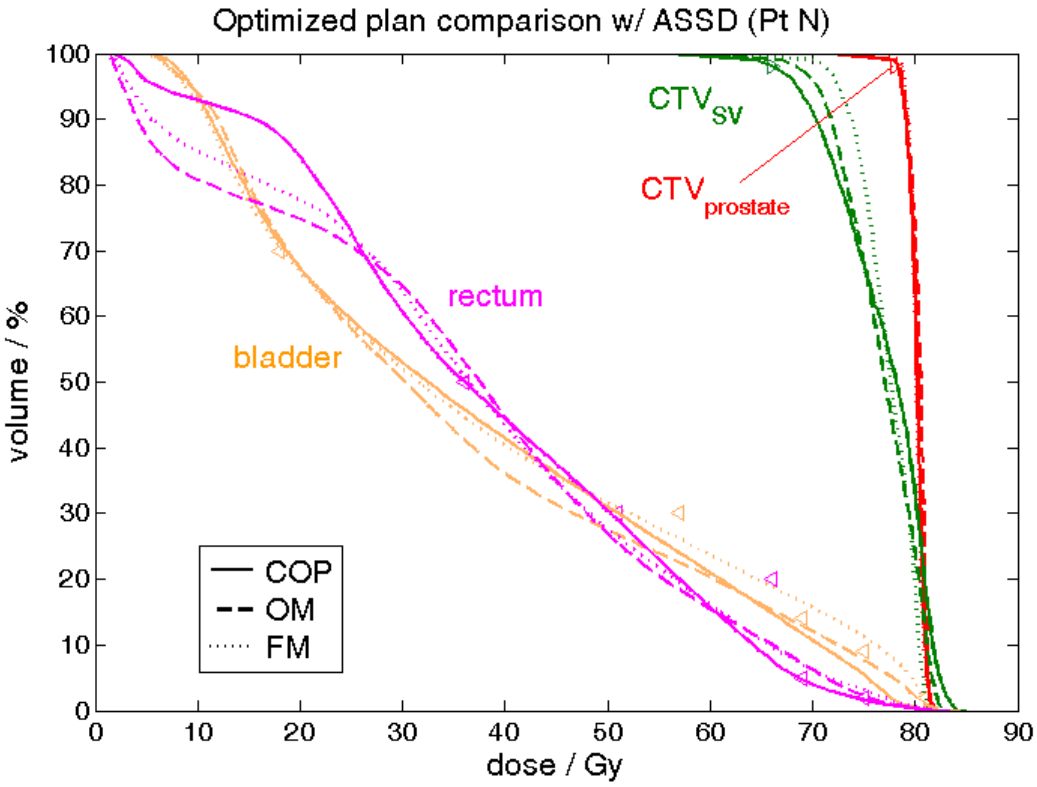

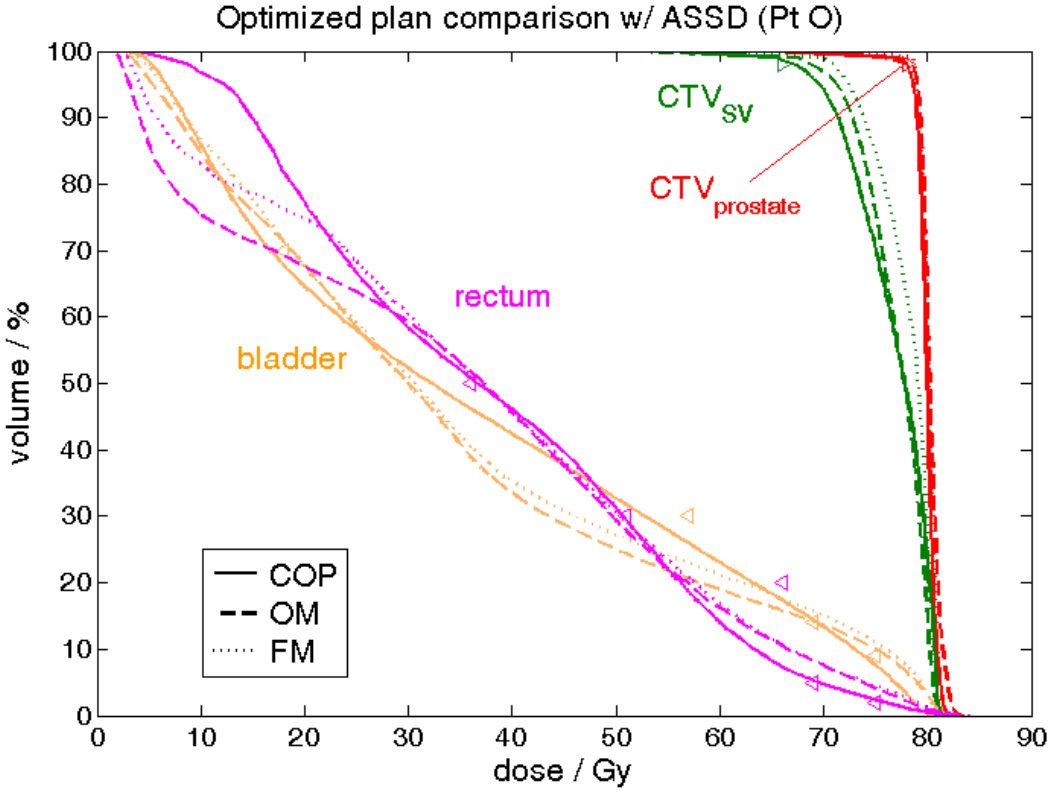

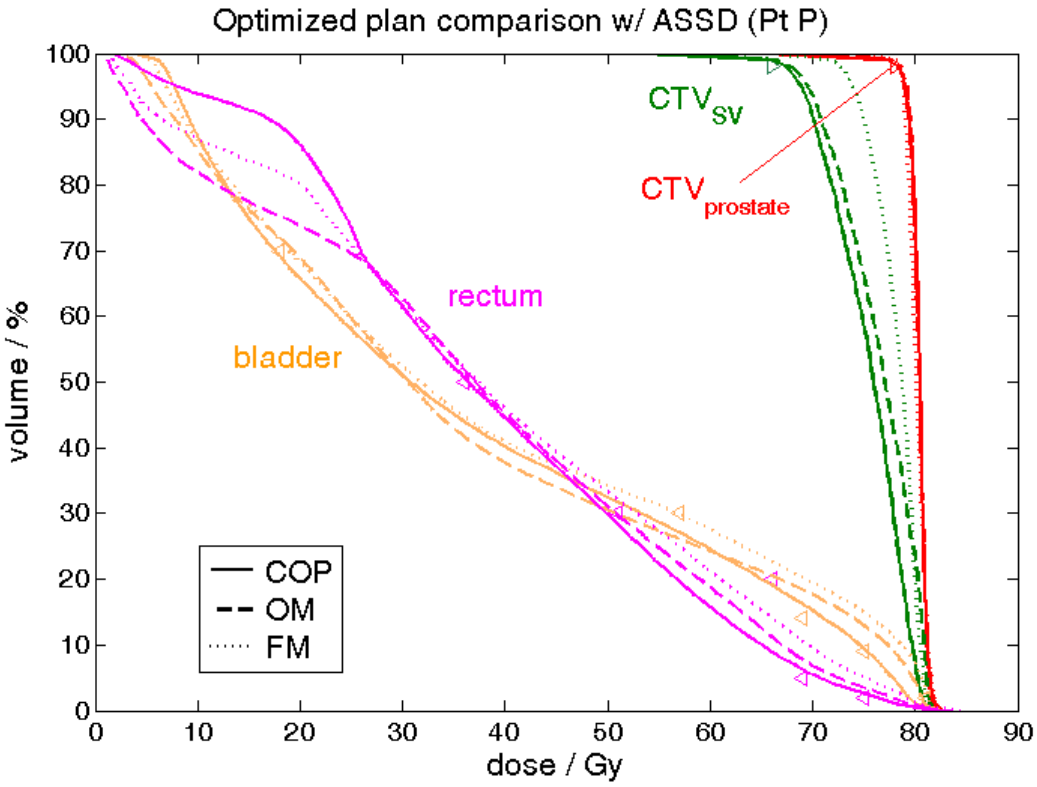

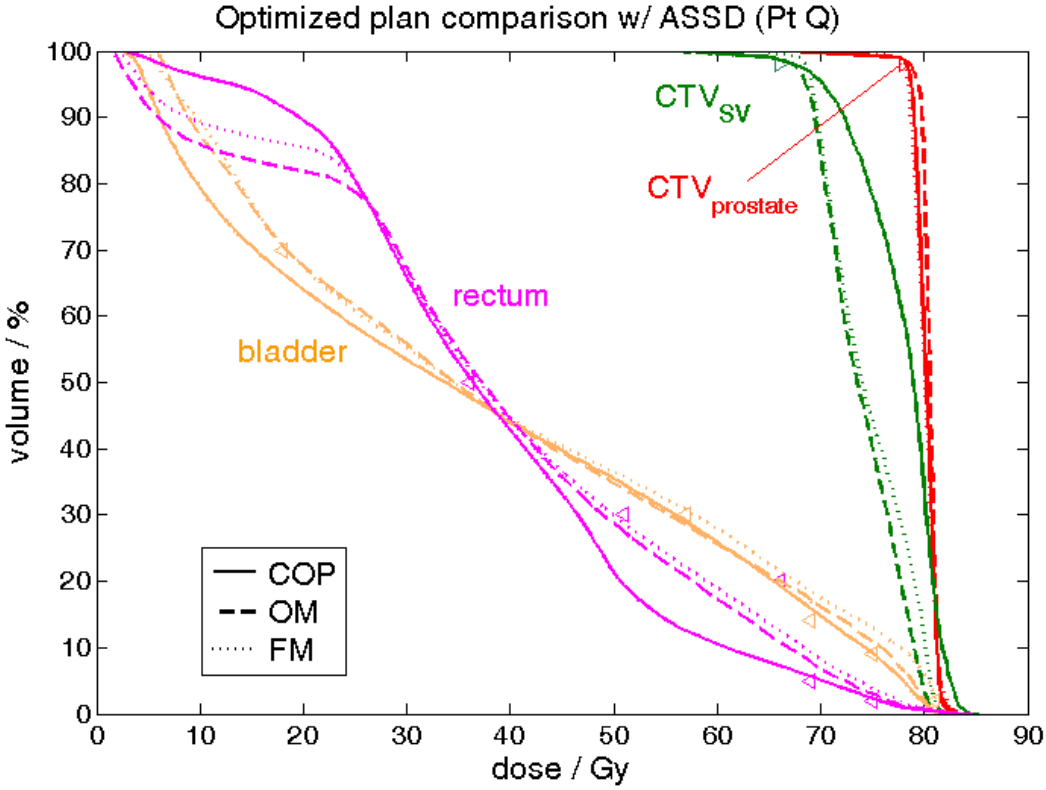

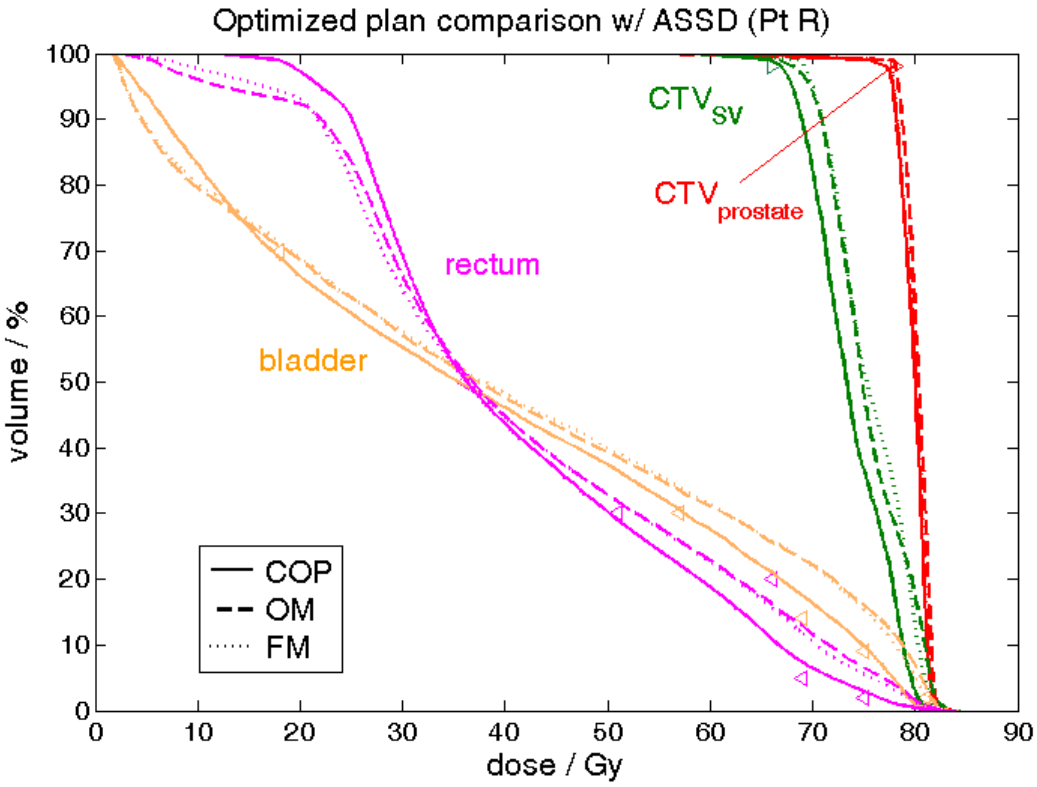

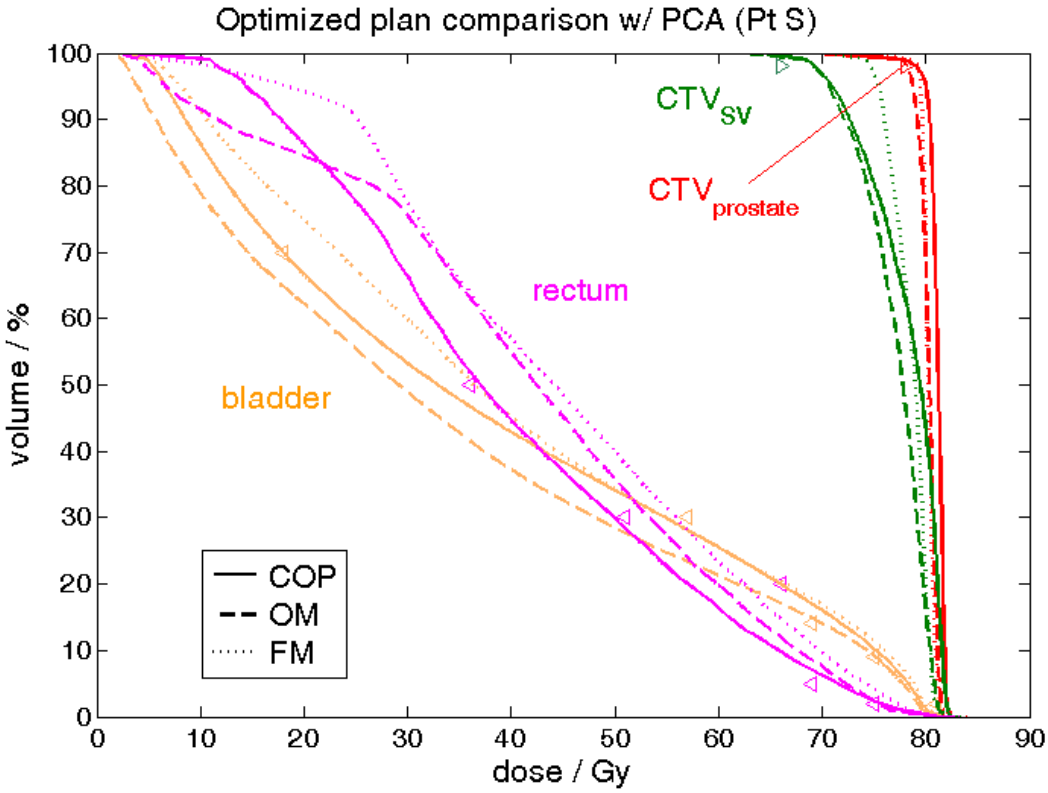

Appendix II. Related projects

a. Plugins developed for IGART plan evaluation

Three Pinnacle^3 plugins have been developed for future IGART plan evaluation. The plugins are the dynamic libraries to extend the functionality of Pinnacle^3. Each plugin is responsible for one main step for a complete plan evaluation. First plugin copies a plan created on one image set to sequential image set(s). The second plugin does dose mapping and accumulation. The third plugin calculates metrics such as DVH, EUD, TCP and NTCP. These plugins can be called by a simple click on a script list once they are loaded in the TPS.

The first plugin is named as "HXCopyBeamComputeDose" (HXCBCD). The workflow of HXCBCD for plan copying is summarized in the Table XVI. Three things need to be noted here. First, the treatment plan is copied by matching the centroid of prostate, assuming that prostate is reliably tracked before being treated in each fraction. Second, a plan is copied mainly by copying beam settings and recomputing the dose. This can be simplified as copying dose only, according to the assumption of dose-shift variance. The dose difference between dose copying and beam copying is within 2%. (Sharma *et al.* 2012) Third, some functions that have been extended from HXCBCD are not included in the Table XVI. An example is that the optimization criteria (Table III, page 22) for either COP or PTV-based plans based on VCU or other protocols can be loaded by calling the functions in HXCBCD plugin.

Table XVI. Workflow of HXCBCD plugin for copying plan to treatment fractions.

Prior manipulation
• Delete extra trials, beams, beam iso-center for resetting (No more included) TPS would crash when executing this task. The reason is unknown. Scripts are written to execute this task. • Check the image set name for each trial in the TrialList. Errors will be returned if any trial for treatment shares the same reference image set.
On the reference trial associated with the reference image set
• Delete beams on reference trial and add seven beams for IMRT Default beam settings: I. Machine 21EX; II. Energy 18 MV; III. Beam type: Static; IV Gantry Angle: V: Isocenter: GTV(prostate) centroid VI Beam Collimator: 90; VII: Initialize and unlock Beam Weight: ~14.28 ~ (100/7); VIII: Set dose prescription as 1.80 Gy/fraction * 44 fractions.) • Load criteria for optimization Default criteria protocol: RTOG 0126 Two structures are created if inexistent: PTV = GTV1+1cm margin. LNT = GTV1 ring 2-4 cm. This is optional for other protocol. • Perform IMRT optimization I. Set dose grid for dose calculation: as large to cover skin II. IMRT setting: DMPO, Allow Jaw Motion, Split beam if necessary
On each fractional trial that is associated with fractional image set
• Set beam isocenter as the centroid of GTV on this image set • Delete beams and copy the beam settings from the reference image set I. Dose grid II. Beam weight III. Beam monitor unit (MU) after optimization • Compute copied beams

The second plugin is named as "HXVolumeWarpingPlugin" (HXVWP). HXVWP performs dose mapping between reference image set and fractional image sets in the region within the dose grid and create an accumulated dose on the reference image. (Readers are referred to Figure 26, page 74 for a graphical illustration.) The input data for this plugin are the DVF from the reference to the fractional image set dose. Based on this DVF, any voxel within a pre-defined dose grid on the reference image set can find its corresponding coordinate on the fractional image set. (As the resolution of dose grid and DVF may be different, interpolation calculations may be involved in the process.) The voxel dose on the fractional image set is read and then mapped back to the reference image set. Often, the actual delivered dose distribution is degraded compared with the static dose distribution planned on the reference image set. The accuracy of the dose mapping algorithm remains a concern for this tool. Though many test cases (e.g, on a homogeneous or heterogeneous phantom) have been carried out, verification of dose mapping for real patient is challenging due to no metric being upon which to base the accuracy of the dose accumulation. (Schultheiss *et al.* 2012)

Compared to the other plugins, HXVWP has been developed to be more user-friendly. Figure 53 shows the graphical user interface (GUI) of HXVWP. Users can select dose mapping algorithm, DVF type according to their need. An attached application called "TrialStoreEditor" can record the dose mapping parameters.

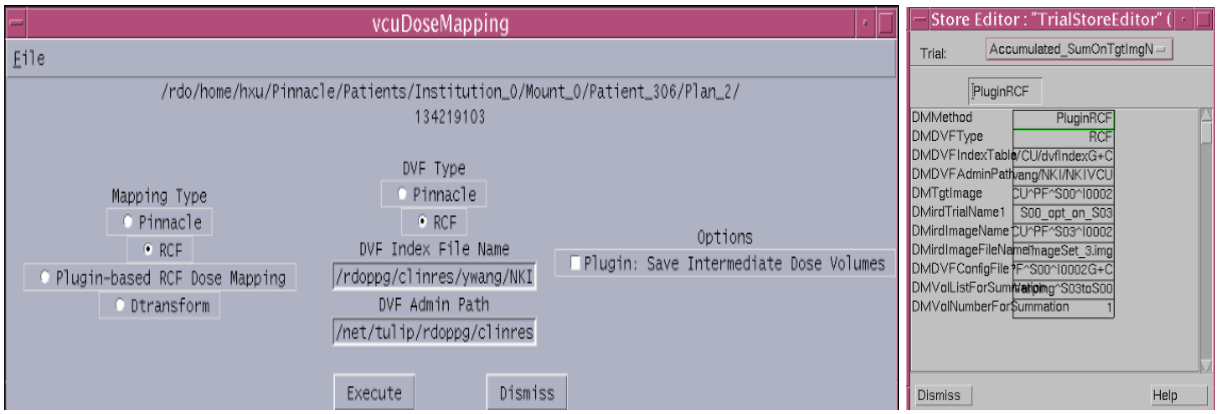

Figure 53. Interfraces of the GUI to launch HXVWP and the application to store the information of dose mapping. Note the mapping type for HXVWP is Plugin-based RCF DoseMapping. (Copyright JV Siebers 2011©)

The third plugin is named as "HXRoiDVHPlugin" (HXRDP). This plugin first calculates a DVH (for either physical dose or BED) and then transfers the DVH to biological metrics EUD, TCP and NTCP. A workflow of this plugin is shown in Figure 54. The equations and their parameters for biological metric calculation are those mentioned in chapter 3.

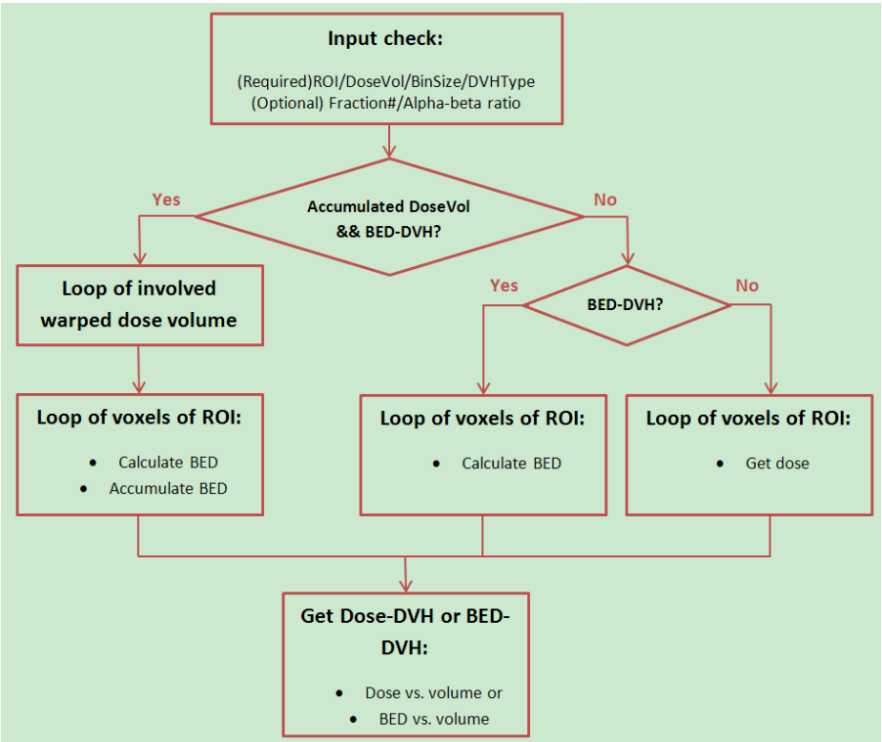

Figure 54. Workflow of DVH calculation of HXRDP

b. Coverage estimates vs. dosimetric margin distribution sampling parameters

Sensitivity of postplanning target and OAR coverage estimates to dosimetric margin distribution sampling parameters

Huijun Xu,[a] J. James Gordon, and Jeffrey V. Siebers
Department of Radiation Oncology, Virginia Commonwealth University, Richmond, Virginia 23298

(Received 28 July 2010; revised 21 December 2010; accepted for publication 23 December 2010; published 31 January 2011)

Purpose: A dosimetric margin (DM) is the margin in a specified direction between a structure and a specified isodose surface, corresponding to a prescription or tolerance dose. The dosimetric margin distribution (DMD) is the distribution of DMs over all directions. Given a geometric uncertainty model, representing inter- or intrafraction setup uncertainties or internal organ motion, the DMD can be used to calculate coverage Q, which is the probability that a realized target or organ-at-risk (OAR) dose metric D_v exceeds the corresponding prescription or tolerance dose. Postplanning coverage evaluation quantifies the percentage of uncertainties for which target and OAR structures meet their intended dose constraints. The goal of the present work is to evaluate coverage probabilities for 28 prostate treatment plans to determine DMD sampling parameters that ensure adequate accuracy for postplanning coverage estimates.

Methods: Normally distributed interfraction setup uncertainties were applied to 28 plans for localized prostate cancer, with prescribed dose of 79.2 Gy and 10 mm clinical target volume to planning target volume (CTV-to-PTV) margins. Using angular or isotropic sampling techniques, dosimetric margins were determined for the CTV, bladder and rectum, assuming shift invariance of the dose distribution. For angular sampling, DMDs were sampled at fixed angular intervals ω (e.g., $\omega = 1°, 2°, 5°, 10°, 20°$). Isotropic samples were uniformly distributed on the unit sphere resulting in variable angular increments, but were calculated for the same number of sampling directions as angular DMDs, and accordingly characterized by the effective angular increment ω_{eff}. In each direction, the DM was calculated by moving the structure in radial steps of size $\delta(=0.1, 0.2, 0.5, 1$ mm) until the specified isodose was crossed. Coverage estimation accuracy ΔQ was quantified as a function of the sampling parameters ω or ω_{eff} and δ.

Results: The accuracy of coverage estimates depends on angular and radial DMD sampling parameters ω or ω_{eff} and δ, as well as the employed sampling technique. Target $|\Delta Q| < 1\%$ and OAR $|\Delta Q| < 3\%$ can be achieved with sampling parameters ω or $\omega_{\text{eff}} = 20°$, $\delta = 1$ mm. Better accuracy (target $|\Delta Q| < 0.5\%$ and OAR $|\Delta Q| < \sim 1\%$) can be achieved with ω or $\omega_{\text{eff}} = 10°$, $\delta = 0.5$ mm. As the number of sampling points decreases, the isotropic sampling method maintains better accuracy than fixed angular sampling.

Conclusions: Coverage estimates for post-planning evaluation are essential since coverage values of targets and OARs often differ from the values implied by the static margin-based plans. Finer sampling of the DMD enables more accurate assessment of the effect of geometric uncertainties on coverage estimates prior to treatment. DMD sampling with ω or $\omega_{\text{eff}} = 10°$ and $\delta = 0.5$ mm should be adequate for planning purposes. © *2011 American Association of Physicists in Medicine.*
[DOI: 10.1118/1.3544364]

Key words: sampling parameters, dosimetric margin distribution, coverage estimates, planning evaluation, prostate cancer

I. INTRODUCTION

In conventional radiation therapy treatment planning, geometric uncertainties such as setup uncertainties, delineation uncertainties, and internal motion[1] are accounted for at the start of the planning process by adding clinical target volume to planning target volume (CTV-to-PTV) margins to the CTV and planning organ-at-risk (OAR) volumes (PRVs) to OARs. The CTV, PTV, and PRV concepts, defined in ICRU Report Nos. 50 (Ref. 2) and 62,[3] are familiar to treatment planners. However, the appropriate margin sizes to ensure target coverage or normal tissue sparing for different treatment sites remain an area for physician judgment. There are many publications that determine margin sizes based on planning studies and simulations. (A ScienceDirect search for "radiotherapy margin studies" returned 31 000+results.) Examples include Muren *et al.*,[4] Lee *et al.*,[5] Button *et al.*,[6] and Ekberg *et al.*[7] Additionally, margin sizing formulas (i.e., guidelines) have been developed by Stroom *et al.*,[8] van Herk *et al.*,[9] and others.[10] Regardless of the details, once a margin is defined, planners typically rely on the PTV to act as a surrogate for the CTV. Planned (or static) dose to the PTV is assumed to represent the dose received by the CTV when geometric uncertainties are accounted for.

Margins that are sized according to margin formulas can be expected to be reasonably accurate in ensuring target coverage or normal tissue sparing in many cases. However, margin formulas are approximations based on sampled data[8] or idealized models.[9] For instance, the margin formula of van Herk *et al.* is based on a model that assumes an error-function-shaped beam penumbra. Real beam penumbras do not fit this assumption, leading to possible inaccuracies in the calculated margins.

Furthermore, margin formulas are based on the assumption that relevant isodose surfaces (e.g., the surface for 95% of the prescription dose) will closely conform to the PTV. Proper margin sizing guarantees that the CTV remains within the PTV most of the time, ensuring the corollary that the CTV also remains within the isodose surface. However, planning rarely results in isodose surfaces that exactly conform to the PTV. Instead, isodose surfaces will touch the PTV in some areas but diverge from the surface in others. This implies a mismatch between the coverage provided by the planned dose distribution and the coverage implied by the PTV: Gaps between isodose surfaces and the PTV can cause the CTV to receive a different (sometimes higher) level of coverage than would be implied by the PTV.[11,12]

Additionally, physicians sometimes choose to shave margins where they impinge on an OAR. Here, the PTV no longer matches the assumptions made by the margin formulation and, consequently, the planned PTV dose might no longer accurately represent received CTV dose. Ultimately, coverage is a function of the margin between the CTV and the treated volume (TV) (the volume enclosed by a critical isodose surface) not the PTV. This is not a new observation. It motivates the conformity index defined in ICRU Report No. 62, and earlier studies that have directly evaluated target coverage through simulation.[13]

For the reasons given above, it is desirable to explicitly evaluate the coverage provided to CTVs and OARs and not simply assume that PTVs and PRVs achieve the nominal coverage that is implied by the PTV/PRV margin. The dosimetric margin (DM) and dosimetric margin distribution (DMD) are tools that can be used to evaluate coverage.[12] Clinically, they can be used to evaluate coverage probabilities for postplanning quality assurance (QA), specifically the probabilities that the desired target coverage and normal tissue structure sparing will be achieved. Additionally, although this option is not considered in the present work, the computed probabilities can be incorporated as an objective into a plan optimization to produce coverage optimized treatment plans.[14,15]

Intuitively, the DM is the distance in a specified direction between a structure—CTV or OAR—and a specified isodose surface. More precisely, the DM $M_{v,d}(\varphi,\theta)$ is the maximum distance that the structure can be offset in the specified direction, while still satisfying a dose constraint $D_v \geq d$ for CTV (or $D_v \leq d$ for OAR), where D_v is the dose to v% of the structure's volume and d is its planned goal. For example, for a CTV dose constraint $D_{\min} \geq 79.2$ Gy (equivalent to $D_{100} \geq 79.2$ Gy), $M_{\min,79.2}(\varphi,\theta)$ [or $M_{100,79.2}(\varphi,\theta)$] denotes the maximum distance the CTV can be offset in the direction (φ,θ) before its $D_{\min}$ falls below 79.2 Gy. Similarly, for an OAR dose constraint $D_{25} \leq 70$ Gy, $M_{25,70}(\varphi,\theta)$ denotes the maximum distance the OAR can be offset in the direction (φ,θ) before its D_{25} exceeds 70 Gy. The DMD is the distribution of DMs $M_{v,d}(\varphi,\theta)$ over all directions.

Once evaluated, the DMD can be used to calculate coverage probabilities for the CTV and OAR. Coverage is defined to be the percentage of uncertainties (e.g., the percentage of organ motions) for which $D_v \geq d$ (see Sec. II). As discussed above, computed coverage is preferred to the nominal coverage implied by PTV and PRV margins. Practical implementation requires the DMD to be sampled over a finite number of directions (φ,θ) using a finite step size along each direction. The accuracy or errors in the calculated dosimetric margins and derived coverage estimates are a function of the angular and distance increments that are utilized in the evaluation. By computing DMDs and coverage values for 28 prostate plans, this paper quantifies the sensitivity of coverage estimates to these sampling parameters. DMD sampling parameters that provide acceptable accuracy for plan evaluation are also determined.

II. METHODS AND MATERIALS

II.A. Prostate plans

This work utilized 28 anonymized prostate anatomies taken from a clinical database with Institutional Review Board approval. Treatment plans were for localized prostate cancer, so targeted only the prostate and proximal seminal vesicles. The CTV consisted of the GTV plus bilateral seminal vesicles lying within 10 mm of the prostate. The PTV was the CTV expanded uniformly by 10 mm. OARs consisted of the rectum, bladder, and femoral heads. Plans utilized seven coplanar (transverse) beams. Optimization criteria for the PTV were $D_{\min} \geq 79.2$ Gy and $D_{\max} \leq 84.7$ Gy. The target minimum dose of 79.2 Gy mirrored the high dose arm of Radiation Therapy Oncology Group (RTOG) Protocol 0126 (www.rtog.org).[16] OAR criteria for the bladder and rectum were taken from RTOG 0126. For the bladder, they were $D_{\max} \leq 84.7$ Gy, $D_{15} \leq 80$ Gy, $D_{25} \leq 75$ Gy, $D_{35} \leq 70$ Gy, and $D_{50} \leq 65$ Gy. For the rectum, they were $D_{\max} \leq 84.7$ Gy, $D_{15} \leq 75$ Gy, $D_{25} \leq 70$ Gy, $D_{35} \leq 65$ Gy, and $D_{50} \leq 60$ Gy. Left and right femoral heads were required to have $D_{\max} \leq 50$ Gy and $D_{50} \leq 35$ Gy. Plans were optimized using a research version (8.1w) of the Pinnacle treatment planning system (Philips Medical Systems, Fitchburg, WI) using standard direct machine parameter optimization and a $2 \times 2 \times 2$ mm dose grid. As the dose distributions in the final optimized plans do not explicitly incorporate setup errors, they are referred to as static plans.

II.B. Geometric uncertainty model

This work considered rigid body interfraction setup uncertainties (i.e., rigid body shifts of the patient anatomy with respect to the treatment beams). Ideally, it would be desirable to use uncertainty models derived from validated deforma-

tion models of the prostate anatomy; however, techniques for generating such models are not yet standardized and remain an active area for research. Given that the goal of the present paper is to find acceptable parameters for DMD evaluation, not to perform DMD evaluation for a specific group of patients, the use of rigid body uncertainties was considered acceptable. Following the model of van Herk *et al.*,[9] uncertainties were assumed to have systematic (preparation) and random (per fraction) components. Both components were assumed to be normally distributed with standard deviations (SDs) Σ (systematic) and σ (random) along each axis [right-left (RL), posterior-anterior (PA), and superior-inferior (SI)]. The 10 mm CTV-to-PTV margin used to design the static plan (above) is consistent with the margin formula of van Herk *et al.*, $M=2.5\Sigma+0.7\sigma\approx 10$ mm for $\Sigma=\sigma=3$ mm.

After optimization, the effect of geometric uncertainties on the planned dose distribution was evaluated. Random errors were incorporated into the plan evaluation by computing the planned dose distribution after convolving beam fluences with a normal kernel having SD $\sigma=3$ mm. This technique is commonly referred to as fluence convolution[17] and is designed to model the blurring effect of many (e.g., 30) random (per fraction) setup uncertainties on the dose distribution. The implementation used here was the same as in the previous studies.[12,14] Fluence convolution was enabled via a script command. When enabled, each beam's 2D fluence after all beam defining elements (jaws and MLC), but before the patient, is convolved with the abovementioned normal kernel using a fast Fourier transform convolution. The patient dose calculation then uses the convolved fluences in place of the original fluences. Fluence convolution has been found to be a reasonable approach to approximate the cumulative effect of random errors for treatment courses consisting of ~30 fractions.[18,19]

Dosimetric margins were calculated for the CTV, bladder, and rectum relative to appropriate isodose surfaces. The dosimetric margins represent the "safety margin" for absorbing systematic uncertainties. That is, as described below, coverage could be calculated from the DMD using the systematic SD Σ only, random uncertainties having been accounted for through fluence convolution.

II.C. Dosimetric margin calculations

The following dosimetric margins were evaluated: CTV $M_{\min,79.2}$, bladder $M_{25,75}$ and bladder $M_{25,80}$, and rectum $M_{25,70}$ and rectum $M_{25,75}$. Dosimetric margin calculations assumed shift invariance of the dose distribution, which has been shown to be reasonable for prostate plans.[18] (Shift invariance may not be a valid assumption for other sites, such as head and neck.) The dosimetric margin in each direction was calculated by moving the structure in steps of δ relative to the dose distribution, until the relevant dose metric (e.g., CTV $D_{\min}$) crossed the specified dose value (e.g., until CTV $D_{\min}$ fell below 79.2Gy). The results were compared for step sizes δ=1, 0.5, 0.2, and 0.1 mm.

In each direction, structures were stepped out to a maximum distance of 25 mm. The reason of this "cutoff" is that for OAR there are directions (e.g., away from the high dose region) for which the relevant dose metric will never cross the specified isodose. For the range of setup errors (Σ values) considered in this work, there is negligible probability of displacements greater than or equal to 25 mm. Therefore, the 25 mm cutoff was sufficiently large to ensure accurate coverage calculations.

DMDs were sampled over differing numbers of directions using two different techniques: Fixed angular increment (FAI) and isotropic sampling (ISO). The FAI method was applied to the CTV, bladder, and rectum. The ISO method was applied to the CTV only. In the FAI method, dosimetric margins were calculated for directions $\varphi=n\omega$ and $\theta=m\omega$, where φ is the elevation angle and θ is the azimuthal angle (φ=90° being the patient's superior-inferior axis and θ=0° being the patient's right-left axis). The values ω=20°, 10°, 5°, 2°, and 1° (for CTV) or ω=20°, 10°, 4°, and 2° (for bladder and rectum) were used, and integers n and m were incremented from $-90/\omega$ to $90/\omega$ and from $-180/\omega$ to $180/\omega-1$, respectively. The number of FAI directions is a function of ω,

$$N_d=2+\left(\frac{180}{\omega}-1\right)\cdot\frac{360}{\omega}, \tag{1}$$

where N_d ranges from 146 for ω=20° to 64 442 for ω=1°. A feature of the FAI method is that the steradians covered by each angular segment become smaller as one approaches the poles (i.e., as φ goes to ±90°).

The ISO method used directions that were approximately isotropically distributed across 4π sr. There is no general analytic solution for sets of N_d isotropic directions covering the unit sphere. Consequently, the spinal point solution was employed.[20] Based on the required number of directions, this method gives a set of angles (φ,θ), which closely approximate an isotropic distribution. In comparing the FAI and ISO results, the same number of directions was employed. ISO results presented below are given as a function of the *effective* angular increment ω_{eff}, which is the fixed angular increment that would give the same number of sampling directions.

In calculating DMDs for a target (i.e., CTV), one is most often concerned with a dose metric (e.g., CTV $D_{\min}$) starting above a dose threshold in the structure's static position and falling below the threshold as the structure moves out of the high dose region (type I target). However, it can sometimes happen that in a particular plan the dose metric starts off already below the desired threshold and can be increased above the threshold for some positional offsets (type II target). Conversely, for an OAR, one is most often concerned with a dose metric starting below a threshold and moving above the threshold as the structure moves into the high dose region (type I OAR). However, for some cases, the metric may start off above the desired threshold and fall below the threshold for some structure offsets (type II OAR).

The presence of type II structures indicates that the static plan does not meet the dose-volume criteria. For example, a CTV, which is of type II for the margin $M_{\min,79.2}$, starts off in

the static plan having $D_{min}<79.2$ Gy but may experience $D_{min}\geq 79.2$ Gy for some offsets. A bladder, which is of type II for the margin $M_{25,75}$, starts off in the static plan having $D_{25}>75$ Gy but may experience $D_{25}\leq 75$ Gy for some offsets. The distinction between type I and type II cases is emphasized here primarily because it affects the details of the DMD calculation. In the "nonstandard' (type II) cases, dosimetric margins are still calculated as the maximum distance that the structure can move before crossing the dose threshold, but coverage formulas are modified as described below. Also, the type I/II distinction helps one understand why type II targets tend to have low coverage values and type II OAR high coverage values, both of which are undesirable situations. However, regardless of whether a structure is of type I or type II (for a given margin/criterion), the interpretation of coverage Q is unchanged.

II.D. Coverage calculation

For both targets and OAR, coverage $Q_{v,d}$ is defined to be the probability that a dose metric D_v exceeds dose d: $Q_{v,d}=\Pr[D_v\geq d]$. For a target dose constraint $D_v\geq d$, $Q_{v,d}$ is the probability that the constraint will be *satisfied*, so high coverage values (e.g., 95%) are desirable. For an OAR dose constraint $D_v\leq d$, $Q_{v,d}$ is the probability that the constraint will be *violated*, so low coverage values (e.g., 5%) are desirable. In the following, the symbol $Q_{v,d}$ is simplified to Q, where v and d are not explicitly required or are clear from the context.

Because random errors are accounted for via fluence convolution, Q is a function of the DMD and the standard deviation of systematic errors Σ. For normally distributed systematic uncertainties, the cumulative distribution function of 3D displacements r is given by[9]

$$F(r,\Sigma)\equiv \text{normcdf}\ \ 3\text{D}(r,\Sigma)$$
$$=\text{erf}(r/\sqrt{2}\Sigma)-(2/\sqrt{\pi})(r/\sqrt{2}\Sigma)\exp(-r^2/2\Sigma^2), \quad (2)$$

where erf() is the error function. Coverage in the direction (φ,θ) is given by

$$Q(\varphi,\theta,\Sigma)=\begin{cases}F(M_{v,d}(\varphi,\theta),\Sigma) & \text{type I target/type II OAR}\\ 1-F(M_{v,d}(\varphi,\theta),\Sigma) & \text{type II target/type I OAR,}\end{cases} \quad (3)$$

where $M_{v,d}(\varphi,\theta)$ is the dosimetric margin in direction (φ,θ). The overall coverage $Q(\Sigma)$ becomes

$$Q(\Sigma)=\sum_{\varphi,\theta}W_{\varphi,\theta}Q(\varphi,\theta,\Sigma), \quad (4)$$

where $W_{\varphi,\theta}$ is a weighting factor equal to the fraction of 4π sr covered by the ray in the direction (φ,θ). For isotropic sampling with N_d directions, $W_{\varphi,\theta}\equiv(1/N_d)\,\forall(\varphi,\theta)$. For the FAI method, it is given by

$$W_{\varphi,\theta}=\begin{cases}\dfrac{1-\cos\left(\frac{\omega}{2}\right)}{2} & \varphi=90^\circ \quad \text{or} \quad \varphi=-90^\circ\\ \dfrac{\omega}{720}\cdot\left[\sin\left(\varphi+\dfrac{\omega}{2}\right)-\sin\left(\varphi-\dfrac{\omega}{2}\right)\right] & \varphi=90^\circ-\omega,90^\circ-2\omega,\ldots,-90^\circ+\omega.\end{cases} \quad (5)$$

Although planning is done assuming $\Sigma=3$ mm, coverage probabilities are computed for a range of potential systematic errors ($\Sigma=0$–7 mm) to ensure identification of DMD sampling parameters that would provide accurate coverage estimates across a range of Σ values. The use of multiple Σ values also illustrates the types of studies that could be performed as part of plan evaluation. Specifically, it address the question: How do target and OAR coverage values vary if the systematic SD Σ differs from its assumed value?

II.E. Coverage uncertainty analysis

Sampling of the DMD over a finite number of directions and using a finite step size δ will introduce some error or uncertainty into coverage estimates. To quantify this uncertainty, we assume that sufficiently small angular and distance sampling parameters give negligible error. Specifically, we assumed that "baseline" coverage estimates with $\omega=1^\circ$ (or 64 442 isotropic directions) for CTV and $\omega=2^\circ$ (or 16 022 isotropic directions) for bladder and rectum give negligible error due to angular gradients in the dosimetric margin. (When quantifying estimation errors due to ω, baseline DM calculations use $\omega=1^\circ$ and $\delta=1$ mm for the CTV and $\omega=2^\circ$ and $\delta=1$ mm for the bladder and rectum.) Similarly, we assumed that baseline coverage estimates with $\delta=0.1$ mm give negligible error due to radial dose gradients. (When quantifying estimation errors due to finite δ, baseline DM calculations use $\omega=10^\circ$ and $\delta=0.1$ mm for the CTV, bladder, and rectum.) For other values of the sampling parameters ω and δ, coverage uncertainty is estimated by taking the difference with respect to baseline parameters. For example, the uncertainty due to $\omega=5^\circ$ for a certain Σ is determined by $\Delta Q(\Sigma)=Q(\Sigma)|_{\omega=5^\circ,\delta=1\ \text{mm}}-Q(\Sigma)|_{\omega=1^\circ,\delta=1\ \text{mm}}$.

In addition to the sampling parameters ω and δ, Q is a function of Σ. As Σ is varied, coverage will vary, as shown

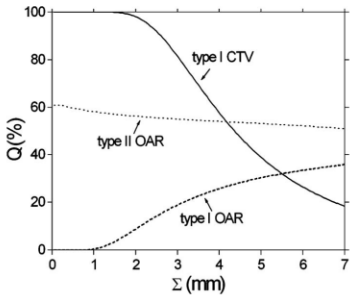

FIG. 1. Variation in the coverage probability Q with systematic standard deviation Σ for type I targets and type I/II OAR. Plots were obtained from patient 28 by calculating CTV $M_{\min,79.2}$ (type I), bladder $M_{25,75}$ (type II), and rectum $M_{25,70}$ (type I) and then computing coverage Q [Eqs. (2)–(4)] for Σ values ranging from 0 to 7 mm. The purpose of these plots is to illustrate the qualitative dependence of Q on Σ, not the specific coverage values obtained for patient 28.

in Fig. 1. Figure 1 was obtained from patient 28 by calculating CTV $M_{\min,79.2}$(type I), bladder $M_{25,75}$ (type II), and rectum $M_{25,70}$ (type I) and then computing the coverage Q [Eqs. (2)–(4)] for Σ values ranging from 0 to 7 mm. The purpose of Fig. 1 is to illustrate the qualitative dependence of Q on Σ for type I targets and type I/II OAR, not the specific coverage values obtained for patient 28. As Σ increases, type I target or type II OAR coverage decreases, while type I OAR coverage increases.

This work calculates $\Delta Q_{\min}$ and $\Delta Q_{\max}$ as the minimum and maximum values of $\Delta Q(\Sigma)$ taken over Σ values in the range [0, 7 mm],

$$\Delta Q_{\min} = \min_{\Sigma}[Q(\Sigma)_{\omega,\delta} - Q(\Sigma)_{\text{baseline}}], \tag{6}$$

$$\Delta Q_{\max} = \max_{\Sigma}[Q(\Sigma)_{\omega,\delta} - Q(\Sigma)_{\text{baseline}}]. \tag{7}$$

Here, $\Delta Q_{\min}$ and $\Delta Q_{\max}$ are sometimes simply referred to as ΔQ for short in the following paragraphs. The results presented below plot the range of 56 ΔQ obtained from the 28 prostate plans as a function of the sampling parameters ω and δ.

DM calculations were performed using a C++ interface to the Pinnacle treatment planning system that allowed the dose distribution to be moved relative to regions of interest (mathematically equivalent to moving structures relative to the dose distribution) and the resulting metric values D_v to be calculated. Additional numerical analysis, including coverage estimation, was performed outside of Pinnacle using MATLAB (MathWorks, Natick, MA).

III. RESULTS

III.A. Coverage values

Figure 2 illustrates the ranges of coverage values obtained for the prostate, bladder, and rectum across the 28 plans. It plots ranges for CTV $Q_{\min,79.2}(\Sigma)$, bladder $Q_{25,75}(\Sigma)$, and rectum $Q_{25,70}(\Sigma)$ for Σ=1, 3, and 5 mm. The results for Σ=1 and 5 mm illustrate what happens if Σ differs from the assumed value Σ=3 mm: Coverage varies substantially. For each box plot, the upper and the lower markers indicate the maximum and minimum values, the box extends from the 10th to 90th percentile, and the triangle is the median value. Coverage values in Fig. 2(a) were calculated using ω=1° and δ=1 mm. Consistent with Fig. 1, CTV coverage decreases as Σ increases. CTV coverage at the prescription dose (79.2 Gy) is ~100% for Σ=1 mm but ranges from approximately 20% to 100% for Σ=5 mm. In the case of the CTV, all plans were of type I (i.e., had CTV static $D_{\min}$ > 79.2 Gy). Figure 2(a) compares coverage values obtained using the FAI (left) versus the ISO (right) methods. The two methods give almost identical results, indicating that for ω =1° and δ=1 mm, the DMD does not depend on the sampling method.

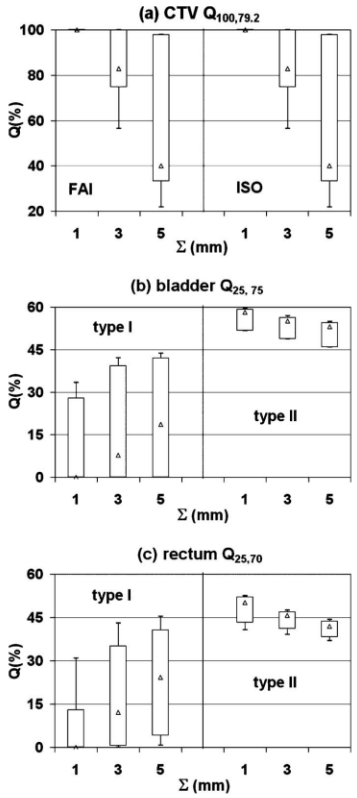

FIG. 2. Box plots of $Q(\Sigma)$: (a) CTV $Q_{\min,79.2}$ obtained using the FAI (left) and ISO (right) methods, (b) bladder $Q_{25,75}$ for type I (left) and type II (right) plans (FAI method), and (c) rectum $Q_{25,70}$ for type I (left) and type II (right) plans (FAI method). The upper and the lower markers are the maximum and minimum values taken over the 28 plans, the box extends from the 10th to 90th percentile, and the triangle is the median value.

Figure 2(b) plots ranges for bladder $Q_{25,75}$. Coverage values in Fig. 2(b) were calculated using $\omega=2°$ and $\delta=1$ mm. For the bladder, 23 plans were of type I (static $D_{25}<75$ Gy) and 5 of type II (static $D_{25}>75$ Gy). Type II plans were for anatomies in which the bladder was in close proximity to the prostate, ensuring that in the planned dose distribution more than 25% of its volume received >75 Gy. Figure 2(b) shows the range of coverage values for the type I (left) and type II (right) plans. Consistent with Fig. 1, as Σ increases, coverage of type I OARs increases, while coverage of type II OARs decreases. Bladder coverage values range from 0% to ~60% across the 28 plans.

Figure 2(c) plots ranges for rectum $Q_{25,70}$. Coverage values in Fig. 2(c) were calculated using $\omega=2°$ and $\delta=1$ mm. In the case of the rectum, 24 plans were of type I (static $D_{25}<70$ Gy) and 4 of type II (static $D_{25}>70$ Gy). Type II plans were for anatomies in which the rectum was in close proximity to the prostate, resulting in a planned dose distribution with more than 25% of its volume receiving >70 Gy. Note that type II rectum plans were mostly distinct from type II bladder plans. Only one of the 28 plans was of type II for both bladder and rectum. Figure 2(c) shows that rectum coverage values range from 0% to ~50% across the 28 plans.

III.B. Coverage uncertainties

III.B.1. CTV

To obtain the coverage uncertainties due to finite sampling of the DMD for 28 patients involved in this study, the minimum and maximum coverage differences $\Delta Q_{\min}$ and $\Delta Q_{\max}$ were calculated as in Eqs. (6) and (7). This produced 28 $\Delta Q_{\min}$ and 28 $\Delta Q_{\max}$ values (and thus a total of 56 ΔQ values) for each group of sampling parameters. Figure 3 presents the range of ΔQ values associated with CTV $Q_{\min,79.2}$. The lower marker in Fig. 3 represents the minimum of the 28 $\Delta Q_{\min}$ values and the upper marker represents the maximum of the 28 $\Delta Q_{\max}$ values. The boxes indicate the 10th and 90th percentiles of the 56 $\Delta Q_{\min}$ and $\Delta Q_{\max}$ values, and the triangle represents the median of the 56 $\Delta Q_{\min}$ and $\Delta Q_{\max}$ values.

Figure 3(a) plots the range of ΔQ values as a function of the angular increment ω. In this case, ΔQ values were calculated relative to baseline coverage values obtained with $\omega=1°$ and $\delta=1$ mm. Figure 3(b) plots the range of ΔQ values as a function of the radial step size δ. In this case, ΔQ values were calculated relative to the baseline coverage values obtained with $\omega=10°$ and $\delta=0.1$ mm. Taken together, Figs. 3(a) and 3(b) show that the uncertainty in the estimated CTV coverage ($|\Delta Q|$) increases from <0.1% for fine sampling parameters ($\omega=2°$ and $\delta=0.2$ mm) up to about 0.8% for coarse sampling parameters ($\omega=20°$ and $\delta=1$ mm).

Also, some differences between the FAI and ISO methods are shown in Figs. 3(a) and 3(b). The ISO method produces smaller ΔQ values. This suggests that more uniform sampling of the DMD over the unit sphere—as in the ISO method—will produce better estimates of the DMD, leading to smaller ΔQ values.

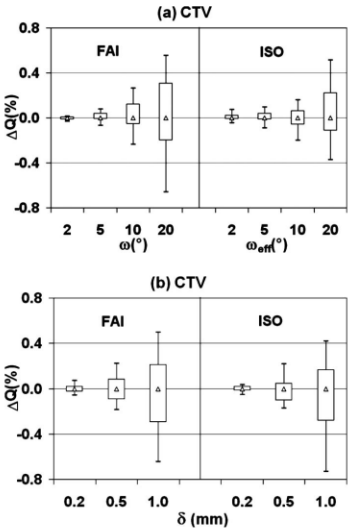

FIG. 3. ΔQ box plots for CTV $Q_{100,79.2}$ obtained using the FAI (left) and ISO (right) calculation methods: (a) ΔQ range versus $\omega=2,5,10,20°$. All Q values were calculated using $\delta=1$ mm. Baseline Q values were obtained using $\omega=1°$. (b) ΔQ range versus $\delta=0.2,0.5,1$ mm. All Q values were calculated using $\omega=10°$. Baseline Q values were obtained using $\delta=0.1$ mm. The upper and the lower markers are the maximum and minimum values taken over the 28 plans, the box extends from the 10th to 90th percentile, and the triangle is the median value.

III.B.2. OAR

Figures 4 and 5 illustrate ΔQ ranges for the bladder and rectum. The minimum, maximum, 10th and 90th percentiles, and median of the 56 ΔQ values are given. The bladder $Q_{25,75}$ corresponds with the bladder optimization criterion $D_{25}<75$ Gy. For this criterion, 23 patient bladders were a type I structure, while the remaining 5 were of type II. The $Q_{25,80}$ plot shows how coverage varies with the isodose surface for which coverage is evaluated. Variability is less for the 80 Gy isodose surface, for which all 28 patient bladders are of type I. Figure 5 presents similar results for the rectum $Q_{25,70}$ and $Q_{25,75}$. There are 24 type I rectums for $Q_{25,70}$ and 28 for $Q_{25,75}$.

IV. DISCUSSION

All IMRT plans used in this study were generated with uniform 10 mm CTV-to-PTV margins. They were evaluated using interfraction setup uncertainties having random SD $\sigma=3$ mm (modeled via fluence convolution) and a range of systematic SDs Σ. According to the margin formula of van Herk *et al.*,[9] for $\sigma=3$ mm and $\Sigma=3$ mm, a 10 mm margin is supposed to ensure that CTV $D_{\min}$ exceeds the prescription dose (strictly, the planned PTV $D_{\min}$) for 90% of motion. That is, the 10 mm margin is supposed to ensure that $Q_{\min,79.2}$ exceeds 90% for all plans.

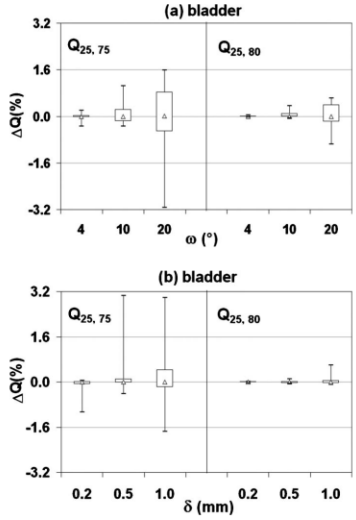

FIG. 4. ΔQ box plots for bladder $Q_{25,75}$ and $Q_{25,80}$ obtained using the FAI calculation method: (a) ΔQ range versus $\omega=4,10,20°$. All Q values were calculated using $\delta=1$ mm. Baseline Q values were obtained using $\omega=2°$. (b) ΔQ range versus $\delta=0.2,0.5,1$ mm. All Q values were calculated using $\omega=10°$. Baseline Q values were obtained using $\delta=0.1$ mm. The upper and the lower markers are the maximum and minimum values taken over the 28 plans, the box extends from the 10th to 90th percentile, and the triangle is the median value.

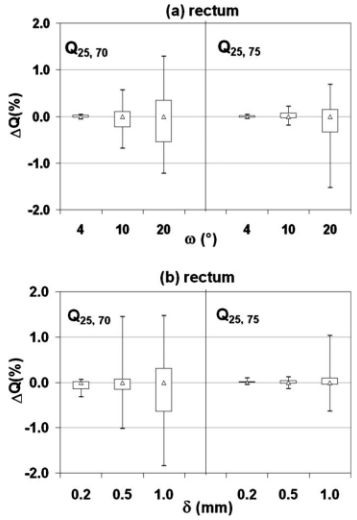

FIG. 5. ΔQ box plot for rectum $Q_{25,70}$ and $Q_{25,75}$ obtained using the FAI calculation method: (a) ΔQ range versus $\omega=4,10,20°$. All Q values were calculated using $\delta=1$ mm. Baseline Q values were obtained using $\omega=2°$. (b) ΔQ range versus $\delta=0.2,0.5,1$ mm. All Q values were calculated using $\omega=10°$. Baseline Q values were obtained using $\delta=0.1$ mm. The upper and the lower markers are the maximum and minimum values taken over the 28 plans, the box extends from the 10th to 90th percentile, and the triangle is the median value.

In clinical plans, this may not occur for two reasons: (a) Competition between target and OAR optimization criteria causes the target dose to fall short of the prescription dose and (b) the treated volume, which is a function of the beam arrangement and individual anatomy, provides a different level of coverage than the PTV was intended to achieve. Both effects contribute to variability of the target coverage. In Fig. 2(a), for $\Sigma=3$ mm, $Q_{\min,79.2}$ varies from ~56% to 100%, with a median value of approximately 83%. These results emphasize the degree to which target coverage depends on the individual patient anatomy and the quality of the IMRT plan, in addition to the PTV margin. In clinical planning, it is common practice to use a standard CTV-to-PTV expansion and simply assume that the resulting PTV ensures an acceptable level of robustness to setup errors and other geometric uncertainties.

Figures 2(b) and 2(c) emphasize the wide range of coverage values that can be experienced by OAR. For $\Sigma=3$ mm, Fig. 2(c) shows that rectum $Q_{25,70}$ varies from 0% to ~50%. That is, for some patients, rectum D_{25} could exceed the 70 Gy constraint (tolerance dose) for as many as 50% of the treatment courses. Most OARs are of type I versus type II. Type I (II) OARs are those that satisfy (violate) the dose constraint (e.g., rectum $D_{25}\leq 70$ Gy) in the static plan. Based on the static plan, it appears that type I OARs are adequately protected—they satisfy their optimization constraints. However, Figs. 2(b) and 2(c) show that even a type I OAR can have a significant probability of exceeding optimization constraints, once probable patient offsets are considered. In general, one would like to ensure that OAR dose constraints (e.g., rectum $D_{25}\leq 70$ Gy) are violated for only a small percent, e.g., 5%, of treatment courses.

Figure 2 emphasizes the desirability of evaluating the actual, as opposed to the nominal, level of the target coverage provided by a PTV expansion. For some patients, if a standard PTV does not provide acceptable coverage, it may be desirable to further expand the PTV until treatment goals are achieved. For others, PTV reduction might continue to yield adequate CTV coverage while affording lower coverage probabilities for OARs. Figure 2 also emphasizes the desirability of postplanning evaluation of OAR coverage. The clinical significance of Fig. 2 is that when geometric uncertainties are considered, patient-specific characteristics can have a large effect on the target and OAR coverages even when the plans are created with the same margin and analyzed using the same assumptions regarding setup errors. Coverage analysis would identify those plans whose CTV coverage falls below some threshold (e.g., 90%, as in the margin formula of van Herk *et al.*), or whose OAR coverage exceeds some threshold (e.g., 10%), allowing replanning to be performed.

In Figs. 2(b) and 2(c), there are differences between the type I and type II results. Type I OARs are from patients with favorable anatomies, in which the rectum and bladder were adequately separated from the prostate. In these patients, OAR coverage values tend to be low. A small number of

patients had unfavorable anatomies, in which the (type II) rectum and bladder were close to the prostate. In these patients, OAR coverage values tend to be high. The gap between type I and type II coverage ranges in Figs. 2(b) and 2(c) is hypothesized to be due to the relatively small number of type II "outlier" patients in the sample. A larger sample might include patients with OAR that are intermediate between the type I and type II samples in Fig. 2. One can speculate that in this case, the coverage ranges for types I and II would join (at Q around 50%) and become contiguous. These hypotheses would need to be proved or rejected by sampling a larger patient population, which is outside the scope of the present paper.

The DMD is a useful tool for evaluating target and OAR coverage. When combined with a geometric uncertainty model, such as the simple normal uncertainty model given in Eq. (2), or more complex models derived from imaging studies, it can be used to quantify coverage as in Eqs. (3) and (4). Practical implementation requires one to sample the DMD using a finite number of directions and finite spatial step size. As a practical issue, it therefore becomes necessary to determine how finely one must sample the DMD in order to derive sufficiently accurate coverage estimates. Figure 3 shows that for a compact target such as the prostate, accuracy of better than 1% ($|\Delta Q|<1\%$) can be achieved with quite coarse sampling parameters, e.g., $\omega=20°$, $\delta=1$ mm, while $\omega=10°$, $\delta=0.5$ mm will ensure $|\Delta Q|<0.5\%$. The use of isotropic sampling gives lower estimation errors due to more uniform sampling of the DMD.

Comparison of Fig. 3 with Figs. 4 and 5 shows that for the same sampling parameters ω and δ, the uncertainty $|\Delta Q|$ is higher for an OAR than it is for the CTV. For example, ΔQ values in Figs. 4 and 5 extend to $\pm 3\%$, whereas in Fig. 3 $|\Delta Q|<1\%$. Figure 6 indicates that this is most likely due to the fact that OAR coverage will be significant only for a subset of directions—specifically, those that move the OAR toward the high dose region. OAR coverage calculations therefore rely more heavily on dosimetric margins for a few directions and are consequently more sensitive to DM estimation errors for those directions.

For CTVs, one will typically require coverage at the prescription dose to be high (e.g., CTV $Q_{\min,79.2}>95\%$). Certainly one would hope that, in most cases, target coverage falls in the range of 90%–100%. In that case, it would be reasonable to require 1% accuracy for coverage estimates: $|\Delta Q|<1\%$. Accuracy of 1% allows one to distinguish with confidence plans that have, e.g., 93% or 97% target coverage from those with 95% coverage. Accuracy of 5% would clearly be too poor, whereas accuracy of much less than 1% would be unnecessary. We therefore propose $|\Delta Q|<1\%$ as a reasonable criterion for target coverage estimates. For an OAR, the goal will typically be to achieve low coverage values ($Q<5\%$) at tolerance doses. However, this goal may be sacrificed if it is in conflict with target coverage. One may end up being satisfied, for example, with rectum $Q_{25,70}<20\%$. In this case, it may not be necessary to estimate OAR coverage values to the same degree of accuracy as

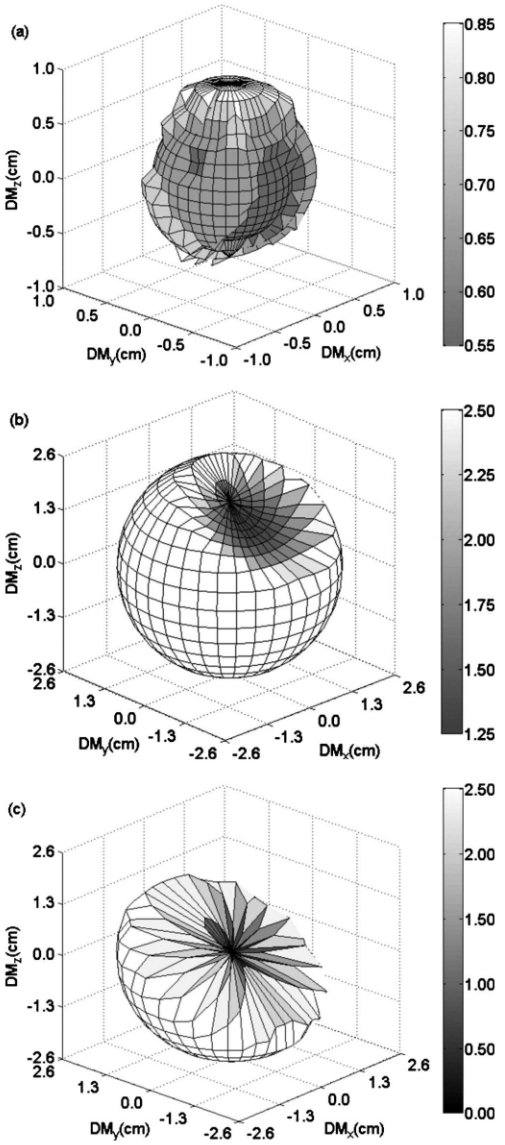

FIG. 6. Example DMDs obtained using the FAI method, plotted on the 3D axes. (a) Patient 4 CTV $D_{\min,79.2}$ (type I), (b) patient 27 bladder $D_{25,75}$ (type I), and (c) patient 21 bladder $D_{25,75}$ (type II). DM_x is the RL component of the dosimetric margin (i.e., the dosimetric margin projected onto the patients RL axis). DM_y and DM_z are the PA and SI components.

CTV coverage values. It may be acceptable, for example, if $|\Delta Q|<3\%$. This can be achieved with sampling parameters: $\omega=20°$, $\delta=1$ mm. More accurate OAR coverage estimates can be achieved by using finer sampling parameters or by

using an adaptive strategy that samples the DMD more finely in the directions that move the OAR toward the high dose region. The latter remains an area for further research. We note that our suggested accuracy criteria—$|\Delta Q|<1\%$ for targets and $|\Delta Q|<3\%$ for OAR—are a reasonable but subjective choice. The purpose of this paper is to quantify the dependence of $|\Delta Q|$ on sampling parameters. Using the results of this paper, users can set DMD sampling parameters to appropriate values to give more accurate coverage estimates, if desired.

This work assumed a simple rigid body uncertainty model, in which interfraction setup uncertainties are normally distributed. Intrafraction motion was not modeled. The assumed baseline parameter values $\Sigma=\sigma=3$ mm are broadly in line with the values reported in literature for setup to external markers.[21] For image-guided setup, interfraction setup errors will be smaller, but in order to properly account for geometric uncertainties, one should also account for intrafraction motion[22–24] and delineation errors.[25] The present work did not go to this level of detail. One could also contemplate adaptive replanning throughout the treatment course. This approach complements image-guided setup and has the potential to further reduce geometric uncertainties by generating plans that are tailored to the patient's anatomy on each treatment day. However, even with adaptive planning, geometric uncertainties are likely to persist due to factors such as image-registration errors and intrafraction motion.

It is important to note that the results in Fig. 2 are strongly dependent on the assumed uncertainty model and on the margin that was employed. Different setup and adaptive planning strategies will produce different uncertainty models and therefore will produce quantitatively different results from Fig. 2. Nevertheless, the qualitative features in Fig. 2 are expected to occur for other uncertainty models: It is expected that target and OAR coverage will vary significantly between patients even when the same motion model and CTV-to-PTV margin are employed. Thus, our conclusions regarding the desirability of performing postplan coverage evaluation are likely to remain valid, regardless of the uncertainty model specifics.

Figures 3–5 quantify the relative errors that can occur in coverage estimates based on the sampling parameters ω and δ. These results are chiefly a function of the DMD algorithm, not the uncertainty/motion model. In the future, it will be desirable to perform postplan coverage evaluation using validated deformable motion models for prostate, bladder, and rectum. These types of deformable models are being actively researched and are likely to emerge from principle components analysis once sufficient data and experience have been accumulated. Our conclusion regarding adequate values for ω and δ are expected to remain valid for these models.

Postplan coverage evaluation will add some time to the overall therapy process. The nonoptimized DMD algorithm used for this work took on the order of 30 min/patient for parameter values $\omega=10°$, $\delta=0.5$ mm on a 1.6 GHz SunFire V445. Run times on modern hardware and with optimized code would likely be substantially less. The algorithm was completely scripted within the Pinnacle treatment planning system and could be executed with a single (script) button push. Clinically, we envision that coverage evaluation could be performed as a standard part of postplanning QA. Coverage that is judged to be unacceptable could require replanning. This decision would need to be made on-balance with respect to other plan evaluation parameters such as DVHs, isodoses, and the physician's knowledge/experience. As in other cases where a plan fails a QA step, replanning would need to be performed with alternative planning parameters—most likely, a change in margin, either for an entire structure, or in a specific location. However, replanning might also entail a change in treatment angles or other parameters that affect the shape of the periphery of the dose distribution. As experienced is gained, we speculate that efficient ways to adjust plans will likely be discovered by the dosimetrists/treatment planners. This provides a model for how postplan coverage evaluation could be performed as part of the treatment workflow without imposing an undue burden.

V. CONCLUSIONS

Postplanning evaluation shows that realized target coverage can fall short of the nominal value implied by standard CTV-to-PTV margin expansions. The evaluation of OAR coverage shows a wide range of realized coverage values. In most cases, OARs are of type I (i.e., satisfy their dose constraints in the static plan) but can still have a significant probability of exceeding the dose constraints when patient offsets are accounted for. These results emphasize the desirability of performing postplanning coverage evaluation. Target and OAR coverage vary with individual patient anatomy and with plan quality. Postplan evaluation enables the effect of geometric uncertainties to be accurately assessed prior to treatment.

The accuracy of coverage estimates depends on angular and radial DMD sampling parameters ω and δ. The results suggest that coarse sampling parameters ($\omega=20°$, $\delta=1$ mm) will achieve accuracy $|\Delta Q|<1\%$ in target coverage estimates and accuracy of $|\Delta Q|<\sim 3\%$ in OAR coverage estimates. Finer sampling parameters ($\omega=10°$, $\delta=0.5$ mm) will achieve accuracy $|\Delta Q|<0.5\%$ in target coverage estimates and accuracy of $|\Delta Q|<\sim 1\%$ in OAR coverage estimates, which is judged to be sufficiently accurate for planning purposes. Even finer DMD sampling ($\omega<10°$, $\delta<0.5$ mm), which would require significant processing time by the treatment planning system, is unlikely to be required.

ACKNOWLEDGMENTS

This work was supported, in part, by NIH Grant No. P01CA116602 and by a research contract with Philips Medical Systems.

[a]Electronic mail: xuh2@vcu.edu

[1]J. M. Wilkinson, "Geometric uncertainties in radiotherapy," Br. J. Radiol. **77**(914), 86–87 (2004).
[2]ICRU, "Prescribing, recording and reporting photon beam therapy," Report No. 50 (ICRU, Bethesda, MD, 1994).
[3]ICRU, "Prescribing, recording and reporting photon beam therapy (Supplement to ICRU Report 50)," Report No. 62 (ICRU, Bethesda, MD, 2000).

[4]L. P. Muren, R. Smaaland, and O. Dahl, "Organ motion, set-up variation and treatment margins in radical radiotherapy of urinary bladder cancer," Radiother. Oncol. **69**(3), 291–304 (2003).
[5]S. W. Lee *et al.*, "Patterns of failure following high-dose 3-D conformal radiotherapy for high-grade astrocytomas: A quantitative dosimetric study," Int. J. Radiat. Oncol., Biol., Phys. **43**(1), 79–88 (1999).
[6]M. R. Button, C. A. Morgan, E. S. Croydon, S. A. Roberts, and T. D. Crosby, "Study to determine adequate margins in radiotherapy planning for esophageal carcinoma by detailing patterns of recurrence after definitive chemoradiotherapy," Int. J. Radiat. Oncol., Biol., Phys. **73**(3), 818–823 (2009).
[7]L. Ekberg, O. Holmberg, L. Wittgren, G. Bjelkengren, and T. Landberg, "What margins should be added to the clinical target volume in radiotherapy treatment planning for lung cancer?," Radiother. Oncol. **48**(1), 71–77 (1998).
[8]J. C. Stroom, H. C. de Boer, H. Huizenga, and A. G. Visser, "Inclusion of geometrical uncertainties in radiotherapy treatment planning by means of coverage probability," Int. J. Radiat. Oncol., Biol., Phys. **43**(4), 905–919 (1999).
[9]M. van Herk, P. Remeijer, C. Rasch, and J. V. Lebesque, "The probability of correct target dosage: Dose-population histograms for deriving treatment margins in radiotherapy," Int. J. Radiat. Oncol., Biol., Phys. **47**(4), 1121–1135 (2000).
[10]M. van Herk, "Errors and margins in radiotherapy," Semin. Radiat. Oncol. **14**(1), 52–64 (2004).
[11]J. J. Gordon, A. J. Crimaldi, M. Hagan, J. Moore, and J. V. Siebers, "Evaluation of clinical margins via simulation of patient setup errors in prostate IMRT treatment plans," Med. Phys. **34**(1), 202–214 (2007).
[12]J. J. Gordon and J. V. Siebers, "Evaluation of dosimetric margins in prostate IMRT treatment plans," Med. Phys. **35**(2), 569–575 (2008).
[13]B. C. Cho, M. van Herk, B. J. Mijnheer, and H. Bartelink, "The effect of set-up uncertainties, contour changes, and tissue inhomogeneities on target dose-volume histograms," Med. Phys. **29**(10), 2305–2318 (2002).
[14]J. J. Gordon and J. V. Siebers, "Coverage-based treatment planning: Optimizing the IMRT PTV to meet a CTV coverage criterion," Med. Phys. **36**(3), 961–973 (2009).
[15]J. J. Gordon, N. Sayah, E. Weiss, and J. V. Siebers, "Coverage optimized planning: Probabilistic treatment planning based on dose coverage histogram criteria," Med. Phys. **37**(2), 550–563 (2010).
[16]Radiation Therapy Oncology Group, RTOG Protocol 0126: A phase III randomized study of high dose 3D-CRT/IMRT versus standard dose 3D-CRT/IMRT in patients treated for localized prostate cancer.
[17]W. A. Beckham, P. J. Keall, and J. V. Siebers, "A fluence-convolution method to calculate radiation therapy dose distributions that incorporate random set-up error," Phys. Med. Biol. **47**(19), 3465–73 (2002).
[18]T. Craig, J. Battista, and J. Van Dyk, "Limitations of a convolution method for modeling geometric uncertainties in radiation therapy. I. The effect of shift invariance," Med. Phys. **30**(8), 2001–2011 (2003).
[19]M. van Herk, M. Witte, J. van der Geer, C. Schneider, and J. V. Lebesque, "Biologic and physical fractionation effects of random geometric errors," Int. J. Radiat. Oncol., Biol., Phys. **57**(5), 1460–1471 (2003).
[20]E. Saff and A. Kuijlaars, "Distributing many points on a sphere," Math. Intell. **19**(1), 5–11 (1997).
[21]B. Schaly, G. S. Bauman, W. Song, J. J. Battista, and J. V. Dyk, "Dosimetric impact of image-guided 3D conformal radiation therapy of prostate cancer," Phys. Med. Biol. **50**(13), 3083–3101 (2005).
[22]K. Langen *et al.*, "Observations on real-time prostate gland motion using electromagnetic tracking," Int. J. Radiat. Oncol., Biol., Phys. **71**(4), 1084–1090 (2008).
[23]H. Li *et al.*, "Dosimetric consequences of intrafraction prostate motion," Int. J. Radiat. Oncol., Biol., Phys. **71**(3), 801–812 (2008).
[24]K. T. Malinowski *et al.*, "Efficient use of continuous, real-time prostate localization," Phys. Med. Biol. **53**(18), 4959–4970 (2008).
[25]C. Njeh, "Tumor delineation: The weakest link in the search for accuracy in radiotherapy," Journal of Medical Physics **33**(4), 136 (2008).

c. Interobserver contour variations with respect to margin size

Dosimetric Consequences of Interobserver Contour Variations for Localized Prostate Treatment Plans with Respect to Margin Size

Syed Naeem, Ph.D., Huijun Xu, B.S., J. James Gordon, Ph.D. , Jeffrey V. Siebers, Ph. D.*

*Department of Radiation Oncology, Virginia Commonwealth University

Corresponding Author: Jeffrey V. Siebers, Department of Radiation Oncology, Virginia Commonwealth University, 401 College Street, PO Box 980058, Richmond, VA 23298. Tel: (804) 628-7771; E-mail: jsiebers@vcu.edu

Summary

Contours for 3 prostate cancer patients were independently drawn by 4 physicians. We quantified the impact of inter-physician contour variations on DVH, TCP/NTCP, and coverage-based metrics for IMRT plans as a function of margin size. DVH-based metrics variability increased with margin due to contour deviations that are exacerbated by margin expansion. CTV, TCP, and coverage metrics variation was less; however, OAR differences persisted. Margins are insufficient to create plans that are robust to contour variations.

Abstract

Purpose: This study quantified the dosimetric impact of inter-physician contour variations as a function of margin size for prostate treatment plans and determined if margins eliminate the dosimetric consequences of contouring variability.

Methods and Materials: For 3 prostate cancer patients, independent contours of the prostate, bladder, and rectum were contoured by four independent observers. For each observer contour set, PTV-OAR and PTV-PRV based IMRT plans were generated with 0, 5, and 10 mm margins. Plans were optimized to meet RTOG-0126 protocol DVH criteria. Treatment plans were re-evaluated for the PTVs-OAR/PRVs created from contours drawn by the other three observers. Evaluation metrics include: DVH-based metrics; tissue control probability (TCP) and normal-tissue complication probability (NTCP); CTV and OAR coverage probabilities.

Results: Evaluating observer-specific PTV-OAR–based plans with alternative observers, the PTV D_{98} differed by <5% for 83%, 81%, and 72% respectively for 0, 5, and 10 mm margin plans. For PTV-PRV based plans, the PTV D_{98} differed by <5% for 83%, 86%, and 86% respectively for 0, 5, and 10 mm plans. The TCP improved from ~10% to >95% with increasing margins. The spread of interobserver coverage probability decreased (P<0.05) with increasing margins.

Conclusions: Contrary to the initial expectations, achievement of DVH-based metrics with alternative observers' contours did not increase with margin size due to protruding portions in some observers' contours which were exacerbated when margin expansion was performed. TCP and coverage probability metrics indicate that interobserver contouring variations may have little real clinical impact on the CTV; however, differences in OARs persist. Simply adding standard margins to a contour was insufficient to create a plan that was robust to interobserver

contour variability in the CTV and OARs encountered in the prostate radiation therapy plans studied.

Keywords: Contour variations, Dosimetric effect evaluation, Margin design, Prostate cancer

Introduction

Intensity-modulated radiation therapy (IMRT) treatment plans utilize target and critical structures contoured by a physician-observer. The IMRT treatment plan is designed to conform the radiation dose distributions to the target volume while limiting the dose to critical structures to be below user/protocol specified values. The use of alternative contours constructed by the same or a different physician would yield a different treatment plan. Interobserver dose-volume coverage to the prostate is known to vary due to interobserver contouring variations (1). Furthermore, interobserver critical structure variations alter dose toxicity risk assessments. While interobserver contouring deviations have been documented (1–6), only Bhardwaj et al. (1) has investigated the dosimetric consequences of such variations, finding statistically significant differences in dose-volume histograms (DVH), tumor-control probability (TCP), and normal tissue complication probability (NTCP) values for differing observer's contours with 0.6 cm posterior 1 cm elsewhere prostate margins.

Generally, safety margins are incorporated into the delineated structures to account for systematic and random uncertainties during the treatment course (7, 8). Planning target volume (PTV) and planning risk volumes (PRVs) are created from the clinical target volume (CTV) and organs at risk (OARs) by adding CTV-to-PTV and OAR-to-PRV margins in the treatment planning system (TPS) (7, 8) to account for patient offsets. Different algorithms and recipes to determine the margin size have been described, with the goal being to ensure primary target coverage (9–11). The margin formula derived by van Herk *et al.* (11) (VHMF) is designed to ensure that 90% of the patients receive at least 95% of the prescribed dose to the target structure.

It has been argued (and seems logical) that the margins can also account for interobserver contouring variations (2), however, the ability of margin expansion to remediate dosimetric consequences of interobserver contouring variations has not, to our knowledge, been documented. Target coverage and normal tissue sparing may vary due to interobserver contour variations.

Our hypothesis is that interobserver target dose-volume coverage variation will decrease with increasing margin size for prostate cancer patients. To test the hypothesis, 3 evaluation metrics were used: (1) DVH; (2) biological response indices which are TCP, NTCP, and uncomplicated tumor control probability (P+) (12); and (3) target and OAR coverage probabilities, which account for rigid body random and systematic setup errors (13, 14).

Methods and Materials

Four observers independently delineated prostate, bladder, and rectum contours for 3 prostate cancer patients. (5) Two types of IMRT plans were generated, each using 0, 5, and 10 mm margins: PTV-OAR plans and PTV-PRV plans. A total of 20 observer-specific IMRT plans were generated for each patient, each with 7 beams respectively positioned at 30°, 80°, 130°, 180°, 230°, 280°, and 330°. The plans were optimized using a 2×2×2 mm^3 dose grid resolution using Pinnacle^3 (version 9.100; Philips RadOnc Systems) to meet the DVH objectives of the high-dose arm of the RTOG-0126 protocol as follows: (1) the PTV D_{98} (dose received by 98% of the PTV volume) and D_2 of 79.2 and 84.7 Gy respectively; (2) the D_{50}, D_{35}, D_{25}, and D_{15} of the bladder (OAR/PRV) of 65, 70, 75, and 80 Gy respectively; and (3) the D_{50}, D_{35}, D_{25}, and D_{15} of the rectum (OAR/PRV) of 60, 65, 70, and 75 Gy respectively. The treatment plans were optimized with direct machine parameter optimization (DMPO).

The evaluation metrics discussed next for each observer-specific treatment plan were re-evaluated for contours drawn by each of the 3 other observers.

i. DVH

The DVH-specific metrics evaluated include the: PTV D_{98}, D_{95}, and D_{90}; the bladder-OAR/PRV D_{25}; and the rectum-OAR/PRV D_{25}. The relative difference ΔD_v between the planner and the observer were computed as:

$$\Delta D_v = \left(\frac{OD_v - PD_v}{PD_v}\right) \times 100, \qquad (1)$$

where OD_v is the dose evaluated for the observer's contour and PD_v is the dose evaluated for the planner's contour.

ii. TCP-NTCP and P+

Similarities/differences in the interobserver treatment plans (as a function of margin size) were also quantified by comparing TCP and NTCP values for structures based on the planner's and observer's contours. The PTV-TCP metric was computed for the primary target structure, whereas OAR-NTCP/PRV-NTCP was computed for each of the critical structures in the observer-specific IMRT plans. A representative P+ metric was also computed as the product of TCP, 1-$NTCP_{Bladder}$, and 1-$NTCP_{Rectum}$. The goal of these biological response metrics is to evaluate not only the distribution of alternative observers but also the differences between the planner and observers TCP-NTCP with respect to increasing margin size. The TCP-NTCP metrics were respectively evaluated using the Kallman S-model for the primary target and critical structures. The D_{50}, γ, α/β, and seriality used have previously been published (15) and correspond with default Pinnacle^3 parameters which were taken from the literature. (16, 17)

iii. Coverage Probability

The quantification of interobserver dose variation with respect to adding margins can alternatively be evaluated based upon coverage probability computations. Coverage probability Q was defined as the percentage of the systematic uncertainties introduced in the CTV and OAR positions that can be absorbed by a treatment plan. Coverage probability computations account for systematic (Σ) and random (σ) rigid body setup uncertainties (18). For the case of target (CTV), coverage $Q_{v,d}$ is the probability that the target's dose-volume metric D_v exceeds the prescribed dose d, i.e., $Q_{v,d} = Pr[D_v \geq d]$. This study evaluated both the alternative observers' coverage values, the absolute differences between the planner and observers' coverage, and whether the CTV's coverage probability ($Q_{98,79.2}$) was maintained within the planned dose distribution under the assumption that Σ and σ uncertainties are 1, 2, and 3 mm for PTV-OAR and PTV-PRV based IMRT plans. According to the VHMF , Σ = σ = 1, 2, 3 mm respectively

117 correspond to approximately 3, 6, and 10 mm margins (11). Recall that plans are generated

118 with 0, 5, and 10 mm margins in this study.

Results

Figure 1 shows the DVHs of the observer-specific treatment plans (shown in black bold) and the DVHs of alternate observers' contours for 0, 5, and 10 mm margins for patient 1. When the observer-specific PTV-OAR–based plan DVH metrics were compared with metrics based on the alternative observers' contours (

Figure 2A), less than 5% differences were observed in PTV D_{98} dose values for 83%, 81%, and 72% of the cases respectively for 0, 5, and 10 mm margins. This contradicts the hypothesis that interobserver target dose-volume variation between the planner and observer decreases with increasing margin. The observed variation at a 10 mm margin is significant (P<.05) for PTV D_{98}, D_{95}, and D_{90}. The percentage of alternative observers' rectum-OAR D_{25} within ±5% of the observer-specific planners' did not significantly decrease (P>.05), but significantly increased (P<.05) for the bladder-OAR D_{25} 5 and 10 mm margin plans. On the other hand, evaluating observer-specific PTV-PRV based plans (

Figure 2B) with the alternative observers' showed less than 5% differences in PTV D_{98} dose values for 83%, 86%, and 86% of the cases respectively for 0, 5, and 10 mm margins. Even though a slight improvement was observed in evaluating dose-volume metrics for PTV-PRV based plans, the change is not significant (P>.05) except when evaluating PTV D_{95} for 5 mm margin where the improvement is significant (P<.05). The percentage of alternative observers' rectum-PRV D_{25} within ±5% of the observer-specific planners' significantly decreases (P<.05), but the percentage of the alternative observers' bladder-OAR D_{25} significantly increased (P<.05) by adding 5 and 10 mm margins. Additionally, at 5 and 10 mm margins, the dose tolerance exceeded the rectum-OAR D_{25} by 8% and 47%, and the bladder-OAR D_{25} by 31% and 53%.

Moreover, at 5 and 10 mm margins, the dose tolerance exceeded the rectum-PRV D_{25} by 3% and 22%, and the bladder-PRV D_{25} by 31% and 67%. Figure 2C displays two physician CTV contours on a single patient slice as well as the PTVs obtained by expanding those contours. Expansion from relatively small protruding differential volumes at the contour edges resulted in larger non-overlap PTV volumes, the cause of decreased coverage with increased margin.

TCP/NTCP metrics were evaluated with respect to the hypothesis that increasing margins would decrease interobserver variations in these metrics. Evaluation of observer-specific PTV-OAR–based plans with alternative observers (Figure 3A) showed median TCP values of 99.9% for both planners and observers for 0, 5, and 10 mm margins. For 0, 5, and 10 mm margins, the median planners' rectum-OAR NTCP values were 16.7%, 28%, and 32.2%, and the median observers' rectum-OAR NTCP values were 16.5%, 27.4%, and 32.1%. Similarly, for 0, 5, and 10 mm margins, the median planners' bladder-OAR NTCP values were 0.1%, 8.2%, and 18%, and observers' bladder-OAR NTCP values were 0.1%, 7.6%, and 16.4%. Evaluating observer-specific PTV-PRV based plans with alternative observers (Figure 3B) also showed median TCP values of 99.9% for both planners and observers for 0, 5, and 10 mm margins. For 0, 5, and 10 mm margins, the median planners' rectum-PRV NTCP values were 16.7%, 29.7%, and 32.9%, and the observers' rectum-PRV NTCP values were 16.5%, 28.7%, and 33%. Similarly, for 0, 5, and 10 mm margins, the median planners' bladder-PRV NTCP values were 0.1%, 6.6%, and 12.9%, and the observers' bladder-PRV NTCP values were 0.1%, 6.4%, 12.7%. Figure 3 summarizes the TCP-NTCP distribution and the distribution of absolute differences between alternative observers and observer-specific planners for PTV-OAR and PTV-PRV based plans. The extreme interobserver's TCP value decreased with increasing margin size, but at the

expense of increasing predicted dose-toxicity to the critical structures. The increasing NTCP spread for alternative observers with respect to increasing margins is significant (P<.05).

Coverage probability analysis results are presented in Figure 4–6. The range of alternative observers CTV and OAR coverage uncertainties increased around the median as both Σ=σ increases from 1 to 3 mm. The spread of interobserver coverage around the median (shown as stars for observer-specific planners and triangles for alternative observers) significantly decreased (P<.05; Figure 4) with increasing margins in PTV-OAR and PTV-PRV based plans. This is expected from the VHMF, which estimates the margin required to absorb systematic and random uncertainties. The interobserver CTV $Q_{98,79.2}$ variation decreased with increasing margin but, again, at the expense of increasing dose-toxicity to critical structures as noted in Figure 5 and Figure 6.

Discussion

The differences we observed in DVH metrics for different observer contours agrees with the findings of Bhardwaj (1), who only studied a single margin size. Contrary to our initial hypothesis, the DVH-based evaluation metrics showed an increase in interobserver variability as margins increased, especially for the 10 mm margin. For some patients, evaluation with another observer's contours resulted in an apparent failure to cover the PTV as the margin increased. The cause of this effect was traced to protruding portions in some observer's contours which resulted in an expanded volume extending into otherwise unoccupied volumes (Figure 2C). The DVH based dose-volume metrics suggest that adding a margin to the target is not beneficial for the purpose of reducing or eliminating dose-volume-based dosimetric differences between plans developed using different observers contours.

Both PTV-OAR–based plans and PTV-PRV–based plans were used in this study as the former plan represents clinical practice used at our institution (and many others) , while the latter plan corresponds with ICRU recommendations, and would be expected to afford greater protection to critical structures. The slight improvement observed in DVH-based metrics for PTV-PRV based plans was not significant. Although the bladder D_{25} interobserver dose variation significantly decreased as the margin increased, many of the large margin alternative-observer OARs and PRVs exceed the optimization dose tolerance.

Computing biological response indices is suitable for this study as it provides a surrogate for expected relative clinical response. The effect of the small protruding volumes of the CTV, which negatively affected the dose-volume metrics, had no effect on TCP values. PTV TCP value variability was found to decrease with increasing margins for both PTV-OAR and PTV-PRV–

196 based plans (Figure 3). As expected, the effect of dose toxicity on critical structures was
197 significantly increased as the margin increased, and increased interobserver NTCP variability
198 was also observed with increasing margins. These results indicate that there is a compromise in
199 dealing with the effects of differing (protruding) volumes of the CTV; however, better NTCP can
200 be achieved by adding margins to the critical structures in the treatment plans.

201 P+ summarizes the biological response of added margins (Figure 3). The PTV-PRV–based
202 plans have less NTCP variation than PTV-OAR–based plans. Additional metrics, such as
203 probability maps (19), could additionally be used to quantify interobserver dose coverage
204 variations.

205 The coverage probability metric additionally demonstrated that the effect of small
206 protruding volumes of the CTV is insignificant as uncertainties introduced in the CTV (Figure 4)
207 are absorbed with increasing margins for both the PTV-OAR and PTV-PRV–based plans. For 5
208 mm margin plans, the median planners' and observers' $Q_{98,79.2}$=93% at $\Sigma = \sigma$=2 mm. The VHMF
209 recommends a 6 mm margin to absorb 2 mm systematic and random uncertainties (11).
210 Furthermore, the median planners' and observers' $Q_{98,79.2}$=96% at $\Sigma=\sigma$=3mm, and 10 mm
211 corresponds with the VHMF margin required to absorb these uncertainties. Together, these
212 results demonstrate that the coverage results found here correspond with values expected
213 from the VHMF. Nonetheless, there is a compromise: substantial variability in OAR coverage
214 persists when alternative observer's contours are used for evaluation (Figure 5 and Figure 6).

215 The contours used in this study were drawn by four independent physician-observers
216 for the purpose of evaluating interobserver contouring variations (5). While it was desired and
217 expected that these contours be equal to those that would be used in treatment planning by
218 the same physicians, this cannot be assured. It is possible that the physician-observers relaxed

their contour quality assurance criteria in the contouring study. It is equally (prehaps more) likely, however, that the physician took extra care in the contouring process. In either case, the resultant contour sets did result in differences in DVH metrics that increased as the margin increased due do protruding sections of the base contours that were then magnified by the margin expansion process. Although not tested in this study, it is possible that use of model based segmentation or auto segmentation which restricts organs to be realistically shaped, either for patient contouring, or for manual contouring QA, or that using organ-shape databases to QA contours, may reduce the dosimetric impact of interobserver contour variability.

Conclusions

For the set of patients/contours included in this study, interobserver contour variations resulted in statistically and dosimetrically significant DVH metric differences that persist with increasing margin size. This was contrary to our expectation that dosimetric differences would decrease as margin size increased. The cause of the differences was protruding portions of the prostate contour on some observer's contours which were magnified with increased margin size. In alignment with our expectations, evaluation of the TCP showed decreased variation with increased margin size. Similarly, alternate-observer CTV coverage evaluations showed decreased variability with respect to the planners CTV coverage with increased margin size. OAR variability in NTCP and coverage values, however, persisted in spite of increased margins. Simply adding standard margins to a contour was insufficient to create a plan that was robust to interobserver contour variability in the CTV and OARs encountered in the prostate radiation therapy plans studied. It may be necessary to use organ models or databases in contour quality assurance procedures to identify aberrant patient contours.

Acknowledgements

This work is supported in part by NIH-P01-CA 116602 and Philips Medical Systems. We would like to thank Kevin T. Hogan for editorial assistance with the manuscript and Drs. Elisabeth Weiss, Priya Mitra, Michael Myers, and Tatjana Ivanova for performing the contouring study.

Bibliography

1. Bhardwaj AK, Kehwar T s., Chakarvarti S k., *et al.* Variations in inter-observer contouring and its impact on dosimetric and radiobiological parameters for intensity-modulated radiotherapy planning in treatment of localised prostate cancer. *Journal of Radiotherapy in Practice*. 2008;7:77–88.

2. Fiorino C, Reni M, Bolognesi A, *et al.* Intra- and inter-observer variability in contouring prostate and seminal vesicles: implications for conformal treatment planning. *Radiother Oncol*. 1998;47:285–292.

3. Petric P, Dimopoulos J, Kirisits C, *et al.* Inter- and intraobserver variation in HR-CTV contouring: intercomparison of transverse and paratransverse image orientation in 3D-MRI assisted cervix cancer brachytherapy. *Radiother Oncol*. 2008;89:164–171.

4. Weiss E, Richter S, Krauss T, *et al.* Conformal radiotherapy planning of cervix carcinoma: differences in the delineation of the clinical target volume. A comparison between gynaecologic and radiation oncologists. *Radiother Oncol*. 2003;67:87–95.

5. Weiss E, Wu J, Sleeman W, *et al.* Clinical evaluation of soft tissue organ boundary visualization on cone-beam computed tomographic imaging. *Int. J. Radiat. Oncol. Biol. Phys*. 2010;78:929–936.

6. Vorwerk H, Beckmann G, Bremer M, *et al.* The delineation of target volumes for radiotherapy of lung cancer patients. *Radiother Oncol*. 2009;91:455–460.

7. ICRU Report 50. *Prescribing, recording and reporting photon beam therapy*. Bethesda MD: ICRU Publications; 1994.

8. ICRU Report 62. *Prescribing, recording and reporting photon beam therapy (Supplement to ICRU Report 50)*. Bethesda MD: ICRU Publications; 2000.

9. Stroom JC, Storchi PRM. Automatic calculation of three-dimensional margins around treatment volumes in radiotherapy planning. *Physics in Medicine and Biology*. 1997;42:745–755.

10. Stroom JC, de Boer HC, Huizenga H, *et al.* Inclusion of geometrical uncertainties in radiotherapy treatment planning by means of coverage probability. *Int. J. Radiat. Oncol. Biol. Phys*. 1999;43:905–919.

11. van Herk M, Remeijer P, Rasch C, *et al.* The probability of correct target dosage: dose-population histograms for deriving treatment margins in radiotherapy. *Int J Radiat Oncol Biol Phys*. 2000;47:1121–35.

12. Lyman JT. Complication probability as assessed from dose-volume histograms. *Radiat Res Suppl*. 1985;8:S13–19.

13. Gordon JJ, Siebers JV. Coverage-based treatment planning: Optimizing the IMRT PTV to meet a CTV coverage criterion. *Med. Phys.* 2009;36:961–973.

14. Gordon JJ, Siebers JV. Evaluation of dosimetric margins in prostate IMRT treatment plans. *Med.Phys.* 2008;35:569–575.

15. Moore JA, Gordon JJ, Anscher MS, *et al.* Comparisons of treatment optimization directly incorporating random patient setup uncertainty with a margin-based approach. *Med Phys.* 2009;36:3880–3890.

16. Källman P, Agren A, Brahme A. Tumour and normal tissue responses to fractionated non-uniform dose delivery. *Int. J. Radiat. Biol.* 1992;62:249–262.

17. Deb P, Fielding A. Radiobiological model comparison of 3D conformal radiotherapy and IMRT plans for the treatment of prostate cancer. *Australas Phys Eng Sci Med*. 2009;32:51–61.

18. Xu H, Gordon JJ, Siebers JV. Sensitivity of postplanning target and OAR coverage estimates to dosimetric margin distribution sampling parameters. *Med. Phys.* 2011;38:1018.

19. Korporaal JG, van den Berg CAT, Groenendaal G, *et al.* The use of probability maps to deal with the uncertainties in prostate cancer delineation. *Radiotherapy and Oncology*. 2010;94:168–172.

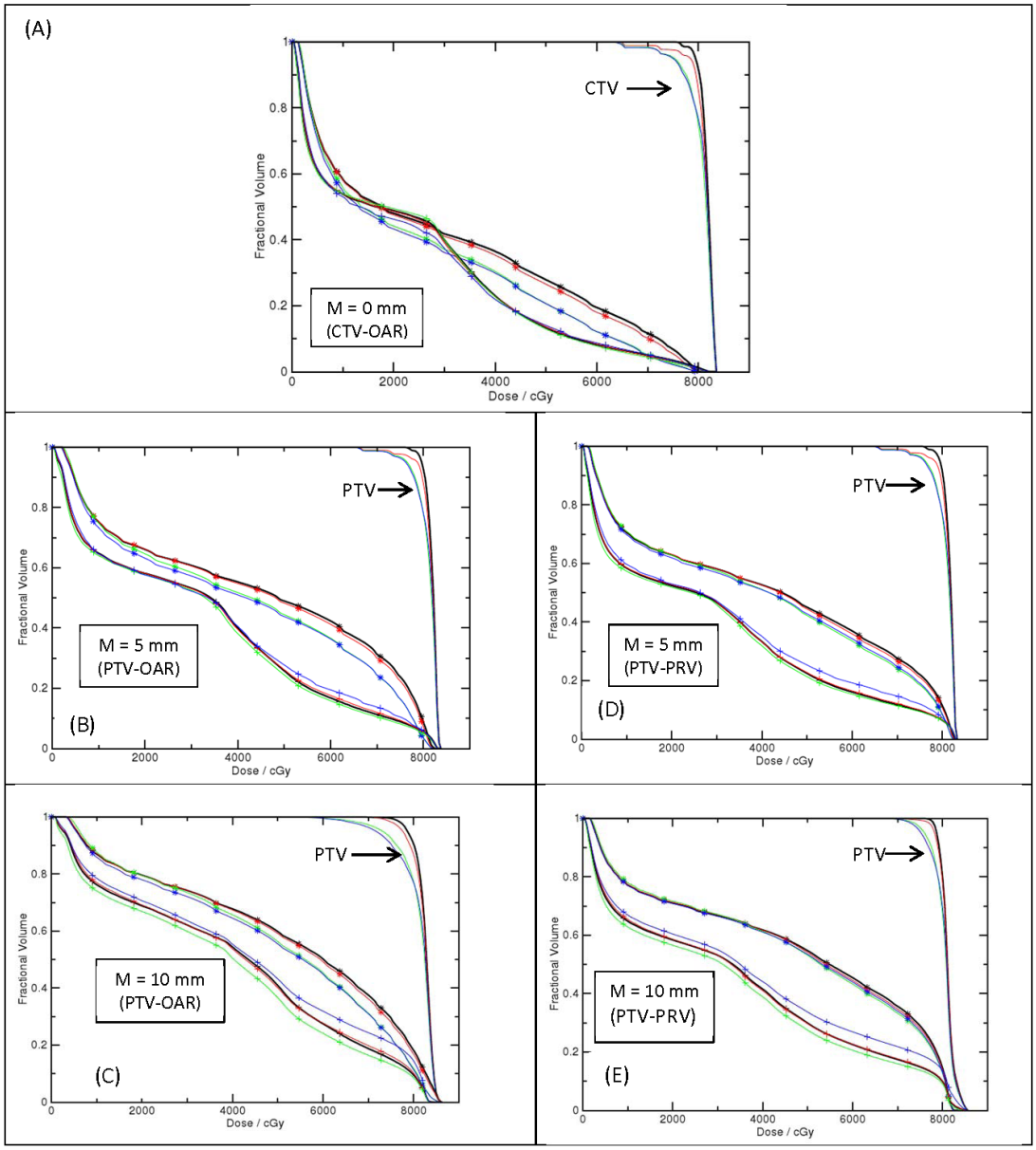

298 Figure 1. DVHs of observer-specific planner A (black bold lines) and alternative observers' contours
299 (colored lines) for (A) 0 mm CTV-OAR, (B) 5 mm PTV- OAR, (C) 10 mm PTV- OAR, (D) 5 mm PTV-PRV, and
300 (E) 10 mm PTV-PRV plans. Rectum is demarked with +, Bladder with *.
301

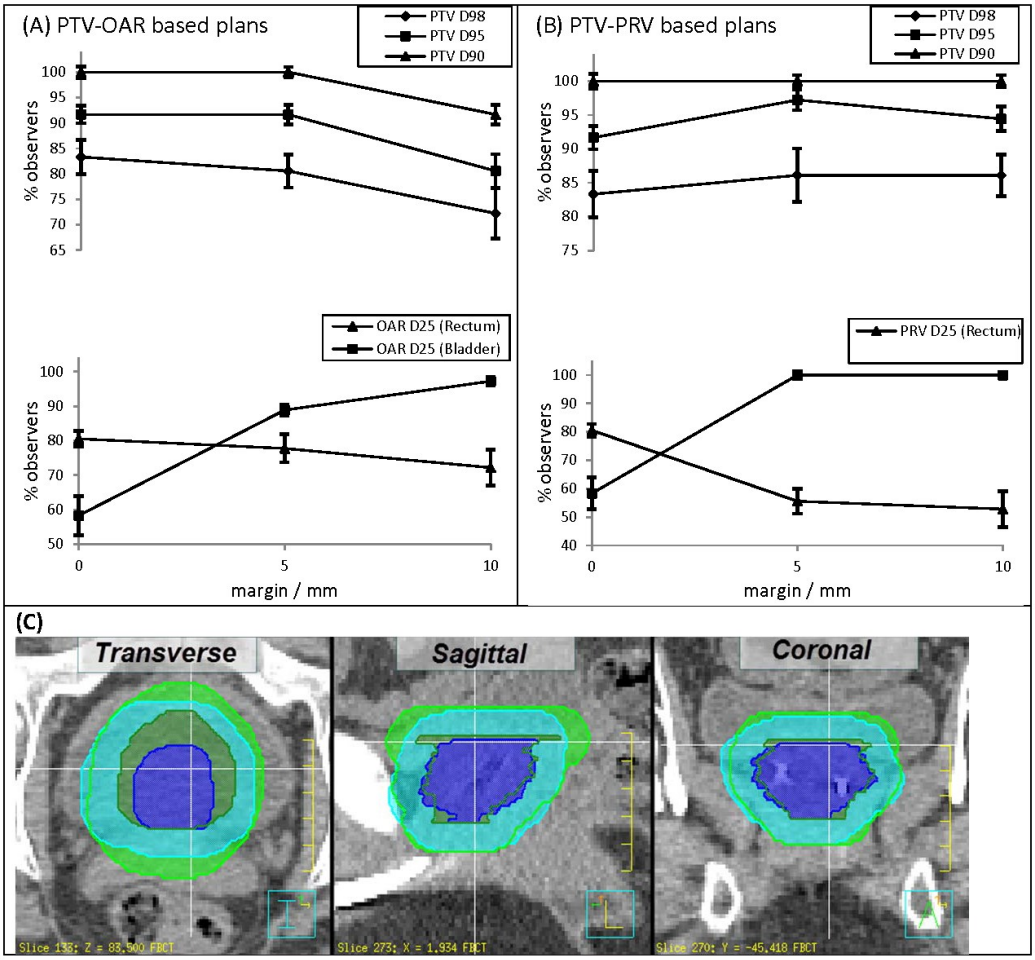

Figure 2. Percentage of alternative observers (A) within ±5% of the observer-specific planners for PTV D_{98}, D_{95}, D_{90} and OAR D_{25} for rectum and bladder dose-volume metrics in PTV-OAR based plans and (B) PTV-PRV based plans. The cause of decreased PTV agreement with increasing margin is demonstrated in (C) where two observers' CTV contours are shown (blue and forest green) as well as the PTV contours for 1 cm margins (sky blue and light green respectively). The protruding portion on the top of the forest green CTV (sagittal view) results in a PTV (light green) that has poor overlap with PTV constructed from the alternative observers' contour (sky blue).

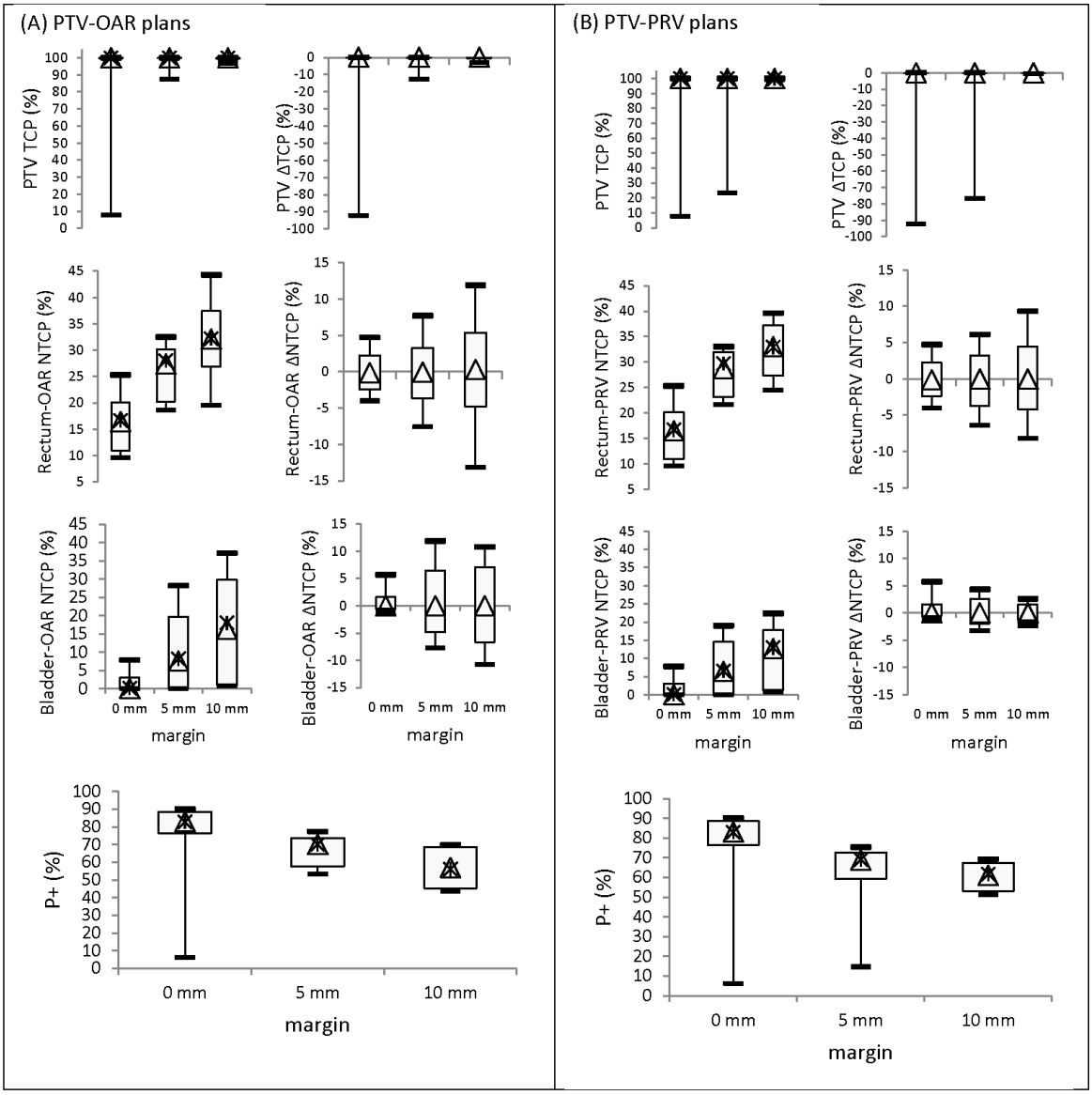

311
312 Figure 3. Box plots (10th to 90th percentile) for alternative observers TCP, NTCP and P+ for (A) PTV-OAR
313 and (B) PTV-PRV-based plans. Additionally, absolute differences between alternative observers and
314 observer-specific plans are given. The upper and lower whiskers are the maximum and minimum values,
315 the triangle is the median value of alternative-observers. The star is the median of observer-specific
316 planners.
317

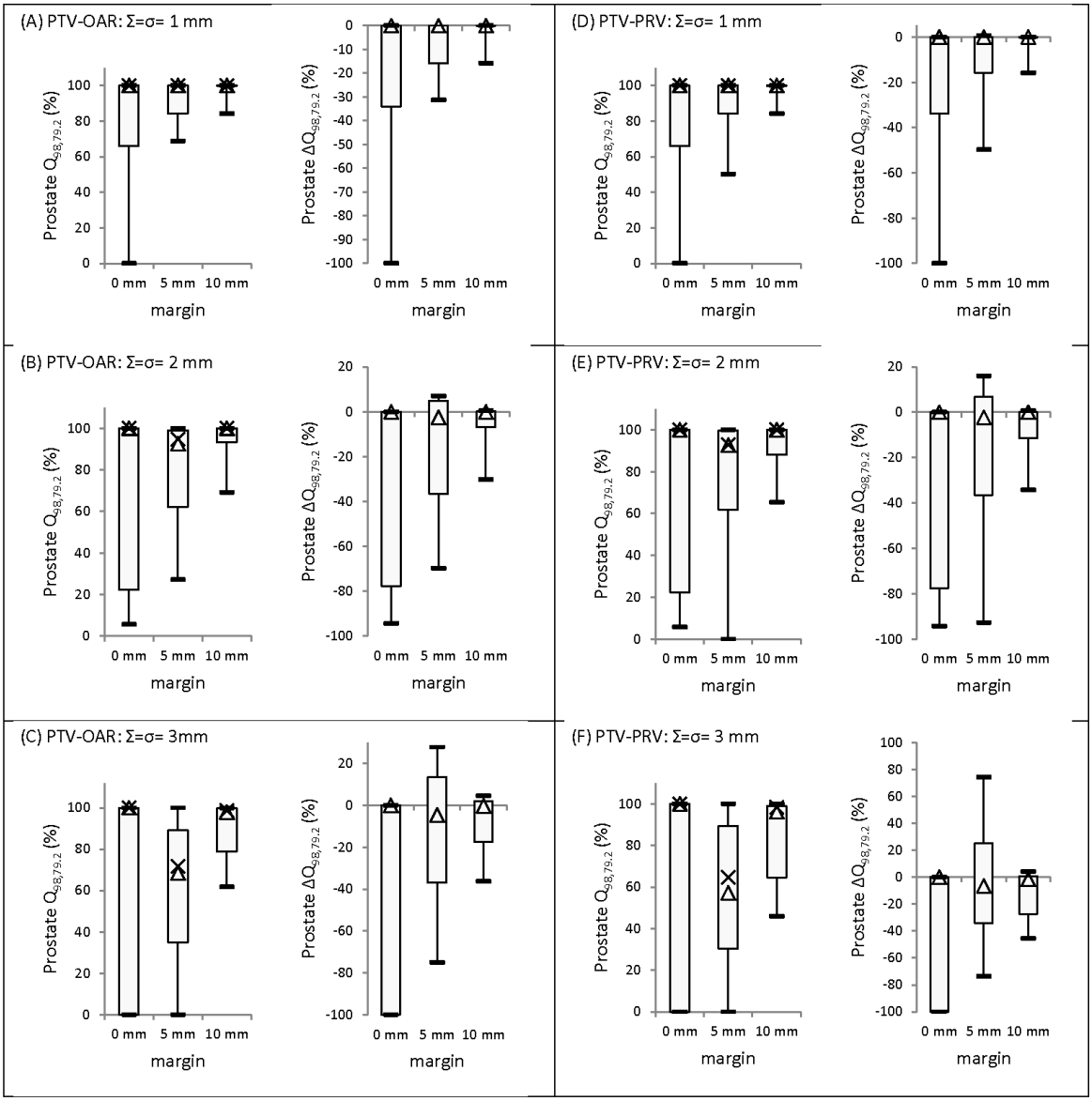

Figure 4. Box plots (10th to 90th percentile) of alternative observers CTV $Q_{98,79.2}$ for PTV-OAR and PTV-PRV-based plans and absolute differences between alternative observers' and observer-specific plans. The upper and lower whiskers are the maximum and minimum values, the triangle is the median value of alternative-observers. The star is the median of observer-specific plans.

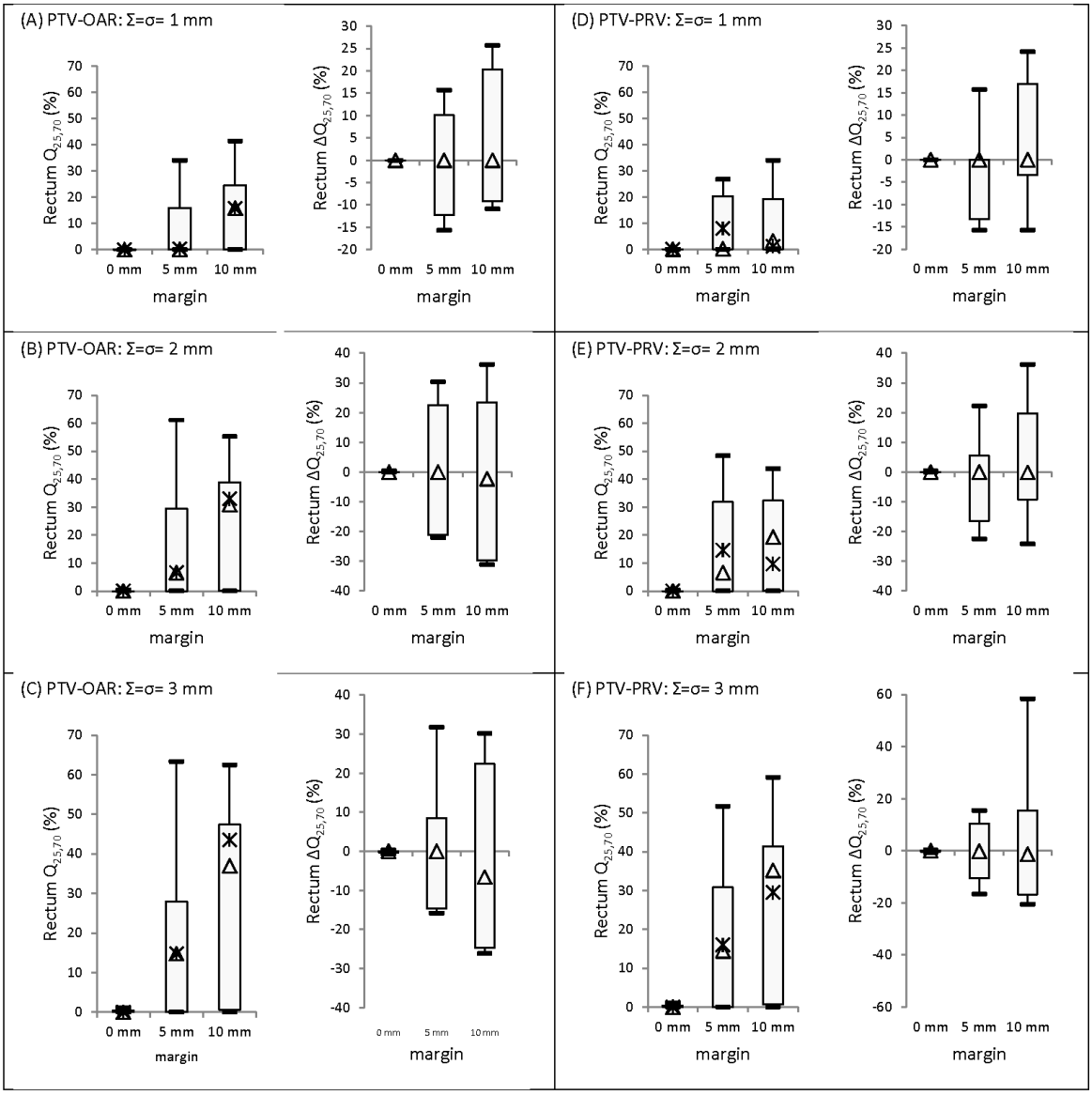

Figure 5. Box plots (10^{th} to 90^{th} percentile) of alternative observers' Rectum-OAR $Q_{25,70}$ for PTV-OAR and PTV-PRV based plans and absolute differences between alternative observers' and observer-specific plans. The upper and lower whiskers are the maximum and minimum values and the triangle is the median value of alternative-observers. The star is the median of observer-specific plan.

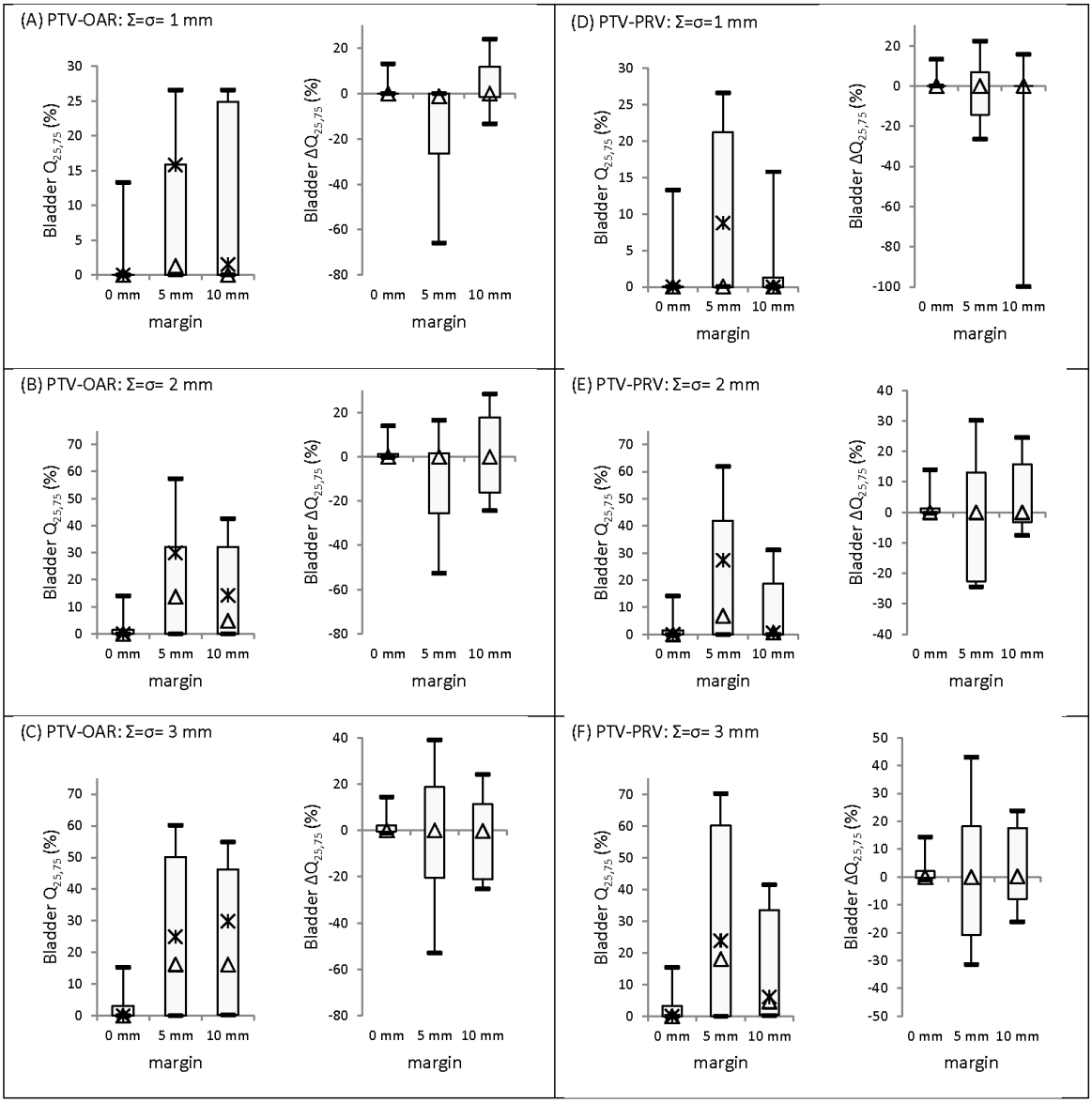

330

331 Figure 6. Box plots (10th to 90th percentile) of alternative observers' Bladder-OAR $Q_{25,70}$ for PTV-OAR and
332 PTV-PRV based plans and absolute differences between alternative observers' and observer-specific
333 plans. The upper and lower whiskers are the maximum and minimum values and the triangle is the
334 median value of alternative-observers. The star is the median of observer-specific plans.

d. Bladder wall characteristics

Characteristics of bladder wall deformation as a function of bladder filling

H. Xu and J.V. Siebers

Virginia Commonwealth University, 401 College Street, Richmond, VA, USA

E-mail: xuh2@vcu.edu

Abstract. The purpose of this study was to verify how base characteristics of the bladder wall change as a function of bladder filling so as to guide interfractional bladder wall delineation and image registration for adaptive radiation therapy. Two freshly removed pig bladders were imaged by computed tomography (CT) at different filling volumes: one bladder was imaged in air while filled with up to 400 cm^3 air; the other was imaged in water while filled with up to 600 cm^3 water. The CT images were imported into a commercial treatment system for delineation and statistical analysis of bladder wall thickness (BWT) and bladder wall density. As the bladder expanded, the bladder wall thinned from 3.1 mm to 1.1 mm, but the average apparent density (mean CT number) varied less than 2.3%. The BWT changes as a function of bladder filling, while the bladder wall density can be regarded as constant. This implies that, when used for interfractional delineation in adaptive radiation therapy, ICRU 83 recommended bladder wall contours should account for thickness variations and registrations should conserve bladder wall mass/volume between different bladder filling states.

1. Introduction

Understanding the role of bladder wall volume variation in planning external beam radiation therapy (EBRT) is important not only for treating bladder cancer, but also for estimating the expected normal tissue toxicity for other cancers. Prostate cancer using intensity-modulated radiation therapy (IMRT) treatment planning is an example: ICRU 83 report (ICRU Report 83 2011) recommends that for hollow organs-at-risk (OAR) such as the bladder, the wall should be used instead of the whole organ. As the bladder is not only a dose limiting structure in EBRT, but also the main driver of pelvic organ motion (Ten Haken *et al* 1991) due to filling-induced movement and deformation, knowledge of bladder wall variation due to the filling effect is essential. Inappropriate delineation or image registration of bladder wall during planning and treatment of EBRT may result in incorrect OAR dose evaluation. This can lead to suboptimal OAR sparing or missed opportunities for target coverage due to overrepresentation of the OAR dose during the planning process.

Studies that quantify bladder properties at different filling status are limited. For patient cases, imaging quality is limited due to the realistic concerns such as imaging dose constraints, image data size and medical cost. Consequently, poor imaging quality complicates delineation. With ultrasound imaging, the boundaries of the inner and outer bladder walls are both blurred, yielding thickness precision that at best is tenths of millimeters (Hakenberg *et al* 2000). In computed tomography (CT), insufficient contrast exists between the bladder inner wall and the uterine wall due to their similar apparent density. Furthermore, when voxel dimensions (e.g., 2 mm) are similar to the BWT, bladder wall measurements have limited accuracy. Magnetic resonance imaging (MRI) has superior image quality, but is rarely used in EBRT, especially for prostate cancer.

To date, no study has directly addressed how to perform delineation and image registration of bladder wall according to its characteristics as a function of bladder filling. Only some ultrasonography observations of bladder wall thickness (BWT) or weight at different states have been published. (Here, bladder weight is the organ weight excluding the weight of the contents). For BWT, there is a consensus that BWT decreases with filling states, even though different average values for a full bladder in healthy men has been reported e.g., 3.3 mm and 1.4 mm in two different studies,. (Hakenberg *et al* 2000, Oelke *et al* 2006). For bladder weight, it is indicated (Bright *et al* 2011, Hakenberg *et al* 2000) that bladder filling has a smaller effect on bladder weight that BWT. The estimated bladder weight was found to be "fairly consistent"(Bright *et al* 2011), assuming a constant bladder specific gravity (a quantity that correlates with density) (Kojima *et al* 1996). But this weak finding needs verification. Mathematical models have been built to estimating dosimetric or biological variations due to bladder deformations (Söhn *et al* 2005, Chow *et al* 2009, Lotz *et al* 2004, Chai *et al* 2011), however they cannot be used to investigate the base thickness and density characteristics.

Due to the limited guidance, the interfractional variations in bladder wall thickness are currently ignored in the clinical practice (e.g., prostate treatment plan optimization and evaluation usually uses the entire bladder in spite of the recent ICRU 83 recommendations (ICRU Report 83 2011). Even if the bladder wall is used, delineation and image registration of bladder wall is performed differently between institutions and sometimes largely depends on the experience and preference of the delineators. For instance, BWT is often assumed a constant (e.g.,3-5mm (Harsolia *et al* 2007, Cheung *et al* 2007)) independent of the filling state. One study (Rosewall *et al* 2011) stated that using a 2.5mm margin contraction of outer surface of bladder can be a quick and reproducible substitute for tedious manual bladder wall delineation. This result should be treated with caution as it may work in limited cases. After all, assuming a constant BWT at different filling states oversimplifies the true bladder wall dynamics, contradicts to the changing thickness /constant mass observations mentioned above, and may cause problems when multiple images are utilized in the dose evaluation and/or planning in EBRT.

In order to guide bladder wall delineation and image registration to aid pelvic (prostate/uterine) EBRT treatment planning, this work quantifies how bladder wall density (and therefore volume when mass is assumed to be conserved) varies in a controlled filling process in air and water environments.

Harvested pig bladders were used because: (1) they are excellent approximation of human urinary bladder due to similar thickness and histological arrangement (Borin *et al* 2008) and have been used as models in many studies (Gözen *et al* 2011, Schout *et al* 2008, Sugiono *et al* 2007, Teber *et al* 2005); (2) their filling process is easy to control; and (3) imaging quality can be greatly improved in a controlled environment with no patient motion and when there are no imaging dose constraints.

The hypothesis of this study is that, like a balloon, the bladder thins as it expands. As no mass is lost or gained by the wall during expansion, the mass can be regarded as conserved. In this case, constant density necessitates a constant volume of the bladder wall at different filling states. The implication of this hypothsesis is that bladder wall mass and/or volume constancy should be used to guide delineation and registration on multiple image sets of the same patient.

2. Methods and Materials

2.1 Pig bladders and filling setup

Two fresh bladders were harvested from deceased pigs which were used in an Institutional Animal Care and Use Committee approved study. Prior to imaging, which occurred between 6 and 48 hour post harvesting, the bladders were refrigerated in a water/ice solution to ensure freshness. One bladder was imaged in air on a low-density holder with air used to inflate the bladder. The second bladder was imaged in a water-filled plastic tank with water used to fill the bladder (Figure 1). Both bladders were filled via a syringe connected to the bladder by a 1.1 g/cm^3 tube. An air and water tight seal between the tubing and bladder was achieved by super-gluing the tube to the urethral opening.

2.2 Imaging scans and ROI delineation

The pig bladders were imaged by a Philips Brilliance CT scanner at multiple filling states. The bladders were filled with up to 360 cm^3 air or 600 cm^3 water in ~60 cm^3 increments. CT acquisition parameters are listed in Table 1. The CT images were imported into the Pinnacle^3 planning system (Philips Medical Systems, Fitchburg, WI) for analysis. The clinically used HU-to-density translation table was used. (HU_{air} = 0, HU_{water} = 1000)

Regions of interest (ROIs) were created to define the bladder wall. For the in air scenario, the original inner and outer bladder surfaces (the original bladder wall (oBW) was auto-contoured using a CT number threshold of 800-1200, followed by manual slice-by-slice review and editing to ensure adherence to the wall contour. For the in water scenario, the oBW was manually delineated since the auto-contouring algorithm poorly differentiates the water/bladder tissue interface. The tubing connected to the bladder tissue was excluded from oBW via auto-contouring with a CT number threshold greater than water. Due to contouring imprecision, the manually delineated contours inherently contain some water. To correct for this, a water volume outside the bladder and distant from the oBW was sampled to represent the HU distribution of water to be removed. Expanded bladder wall volumes were created via 2 mm, 3 mm, and 4 mm uniform expansions from the oBW. From this, water in the margin area (W_xmm = expansions – oBW, x = 2,3,4), was used to represent the extraneous water included in the oBW contour. Namely, water removed from oBW was assumed to have the same mean and the same SD values as the W_xmm rings. Given the oBW and W_xmm statistics, the statistics of the true bladder wall (BW) were determined.

2.3 CT number analysis (Bladder wall in air)

In air, the contrast between the bladder and the surrounding environment is large. For each filling state, the coronal CT slice with the largest cross-section of bladder wall was selected to determine the wall thickness. On this slice, 50 CT profiles normal to the tangent of wall arc were sampled evenly on the cross section. The full width at half maximum (FWHM) of each the profiles was calculated (as the example in Figure 3b) and the average over all profiles computed. The resulting average value was regarded as the BWT for the given filling state. Sagittal or transverse slices were excluded because residual water on top of the bladder and that absorbed on the bladder base holder negatively affects the wall thickness distributions.

2.4 CT number analysis (Bladder wall in water)

In water, the low image contrast necessitated the use of statistical analysis to separate the bladder wall from the surrounding wall. Two methods were used.

The first method (M1) used mathematical deduction, which assumed that the CT number data of oBW, W_xmm and BW follow normal distributions. The CT data for the oBW and W_xmm contours

(Table 2) were imported into Matlab to calculate mean and SD values of two assumed Gaussian distributions of oBW and W_xmm. Prior to statistical analysis, a cutoff was applied to the original histograms to eliminate the data contributed by an air bubble in the bladder inner volume or the outer limits of the water tank. As the BW was also assumed to be normally distributed, the CT number (x) distribution of oBW, W_xmm or BW can be written as

$$f(x;\mu,\sigma)=\frac{1}{\sqrt{2\pi}\sigma}e^{-\frac{(x-\mu)^2}{2\sigma^2}} \tag{1}$$

with μ and σ being the mean and standard deviation of the distribution respectively. The corresponding expectation values of x, x^2, x^3 are

$$E[x]=\mu \tag{2}$$

$$E[x^2]=\mu^2+\sigma^2 \tag{3}$$

$$E[x^3]=\mu(\mu^2+3\sigma^2) \tag{4}$$

Assuming that the distribution of W_xmm was representative to the water to be excluded in oBW, we have

$$f_{oBW}(x)=af_{W\_xmm}(x)+(1-a)f_{BW}(x) \tag{5}$$

where a is the proportion of water. According to the definition of expectation value and (5),

$$E[x]_{oBW}=aE[x]_{W\_xmm}+(1-a)E[x]_{BW} \tag{6}$$

$$E[x^2]_{oBW}=aE[x^2]_{W\_xmm}+(1-a)E[x^2]_{BW} \tag{7}$$

$$E[x^3]_{oBW}=aE[x^3]_{W\_xmm}+(1-a)E[x^3]_{BW} \tag{8}$$

Via substitution, two reasonable solutions were found

$$\begin{cases} a=\dfrac{3({\sigma_{oBW}}^2-{\sigma_{W\_xmm}}^2)-(\mu_{oBW}-\mu_{W\_xmm})^2}{3({\sigma_{oBW}}^2-{\sigma_{W\_xmm}}^2)+(\mu_{oBW}-\mu_{W\_xmm})^2} \\ \mu_{BW}=\dfrac{{\mu_{oBW}}^2-{\mu_{W\_xmm}}^2+3{\sigma_{oBW}}^2-3{\sigma_{W\_xmm}}^2}{2(\mu_{oBW}-\mu_{W\_xmm})} \\ \sigma_{BW}=\dfrac{\sqrt{(\mu_{oBW}-\mu_{W\_xmm})^4-3({\sigma_{oBW}}^2-{\sigma_{W\_xmm}}^2)^2+2(\mu_{oBW}-\mu_{W\_xmm})^2({\sigma_{oBW}}^2+{\sigma_{W\_xmm}}^2)}}{2(\mu_{oBW}-\mu_{W\_xmm})} \end{cases} \tag{9}$$

or

$$\begin{cases} a=0 \\ \mu_{BW}=\mu_{oBW} \\ \sigma_{BW}=\sigma_{oBW} \end{cases} \tag{10}$$

Complex (non-real) solutions were removed. As we believe oBW contains water in most cases, solution set (9) was used first. In one case solution set (9) yielded an $a<0$; therefore, solution set (10) was used. As a result, with known $\mu_{oBW}, \sigma_{oBW}, \mu_{W\_xmm}$ and σ_{W_xmm}, μ_{BW} and σ_{BW} can be calculated.

The second method (M2) to determine the bladder wall distribution only assumed that the CT number data of water and BW were normally distributed. This was deemed reasonable to account for CT noise

and normal tissue variations. The cutoff-truncated CT data in Table 2 were fitted to a sum of normal distributions of BW and water using non-linear least squares. The initial parameters of the fit (obtained from M1) set the mean and SD of W_xmm distribution to that of the input data. Matlab was used to execute the fitting.

The CT number of each ROI can be influenced by different kVp and mAs during CT scanning, due to effects such as beam hardening and scatter. To eliminate this influence, μ_{BW} was normalized to $\mu_{BW,n}$ as

$$\mu_{BW,n} = (\mu_{BW} / \mu_{W\_xmm}) \times 1000, \quad (11)$$

where 1000 is the CT number corresponding to water.

3. Results

CT images for the bladder wall at three filling states in either air or water are shown in Figure 2. The bladder wall contrast degraded as the filling volume increased, especially in the water environment. The different CT parameters used in the scanning (Table 1) did not result in a pronounced difference in contrast.

3.1 Bladder wall in air

When in an air environment, the bladder was filled with up to ~360 cm^3 air. The inner air volume increased from 43 to 410 cm^3 ($\Delta V = 367$ cm^3). The bladder wall thinned with increased internal volume (Figure 3a). The measured BWT decreased from 3.1 to 1.1 mm. The relationship between ΔV and BWT was fitted as

$$BWT = 1.7102 \cdot \Delta V^{-0.468} \tag{12}$$

where $R^2 = 0.9924$ showing that the goodness of fitting is very close to the perfect value $R^2 = 1$.

With an inner volume of ~200 cm^3, the bladder was scanned at 90 kVp, 99 mAs and with 120 kVp, 400 mAs. There were no discernible differences in our measured BWT for these scans, indicating an insensitivity of our results to scanning parameters. With the same CT scan parameters at the emptiest and fullest filling states, the average peak CT number of 50 CT profiles decreased from 1070 to 588. As the bladder wall CT number was greater than that of water when the bladder was scanned in water (Figure 2), the in air decrease in bladder wall CT number was attributed to partial volume effects (bladder and air in single voxel) caused by the 0.5 mm voxels.

3.2 Bladder wall in water

In the water environment, filling the bladder with water resulted in the inner bladder volume increasing from 123 cm^3 to 600 cm^3 ($\Delta V = 477$ cm^3). After truncation (Table 2), the CT number distribution is similar to that of a normal distribution. The poorest (V =123 cm^3) and best (V =260 cm^3) fits for the mathematical deduction method are illustrated in Figure 4. The distributions for the poorest case are not strictly normal and yield little difference between the oBW and the sum of BW and water volume histograms. For all other filling states, the mathematical deduction M1 yields results in which the subtraction of water from oBW gives an acceptable normal distribution of BW, similar to that shown for the best case.

The means ($\pm 2 \cdot$ SEM (standard error of the mean)) for BW and water volumes (using W_2mm, W_3mm and W_4mm data) obtained from equation (9) or (10) as a function of the filling volume are shown in Figure 5a. The 2 x SEM (~ 95% confidence interval) is small because of the large number of samples. The mean CT values based on different W_xmm differ by less than 0.5% with respect to each other. The changing trend of CT numbers during bladder expansion for both BW and the water volumes are very similar, with both within a ±3% variation. This variation range also agrees with the results obtained from the M2 fitting (Figure 5b). Here, root-mean-square error (RMSE of fitting results is 1058 for the first filling states and smaller than 493 for the rest. RMSE is also known as the standard deviation for an unbiased estimator.

To eliminate the influence of different kVp and mAs during the filling process, the normalized mean CT number of BW was also calculated using equation (11) (Figure 5c). The variation through all filling states was reduced to 1.5% for the M1 method and 2.3% for the M2 fitting. These results indicate that the mean CT number (mean density) of the bladder wall changes little at different filling states, in adherence to expectations

4. Discussion

Motivated by the desire to apply ICRU 83 recommendations to hollow organs, this work intended to provide the starting point to guide self-consistent delineations, image registration and accumulated dosimetric assessment of bladder wall specifically for multifractional image guided adaptive radiation therapy. According to the ICRU 83 recommendations, additional clinical guidance for bladder wall delineation and registration is required. Though a spectrum of different methods can be found in the literature, this guidance to delineate/ register bladder wall at different filling states is still lacking. Currently, methods used for delineation and image registration of bladder wall vary between institutions. In the presence of poor image contrast, current bladder wall contours turn are somewhat arbitrary and may largely depend on subjective preference of users. While subjective contouring may or may not be adequate for single-image based radiotherapy, when adaptive processes are used with deformable image registration (DIR), dose mapping and dose assessment of bladder wall plan objectives may play a key role in the plan refinement. Therefore, accurate, or at least pseudo-realistic delineations of bladder and other deforming hollow organs may be necessary.

While it may seem intuitive that bladder wall thickness will thin as the volume increases and that the total volume (mass) of the bladder wall does not change from deformations, these assertions require verification. By investigating CT images of pig bladders at different filling status, this work addresses issues such as: "What is the relationship between bladder wall thickness and filling volume corresponding to the human bladder capacity?" and "Is it reasonable to assume that bladder wall density/volume remains unchanged at different filling status?"

The pig bladder filling volumes that were used in this study are similar to those of human beings. The filling state of the pig bladder ranged from 43 to 410 cm^3 in the air environment and from 123 to 600 cm^3 in the water environment. Though if differs from person to person, a moderately full bladder holds about 500 cm^3 urine, and can contain as much as twice of this amount. (Marieb 2008) . The micturition point at which a person feels the urge to void is between 150 cm^3 and more than 300 cm^3. (Hole 1996, Marieb 2008) For those using bladder filling control protocols prior to treatment, the range of volume change is still within the range in our study.

Compared to the whole bladder volume, with present techniques, the delineated bladder wall volume is more likely to be biased in volume and dose evaluation. In CT images, for example, clinical practice might create the bladder wall by applying a ~3 mm uniform margin from the outer bladder contour to create the wall region of interest regardless of the filling state since the inner boundary of bladder wall has poor contrast. The fault in this approach can be seen in the following scenario. Suppose the bladder is a sphere with an initial radius of 3 cm and wall thickness of 3 mm (about 82.45 cm^3 urine volume and 30.05 cm^3 bladder wall volume). If the wall is assumed to have a constant thickness, when the micturition point (point at which a person has to urinate) of 200 cm^3 is reached, the bladder wall volume would be about 54.25 cm^3, almost a two-fold increase. A constant-wall thickness assumption can result in missing volume for low bladder filling volumes and/or additional non-bladder volume at large filling volumes.

This work verifies that the bladder wall thins when the bladder expands. Bladder wall was placed in the air to get good contrast for the convenience to calculate FWHM. An empirical mathematical relationship (equation (12)) was found between BWT and estimated filling volume. This equation is not accurate due to the uncertainties introduced by filling volume estimation and FWHM sampling. However, it provides an approximation of BWT as a function of estimated filling volume. According to this, the common method to get bladder wall by uniform contraction using a constant margin can be used only when filling process is well controlled.

With the increase of bladder volume, partial volume effect becomes an issue. To further evaluate the consistency of thickness changes, we cut a piece of bladder tissue from a third bladder and used calipers to measure thickness without and with stretching. The measurements at two different positions of bladder thickness without and with stretching are 2.49 and 1.25 mm, 1.75 and 0.9 mm. These results agree with the number range obtained from the CT scans. Also, the continuous BWT decrease in Figure 3(a) indicates that even when partial volume effect the CT images, our results still seems reasonable.

This work also evaluated how the density/volume of bladder wall varies at increasing filling state. With the assumption of bladder-wall mass conservation, a constant density indicates a constant volume. It is reasonable to believe that water has consistent density in our different images, based on the results in Figure 5c. There was no apparent trend that indicates that bladder wall density changes with filling and the observed 2% variation is within the uncertainty range of the measurement. The constant volume finding can be used clinically to test if the delineations of bladder wall of e.g., different fractions are robust. It can be also used as a constraint for image registration algorithm for a deformed bladder wall.

Rosewall *et al* (Rosewall *et al* 2011) suggested contracting outer surface by a uniform margin to create bladder wall volume. With bladder filling of approximately 330 cm^3, they found bladder DVHs based on a constant contraction using 2.5mm margin and a volume-conserved contraction did not differ much from the one based on the manual delineation. However, this does not mean that these two contraction methods yield the same dosimetric effect. First, DVHs may not be representative to the true dosimetric effect since they lose spatial information of three-dimensional dose distribution. The decreases/increases in the dose evaluated to the bladder caused by bladder wall thinning/thickening may cancel out coincidentally when 3D information is substituted into 2D. More metrics such as equivalent uniform dose (EUD), normal tissue complication probability (NTCP) should also be calculated and compared as they are very sensitive to the dose difference in the high dose region. Otherwise, inappropriate inclusion or exclusion bladder wall volume makes dose distribution optimization more difficult, e.g., for prostate cancer when balancing the tradeoff of bladder dose sparing and target coverage. Second, it is not easy to directly determine the constant margin for outer surface contraction. The magnitude of BWT may be affected greatly by the factors such as different patient and filling protocol. So a more realistic way to account for bladder wall compression/ expansion is recommended as follows; First, start from a well delineated bladder wall contour (by some delineation experts). And then follow the rule of volume conservation for delineation and DIR of bladder wall at different filling states. Specifically for DIR, a volume-conserved objective can be used.

5. Conclusions

This work evaluates the variations in bladder wall thickness and density as a function the amount bladder filling. As expected, the pig BWT decreases with increased filling. The CT number (hence apparent density) of the bladder wall changes little as the bladder expands. For a mass-conserved bladder wall, it is appropriate to assume a constant volume for bladder wall delineation and to use this property to quality assure of assist with image registration.

Acknowledgements

This work is supported by P01CA116602. We wish to thank Prof. Kevin R. Ward and Ms. Juliana A. Medina for providing the pig bladders, and Kevin T. Hogan for editorial assistance with the manuscript.

References

Bright E, Pearcy R and Abrams P 2011 Automatic evaluation of ultrasonography-estimated bladder weight and bladder wall thickness in community-dwelling men with presumably normal bladder function *BJU International*

Chai X, Van Herk M, Van de Kamer J B, Hulshof M C C M, Remeijer P, Lotz H T and Bel A 2011 Finite element based bladder modeling for image-guided radiotherapy of bladder cancer *Med. Phys.* **38** 142

Chow J C L, Jiang R and Markel D 2009 The effect of interfraction prostate motion on IMRT plans: a dose-volume histogram analysis using a Gaussian error function model *J Appl Clin Med Phys* **10** 3055

Hakenberg O W, Linne C, Manseck A and Wirth M P 2000 Bladder wall thickness in normal adults and men with mild lower urinary tract symptoms and benign prostatic enlargement *Neurourol. Urodyn.* **19** 585–93

Hole J W 1996 *Human Anatomy and Physiology* (McGraw-Hill College)

ICRU Report 83 2011 *Prescribing, Recording, and Reporting Intensity-Modulated Photon-Beam Therapy (IMRT)* (Bethesda MD: ICRU Publications)

Kojima M, Inui E, Ochiai A, Naya Y, Ukimura O and Watanabe H 1996 Ultrasonic estimation of bladder weight as a measure of bladder hypertrophy in men with infravesical obstruction: a preliminary report *Urology* **47** 942–7

Lotz H T, Remeijer P, Van Herk M, Lebesque J V, De Bois J A, Zijp L J and Moonen L M 2004 A model to predict bladder shapes from changes in bladder and rectal filling *Med Phys* **31** 1415–23

Marieb E 2008 *Essentials Of Human Anatomy And Physiology,9th Edition* (Benjamin Cummings)

Oelke M, Höfner K, Jonas U, Ubbink D, De la Rosette J and Wijkstra H 2006 Ultrasound measurement of detrusor wall thickness in healthy adults *Neurourol. Urodyn.* **25** 308–317; discussion 318

Rosewall T, Bayley A J, Chung P, Le L W, Xie J, Baxi S, Catton C N, Currie G, Wheat J and Milosevic M 2011 The effect of delineation method and observer variability on bladder dose-volume histograms for prostate intensity modulated radiotherapy *Radiother Oncol* **101** 479–85

Söhn M, Birkner M, Yan D and Alber M 2005 Modelling individual geometric variation based on dominant eigenmodes of organ deformation: implementation and evaluation *Phys Med Biol* **50** 5893–908

Ten Haken R K, Forman J D, Heimburger D K, Gerhardsson A, McShan D L, Perez-Tamayo C, Schoeppel S L and Lichter A S 1991 Treatment planning issues related to prostate movement in response to differential filling of the rectum and bladder *Int. J. Radiat. Oncol. Biol. Phys* **20** 1317–24

Table 1. CT[a] parameters for bladder scanning

Parameter	Air	Water
kVp,mAs	90 kVp, 99 mAs or	120 kVp, 400 mAs or
	120 kVp, 400 mAs	90 kVp, 200 mAs
Pixel size	LR, AP, SI: <0.5 mm	LR, AP: <0.5 mm, SI: <1mm

[a] CT = computed tomography.

Table 2. CT[a] number statistics of bladder wall at different filling state in water environment

Filling volume (cm^3)	CT data cutoff	
	oBW[b]	W_xmm[c]
123	960, 1060	960,1040
188	950, 1150	960,1100
260	950, 1150	960,1120
360	950, 1050	960,1040
400	900, 1100	900,1080
520	900, 1100	900,1080
600	950, 1050	940,1040

[a] CT = computed tomography.
[b] oBW = original bladder wall.
[c] W_xmm = expansions – oBW, x = 2,3,4.

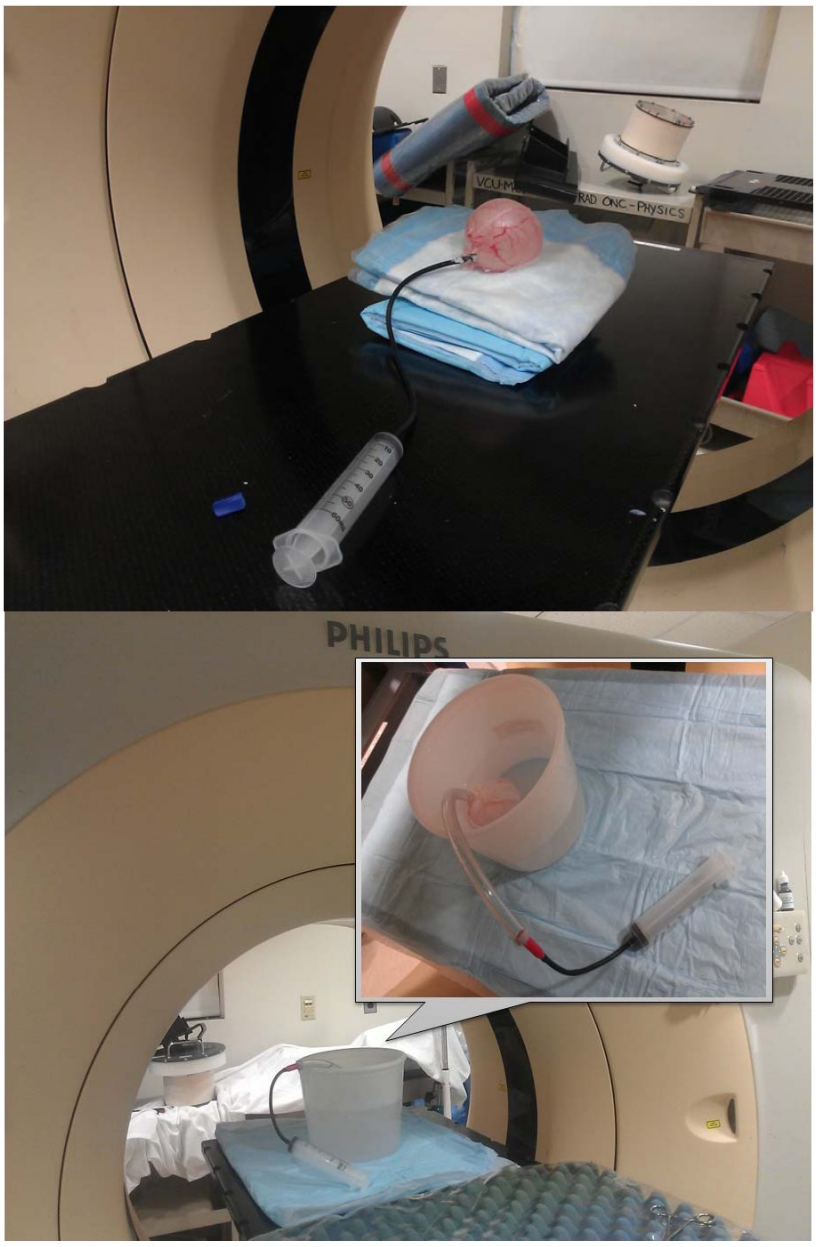

Figure 1. Setup of the filling system for the bladder in an air environment (top) and a water environment (bottom).

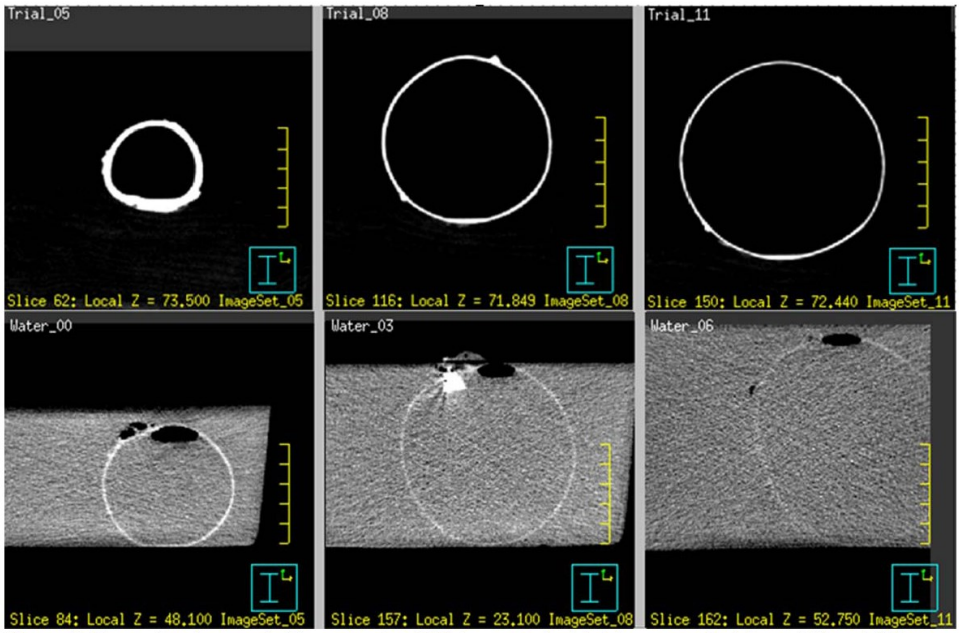

Figure 2. Example of computed tomography (CT) images of a bladder scanned at three different filling states in an air (upper row) and water (lower row) environment.

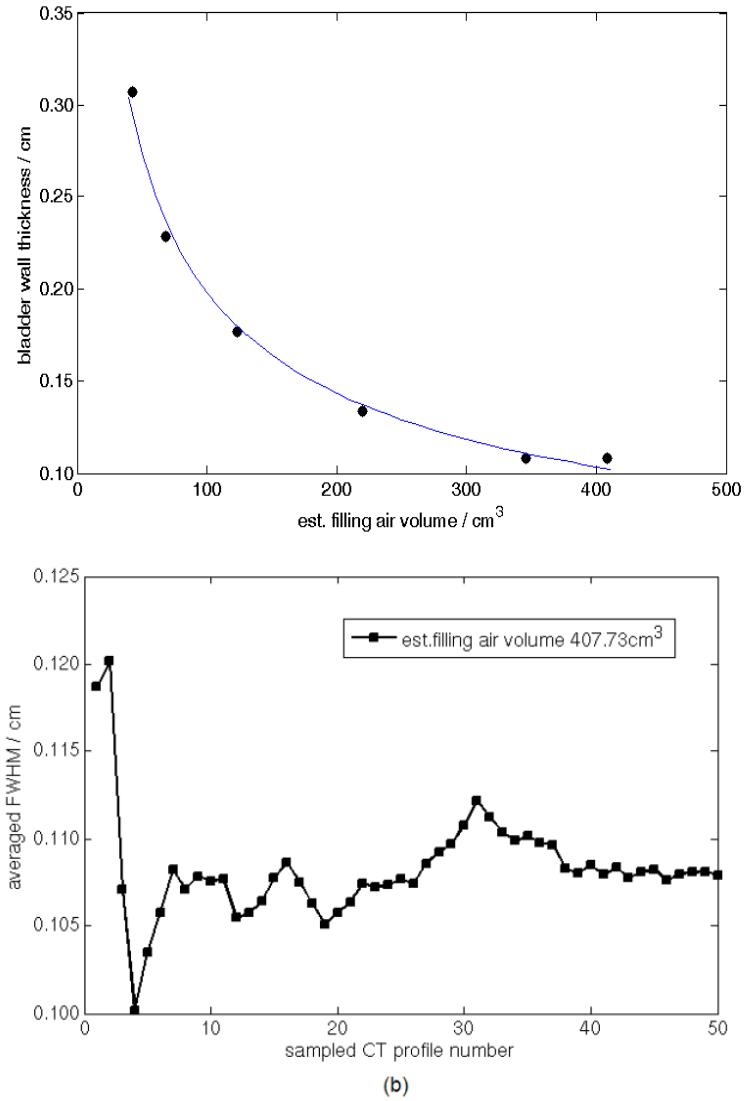

Figure 3. (a) Using 50 computed tomography (CT) profiles per filling state, bladder wall thickness (BWT) variation (round dots) and its fitting curve as a function of filling state with different estimated filling volume in air environment; (b) Variation of averaged full width at half maximum (FWHM) of CT number data with different number of sampled CT profiles indicating that 50 samples was sufficient.

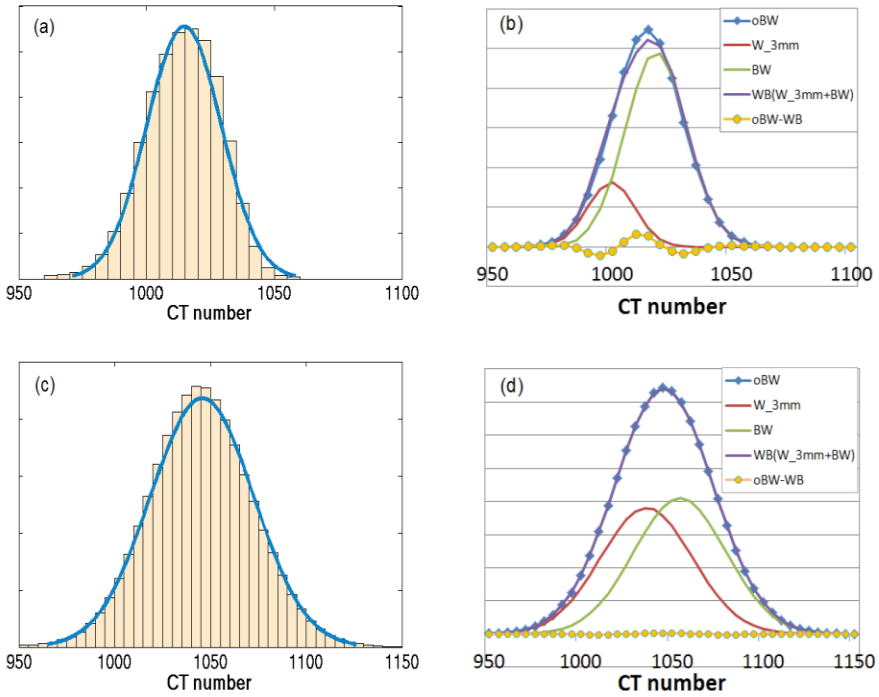

Figure 4. Examples of poorest and best fitting results using the mathematical deduction for filling states of (poorest) V=123 cm^3 (a, b) and (best) V=260 cm^3 (c, d). (a, c) Histogram and normal fitted curve (blue solid line) of the original bladder wall (oBW) after the thresholding in Table 2 was applied. (b, d) Mathematically deduced normal distributions of the water volume W_3mm (red solid line), the bladder wall (green solid line), and their sum (purple solid line), compared with oBW (blue solid line with diamond markers) and their difference (yellow solid line with round marker).

Characteristics of bladder wall deformation as a function of bladder filling

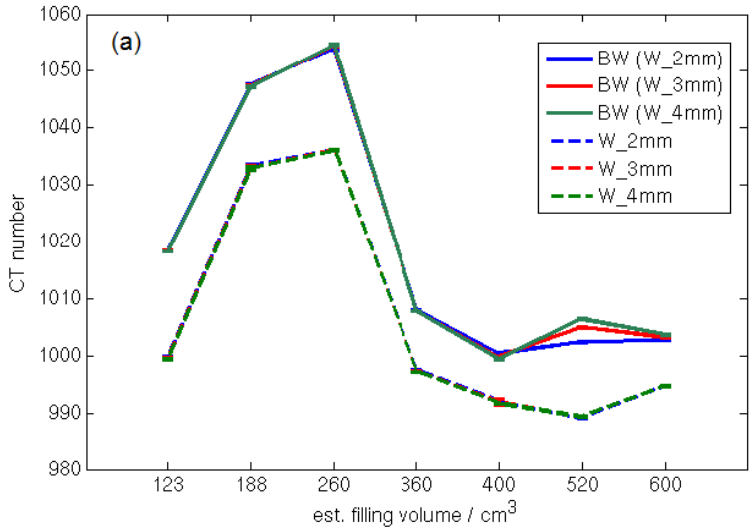

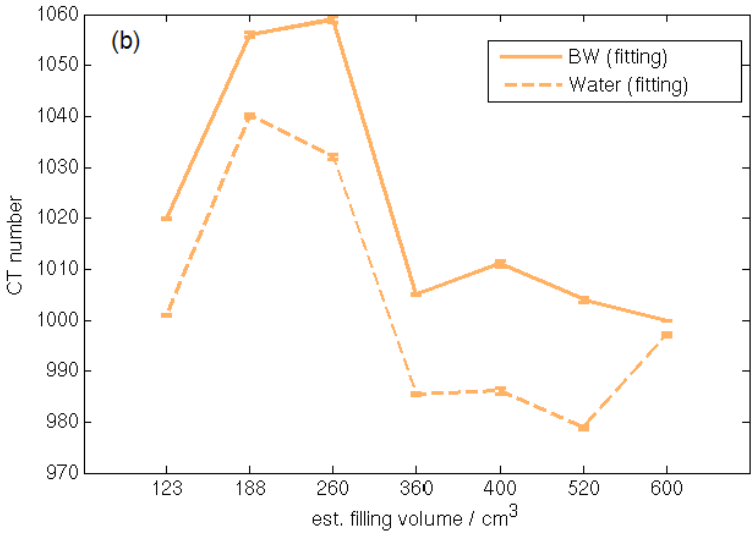

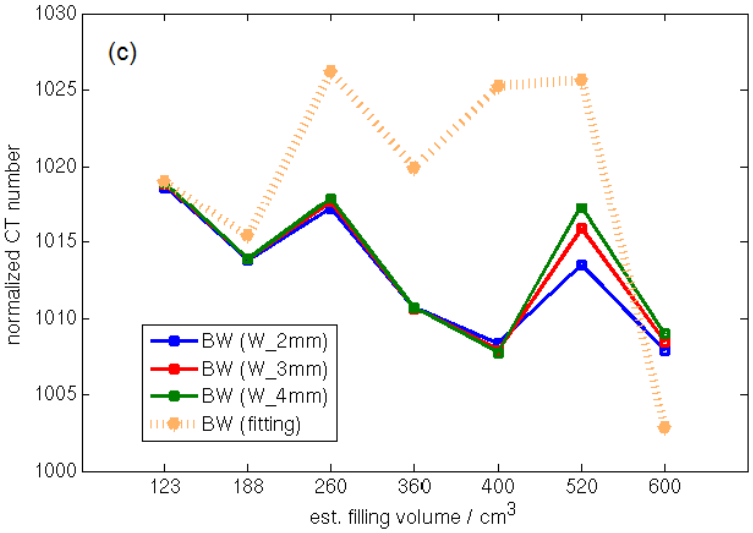

Figure 5. (a) Mean (±2xSEM) computed tomography (CT) numbers as a function of the estimated inner bladder volume for the bladder wall (BW) obtained from mathematical deduction (solid line) and the corresponding means for the water volumes (dashed line) W_2mm (blue), W_3mm (red) and W_4mm (green). (b) Mean (±2xSEM) CT number for the BW (solid orange line) and water volume (dashed orange line) obtained from fitting the oBW to the sum of two normal distributions. (c) Mean CT numbers normalized to that of water for the scan as a function of the filling volume for the BW obtained from M1 mathematical deduction using W_2mm (solid blue with square marker), W_3mm (solid red with square marker) and W_4mm (solid green with square marker) and from M2 fitting (dashed orange line with triangle marker) at different estimated filling volume.

Vita

Huijun Xu was born on January 11, 1986, in Shanghai, China, and is a Chinese citizen. She graduated from Shanghai Kongjiang Senior High School, Shanghai, China in 2004. She received her Bachelor of Science in Applied Physics from Shanghai Jiao Tong University, Shanghai, China in 2008.